uOttawa

L'Université canadienne
Canada's university

FACULTÉ DES ÉTUDES SUPÉRIEURES ET POSTOCTORALES

uOttawa

L'Université canadienne
Canada's university

FACULTY OF GRADUATE AND POSDOCTORAL STUDIES

Michelle Chrétien
AUTEUR DE LA THÈSE / AUTHOR OF THESIS

Ph.D. (Chemistry)
GRADE / DEGREE

Department of Chemistry
FACULTÉ, ÉCOLE, DÉPARTEMENT / FACULTY, SCHOOL, DEPARTMENT

Photochemical, Photophysical, and Photobiological Studies of Zeolite Guest-Host Complexes

TITRE DE LA THÈSE / TITLE OF THESIS

Tito Scaiano
DIRECTEUR (DIRECTRICE) DE LA THÈSE / THESIS SUPERVISOR

CO-DIRECTEUR (CO-DIRECTRICE) DE LA THÈSE / THESIS CO-SUPERVISOR

EXAMINATEURS (EXAMINATRICES) DE LA THÈSE / THESIS EXAMINERS

John Arnason

André Beauchemin

Edward Clennan

Robert Crutchley

Gary W. Slater
LE DOYEN DE LA FACULTÉ DES ÉTUDES SUPÉRIEURES ET POSTDOCTORALES /
DEAN OF THE FACULTY OF GRADUATE AND POSTDOCORAL STUDIES

Photochemical, Photophysical, and Photobiological Studies of Zeolite Guest-Host Complexes

Michelle N. Chrétien

A thesis submitted to the
Faculty of Graduate and Postdoctoral Studies
in partial fulfillment of the requirements for the degree of
Doctor of Philosophy
in the Ottawa-Carleton Chemistry Institute
Department of Chemistry, University of Ottawa

Université d'Ottawa · University of Ottawa

Candidate	Supervisor
Michelle N. Chrétien	Professor J. C. Scaiano

Your file Votre référence
ISBN: 0-494-10958-0
Our file Notre référence
ISBN: 0-494-10958-0

To my family, for always believing.

Abstract

This thesis focuses on the photochemistry and photophysics of a variety of zeolite complexes, from catalysts to sunscreens. The first chapter describes the preparation and photophysical and photochemical characterization of two new photocatalytic materials. The catalysts are based on a multi-component zeolite, host-guest complex and the interaction between components was probed using time-resolved spectroscopic techniques. The catalytic efficiency, in terms of the ability to photodegrade biological contaminants, was also investigated. These studies were performed with the aim of developing efficient catalysts for waste-water remediation which can be used with solar (visible) radiation.

In subsequent chapters, zeolite materials have been used as matrices for the stabilization of various transient or reactive species. In the case of ZSM-5-type zeolite, the dibenzotropylium cation was rendered indefinitely persistent allowing the examination of its excited-state behaviour. The geometric restriction within the cavities also permits the observation of electron transfer chemistry in the absence of a nucleophilic addition reaction with the electron donor. In a second example, ketoprofen (a non-steroidal anti-inflammatory drug) was found to undergo intrazeolite photodecarboxylation to generate a benzylic carbanion. The lifetime of the zeolite-encapsulated carbanion was found to be fifty times longer than in solution. The enhanced lifetime allows intermolecular nucleophilic addition chemistry to compete with protonation, effectively, a photo-initiated Grignard-type reaction is observed.

In Chapter 6, fluorescence is used as tool to probe both intra- and interzeolite interactions. In the first part, a zeolite-entrapped radical probe was prepared by ship-in-a-bottle synthesis for the investigation of radical percolation in the zeolite matrix. The probe is a molecular dyad containing a persistent free-radical and a

quenched fluorophore. When the probe radical couples with a carbon-centered radical, the probe fluorescene is restored and in this way free-radical species in heterogeneous systems can be conveniently examined. In the second section, zeolite particles were irreversibly labeled with a biologically-compatible fluorophore (also by ship-in-a-bottle synthesis). The system was characterized spectroscopically and the fluorescent material was used to examine the interaction between zeolite paricles and skin cells.

The last part of this thesis deals with a project relating to supramolecular sunscreens. In this work, a series of zeolite-encapsulated sunscreens were prepared and their photophysics and photochemistry thouroughly characterized. This project was undertaken with the aim of developing a modified sunscreen ingredient, which would incorporate radiation-filtering properties while also preventing both skin contact and the interaction between individual ingredients. These new sunscreen materials were shown to offer protection comparable to classical sunscreens and preliminary photobiological studies indicate that the sunscreen-zeolite complexes have a reduced cellular toxicity as compared to the naked sunscreens.

Acknowledgements

There are so many people who have supported and encouranged me over the course of my, seemingly endless, student career that I hardly know where to begin. Thank you Tito, for so much. Thank you for being an amazing teacher and mentor and for being a role model for the kind scientist, and the kind of person, I would like to be. Thank you for believing in me when I didn't believe in myself and allowing me the oppourtunity to experience scientific research in such a dynamic and nurturing environment. Ottawa felt very far from home when I first arrived but when you offered to adopt me so that wouldn't have to pay tuition, I knew I was in the right spot. Thank you also to Elda for welcoming me into your extended, photochemistry family.

Thank you Mom, Dad, and Nicole for your unflagging support and encouragement. Thank you for always pushing me to succeed, for picking me up when I fall, and for always believing that I could accomplish anything. I could never have come this far without the support of the "collective", you guys are truly inspiring.

I would like to thank Prof. Hermenegildo García for welcoming me into his lab during my stay at the Instituto de Tecnología Química in Valencia, Spain. Our continued collaboration has been an extremely rewarding aspect of my graduate career. I'm grateful for his willingness to always answer all of my questions and for sharing his infectious enthusiasm for science. Thanks to Prof. Andy Beeby for many interesting scientific discussions during my stay in his lab at the University of Durham in Durham, UK. I'm also grateful to Andy for introducing me to the "ultrafast" world through his collaborators at the Rutherford Appleton Laboratories.

I have encounterd many amazing people during my time as a member of this research group and I have learned so much from them all. Many thanks to members of the group, past and present, who made the last five years so fulfilling. Thank you Will Skene and Gonzalo Cosa for taking me under your wing and teaching me so much, about photochemistry and about determination. I'm also indebted to many former labmates including Sonia Corrent, Tanya Hancock-Chen, Alexis Aspee, Enrique Font-Sanchis, Luca Maretti, and Matt Lukeman, each of whom have given generously of their knowledge and experience. Andrea Ricci, so full of enthusiam and creativity, was like a breath a fresh air in the lab (or perhaps a tornado). I'm happy to have had the chance to work with him and I will always value our friendship. I'd also like to acknowledge the support and friendship of Carolina Aliaga, Kathy-Sarah Focsaneanu and other current group members, including Claudio (interrogative point) Carra and newbie, Jessie Blake. Thanks also to Belinda Heyne for her help in culturing the next generation of "babies" for sunscreen testing.

I want to thank Sales Galletero, Pilar Formentin, Angel Cantin, Carlos Balzeio, la Rubia, Ale Belvedere, and especially Xelo Cuquerella for their friendship and help during my time in Valencia. I will never forget my "Hora Española con Chelo y Albertito" or our evenings at the bodeguita, they were "amazing". Thanks also to Sylvia Bettington, Karen Findlay, and Paul Low who were equally helpful and kind during my stay in Durham.

I have had the priviledge of supervising several talented undergraduate students over the last several years, working with them and learning from them was a great experience for me. Thank you Larisa Mikelsons, Fan Mo, Lamiaa Migahed, Kathy McGilvray, and Eve Heafey for all of your hardwork and enthusiasm. I hope you learned as much as I did!

Thank you Betty Yakimenko, Anita Cheslock, Gerry Charette, and Gino Cuglietta for finding what was lost and fixing what was broken. Thanks for your

good humour, your endless patience, and for keeping things running as smoothly as possible.

Good friends are not always easy to find and I want to acknowledge the people who made Ottawa feel like my home and made my life outside of the lab so much fun. Thanks to my girls, Christie and Michelle #2, for your amazing friendship and for always believing I could do it....even when you weren't sure what "it" was. Suzie, thanks for always looking out for me and for being my safe harbour on the stormy days. Rubino, thank you (I think) for making sure my life never got too serious and for always having an ear to listen. Lisa, Dave, and Ally; you've been behind me, cheering me on for as long as I can remember. Thank you, and yes, I'm finally done! Thanks also to Gig and Jodie, for being the best roommates anyone could ask for over these last few hectic months.

Shawn, you are a model of determination and I've looked up to you since the day we met. I'm so grateful for your endless supply of encouragement and support. It's been a long journey and I'm glad I made it with you by my side. Thank you.

Finally, I'd like to acknowledge the financial support I've received from NSERC, the Government of Ontario, Boehringer Ingelheim, and the University of Ottawa.

Table of Contents

Abstract III

Acknowledgements V

Table of Contents VIII

List of Figures XII

List of Schemes XX

List of Tables XXII

List of Abbreviations XXIII

1. Introduction 1

1.1 Historical Perspective 2
1.2 Characteristics of Zeolite Materials 4
1.2.1 Zeolite Structure 4
1.2.2 Characteristics of the Zeolite Reaction Cavity 11
1.3 Synthesis and Manipulation 21
1.3.1 Zeolite Synthesis and Post-synthetic Modification 21
1.3.2 Preparation of Host-Guest Complexes 23
1.3.3 Location and Distribution of Guests within Zeolites 26
1.3.4 Notes on Sample Preparation 28
1.4 Examples of Supramolecular Photochemistry 31
1.4.1 Intrazeolite Photooxidation Reactions 31
1.4.2 Energy, Charge, and Electron Transfer in Zeolites 35
1.4.3 Supramolecular Control of Radical Reactions 39
1.4.4 Asymmetric Photoreactions using Zeolite Hosts 43
1.5 Concluding Remarks 46
1.6 References 47

2. Time-Resolved Spectroscopic Techniques 55

2.1 Introduction 56
2.2 Traditional Laser Flash Photolysis 57
2.2.1 Background 57
2.2.2 Laser Flash Photolysis Fundamentals 58
2.2.3 Absorption Detection for Transparent Samples 60
2.2.4 Diffuse Reflectance Detection for Opaque Samples 66
2.3 Time-Resolved Luminescence Techniques 72
2.3.1 Fluorescence Fundamentals 72
2.3.2 Experimental Set-up 74
2.4 Ultrafast Transient Absorption Techniques 78
2.4.1 Introduction 78
2.4.2 Experimental Set-up and Considerations 78

2.5 References 81

3. Multi-component Donor-Acceptor Systems in Zeolites 83

3.1 Background 84
3.2 Multi-component Photocatalytic Systems Based on TiO_2 90
3.2.1 Preparation of Titanium Dioxide-Sensitizer Combinations 90
3.2.2 Sample Characterization 92
3.2.3 Time-Resolved Studies 98
3.2.4 Photocatalytic Studies 107
3.3 Medium Effects in Multi-component Systems 115
3.3.1 Sample Preparation and Characterization 115
3.3.2 Photophysical Studies 119
3.4 Conclusions 125
3.5 Experimental 127
3.5.1 Sample Preparation 127
3.5.2 Steady-state Spectroscopy 129
3.5.3 Time-resolved Spectroscopy 130
3.5.4 Photocatalytic Studies 130
3.6 References 132

4. Photophysical Properties of Dibenzotropylium Cation 137

4.1 Background 138
4.2 Sample Preparation and Characterization 140
4.3 Photophysical Studies 144
4.3.1 Fluorescence Spectroscopy 144
4.3.2 Laser Flash Photolysis of Dibenzotropylium Cation 146
4.3.3 Quenching Studies 148
4.3.4 Electron Transfer Interactions 150
4.4 Conclusions 154
4.5 Experimental 155
4.5.1 Sample Preparation 155
4.5.2 Steady-state Spectroscopy 156
4.5.3 Time-resolved Spectroscopy 157
4.6 References 158

5. Stabilization and Reactivity of a Ketoprofen Derived Carbanion 160

5.1 Background 161
5.2 Nature of the Ketoprofenate Excited State 165
5.2.1 Solvent Dependent Observation of Reactive Intermediates 165
5.2.2 Suggested Mechanism for Solvent Dependence 166
5.2.3 Photophysics of a Ketoprofen Analogue 169
5.2.4 Conclusions to this Section 174
5.3 Reactivity of the Carbanion Intermediate 176
5.3.1 Preparation of KP@Y 176
5.3.2 Intrazeolite Decarboxylation 179
5.3.3 Intrazeolite Carbanion Reactivity 182
5.3.4 Conclusions to this Section 191
5.4 Experimental 193
5.4.1 Sample Preparation 193
5.4.2 Steady-state Spectroscopy 194
5.4.3 Time-Resolved Spectroscopy 194

5.4.4 Product Studies 196
5.5 References 198

6. Fluorescent Sensors for Intra- and Interzeolite Interactions 202

6.1 Background 203
6.2 Zeolite-Incorporated Sensor for Monitoring In-cage Interactions 206
6.2.1 Sample Preparation and Characterization 206
6.2.2 Intrazeolite Radical Detection by DT@NaY 210
6.2.3 Intrazeolite Hydrogen-atom Abstraction by DT@NaY 215
6.2.4 Conclusions to this Section 217
6.3 Fluorescently Labeled Zeolites for Imaging 219
6.3.1 Preparation and Characterization 219
6.3.2 Photophysical Studies 225
6.3.3 Microscopy Studies 229
6.3.4 Conclusions to this Section 235
6.4 Experimental 236
6.4.1 Sample Preparation 236
6.4.2 Steady-state Spectroscopy 237
6.4.3 Time-Resolved Spectroscopy 237
6.4.4 Intrazeolite Reactivity of DT@NaY 238
6.4.5 Fluorescence Microscopy 239
6.5 References 241

7. Supramolecular Sunscreens 245

7.1 Background 246
7.2 Modified Sunscreens 254
7.2.1 Oxybenzone 256
7.2.2 Octyl Salicylate 257
7.2.3 Octyl Methoxycinnamate 258
7.2.4 Octocrylene 260
7.2.5 *p*-Aminobenzoic Acid 261
7.3 Photophysical Studies 263
7.3.1 Oxybenzone 263
7.3.2 Octyl Salicylate 268
7.3.3 Octyl Methoxycinnamate 271
7.3.4 Octocrylene 274
7.3.5 *p*-Aminobenzoic Acid 275
7.4 Photostability Studies 278
7.4.1 Photostability of Sunscreens in Solution 278
7.4.2 Photostability of Supramolecular Sunscreens 286
7.5 Photobiological Studies 293
7.5.1 PABA: A Case Study 293
7.5.2 Biological Impact of Supramolecular Sunscreens 297
7.6 Concluding Remarks 311
7.7 Experimental 314
7.7.1 Zeolite Sample Preparation 314
7.7.2 Spectroscopy 314
7.7.3 Photostability of Sunscreens in Solution 315
7.7.4 Photostability of Supramolecular Sunscreens 317
7.7.5 Biological Impact Studies 317
7.8 References 322

8. Final Comments and Future Directions 327

8.1 Final Comments 328
8.2 Future Directions 331
8.3 Claims to Original Research 333
8.3.1 Work Presented in this Thesis 333
8.3.2 Work not Presented in this Thesis 335
8.4 Publications 337
8.4.1 Publications Resulting from Research Presented in this Thesis 337
8.4.2 Other Publications 338

List of Figures

Figure 1.1 Representation of the $[SiO_4]^{4-}$ and $[AlO_4]^{5-}$ tetrahedra that are the primary building blocks of zeolites, as well as the sodalite PBU and zeolites A, X, and Y.. 4

Figure 1.2 Sodalite cage that is the building block for zeolites (from left to right) X and Y, sodalite, and zeolite A. 5

Figure 1.3 The pentasil periodic building unit along with the structures of zeolites ZSM-5 and ZSM-11....6

Figure 1.4 Alternate depiction of the channel structure of zeolites ZSM-5 (right) and ZSM-11 (left)....6

Figure 1.5 Supercage structure of faujasite zeolites X and Y showing cation locations, site I, II, and III (top). The relative cavity space reduction with increased cation size (bottom).....8

Figure 1.6 Possible mechanisms for the formation of MCM-41. (Adapted from reference 31).....10

Figure 1.7 Horváth-Kawazoe pore size distributions for MCM-41, zeolite Y, and amorphous silica. 11

Figure 1.8 Diagram illustrating the ability of the reaction cavity to disfavour certain reactive pathways in cases where the transition state is not accommodated by the non-deformable cavities....12

Figure 1.9 Ship-in-a-bottle synthesis of triarylmethylium cations acid-catalyzed condensation of benzaldehydes and activated arenes. 26

Figure 1.10 Position of benzene within the supercage associated with the site II cations (left) and at the window site (right)....27

Figure 2.1 Plot of the PMT output versus time for a period before and after the laser pulse. 60

Figure 2.2 Schematic of the laser flash photolysis system for monitoring absorption changes in a transparent sample....61

Figure 2.3 Top view of a stylized sample cell illustrating the increased overlap between the laser beam and the monitoring beam when using a front-face configuration (right) versus a side-on arrangement (left).....64

Figure 2.4 Schematic of the laser flash photolysis system for monitoring reflectance changes in opaque samples. 68

Figure 2.5 Pictorial representation of the early events of a time-resolved fluorescence experiment. ..75

Figure 2.6 Schematic of an electronic streak camera.....76

Figure 2.7 Schematic of the experimental set-up for time-resolved emission. SHG and THG stand for second and third harmonic generator respectively. 77

Figure 2.8 Simplified schematic of a system for ultrafast transient absorption spectroscopy. WLC represents the white light continuum generator. 79

Figure 3.1 Structures of *tris*(2,2'-bipyridine)ruthenium(II) ($Ru^{2+}(bpy)_3$) and 2,4,6-triphenylpyrylium cation, TP^+.....87

Figure 3.2 Aromatic region of the FT-IR spectra recorded of (A) $Ru^{2+}(bpy)_3$ and (B) TP^+ encapsulated in zeolite Y following outgassing at 200 °C under reduced pressure for 1 h before (a) and after (b) inclusion of TiO_2. 94

Figure 3.3 Diffuse reflectance spectra (plotted as the Kubelka-Munk function of the reflectance) of (A) $Ru^{2+}(bpy)_3$@Y and (B) TP^+@Y before (a) and after (b) incorporation of TiO_2. 95

Figure 3.4 DRS of TiO_2@Y prepared according to the procedure described above. Ti content ca. 0.9% by combustion elemental analysis. 96

Figure 3.5 Emission spectrum of $Ru^{2+}(bpy)_3$@Y (a) and $Ru^{2+}(bpy)_3/TiO_2$@Y (b) following excitation at 466 nm. The area of the photoluminescence spectra determined as an average of 18 independent measurements was (2.3 ± 0.2) x 10^7 and (1.7 ± 0.1) x 10^7 for (a) and (b) respectively. 97

Figure 3.6 Emission spectrum of TP^+@Y (a) and TP^+/TiO_2@Y (b) following excitation at 420 nm. The area of the photoluminescence spectra determined as an average of 20 independent measurements was (1.0 ± 0.1) x 10^7 and (0.6 ± 0.1) x 10^7 for (a) and (b) respectively. 97

Figure 3.7 Fluorescence decay of TP^+@Y (●) and TP^+/TiO_2@Y (○) following pulsed irradiation at 355 nm under a N_2 atmosphere. Sample characteristics are given in Table 3.1. Instrument response (—). 99

Figure 3.8 Fluorescence decay of $Ru^{2+}(bpy)_3$@Y (●) and $Ru^{2+}(bpy)_3/TiO_2$@Y (○) following pulsed irradiation at 355 nm under a N_2 atmosphere. Sample characteristics are given in Table 3.1. 101

Figure 3.9 Transient DRS recorded (●) 3.2 μs, (○) 18.4 μs, (■) 59.2 μs, and (□) 140 μs after 355 nm laser excitation of N_2 purged TP^+@Y. 103

Figure 3.10 Transient DRS of TP^+@Y (●) and TP^+/TiO_2@Y (○) recorded ~6 μs after 355 nm laser excitation. The TP^+ triplet can be seen at ca. 450 nm and the $TP^•$ radical at 570 nm. 104

Figure 3.11 Transient decay traces for TP^+@Y (●) and TP^+/TiO_2@Y (○) recorded at 450 nm following 355 nm laser excitation. Inset: decay traces for the same samples recorded at 570 nm. ... 105

Figure 3.12 Transient DRS recorded 6.4 μs after 532 nm excitation of a nitrogen purged sample of $Ru^{2+}(bpy)_3/TiO_2$@Y. 107

Figure 3.13 Absorption spectra of ABTS (○) and ABTS radical cation (●) in acetate buffer at pH 4.4. 108

Figure 3.14 Representative curves showing the HRP catalyzed oxidation of ABTS as a function of time for samples containing TiO_2 (●), TiO_2@Y (○), and no catalyst (■). Data fitted with dotted lines were exposed to UVA radiation. Data fitted with solid lines were not irradiated... 110

Figure 3.15 Calculated initial slopes for irradiated (striped bars) and un-irradiated (solid bars) samples, where Ru = $Ru^{2+}(bpy)_3$. 111

Figure 3.16 Calculated initial slopes for irradiated (striped bars) and un-irradiated (solid bars) samples. 112

Figure 3.17 Relative enzymatic activities for HRP in the presence of various photocatalysts. 113

Figure 3.18 Relative enzymatic activities for HRP in the presence of various photocatalysts. 113

Figure 3.19 Diffuse reflectance spectrum of $Ru^{2+}(bpy)_3/TP^+$@Y showing a broad absorption envelope for the two chromophores. 118

Figure 3.20 Aromatic region of the FT-IR spectrum of $Ru^{2+}(bpy)_3/TP^+@Y$ recorded following outgassing at 200 °C for 1 h. The characteristic peaks for $Ru^{2+}(bpy)_3$ (🡻) and TP^+ (*) are labeled. 118

Figure 3.21 Map of the emission spectrum as a function of excitation wavelength for $Ru^{2+}(bpy)_3/TP^+@Y$ recorded under N_2. 119

Figure 3.22 DRS spectrum of $Ru^{2+}(bpy)_3/TP^+@Y$ recorded 13.2 μs after the 532 nm laser pulse. The shaded area indicates a region where artifacts are present as a result of the 532 nm laser line. 120

Figure 3.23 Transient DRS spectrum of $Ru^{2+}(bpy)_3/TP^+@Y$ (same sample as Figure 3.22) recorded 0.40 μs (O), 0.88 μs (□), 3.44 μs (5), and 13.2 μs (●) after the 532 nm laser pulse. 121

Figure 3.24 Emission spectra recorded of (a) $Ru^{2+}(bpy)_3/TP^+@Y$, (b) $Ru^{2+}(bpy)_3/TP^+/TiO_2@Y$ (0.9% Ti w/w), (c) $Ru^{2+}(bpy)_3/TP^+/TiO_2@Y$ (1.8% Ti w/w), (d) $Ru^{2+}(bpy)_3/TiO_2@Y$, and (e) $Ru^{2+}(bpy)_3@Y$ as an average of 9 independent measurements. λ_{ex} = 466 nm. 122

Figure 3.25 Emission spectra recorded of (a) $Ru(bpy)_3^{2+}/ TP^+/TiO_2@Y$ (1.8% Ti w/w), (b) $Ru(bpy)_3^{2+}/TP^+/TiO_2@Y$ (0.9% Ti w/w), (c) $Ru(bpy)_3^{2+}/TP^+@Y$, and (d) $Ru(bpy)_3^{2+}/TP^+/PA@Y$ as an average of 9 independent measurements. λ_{ex} = 466 nm. ... 123

Figure 4.1 Structures of the parent hydrides included in acidic zeolites in the study discussed above... 140

Figure 4.2 UV-vis absorption spectrum of DBOH (O) in acetonitrile, DB^+ (●) prepared by dissolving DBOH in acetonitrile containing 0.3 M TFAA, and the DRS of $DB^+@ZSM-5$ (◆) plotted as a function of the reflectance. 142

Figure 4.3 Aromatic region of the IR spectra of (a) DB^+ in HZSM-5, (b) DB^+ obtained by dissolving DBOH in H_2SO_4, and (c) DBOH. 143

Figure 4.4 DRS (●) and emission spectra (O) of nitrogen purged $DB^+@HZSM-5$. The excitation wavelength was 355 nm. 145

Figure 4.5 Emission decay monitored at 580 nm following 355 nm pulsed excitation (ns Nd-YAG laser) of $DB^+@HZSM-5$ 146

Figure 4.6 Transient DRS recorded (●) 0.96 μs, (O) 2.56 μs, (■) 9.60 μs, and (□) 29.9 μs after 355 nm laser excitation of a nitrogen purged sample of $DB^+@HZSM-5$. 147

Figure 4.7 Transient UV-vis spectrum recorded (●) 0.16 μs, (O) 0.96 μs, (■) 6.88 μs, and (□) 15.2 μs after 532 nm excitation of a 6.9 x 10^{-5} M solution of DBOH in deaerated TFE containing TFAA to generate the DB^+ cation. 148

Figure 4.8 Decay profile monitored at 500 nm following 355 nm laser excitation of a nitrogen purged (●) and an oxygen purged (O) sample of $DB^+@HZSM-5$. 150

Figure 4.9 Transient DRS recorded (O) 0.96 μs, (●) 2.56 μs, (■) 9.60 μs, and (□) 29.9 μs after 532 nm laser excitation of a nitrogen purged sample of $DB^+@HZSM-5$ containing TEA 151

Figure 4.10 Transient absorption spectrum recorded (●) 0.40 μs, (O) 1.04 μs, (■) 3.84 μs, and (□) 14.4 μs after 308 nm excitation of a 5.3 x 10^{-5} M solution of DBCl in nitrogen purged hexane. 153

Figure 4.11 Transient absorption spectrum recorded (●) 0.24 μs, (O) 0.72 μs, (■) 3.04 μs, and (□) 14.6 μs after 308 nm excitation of a 5.3 x 10^{-5} M solution of DBCl in oxygen purged hexane... 153

Figure 4.12 UV-vis absorption spectrum of DBOH (O, 1.1 x 10^{-4} M) and DBCl (●, 4.7 x 10^{-5} M) in acetonitrile solution. 156

Figure 5.1 Molar absorptivity of ketoprofen in phosphate buffer solution (pH 7.4). 162

Figure 5.2 Transient absorption spectrum recorded 55 ns after 308 nm laser excitation of a 4.0 x 10^{-4} M methanol solution of KP containing 10 mM sodium methoxide. 166

Figure 5.3 State diagram for benzophenone showing approximate energy levels (not to scale). Wavy lines indicate radiationless transitions. 168

Figure 5.4 Pictorial description of the implications of triplet energy level changes. 169

Figure 5.5 Emission spectra of 3-methylbenzophenone in 96% water (●), acetonitrile (□), and hexane (■). Solutions were optically matched at the excitation wavelength (288 nm) with an absorbance of 0.1. 170

Figure 5.6 Transient absorption spectrum recorded 200 ps after 267 nm excitation of 3-methylbenzophenone in hexane (□, 9.9 x 10^{-4} M), acetonitrile (●, 7.3 x 10^{-4} M), ethanol (○, 4.4 x 10^{-4} M), and 90% water (■, 4.7x 10^{-4} M). 171

Figure 5.7 Transient absorption spectrum of 7.3 x 10^{-4} M 3-methylbenzophenone in acetonitrile 2 to 500 ps after 267 nm excitation. 172

Figure 5.8 Change in absorbance following 267 nm excitation of 3-methylbenzophenone in hexane (●, 9.9 x 10^{-4} M), acetonitrile (□, 7.3 x 10^{-4} M), ethanol (○, 4.4 x 10^{-4} M), and 90% water (■, 4.7x 10^{-4} M). 173

Figure 5.9 Plot of k_{growth} vs $E_T(30)$ (●) and H-bond donating ability (○) for the solvents studied... 174

Figure 5.10 UV-vis absorption spectrum of 1.2 x 10^{-5} M KP in PBS (pH 7.4) (●) and diffuse reflectance spectrum of KP@Y under vacuum (○) plotted as the Kubelka-Munk function of the reflectance. 178

Figure 5.11 Transient DRS recorded 1.36 μs (●), 4.72 μs (○), and 14.5 μs (■) after 266 nm laser excitation of a vacuum sealed sample of KP@Y. 180

Figure 5.12 Lifetime distribution analysis compiled from kinetic data acquired at 600 nm at various times after 266 nm excitation of KP@Y under vacuum. 181

Figure 5.13 Signal recorded at 600 nm following 266 nm excitation of a sample of KP@Y under vacuum (●) and after exposure to moisture (○). 183

Figure 5.14 Schematic of the laser cell used for examining quencher effects on carbanion lifetime in the absence of moisture. 184

Figure 5.15 Signal recorded at 600 nm following 266 nm excitation of a sample of KP@Y under vacuum in the presence of frozen (●) and thawed (○) 1-bromoethane, <S> ~ 2. 185

Figure 5.16 Signal recorded at 600 nm following 266 nm laser excitation of a sample of KP@Y under vacuum in the presence of frozen (●) and thawed (○) acetaldehyde, <S> ~ 15 190

Figure 6.1 Ground state DRS of DT@NaY (●) and UV-vis absorption spectrum of DT in ACN, 5.0 x 10 M (○) 209

Figure 6.2 Emission spectra (λ_{ex} = 330 nm) of a benzene solution of DT (1.0 x 10^{-4} M, ○), a solid sample of DT@NaY (●), and a benzene slurry of DT@NaY (1.0 mg mL^{-1}, ■) 210

Figure 6.3 Fluorescence increase (normalized to 1.0 at t = 0 min) recorded after heating (70°C) a solid sample of DT@NaY with co-included AIBN ($<S>_{DT}$ ~ 0.1, $<S>_{AIBN}$ ~ 0.5). λ_{ex} = 305 nm, λ_{em} = 550 nm 212

Figure 6.4 Fluorescence growth (normalized to 1.0 at t = 0 s) for a hexane slurry of 1.0 mg mL^{-1} DT@NaY in the absence (●) and presence (O) of 1.3 x 10^{-3} M PC-PC. λ_{ex} = 330 nm and λ_{em} = 550 nm 215

Figure 6.5 Fluorescence growth (normalized to 1.0 at t = 5 min) for a slurry containing 1.0 mg mL^{-1} DT@NaY in a deaerated benzene solution of 3-phenyl-3-coumaranone (0.01 M) at room temperature. 217

Figure 6.6 CP/MAS ^{13}C NMR spectrum of F@HY. 221

Figure 6.7 DRS (O) and emission spectrum (●) of F@HY recorded under air following excitation at 440 nm. 222

Figure 6.8 DRS recorded of F@HY (●) and F@CsY (O). 225

Figure 6.9 Fluorescence decay of F@HY following pulsed excitation at 355 nm under air. Instrument function is shown (—). 226

Figure 6.10 Fluorescence decay of F@CsY following 355 nm pulsed excitation under air. Instrument response is shown (—). 227

Figure 6.11 Emission spectra of F@HY in water before (■) and 0.5 min (□), 5 min (●), 15 min (×), and 45 min (O) after the addition of TEMPO. 228

Figure 6.12 Graphical representation of time dependent fluorescence quenching. $T^{\bullet}$= TEMPO 229

Figure 6.13 Fluorescence microscope image of F@HY suspended in water (a) and in an aqueous solution of fluorescein after 10 s (b), 20 s (c), and 30 s (d) of continuous illumination by the microscope excitation source. Filter set XF02-02, 330 nm WB excitation and > 400 nm emission. 230

Figure 6.14 Confocal fluorescence microscopy images of CMTMR stained human skin fibroblasts after 1 h (a) and 27 h (b) and incubation with F@HY. λex = 543 nm for CMTMR and 488 nm for F@HY, emission monitored between 560-580 nm and 510-530 nm respectively. DIC images (c) and (d) recorded of the same samples as shown in (a) and (b). Different regions of the sample were imaged at 1 and 27 h. 232

Figure 6.15 Z-series compliled from confocal fluorescence microscopy images of CMTMR stained human skin fibroblasts after 1 h incubation with F@HY in 0.9% saline. Excitation at 543 nm for CMTMR and at 488 nm for F@HY, emission monitored at 560-580 nm and 510-530 respectively. Image slices were recorded beginning at the "bottom" of the sample (top left). 233

Figure 6.16 Z-series compiled from confocal fluorescence microscopy images of CMTMR stained human skin fibroblasts after 27 h incubation with F@HY in 0.9% saline. Excitation at 543 nm for CMTMR and at 488 nm for F@HY, emission monitored at 560-580 nm and 510-530 respectively. Image slices were recorded beginning at the "bottom" of the sample (top left). 234

Figure 7.1 Spectral distribution of solar radiation before (red) and after (blue) attenuation by the atmosphere. 246

Figure 7.2 Penetration of human skin by ultraviolet radiation. 247

Figure 7.3 Absorption spectrum of OXB in hexane (O, 4.4 x 10^{-5} M) and DRS of OXB@Y (●, <S> ~ 0.1). 257

Figure 7.4 Absorption spectrum of OSA in hexane (O, 6.0 x 10^{-6} M) and DRS of OS@Y (●, <S> ~ 0.1).. 258

Figure 7.5 Absorption spectrum of OMC in hexane (O, 1.0 x 10^{-5} M) and DRS of OMC@Y (●, <S> ~ 0.1). 259

Figure 7.6 Absorption spectrum of OCT in hexane (●, 6.7 x 10^{-6} M) and DRS of OCT@Y (O, <S> ~ 0.1). 261

Figure 7.7 Absorption spectrum of PABA in ACN (O, 2.9 x 10^{-6} M) and DRS of PABA@Y (●, <S> ~ 0.8). 262

Figure 7.8 Transient absorption spectrum recorded 0.32 μs (●), 1.36 μs (O), 6.88 μs (□), and 14.2 μs (×) after 308 nm laser excitation of a deaerated solution of OXB in ACN (3.5 x 10^{-5} M). Inset: Comparison of spectra recorded for the same solution under nitrogen (O) and oxygen (●) after 14.2 μs. 265

Figure 7.9 Transient absorption spectrum recorded 48 ns (●), 0.24 μs (O), 0.66 μs (□), and 2.58 μs (×) after 308 nm laser excitation of a deaerated solution of 4-methoxybenzophenone in ACN (3.5 x 10^{-5} M). Inset: Transient decay traces recorded at 500 nm for the same solution under nitrogen (O) and oxygen (●). 266

Figure 7.10 Transient DRS recorded 0.64 μs (●), 2.56 μs (O), 8.64 μs (■), and 26.7 μs (□) after 308 nm excitation of OXB@Y under vacuum (<S> ~ 0.1). Data below 350 nm in the first time window, corresponding to bleaching of the ground state, have been omitted for clarity. 268

Figure 7.11 Transient absorption spectrum recorded 0.40 μs (●), 1.12 μs (O), 2.40 μs (■), and 13.2 μs (□) after 308 nm laser excitation of a deaerated solution of OSA in ACN (7.5 x 10^{-5} M). Inset: Comparison of spectra recorded for the same solution under nitrogen (●) and oxygen (O) after 0.40 μs. 269

Figure 7.12 Transient absorption spectrum recorded 0.40 μs after 308 and 266 nm laser excitation of deaerated ACN solutions of OSA (O, 7.5 x 10^{-5} M) and 2-ethylhexylbenzoate (●, 4.4 x 10^{-5} M). 270

Figure 7.13 Transient DRS recorded 0.8 μs after 308 nm laser excitation of OSA@Y under vacuum (●) and under air (■). 271

Figure 7.14 Transient absorption spectrum recorded 0.64 μs (●), 3.84 μs (O), 13.6 μs (□), and 28.6 μs (×) after 308 nm excitation of OMC in deaerated ACN (4.6 x 10^{-5} M). 272

Figure 7.15 Transient DRS recorded 0.60 μs (O), 2.44 μs (■), and 6.40 μs (×) after 308 nm excitation of OMC@Y under air (<S> ~ 0.1). 273

Figure 7.16 Transient DRS recorded 0.80 μs (O), 2.12 μs (■), and 5.92 μs (×) after 308 nm excitation of OCT@Y under air (<S> ~ 0.1). 275

Figure 7.17 Transient absorption spectrum recorded 16 ns (●), 0.11 μs (O), 0.30 μs (■), and 1.22 μs (×) after 308 nm excitation of PABA in deaerated ACN (1.8 x 10^{-4} M). 276

Figure 7.18 Transient DRS recorded 0.32 μs (●), 0.68 μs (O), 2.80 μs (■), and 6.72 μs (×) after 308 nm excitation of PABA@Y under air (<S> ~ 0.5). Data below 350 nm in the first time window, corresponding to bleaching of the ground state, have been omitted for clarity. 277

Figure 7.19 Absorption spectra of OCT (O), OXB (□), OSA (×), and OMC (●) in methanol and absorption/scattering by TiO_2 in water (■). The shaded area indicates the UVA portion of the spectrum. 279

Figure 7.20 QT fluorescence increase monitored under the following conditions; [micelles] = 6.5 x 10^{-4} M, no TiO_2 (O), [micelles] = 6.5 x 10^{-4} M, [TiO_2] = 0.5 mg mL^{-1} (□), [micelles] = 6.5 x 10^{-4}

M, [TiO_2] = 1.0 mg mL^{-1} (●), and [micelles] = 1.9 x 10^{-4} M, [TiO_2] = 1.0 mg mL^{-1} (■). Inset: QT structure. 284

Figure 7.21 Amount of OXB recovered following framework dissolution (left), expressed as a percentage of the amount recovered from the control (right). Horizontal line (left) indicates the theoretical recovery value. 289

Figure 7.22 Amount of OSA recovered following framework dissolution (left), expressed as a percentage of the amount recovered from the control (right). Horizontal line (left) indicates the theoretical recovery value. 290

Figure 7.23 Amount of OMC recovered following framework dissolution (left), expressed as a percentage of the amount recovered from the control (right). Horizontal line (left) indicates the theoretical recovery value. 291

Figure 7.24 Amount of OCT recovered following framework dissolution (left), expressed as a percentage of the amount recovered from the control (right). Horizontal line (left) indicates the theoretical recovery value. 292

Figure 7.25 Calculated initial slopes for samples of HRP (0.1 mg mL^{-1}) in ddH_2O with or without PABA (7.3 x 10^{-4} M) after 2 h UVB irradiation or dark incubation (left) and relative enzymatic activities for the same samples (right). 294

Figure 7.26 Calculated initial slopes for samples of HRP (0.1 mg mL^{-1}) in ddH_2O with or without PABA@Y (1.0 mg mL^{-1}, <S> ~ 0.99, equivalent to *ca.* 6.0 x 10^{-4} M) after 2 h UVB irradiation or dark incubation (left) and relative enzymatic activities for the same samples (right). .. 295

Figure 7.27 Calculated initial slopes for samples containing HRP (1.0 mg mL^{-1}) with or without NaY (1.0 mg mL^{-1}) after 2 h UVB irradiation or dark incubation (left), and relative enzymatic activity ratios for the same samples (right). 296

Figure 7.28 Typical comets observed by fluorescence microscopy from an undamaged (A), moderately damaged (B), and heavily damaged (C) cell after alkaline comet assay. (Figure from A. L. Vinette) 300

Figure 7.29 Cell viability (left) and DNA damage determined by alkaline comet assay (right) for HEK cells incubated for 24 h with irradiated (stripes) or un-irradiated (grey) media containing OXB, OXB@Y, or NaY. Data is given as the mean value ± standard error for three experiments, 100 comets were evaluated per experiment. 302

Figure 7.30 Cell viability (left) and DNA damage determined by alkaline comet assay (right) for HEK cells incubated for 24 h with irradiated (stripes) or un-irradiated (grey) media containing OSA, OSA@Y, or NaY. Data is given as the mean value ± standard error for three experiments, 100 comets were evaluated per experiment. 303

Figure 7.31 Cell viability (left) and DNA damage determined by alkaline comet assay (right) for HEK cells incubated for 24 h with irradiated (stripes) or un-irradiated (grey) media containing OMC, OMC@Y, or NaY. Data is given as the mean value ± standard error for three experiments, 100 comets were evaluated per experiment. 304

Figure 7.32 Cell viability (left) and DNA damage determined by alkaline comet assay (right) for HEK cells incubated for 24 h with irradiated (stripes) or un-irradiated (grey) media containing OCT, OCT@Y, or NaY. Data is given as the mean value ± standard error for three experiments, 100 comets were evaluated per experiment. 304

Figure 7.33 *In vitro* SPF values determined using the Labsphere UTA for free (0.12 mmol, stripes) and encapsulated (200 mg of <S> ~ 1.0, 0.12 mmol equiv., grey) sunscreens suspended in

ethylene glycol. The cocktail contained equal amounts of all four free (0.12 mmol total) or encapsulated (200 mg total) sunscreens. 306

Figure 7.34 Cell viability (left) and DNA damage determined by alkaline comet assay (right) for samples exposed to SSR without or with protection (vehicle, OXB, or OXB@Y). Data is given as the mean value ± standard error for three experiments, 100 comets were evaluated per experiment. 308

Figure 7.35 Cell viability (left) and DNA damage determined by alkaline comet assay (right) for samples exposed to SSR without or with protection (vehicle, OSA, or OSA@Y). Data is given as the mean value ± standard error for three experiments, 100 comets were evaluated per experiment. 308

Figure 7.36 Cell viability (left) and DNA damage determined by alkaline comet assay (right) for samples exposed to SSR without or with protection (vehicle, OMC, or OMC@Y). Data is given as the mean value ± standard error for three experiments, 100 comets were evaluated per experiment. 309

Figure 7.37 Cell viability (left) and DNA damage determined by alkaline comet assay (right) for samples exposed to SSR without or with protection (vehicle, OCT, or OCT@Y). Data is given as the mean value ± standard error for three experiments, 100 comets were evaluated per experiment. 309

Figure 7.38 Cell viability for samples exposed to SSR for 10 min (grey), 15 min (striped), and 20 min (white) with or without protection as indicated. Data is given as the mean value ± standard error for three experiments. 310

List of Schemes

Scheme 1.1 Photodimerization of acenaphthylene yielding the *cis* and *trans* dimers. 20

Scheme 1.2 Monomer and H-dimer forms of cationic thionin. 29

Scheme 1.3 Formation of the allylic hydroperoxide from photooxidation of *trans*-butene in zeolite NaY. 32

Scheme 1.4 Mechanism for the photooxygenation of cyclohexane in zeolite NaY. 33

Scheme 1.5 Plausible mechanism for the singlet oxygen *ene* reaction showing the perepoxide intermediate. 33

Scheme 1.6 Type II photooxidation of tetrasubstituted alkenes. 34

Scheme 1.7 Fluorescent dyes used to demonstrate energy transfer in zeolite L microcrystals. 36

Scheme 1.8 Typical species formed following photolysis of unsymmetrical ketone ACOB. 39

Scheme 1.9 Schematic representation of DBK photolysis in the channels of ZSM-5. 41

Scheme 1.10 Possible pathways following DBK photolysis: decarbonylation followed by secondary radical pair recombination (top) or primary radical pair recombination (middle, bottom). 42

Scheme 1.11 Photocyclization of substituted cyclohexyl ketones to give the chiral cyclobutanol. .44

Scheme 1.12 Photocylization of tropolone ethylphenyl ether. 44

Scheme 2.1 Steps for performing a lifetime distribution analysis. 70

Scheme 3.1 Generation of reactive oxygen species (ROS) following scavenging of conduction band electrons and valence band holes by oxygen and water. 86

Scheme 3.2 Hydrolytic ring opening of TP^+ to give the 1,3,5-triphenylpent-2-en-1,5-dione. 88

Scheme 3.3 Step-wise preparation of multi-component photocatalyst $Ru^{2+}(bpy)_3/TiO_2$@Y. 90

Scheme 3.4 Step-wise preparation of multi-component photocatalyst TP^+/TiO_2@Y. 91

Scheme 3.5 The products of photoinduced electron transfer between TiO_2 and the two dyes. 102

Scheme 3.6 HRP catalyzed decomposition of H_2O_2 concomitant with oxidation of ABTS to its radical cation. 108

Scheme 3.7 Possible reactive oxygen species generated in an aqueous aerobic environment. 114

Scheme 3.8 Stepwise preparation of $Ru^{2+}(bpy)_3/TP^+$@Y containing either TiO_2 nanoparticles or co-included polyacetylene (PA). 116

Scheme 4.1 Preparation of DB^+ cation in acidic zeolite HZSM-5 141

Scheme 4.2 Preparation of DBCl from DBOH and thionyl chloride. 152

Scheme 5.1 Proposed mechanism of ketoprofen decarboxylation. 163

Scheme 5.2 Alternate structure of the transient resulting from ketoprofenate photolysis 163

Scheme 5.3 Intramolecular S_N2 reaction of modified ketoprofen. 164

Scheme 5.4 Photorelease of X^- from a modified ketoprofen. 164
Scheme 5.5 Schematic representation of a possible carbanion stabilization mode in NaY. 182
Scheme 5.6 Reaction of KP-derived carbanion with a 1-bromoalkane. 185
Scheme 5.7 Alternate formation of EB in the presence of 1-bromoethane. 188
Scheme 5.8 Reaction of the carbanion with acetaldehyde. 189
Scheme 6.1 Mechanism of radical detection by pre-fluorescent probes. 204
Scheme 6.2 Reaction of the DT probe with vitamin C 207
Scheme 6.3 Synthesis of dansyl-TEMPO 208
Scheme 6.4 Reactivity of 3,3'-diphenyl-3*H*,3*H*'-[3,3']*bis*benzofuranyl-2,2'-dione. 213
Scheme 6.5 Intracavity reaction between 3-phenyl-2-coumaranone and DT. 216
Scheme 6.6 Acid-catalyzed synthesis of fluorescein. 220
Scheme 6.7 The protolytic equilibria of fluorescein in the ground state. 223
Scheme 6.8 Structures of fluorescein derivatives 229
Scheme 7.1 Excited-state intramolecular proton transfer in oxybenzone. 267
Scheme 7.2 Possible mechanism for generation of phenoxyl radicals in OXB 267
Scheme 7.3 Trapping of an acetonitrile-derived radical by QT. 285

List of Tables

Table 1.1 Calculated cation dependence of supercage free volume, calculations performed using a modification of the POLYVOL program. 13

Table 1.2 Synthesis conditions and physicochemical properties of zeolites NaA and TPA-ZSM-5. TPA, tetrapropylammonium 22

Table 2.1 Selected lasers available at the University of Ottawa with pulse energies and durations. YAG is Yttrium Aluminum Garnet. 56

Table 3.1 Spectroscopic and analytical data for prepared samples. Loadings derived from combustion elemental analysis. Diffuse reflectance spectra (DRS) recorded of air equilibrated samples and IR spectra recorded of self-supported wafers after outgassing at 200 °C under 10^{-2} Pa for 1 h. [a]Prepared from 0.2 M aqueous solutions of $(NH_4)_2(Ti{=}O)(C_2O_4)_2{\cdot}H_2O$ 92

Table 3.2 Fluorescence decay parameters determined for selected samples studied. k_x is the rate constant and A_x the pre-exponential factor 100

Table 3.3 Analytical data for selected samples. [a] Prepared using a 0.2 M titanyl oxalate solution. [b] Prepared using a 0.4 M titanyl oxalate solution. 117

Table 5.1 $E_T(30)$, H-bond donor ability (α_H), and photophysical data for the solvents measured.[36] [a]10% acetonitrile v/v 173

Table 7.1 Five most commonly used organic sunscreens in order of popularity as well as PABA. For structures see Table 7.2. 250

Table 7.2 Structures, names, abbreviations, and spectral data for sunscreens studied.[28] [a]These values correspond to the *trans* isomer. 255

Table 7.3 Sunscreen recovery (%) as determined by GC after 20 h (OXB, OSA, OCT) and 1.5 h (OMC) UVA irradiation. Concentrations: [sunscreen] = 5.0×10^{-4} M, $[TiO_2]$ = 1.0 mg mL^{-1}, [micelles] = 6.5×10^{-4} M. All samples prepared in ddH_2O. 280

Table 7.4 Sunscreen recovery (%) measured by GC after 7 h (OXB, OSA, OCT) and 1.5 h (OMC) irradiation. Concentrations: [sunscreen] = 5.0×10^{-4} M, $[TiO_2]$ = 1.0 mg mL^{-1}. All samples were prepared in ddH_2O. 282

Table 7.5 Sample composition and experimental conditions. All samples were prepared in 10 mL of ddH_2O and irradiated in Pyrex tubes. 288

List of Abbreviations

μJ	microjoule
μM	micromolar
ΔOD	change in sample absorbance before and after laser excitation
μs	microsecond
<S>	occupancy, defined as the number of molecules per zeolite cavity
1,4-CHD	1,4-cyclohexadiene
$^1O_2$	singlet oxygen
3D	three dimensional
A	pre-exponential factor
ABTS	2,2′-azino-*bis*(3-ethylbenzthiazoline-6-sulfonic acid) diammonium salt
ACN	acetonitrile
AIBN	2,2′-azo*bis*isobutyronitrile
ALS	alkaline labile sites
BeT	back electron transfer
BP	benzophenone
bpy	bipyridyl
CCD	charge capture device
CE	cage effect
CIE	Commission International de l'Eclairage
cm	centimeter
CMC	critical micelle concentration
CMTMR	5-(and-6-)-(((4-chloromethyl)benzoyl)amino) tetramethylrhodamine
CP	cross polarization
CT	charge transfer
CT^3	triplet charge transfer state
$DB^•$	dibenzosuberenyl radical
DB^+	dibenzotropylium cation
DBCl	5-chlorodibenzosuberene
DBH	dibenzosuberene
DBK	dibenzylketone
DBOH	dibenzosuberenol
DCB	1,4-dicyanobenzene
DCM	dichloromethane
ddH_2O	distilled deionized water
DIC	differential image constrast
DMEM	Dulbecco's modified Eagle's medium
DMSO	dimethylsulfoxide

DNA	deoxyribonucleic acid
DPE	diphenylethane
DR	diffuse reflectance
DRA	diffuse reflectance accessory
DRS	diffuse reflectance spectrum
DSB	double strand break
DT	dansyl-TEMPO
DTH	dansyl-TEMPO hydroxylamine
e^-/h^+	electron/hole pair
EBr	ethidium bromide (2,7-diamino-10-ethyl-9-phenylphenanthridium)
EB	3-ethylbenzophenone
e_{CB}	conduction band electron
EDTA	ethylenediaminetetraacetic acid
ee	enantiomeric excess
EFAL	extra-framework aluminum
ESIPT	excited-state intramolecular proton transfer
ESM	exponential series method
eT	electron transfer
ET	energy transfer
eV	electronvolt
e_{VB}	valence band electron
F	fluorescein
F^+	fluorenylium cation
FCS	fetal calf serum
FD	fluorescein diacetate
FDA	Food and Drug Administration (USA)
FH	9*H*-fluorene
FID	flame ionization detection
fs	femtosecond (10^{-15} s)
GC	gas chromatography
GS	ground state
HBSS	Hank's balanced salt solution
HEK	human epidermal keratinocytes
HRP	horseradish peroxidase
Hz	hertz
IC	internal conversion
IR	infrared
ISC	intersystem crossing
ITQ	Instituto Tecnología Química
k	rate constant
kHz	kilohertz

kJ	kilojoule
KP	ketoprofen
KP⁻	ketoprofenate
LC	ligand centered
LFP	laser flash photolysis
LIOAS	laser-induced optoacoustic spectroscopy
LMCT	ligand-to-metal charge transfer
LSCM	laser scanning confocal microscopy
M	molar
MAP	methyl-β-acetophenone
MAS	magic angle spinning
MB	3-methylbenzophenone
MCM	Mobil's Composition of Matter
MCP	multichannel plate
MED	minimum erythemal dose
mJ	millijoule
mL	milliliter
MLCT	metal-to-ligand charge transfer
mM	millimolar
mm	millimeter
mmol	millimole
mol	mole
ms	millisecond (10^{-3} s)
MS	mass spectrometry
MV^{2+}	methylviologn cation
mW	milliwatt
ng	nanogram
nLFP	nanosecond laser flash photolysis
NLO	non-linear optical
NMR	nuclear magnetic resonance
NMSC	non-melanoma skin cancer
ns	nanosecond (10^{-9} s)
NSAID	non-steroidal anti-inflammatory drug
OCT	octocrylene
OMC	octyl methoxycinnamate
OPA	optical parametric amplifier
OSA	octyl salicylate
OXB	oxybenzone
Pa	pascal
PABA	*p*-aminobenzoic acid
PBS	phosphate buffer solution

PBU	periodic building unit
PC•	3-phenyl-2-coumanone radical
PCH	3-phenyl-2-coumaranone
PC-PC	3,3'-diphenyl-3*H*,3*H*-[3,3']*bis*benzofuranyl-2,2'-dione
PDA	photodiode array
PeT	photoinduced electron transfer
PMT	photomultiplier tube
ps	picosecond (10^{-12} s)
QT	quinoline-TEMPO
ROS	reactive oxygen species
Ru	$Ru^{2+}(bpy)_3$
S_1	lowest energy singlet excited state
SCE	saturated calomel electrode
SDS	sodium dodecyl sulfate
SPF	sun protection factor
SSB	single strand break
SSR	solar simulated radiation
T_1	lowest energy triplet excited state
TEMPO	2,2,6,6-tetramethyl-piperidine-1-oxyl free radical
TFE	trifluoroethanol
TFFA	trifluoroacetic acid
TP•	2,4,6-triphenylpyranyl radical
TP^+	2,4,6-triphenylpyrylium cation
TPA	tetrapropylammonium
T-T	triplet-triplet
TTL	transistor-transistor linked
uLFP	ultrafast laser flash photolysis
UVA	ultraviolet radiation ranging from 315-400 nm.
UVB	ultraviolet radiation ranging from 280-315 nm.
UVC	ultraviolet radiation ranging from 100-280 nm.
UVR	ultraviolet radiation
UV-vis	ultraviolet-visible
V	volt
VPI	Virginia Polytechnic Institute
W	watt
X^+	xanthylium cation
XH	9*H*-xanthene
YAG	yttrium-argon-garnate
YLF	yttrium lithium fluoride
ZSM	Zeolite Socony Mobile

1. Introduction

1. Introduction 1

1.1 Historical Perspective 2
1.2 Characteristics of Zeolite Materials 4
1.2.1 Zeolite Structure 4
1.2.2 Characteristics of the Zeolite Reaction Cavity 11
1.3 Synthesis and Manipulation 21
1.3.1 Zeolite Synthesis and Post-synthetic Modification 21
1.3.2 Preparation of Host-Guest Complexes 23
1.3.3 Location and Distribution of Guests within Zeolites 26
1.3.4 Notes on Sample Preparation 28
1.4 Examples of Supramolecular Photochemistry 31
1.4.1 Intrazeolite Photooxidation Reactions 31
1.4.2 Energy, Charge, and Electron Transfer in Zeolites 35
1.4.3 Supramolecular Control of Radical Reactions 39
1.4.4 Asymmetric Photoreactions using Zeolite Hosts 43
1.5 Concluding Remarks 46
1.6 References 47

1.1 Historical Perspective

Zeolites are a family of crystalline aluminosilicates, similar in composition to many soils, minerals, and clays. The early history of zeolites began in 1756 when Swedish minerologist, Baron Axel F. Cronstead, discovered the first zeolite mineral near a volcanic deposit.[1, 2] Cronstead observed that the crystals exhibited intumescence upon heating in a blowpipe and so the name zeolite was coined from the Greek words *zeo* and *lithos*, meaning "a stone" and "to boil".[3] Since this time approximately 40 natural mineral zeolites have been discovered. One initial observation was the unique property of these minerals to be reversibly dehydrated and it was hypothesized as early as 1896 that zeolites consisted of "open, spongy frameworks", as cited in reference 3. Efforts towards synthetic zeolites were initiated in the mid-1800's and the first synthesis of a zeolite, levynite, was reported in 1862.[2] The structure of zeolite materials was not elucidated until the technique of x-ray diffraction became available, after which the first zeolite structures were determined in 1930.[4] With the availability of techniques for structure elucidation, the structures of early synthetic products were verified and synthetic endeavours intensified; there are currently well over 100 synthetic zeolite structure types.

The first commercial synthetic zeolites (A, X, and Y) were marketed by Union Carbide Corporation in 1954 as a new class of materials for use in separation and purification; the first products were used for the drying of refrigerant gas and natural gas. Following this first commercialization, in 1962 Mobil Oil pioneered the use of synthetic zeolite X as a cracking catalyst for petroleum refining.[2] Since this time, the market for synthetic zeolites has expanded to an annual value of *ca.* $1.7-billion worldwide (1998).[2] The principal commercial applications of zeolites are as adsorbants, catalysts, and ion-exchange materials. The largest market, by volume, is the use of zeolites as cation-exchangers for "water softening" in detergent formulations. The specific uses of zeolites are highly diverse and include wastewater clean-up, heavy-metal uptake from nuclear waste, deodorizing agents

in pet litters, ammonia filters in kidney hemodialysis, and as hydroponic substrates for the growth of plants in *zeoponics*.[5] It is obvious from the plethora of commercial applications that research in the area of zeolite science is wide-ranging, from their behaviour as catalysts to their use as hosts in supramolecular systems. Although the field of zeolite catalysis has been extensively studied over the past four decades the interest of photochemists in zeolites as host systems for supramolecular photochemistry is relatively recent.[2, 6-10] It wasn't until the mid-1980's that researchers began to explore the use of zeolite materials as a constrained media for the control of photochemical and photophysical processes.[11-13] The acknowledgement that zeolites are convenient and versatile solid hosts for a huge variety of photochemical reactions is evidenced by the number of review articles appearing in the last 10 years on the topic of zeolite-hosted supramolecular photochemistry.[1, 14-25] This chapter will endeavour to draw attention to the properties of zeolite materials that make them such appealing substrates for hosting guest molecules during photochemical reactions. A brief review of some classical examples in zeolite host-guest photochemistry will also be presented.

1.2 Characteristics of Zeolite Materials

1.2.1 Zeolite Structure

Zeolites are microporous, crystalline aluminosilicates comprised of TO_4 tetrahedra, where T may be silicon or aluminum, with oxygen atoms connecting neighbouring tetrahedra. These tetrahedra are linked by their corners to form periodic building units (PBU) where no two aluminum atoms share the same oxygen atom in accordance with Lowenstien's Rule, which forbids Al-O-Al linkages in zeolitic frameworks.[26] These building blocks are arranged in a three-dimensional manner to form channels and cages or cavities of a discrete and specific size.

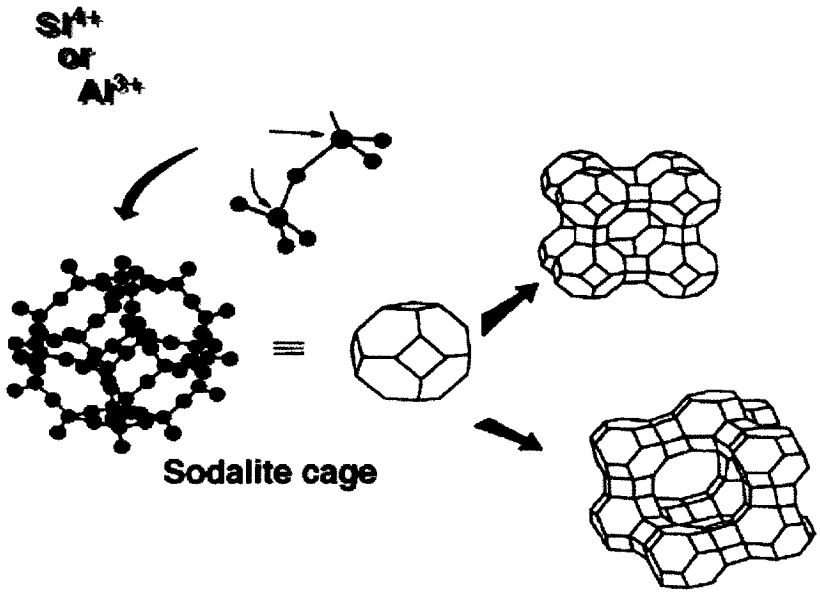

Figure 1.1 Representation of the $[SiO_4]^{4-}$ and $[AlO_4]^{5-}$ tetrahedra that are the primary building blocks of zeolites, as well as the sodalite PBU and zeolites A, X, and Y. (Reproduced with permission from reference 27).

Due to the lower valence of aluminum as compared to silicon, there is a charge difference between the $[SiO_4]^{4-}$ and the $[AlO_4]^{5-}$ tetrahedra resulting in an overall net negative framework charge for aluminum containing zeolites. Framework neutrality is restored by the presence of charge-balancing counterions, typically alkali or alkaline earth metal cations. Taking these cations into account, zeolites can

be represented by the empirical formula $M_{2/n} \cdot Al_2O_3 \cdot ySiO_2 \cdot wH_2O$, where M is a cation with valence n, typically K^+, Na^+, Ca^{2+}, etc., and y has a value anywhere from two to infinity. The structural formula of a zeolite can be expressed for the crystallographic unit cell as $M_{x/n}[(AlO_2)_x (SiO_3)_y] \cdot wH_2O$, where M is still the cation of valence n, w is the number of water molecules, and the y/x ratio (Si/Al ratio) varies from one to infinity depending on the particular structure.[3] The lower limit of Si/Al=1 is a result of the unfavourable electrostatic interactions arising from adjacent $[AlO_4]^{5-}$ tetrahedra. The sum of $x + y$ is the total number of TO_4 tetrahedra per unit cell and the part of the formula within the square brackets represents the framework composition.

Two common PBUs are the sodalite and pentasil units. The sodalite cage is the building block for many different zeolites including zeolite A, faujasite zeolites X, and Y, and also the sodalite zeolite itself. These structures, along with the structure of the sodalite cage, are given in Figure 1.2.[28] This representation of zeolite structures is a simplification, where each atom is not explicitly shown but rather the vertices are meant to represent the Al or Si atoms and the line between them symbolizes the oxygen atom link.

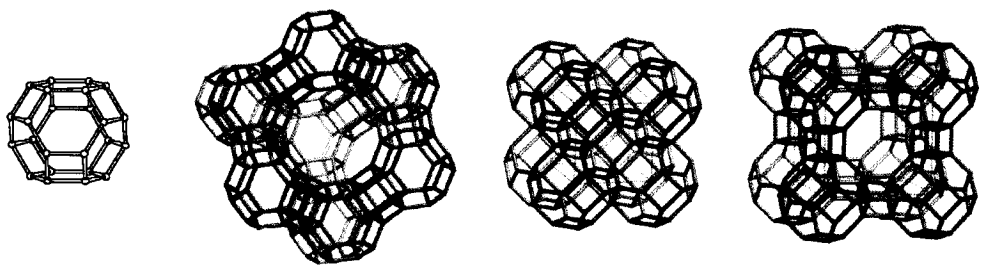

Figure 1.2 Sodalite cage that is the building block for zeolites (from left to right) X and Y, sodalite, and zeolite A. (Compiled from reference 28).

The pentasil unit is the substructure of zeolites mordenite, ZSM-5, ZSM-11, and others. The line drawings of zeolites ZSM-5 and mordenite, along with the pentasil PBU, are given in Figure 1.3.[28] An alternate representation is shown in

Figure 1.4; in order to emphasize the nature of the channel structure only the internal void spaces are indicated and the framework is omitted for clarity.

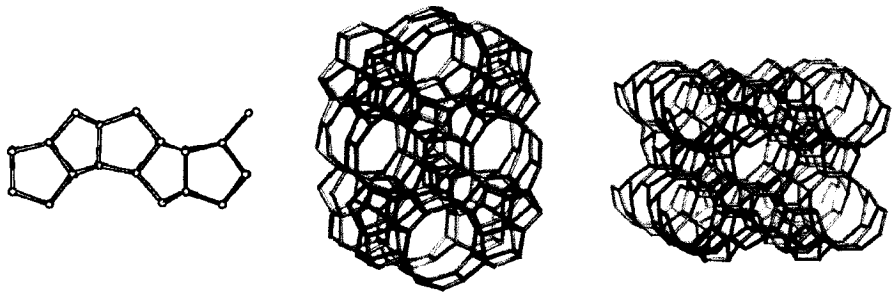

Figure 1.3 The pentasil periodic building unit along with the structures of zeolites ZSM-5 and ZSM-11. (Compiled from reference 28).

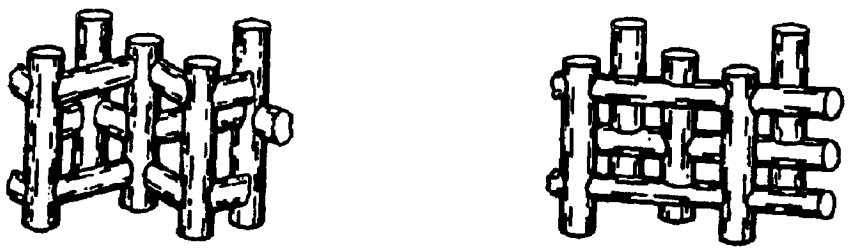

Figure 1.4 Alternate depiction of the channel structure of zeolites ZSM-5 (right) and ZSM-11 (left). (Reproduced with permission from reference 27).

Faujasite type zeolites are well-known as popular catalysts in the crude oil conversion process. The utility of zeolites as materials for catalysis and ion-exchange is largely due to the unique fact that, the highly accessible internal surface can comprise greater than 98% of the total surface area. The internal morphology of the faujasite family of zeolites consists of large spherical cavities or supercages that are tetrahedrally interconnected via a 12-membered ring opening corresponding to a pore aperture of 7.4 Å in the case of zeolite Y. The supercage diameter in zeolite Y is *ca.* 13 Å.[29] These values control the inclusion of guest molecules and the intercavity diffusion of these guests. The size of the cavities is illustrated by their known capacity to include 28 molecules of water, 5.4 molecules of benzene, or 2.1 molecules of perfluorodimethylcyclohexane per cage.[27] The free volume of the

cavities is also related to the nature of the charge-balancing countercation. The charge-compensating cations present in the internal structure of X and Y faujasite zeolites are known to occupy three different, distinct positions. As a result of the different Si/Al ratios for X and Y zeolites the number of countercations is different for these two materials despite the fact that they have the same structure. The first cation position (site I), with 16 cations per unit cell for both X and Y, is located on the hexagonal prism faces between the sodalite units. There are 32 cations per unit cell in site II positions which are located at the open hexagonal faces; this number is also the same for both X and Y. The third cation site (site III) is slightly embedded in the walls of the larger supercage. There are 38 site III cations in the case of X-type zeolites but only eight per unit cell in the case of Y-type.[6] Each unit cell consists of eight supercages and in the case of zeolite Y there are approximately 0.6 mmol of cages per gram of dehydrated zeolite. Only cations in site II and III positions are expected to be accessible for interaction with included guest molecules. The position of each cation type within the supercage can be seen in Figure 1.5. The bottom portion of Figure 1.5 also shows how the presence of a larger cation within the cavity acts to reduce the intracavity volume. These charge-compensating cations are easily exchanged and can be used to alter the properties of the intrazeolite environment, such as the free volume, and this will be discussed in detail later.

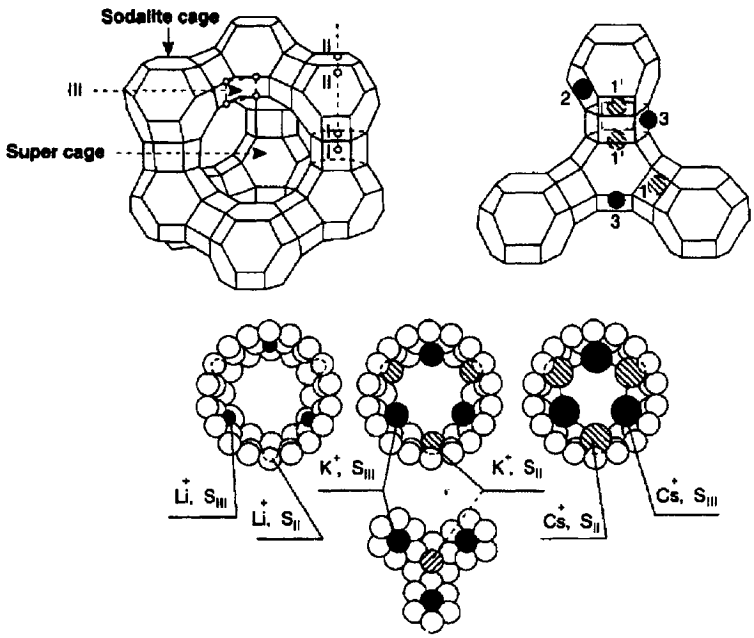

Figure 1.5 Supercage structure of faujasite zeolites X and Y showing cation locations, site I, II, and III (top). The relative cavity space reduction with increased cation size (bottom). (Reproduced with permission from reference 27).

Zeolite structures composed of pentasil units also have an open, three-dimensional internal structure. The major difference between the pentasil type zeolites and the faujasites described above, is that the pentasil interior is not an interconnecting cage system but rather a system of two intersecting channels. These channels can be round or elliptical in nature and may intersect in a straight or sinusoidal fashion (see Figure 1.4). Pentasil zeolites are typically medium-pore size materials and some of the most studied of this class of zeolites are ZSM-5 (and its all-silica isomorph, silicalite) and ZSM-11. The pore openings for these zeolites are 10-membered rings of TO_4 tetrahedra. ZSM-5 has one channel system which is straight and has a free diameter of approximately 5.1 x 5.5 Å intersecting with sinusoidal channels of free diameter 5.4 x 5.6 Å.[26, 27] ZSM-11 has two intersecting straight channels with dimensions of about 5.3 x 5.4 Å. The approximate volume at the intersection of the two channels in these zeolites is estimated to be 370 $Å^3$, corresponding to a free diameter of about 8.9 Å.[26] A list of several common

medium- and large-pore zeolites along with their pore and channel dimensions is given in reference 25.

The term zeolite is reserved for crystalline materials comprised of only $[AlO_4]^{5-}$ and $[SiO_4]^{4-}$ tetrahedra. There are, however, several interesting microporous and mesoporous materials that do not fall into this category but are interesting as possible hosts in supramolecular systems. There are a number of zeolite analogues where the tetrahedral sites in the framework are occupied by cations other than Al^{3+} and Si^{4+}; cations of Be, Mg, Zn, Co, Mn, and Ga to name a few.[30] In particular, aluminophosphate frameworks have attracted much attention. These materials have a neutral framework organized into a one-dimensional channel system; although their neutrality precludes the capacity for ion-exchange. The pore sizes range from large-pore ($AlPO_4$-5 pore size *ca.* 9 Å) to very large-pore (VPI-5 pore size *ca.* 12 Å) and they are of considerable interest to chemists interested in hosting organic molecules.

The classification of molecular sieve materials as small-, medium-, or large-pore depends on the number of atoms defining the pore aperture. As alluded to above, small-pore zeolites have eight oxygen atoms in the pore opening, medium-pore have ten, and large-pore have twelve. By this taxonomy, zeolites X and Y are large-pore molecular sieves and ZSM-5 and ZSM-11 are medium-pore. This classification system is applied to all molecular sieve materials, including non-aluminosilicates so that $AlPO_4$-5 is considered large-pore and VPI-5, with eighteen oxygen atoms in the pore opening, is very large-pore. Molecular sieves with pore apertures larger than *ca.* 13 Å are considered mesoporous molecular sieves. An important example from this class of materials is the aluminosilicate MCM-41.[31] MCM-41 is part of a class of relatively new silicate/aluminosilicate materials synthesized via a liquid crystal templating method where surfactant liquid crystals serve as organic templates. This type of templating mechanism has been proposed for a variety of systems in which inorganic structures are deposited in the presence

of pre-formed micellar arrays, for example in the biochemical formation of shells and bones.[32]

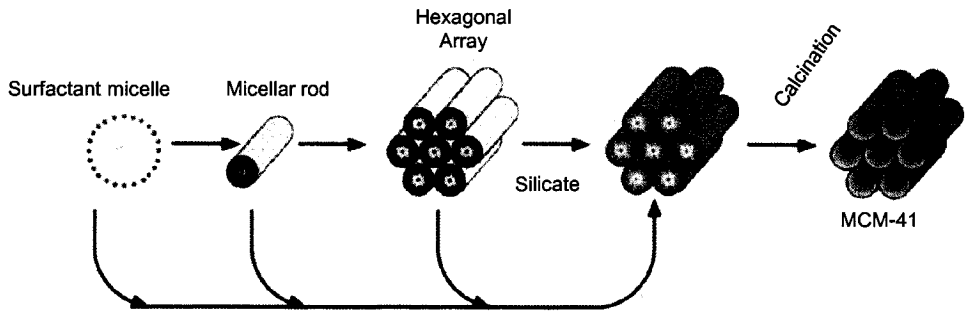

Figure 1.6 Possible mechanisms for the formation of MCM-41. (Adapted from reference 31).

MCM-41 has a hexagonal arrangement of uniform mesopores whose dimensions may be engineered in the range from *ca.* 15 Å to larger than 100 Å depending on the properties of the surfactant template; pore size generally increases with surfactant chain length. A major challenge in the synthesis of molecular sieves with very large pore diameters has been the amorphous or paracrystalline nature that typically characterizes natural mesoporous materials. Although MCM-41 is not strictly crystalline it is comprised of a uniform array of channels and the pore-size distribution determined by argon physisorption is nearly as sharp as traditional zeolite materials (see Figure 1.7).[31] MCM-41 has been shown to have a high surface area and large capacity for sorption of hydrocarbons making it an interesting possibility for hosting supramolecular systems. The silicate nature of MCM-41 also means that this material is transparent in the ultraviolet region of the spectrum making it a very suitable material for hosting photophysical and photochemical reactions. In fact, several reports have appeared in the literature since the discovery of MCM-41 where this material has been used as a host for supramolecular photochemical studies; in the photoinduced electron transfer behaviour of carotenoids[33-35] and the photochromic behaviour of spirobenzopyrans for example.[36]

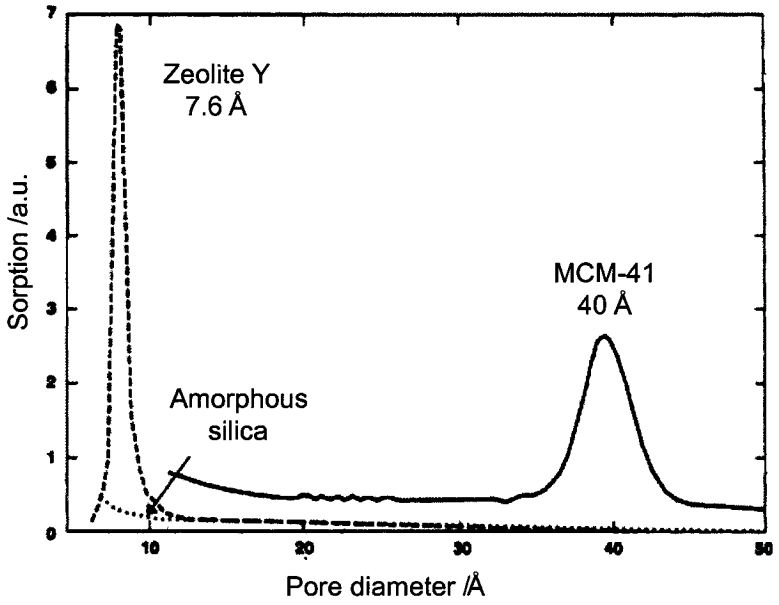

Figure 1.7 Horváth-Kawazoe pore size distributions for MCM-41, zeolite Y, and amorphous silica. (Adapted from reference 31).

1.2.2 Characteristics of the Zeolite Reaction Cavity

1.2.2.1 Microreactor Size

Typically, chemists are accustomed to carrying out reactions in vessels or containers that are disproportionately large in comparison to the size of the molecules involved. In a circumstance where the size of the reaction vessel is similar in dimension to the size of the reactants themselves, new factors must be taken into account. Reactions occurring within the zeolite intracrystalline space can be imagined as occurring within a molecular-scale reaction vessel. When considering the role of the zeolite cavity in photochemical and photophysical processes it is very important to account for molecular restriction. The inclusion characteristics and behaviour of guest molecules once they have been included will depend on every aspect of the host structure including the pore aperture and cavity size and shape. This type of influence is exerted in molecular sieving where only molecules of the appropriate size and shape are permitted access to the zeolite

interior. Once encapsulated, confinement in the zeolite further affects the reactivity by restricting certain reactive pathways, whose transition states or intermediates are not accommodated within the rigid pores, and favouring others.

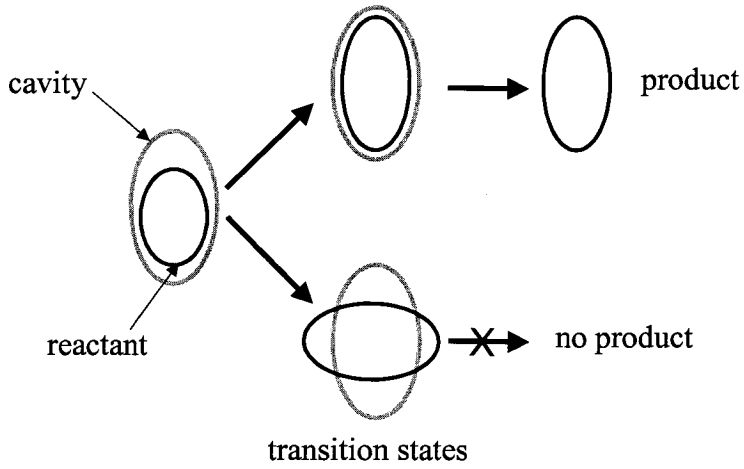

Figure 1.8 Diagram illustrating the ability of the reaction cavity to disfavour certain reactive pathways in cases where the transition state is not accommodated by the non-deformable cavities.

Zeolite encapsulation can also alter guest photochemistry by imposing steric and dynamic restrictions on reactant molecules. The amount of congestion within the pore system and the presence of pores and channels of different sizes and connectivities can combine to dictate the direction and distance that an excited species or reactive intermediate can travel before relaxation or reaction occurs. In this way, reactive pathways are modulated such that products and distributions can be very different from those observed in homogeneous solution. This effect has been elegantly described by Derouane and Gabelica as 'molecular traffic control'.[37]

The shape and free volume of the zeolite cavity will determine, to some extent, the photochemical behaviour of the guest molecule. As alluded to in Section 1.1.2, in the case of aluminum containing zeolites, the volume available inside the zeolite supercage is dependent on the number and nature of the charge-balancing counter-cations. As is intuitively expected, the free volume of the pore is decreased as the size of the cation is increased; this is illustrated in Figure 1.5. Table 1.1 shows

the calculated decrease in the available supercage volume as the cation is changed from Li^+ to Cs^+. Increasing the cation size also has the effect of reducing the size of the pore aperture.

		Supercage Volume (Å^3)	
Cation (M^+)	**Ionic Radius (Å)**	**Y zeolite**	**X zeolite**
Li	0.6	834	873
Na	0.95	827	852
K	1.33	807	800
Rb	1.48	796	770
Cs	1.69	781	732

Table 1.1 Calculated cation dependence of supercage free volume, calculations performed using a modification of the POLYVOL program. (Compiled from reference 27)

1.2.2.2 Polarity and Electric Field

As described above, the zeolite cavity can act as a 'passive' host influencing the guest photobehaviour in a steric fashion. However, the zeolite host can also influence the guest in a more 'active' manner via interactions with charge-balancing cations. In faujasite zeolites X and Y many cations are embedded in the walls of the supercage; these site II and III cations are shielded on one side by the zeolite framework while the other side is unshielded and exposed to the center of the supercage. The partially unshielded cations generate large electric fields that extend into the supercage and are able to modify the environment experienced by an included guest molecule. The fields experienced by a guest molecule can range from 0.1 to 6.4 VÅ^{-1} depending on the Si/Al ratio, the nature of the charge-balancing cation, and the distance between the cation and the guest.[6] A variety of calculations have estimated the contribution of the type and location of the cation to the resulting electric field. Several general observations have been made regarding

zeolite intracavity electric field: (1) the electric field at site III is several times stronger than for the same cation at site II, (2) within the same row of the periodic table, divalent cations exert a stronger field than monovalent cations, (3) the average field increases with increasing Si/Al ratio, and (4) smaller cations with lower atomic numbers, within the same group, produce higher fields.[6] From these observations it is possible to hypothesize that the zeolite supercage will be able to polarize an included guest molecule thereby distorting its electron density. Based on (2) and (4) an organic guest would be polarized more readily in LiY than in CsY, and more easily in CaY than in NaY. It is also expected that the intrazeolite environment will favour reactions, such as heterolytic cleavage or electron transfer, generating ions and radical ions.

The field within the zeolite cavity may be loosely thought of in terms of the polarity of a reaction medium. The two concepts are not exactly the same, especially when considering that the dipoles induced by a polar solvent are constantly fluctuating whereas the zeolite fields are stationary. Several attempts have been made to measure the 'micropolarity' of zeolite cavities but little specific agreement has been found. A variety of different probes have been used including pyrene aldehyde,[38] salicylidenes,[39] and Nile red.[40] All reports generally agree that the nature of the zeolite interior is polar but estimates of the extent of this polarity range from that of water to aqueous acetonitrile to aqueous alcohol mixtures. These disagreements in specific values for polarity are likely due to differences in water content and sample treatment in the various experiments. The contribution of the cation to polarity is much higher in the absence of co-adsorbed water; water molecules are able to coordinate to the cations and effectively shield included guests from the cation-induced field.[40]

1.2.2.3 Acid and Base Properties

Although the formula for X and Y type zeolites, $M_{x/n}[(AlO_2)_x (SiO_3)_y]$, does not indicate reactive acid sites it is well known that activated $M^{2+}X$ and $M^{2+}Y$

zeolites contain Brønstead acid sites and zeolites with monovalent counterions also have various Brønstead acid sites.[2, 3, 6, 41] Zeolite acid and base sites can have a profound effect on guest behaviour. Even a small number of acid sites can have important consequences in catalytic reactions; the unexpected protonation of olefins during catalytic oxidation is a prime example.[42] Therefore, it is imperative to take into account the acid-base properties of zeolites when considering the photobehaviour of included guest molecules. The acid-base nature of zeolite cavities is dependent on four factors: (1) the nature of the acid-base site, i.e. Brønstead or Lewis, (2) the location, (3) the number of sites, and (4) the strength.

Zeolites may potentially contain both aluminol and silanol groups as loci of Brønstead acidity. Aluminol sites are very weak and silanol groups are only significantly acidic when adjacent to a tri-coordinate Al site; i.e. a site of Lewis acidity. As a consequence, sites of Brønstead acidity in zeolites are typically Si-O(H)···Al groups. These types of sites have been hypothesized to form by polarization of water molecules on heating, resulting in the formation of hydroxylic-like groups. Cations can affect the Brønstead acidity of zeolites in two ways; in the case of zeolites where the charge-balancing countercation has been exchanged for a proton, HY for example, Brønstead acidity is introduced directly. Proton exchanged zeolites are prepared by first partially exchanging the existing charge-balancing cation for NH_4^+, followed by heating at high temperatures to release ammonia.[2, 43]

As suggested above, the bridging silanol groups that are principally responsible for Brønstead acidity in alkali and alkaline earth cation-exchanged zeolites X and Y, are largely generated during the activation process, i.e. heating at high temperatures to achieve dehydration. The second way in which cations can affect Brønstead acidity relates to their role in the generation of these hydroxylic-like groups. As a result of the electrostatic field associated with the cation, adsorbed water molecules are polarized, ultimately resulting in the formation of acidic hydroxyl groups. The number of acid sites formed increased linearly with

the polarizing power of the cation.[6] As a result, the number of acid sites generated by heating M^{2+} exchanged zeolites is greater than for M^{+} exchanged zeolites and acid generating power decreases going down the period from magnesium to barium. Although alkali-exchanged X and Y zeolites are generally thought to be largely nonacidic, even these have been found to contain small numbers of Brønstead acid sites.[42]

A number of techniques have been used to probe intrazeolite acidity. UV-visible (UV-vis) spectroscopy was first applied to the characterization of zeolite acidity by Walling in 1950.[44] This method adapted the approach developed by Hammett for determining the strengths of strong solution-phase acids and relies on the use of indicator bases that change colour upon protonation. This technique has been widely applied over the last 50 years but recently, new methodologies employing fluorescence spectroscopy, for example, have emerged.[41] IR and Raman spectroscopy with pyridine and ammonium probes,[45-47] as well as NMR using alkylamines, trialkylphosphines, and other probes[48-51] have also become commonplace. One recent study employing both magic angle spinning (MAS) NMR and colour indicators estimated an average of one Brønstead acid site per two unit cells (16 supercages).[52] This number was much higher for divalent cation exchanged zeolites, approximately 8 acid sites per unit cell for CaY, and values were found to fluctuate depending on sample pre-treatment.

Zeolites may also contain Lewis acid sites in the form of tri-coordinate framework aluminum sites, extra-framework aluminum (EFAL), and charge-balancing countercations. EFAL species are generated when Al is removed from the zeolite framework and subsequently migrates to the surface of the crystal. EFAL can be removed by treatment with $(NH_4)_2SiF_6$ but, when left in place, can play a very important role is solid-acid catalysis.[6] Other Lewis acid sites associated with aluminum are usually only generated when the zeolite is activated at greater than 650°C. The nature and number of Lewis acid sites in zeolites are even less well

characterized than their Brønstead counterparts but it is generally true that zeolites with a decreased Si/Al ratio have a higher Lewis acidity.

In addition to Lewis acidity, each oxygen atom in the zeolite framework is a potential Lewis base site. Oxygen atoms with a more negative charge have a more basic character. Framework oxygen atoms increase their negative charge when bonded to aluminum instead of silicon and, since the negatively charged framework AlO_4^- interacts with the charge-balancing cation, the basicity of the oxygen is indirectly influenced by the nature of the cation. For a zeolite of given aluminum content, the Lewis acid-base behaviour will actually be controlled by the cation. Strongly acidic cations like Li^+ cause the zeolite to behave more like an acid, whereas the zeolite has more basic properties when the cation is less acidic and of lower electronegativity, for example Rb^+ and Cs^+.

1.2.2.4 Light-atom Effects

The light-atom effect, as suggested by the name, refers to the effects of smaller, lighter cations on the photoprocesses of included guest molecules. These small cations, such as Li^+, have a higher charge density and electrostatic potential and, as a result, have a stronger interaction with the guest molecule; the strength of the guest-cation binding interaction is directly dependent on the charge density of the cation. The light-atom effect can have consequences for both the photophysical and photochemical behaviour of guests. The spectral resolution in emission spectra of olefins, arylalkyl ketones, and aromatics included in zeolites varies with the nature of the charge-balancing countercation. Variations in the intensities of vibrational bands and spectral shifts have also been observed for some aromatic molecules.[27] A classic example of modified photophysical behaviour is the spectra of pyrene when included in zeolites with various countercations. The intensity of the 0-0 transition of the $S_0 \rightarrow S_1$ band was found to depend on the charge density of the cation present within the supercages. It has been hypothesized that the strong interaction between the aromatic π system and the cation may result in a slight

bending of the aromatic plane causing a reduction in symmetry.[26] A reduction in the lifetime of excited singlet and triplet states of aromatic molecules has also been observed in the case of light-atom exchanged X and Y zeolites. It is believed that this reduced lifetime is the result of enhanced radiationless processes when the aromatic molecule interacts strongly with the cation.

In the case of ketones the light-atom effect causes a change in the nature of the lowest triplet state. This is readily apparent from the phosphorescence spectra of ketones included in Li^+ exchanged zeolites versus Cs^+ exchanged ones. For example, the phosphorescence spectra of valerophenone in LiX is characteristic of the π,π^* triplet whereas the emission from CsX complexes was attributed to the n,π^* state.[26] Switching of the character of the lowest triplet state is a familiar phenomenon for ketones in polar solvents.

The nature of the cation can also affect the chemistry of guest molecules. The photochemistry of cycloalkanones has been studied both in solution and within the cavities of various cation-exchanged zeolites.[53] In solution these species undergo exclusively a Norrish II γ-hydrogen abstraction. Irradiation in M^+Y zeolites gave Norrish I α-cleavage products as the major photoproducts of the reaction, with the relative yield of type I to type II products depending on the nature of the cation. Smaller, lighter cations were observed to have the greatest effect on product distributions. It has been suggested that the cations in the supercage interact electronically with the ketone functionality to sterically impede the hydrogen-abstraction required for formation of Norrish II products. Cation-binding influences the preferred conformation of the ketone when residing within the supercage; more strongly binding cations are expected to have a greater effect. The cation binding interferes with the rate of γ-hydrogen abstraction, but not the Norrish I α-cleavage, therefore, the presence of a "light atom" is expected to decrease the efficiency of the type II process only.[53] There are multiple other examples of how light atoms are able to affect the photochemistry of carbonyl compounds included in zeolites.[54, 55]

1.2.2.5 Heavy-atom Effects

As was the case with light atoms, heavy atoms can also affect both the photochemistry and photophysics of organic molecules included in zeolites. It has been observed that for fused aromatics the emission spectrum is drastically changed upon inclusion in heavy-atom exchanged zeolites. Naphthalene, for example, exhibits characteristic blue emission when included in Li^+ and Na^+ exchanged zeolites. However, as the mass of the cation increases (going to Rb^+, Cs^+, Tl^+) the blue emission is drastically reduced and a new, longer wavelength emission band appears, corresponding to the naphthalene phosphorescence. This enhanced phosphorescence has been attributed to the heavy-atom effect, a well-known perturbation whereby the presence of a heavy-atom increases the spin-orbit coupling in the system. Spin-orbit coupling mixes orbital and spin angular momenta such that neither is completely conserved resulting in a breakdown of the selection rule.[56] The end result of this interaction is that normally forbidden processes, such as intersystem crossing between singlet and triplet states, become less unfavourable. The spin-orbit coupling constant increases strongly with atomic number and is proportional to Z^4, clearly the effect becomes more important for heavier cations. The effect in zeolites is seen to increase linearly with cation mass.

Heavy-atom exchanged zeolites are observed to cause spin-orbit induced intersystem crossing (ISC) as efficiently as heavy-atom perturbers that are covalently attached to the chromophore. This is likely due to the proximity of the cation as well as the presence of more than one cation per supercage. Heavy-atom exchanged zeolites like TlX and TlZSM-5 have been used as hosts to enhance the phosphorescence in systems that normally have little to no observable emission from the triplet state. The phosphorescence spectra of *trans*-stilbene has been recorded at both 77 and 298 K when included in Tl^+ exchanged ZSM-5.[57] In the past only very weak phosphorescence was observed from *trans*-stilbenes at 77 K in an organic glass containing ethyl iodide as a heavy atom perturber. Thallium-exchanged zeolites were also used to record the first phosphorescence spectra of

trans α,ω-diphenylpolyenes.[57] These compounds typically exhibit very low intersystem crossing and extremely efficient fluorescence; it's quite remarkable that well-resolved, structured phosphorescence spectra were recorded for these molecules.

As discussed above, cations can be used to control the efficiency of intersystem crossing to populate the triplet state of organic molecules residing within the zeolite supercage. Heavy-atom effects can also be used to control the product distribution in a photoreaction. One demonstrative example of this is in the photochemistry of acenaphthylene.[58] Irradiation of acenaphthylene in solution gives both the *cis* and *trans* dimers as photoproducts; the singlet yielding predominantly the *cis* while the triplet gives both *trans* and *cis* equally. Photolysis of acenaphthylene in zeolites gave the expected dependence on charge-balancing cation. In Li^+ and Na^+ exchanged zeolite Y only the *cis* dimer was observed, consistent with a low intersystem crossing yield. In heavy-atom exchanged Y zeolites RbY and CsY, the triplet state is generated much more efficiently and consequently the *trans* dimer product is also observed.

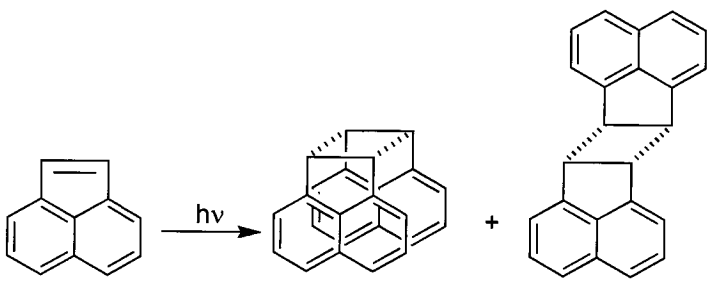

Scheme 1.1 Photodimerization of acenaphthylene yielding the *cis* and *trans* dimers.

Similar effects of heavy atoms have also been observed in the photochemistry of dibenzobarrelene and benzobarrelene.[59]

1.3 Synthesis and Manipulation

1.3.1 Zeolite Synthesis and Post-synthetic Modification

Zeolite synthesis occurs by a hydrothermal process where the reagents are a silica source, an alumina source, a mineralizing agent such as OH^- or F^-, and a structure directing agent.[3] The structure directing agents are typically alkali or alkaline earth metal cations, organic ions, or organic molecules (often ammoniums or amines) and they act to direct the formation of the specific zeolite framework. The synthesis is performed in a closed system at elevated temperatures, typically 60-200 °C. There are a large variety of silica and alumina sources used for synthesis and the choice of each component can have a significant impact on the product morphology. In fact, every aspect of the synthesis (silica/alumina ratio, reaction time, temperature, alkalinity) can have important consequences for the crystallization kinetics and the nature of zeolite formed. After synthesis, any organic structure directing templates will remain trapped in the channels and pores and must be removed by calcination. Table 1.2 below exemplifies how reaction parameters can affect zeolite morphology.

Na A		TPA ZSM-5
	Sample synthesis mixtures (molar oxide ratio)	
1	SiO_2	1
0.5	Al_2O_3	< 0.14
1	Na_2O	0.16
	$TPAO_2$	0.3
17	H_2O	49
> 100	Temperature (°C)	> 150
	Physical and chemical properties	
3D cages connected by windows	**Pore arrangement**	2D intersecting channels
1.28	**Density (g cm^{-3})**	1.77
0.37	**Pore volume (cm^3 g^{-1})**	0.18
Na^+, H_2O	**Lattice stabilizer**	TPA^+
1	**Si/Al ratio**	> 12
low	**Brønstead acidity**	high
hydrophilic	**Affinity**	hydrophobic

Table 1.2 Synthesis conditions and physicochemical properties of zeolites NaA and TPA-ZSM-5. TPA, tetrapropylammonium. (Compiled from reference 2).

There are several post-synthetic modifications that can be made to alter zeolite properties. For example, the Si/Al ratio can be altered after synthesis by steam treatment, acid leaching, ammonium fluorosilicate, or $SiCl_4$ treatment. The aluminum content is an important characteristic of zeolite materials; as discussed in Section 1.2.2.3, the acid-base properties and catalytic activity of zeolites are heavily dependent on the Si/Al ratio. In addition, an increase in the Si/Al ratio results in

an increase in thermal stability and hydrophobicity, while ion-exchange capacity decreases. Pure silica zeolites, such as silicalite, have a neutral framework, are highly hydrophobic, and have no ion-exchange capacity or catalytic activity. The minimum Si/Al ratio is one as a result of the unfavourable interaction between aluminum cations in the case of an Al-O-Al sequence in the framework.

The other important post-synthetic modification involves alternating the charge-balancing cations. As discussed in Section 1.2.2, the nature of the countercation has a very significant effect on the properties of the zeolite including acidity and basicity, cavity size, and guest-binding interactions. The cations present within the zeolite supercages are readily substituted using conventional ion-exchange techniques.[2, 3] Exchange is accomplished by simply stirring the Na^+-exchanged zeolite with an aqueous solution of the chosen cation in the form of a chloride or nitrate salt. The material is dried at high temperatures and the aqueous ion-exchange cycle is repeated twice more. Typical percent ion-exchange values for Y zeolites are 47% for LiY, 97% for KY, 44% for RbY and 47% for CsY.[60] Due to their large size, Rb^+ and Cs^+ only exchange with site II and III cations so the maximum exchange is these cases is 70%. The low percent exchange for LiY is because hydrated Li^+ does not readily exchange site I cations.[60] The simplicity of the ion-exchange process allows the properties of each zeolite to be dramatically altered without affecting the crystalline, nanoporous nature of the material.

1.3.2 Preparation of Host-Guest Complexes

1.3.2.1 Direct Inclusion

The incorporation of guest molecules into the zeolite interior is controlled by both the size of the zeolite cavity and the size of the entrance aperture. If the guest molecule has a kinetic diameter smaller than the pore opening, it can be directly included via either vapour phase or solution inclusion. Zeolite host-guest complexes are designated by the abbreviation 'guest@zeolite'. In all cases the zeolite material must be pretreated by heating at 400-500 °C to remove organic

structure templating agents and, in the case of hydrophilic zeolites such as NaY, to remove absorbed water. After activation, the zeolite sample may be evacuated and exposed to the guest in the form of a gas or vapour. Alternatively, the dry zeolite can be placed in contact with a solution of the guest molecule in an appropriate solvent. In order to favour migration of the guest molecule into the polar cavities of NaY a non-polar solvent is typically used. A volatile solvent is also preferred in order to its facilitate removal. After inclusion, the zeolite complex is collected and washed with fresh solvent in order to remove any guest molecules residing on the particle surface. The resulting complex can be dried in air, under inert gas, or under vacuum and each method may have a distinct effect on the guest photobehaviour. The presence of water or residual solvent will result in increased crowding within the supercage as well as shielding of the charge-balancing cations. The presence of oxygen as a result of drying in air can also have significant effects on the photochemistry and photophysics by interacting with reactive intermediates such as radicals or triplet states. The average loading or *occupancy* (<S>=number of molecules/supercage) of the prepared zeolite complex can be calculated in a variety of ways; for example by spectrometric analysis of the supernatant inclusion solution and comparison with a calibration graph, by combustion elemental analysis of the zeolite complex itself, or by thermogravimetric analysis.

1.3.2.2 Ship-in-a-bottle Synthesis

In the case of a guest molecule whose size cannot be accommodated by the pore aperture other strategies must be pursued. Ship-in-a-bottle synthesis has emerged as a clever methodology for the preparation of inclusion complexes of guest molecules whose dimensions preclude direct inclusion into the zeolite nanopore.[61] As the name suggests, this is accomplished by using precursors that are small enough to freely diffuse into the zeolite interior where they react to form the desired molecule. Once formed, the synthesized molecules are permanently entrapped within the zeolite supercage and can neither escape nor diffuse between

cavities. This strategy was initially applied to the preparation of metallic complexes[61, 62] but has been expanded in recent years to the synthesis of encapsulated metallophthalocyanines[63] and organic ions and molecules.[64, 65] A successful reaction for ship-in-a-bottle synthesis should be high-yielding and generate no by-products that will be permanently entrapped within the zeolite. The only method available for purification of ship-in-a-bottle complexes is solid-liquid extraction to remove starting materials and side products. The occluded complex can be characterized spectroscopically by UV-Vis, IR, and MAS NMR, although low sensitivity can reduce the usefulness of NMR unless guests have been isotopically labeled. If the encapsulated guest is stable to strongly acidic conditions, the zeolite framework can be dissolved in concentrated hydrochloric or hydrofluoric acid and the guest can be recovered and analyzed directly.[15] Unfortunately many species are unstable under these aggressive conditions.

An early example of the ship-in-a-bottle synthesis of a metal complex is the preparation of an encapsulated Co^{2+}-salen complex.[61] Salen is an acronym for the bis(salicylidene)ethylenediamine ligand. The salen ligand is very flexible and is easily included in the zeolite cavities but the resulting metal complex with cobalt is highly rigid and as a result the product is permanently entrapped. This particular complex has high affinity for oxygen but shows an excellent resistance to autooxidation presenting an interesting similarity to hemoglobin. In fact, the resemblance between enzymes, where a catalytic metal complex is embedded in the protein skeleton, and this type of zeolite complex, where the framework acts as an 'inorganic protein' matrix, lead to the introduction of the term *zeozyme*.[66]

The ship-in-a-bottle synthesis of encapsulated triarylmethylium cations is a classic example of a carbon-carbon bond forming reaction to generate an organic species in the pores of a tri-directional zeolite.[64] The fact that the key step in generation of the product is formation of a covalent bond distinguishes this example from earlier work on the formation of metal-ligand complexes. In this example substituted trityl cations were prepared via the acid-catalyzed

condensation of benzaldehyde or *p*-methoxybenzaldehyde with an electron rich aromatic (anisole or *N,N*-dimethylaniline). Each of the precursors was introduced into the H^+-exchanged form of a zeolite from an isooctane solution and the slurry was refluxed for 12 hours. Figure 1.9 gives a pictorial representation of the ship-in-a-bottle synthesis. Interestingly, the reaction catalyzed by the acidic zeolite is actually more efficient than the solution phase condensation using Lewis acid catalysts.

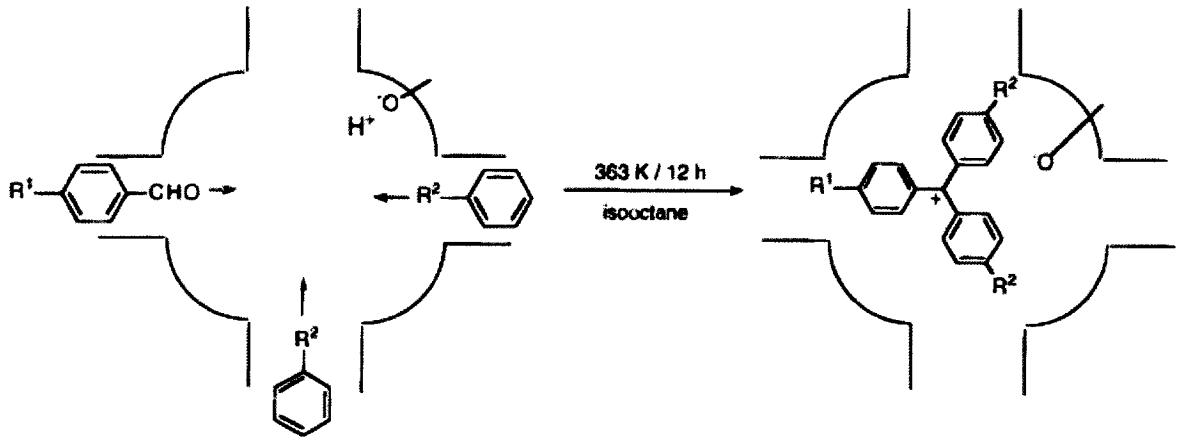

Figure 1.9 Ship-in-a-bottle synthesis of triarylmethylium cations acid-catalyzed condensation of benzaldehydes and activated arenes. (Reproduced with permission from reference 65).

The trityl cation complexes prepared in this example were characterized spectroscopically and their use as heterogeneous photosensitizers was explored.

1.3.3 Location and Distribution of Guests within Zeolites

When considering the behaviour of guests included in zeolites it is useful to consider the location and distribution of molecules within the zeolite cavities. There are many studies describing the characterization of guest molecule location in zeolites, based on techniques such as molecular modeling, X-ray and neutron diffraction, as well as NMR, IR, and optical spectroscopies.[67-74] Many of these studies have employed small molecules such as benzene or pyridine.

The loading of a zeolite can have significant effects on the location and distribution of guest molecules. Loading is sometimes expressed in terms of the occupancy <S> or number of molecules per supercage in the case of X and Y zeolites. It is important to be aware that values of <S> reflect only the average loading and do not give any information about the heterogeneity of guest distribution amongst the zeolite cavities. A sample with a calculated occupancy of one molecule per supercage may still contain both empty and multiply occupied pores. In studies of benzene distribution in faujasite zeolites it was found that, at high loading, there are three distinct types of benzene molecules within the supercages of zeolites X and Y. One type is at the cation site II or III, one at the 12-membered ring window, and the other corresponds to clusters of benzene residing within the supercage (Figure 1.10).

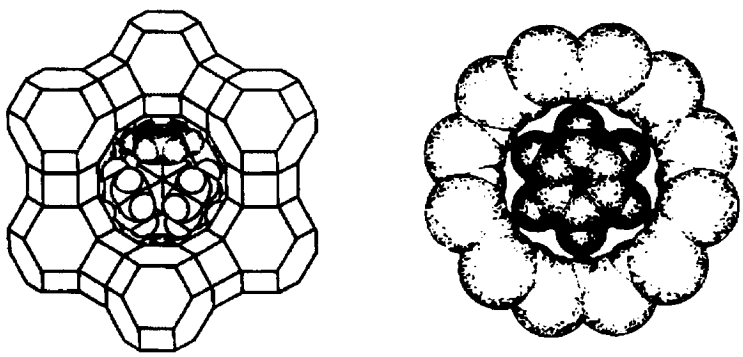

Figure 1.10 Position of benzene within the supercage associated with the site II cations (left) and at the window site (right). (Reproduced with permission from reference 27).

At low loadings the formation of benzene clusters is avoided and distribution between cation sites and window sites is controlled by the cation. At the cation site, benzene molecules are stabilized by cation-π interactions and the binding strength is dependent on the charge density or electrostatic potential of the cation. At the window site the interaction is dominated by van der Waals forces and acid-base interactions between guest C-H bonds and ring oxygen atoms. For pentasil zeolites like ZSM-5, studies have indicated that, at low loadings, the

preferred location of guest molecules is at the intersection between channel systems. As the loading levels increase the channels themselves also become occupied.

The nature of supramolecular hosts like zeolites is such that there will always be a number of different sites available to guest reactants. The possibility of more than one reactive site is rarely encountered in solution. In a fluid solution, reacting molecules experience an average microenvironment as a result of the fast relaxation time of the solvent or the high mobility of reactant molecules. In contrast to solution, the zeolite structure is time-independent. A molecule in a zeolite will only experience an average environment if it is able to establish an equilibrium between various reactive sites during the lifetime of the excited state. This situation is rare since the rates of guest diffusion within the zeolite are generally slow compared to the time scale of photochemical and photophysical processes.[26] These factors have a large impact on the differences observed between solution and intrazeolite photoreactions.

1.3.4 Notes on Sample Preparation

Many different aspects of sample preparation and treatment can have a significant impact on the observed photobehaviour of included guest molecules. These factors include inclusion temperature, drying conditions, presence of co-adsorbed water or solvent, and sample age. Due to the activation energy for diffusion within the micropores, mild heating of the inclusion slurry can have a large impact on the sample loading achieved per time.[15] The temperature of inclusion can also affect the distribution of included guest molecules; bulky molecules incorporated at higher temperatures may have a more homogeneous distribution within the particle. Differences can also be observed depending on whether or not the zeolite is cooled to room temperature prior to inclusion of the guest.

The drying conditions or pre-treatment of the complex with air, inert gas, or vacuum can also significantly affect the subsequent behaviour of the guest. In the

case of air or oxygen the effect may be as simple as the quenching of an intrazeolite excited state or reactive intermediate; for example oxygen-induced quenching of an excited triplet state.[75] There is also the possibility of more unexpected effects, such as the 'lubricating' effect observed for nitrogen. Large aromatic molecules were observed to be more highly mobile in nitrogen purged samples in comparison to evacuated ones. This lubricating effect was attributed to occupation of cation binding sites by nitrogen, thereby reducing the interaction between the cation and the guest molecule.[76] The increased influence of cations on guest molecules in vacuum treated zeolite samples, as opposed to those purged with gas, is an important consideration.

Many zeolites commonly used as hosts for photochemical studies of supramolecular systems are significantly hydroscopic, zeolites NaX and NaY for example. As a result, unless special precautions are taken, water is adsorbed into the pores very quickly upon exposure to ambient moisture. This co-adsorbed water may have the effect of shielding cations, as mentioned above, but it can also play a role in intracavity crowding, as is the case for thionin in NaY. The cationic dye thionin was observed to have drastically different spectroscopic properties in 'wet' versus 'dry' samples of zeolite NaY.[77] The diffuse reflectance spectrum of a hydrated sample of the thionin-exchanged zeolite showed absorption bands for both the monomer and the hydrated H-dimer forms of thionin. When the water was removed, only the monomeric form of thionin was observed. The occurrence of monomeric versus dimeric thionin within the zeolite cavities results in a drastic colour change of the material from blue to pink. The presence of water in this case has a significant impact on the observed properties of the guest molecule

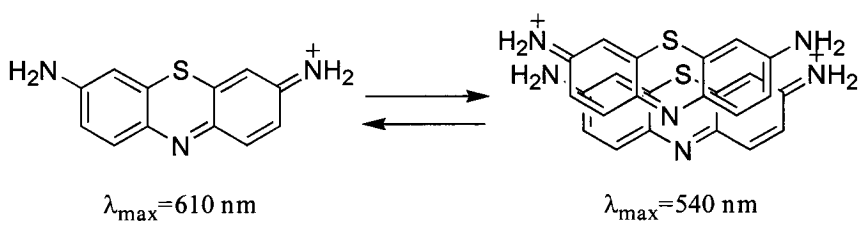

λ_{max}=610 nm λ_{max}=540 nm

Scheme 1.2 Monomer and H-dimer forms of cationic thionin.

The case of pyrene in zeolite Y provides an excellent example of the importance of sample aging. As mentioned above, the heterogeneous distribution and slow equilibration of guests within zeolite particles can have surprising effects on guest photobehaviour. These effects can be more pronounced in the case of bulky guest molecules whose diameters closely match that of the pore aperture. When pyrene is included in the pores of zeolite NaY, emission spectra recorded immediately after preparation indicated the presence of predominantly the excimer (excited dimer) form.[76] Excimer emission is observed despite the fact that the calculated occupancy is well below a value indicating doubly occupied cavities. As the sample is aged over a period of one month, the emission spectrum is seen to shift from primarily excimer to primarily monomer in nature. Aging of the sample results in a re-distribution of pyrene until an equilibrium distribution, with only singly occupied cavities, is achieved. The re-distribution time was found to depend on the presence of both water and inert gases.[76]

The examples presented in this section are intended to emphasize the need for careful attention to consistency in preparing zeolite samples for photochemical studies. The effects discussed above can also help to explain the discrepancies often observed between results from different laboratories.

1.4 Examples of Supramolecular Photochemistry

1.4.1 Intrazeolite Photooxidation Reactions

The selective oxidation of small hydrocarbons is one of the most important reactions in the production of organic chemicals. As an example, many of the building blocks for plastics and other synthetic fibers are generated by the oxidation of hydrocarbons.[78] Molecular oxygen has emerged as a favourite oxidant for large-scale oxidations, largely due to economic factors. The photochemical oxidation of hydrocarbons has been pursued as a means of overcoming the inherent lack of product specificity in thermal oxidation reactions due to secondary chemistry. One of the most attractive approaches to photooxidation is via photoexcitation of hydrocarbon•O_2 charge-transfer complexes.

It has been established that a number of organic molecules are able to form weak, contact charge-transfer complexes with molecular oxygen; the stabilization energy is approximately -0.9 kcal mol^{-1} for oxygen in benzene for example.[79] Unfortunately, in the case of small alkenes, these charge-transfer absorptions lie in the UV region. The necessary use of high-energy photons for the photolysis can reintroduce many of the thermal reaction problems, such as rearrangement and fragmentation.

Frei *et al.* were the first to recognize the usefulness of zeolite materials in the context of stabilizing the hydrocarbon-oxygen complex and several examples of bathochromically shifted charge-transfer bands have since been reported.[80-83] Stabilization of the hydrocarbon•O_2 complex is a result of strong electrostatic interactions within the zeolite cavity. As discussed in Section 1.2.2.2, the presence of charge-balancing cations within the zeolite supercage can generate a large electrostatic field, depending on the Si/Al ratio and the nature of the cation. Interaction between the field and the large dipole generated upon excitation of the hydrocarbon•O_2 couple to a charge-transfer state, results in a strong stabilization of the excited state. The magnitude of the stabilization will depend on a number of

factors, including the orientation of the charge-transfer complex within the supercage, but is typically on the order of one to several electron volts (eV).[81] In the case of *cis*- or *trans*-butene the result is a shift in the onset of absorption from 350 nm (observed in solution, gas phase, or solid O_2) to greater than 600 nm when included in zeolite NaY.[81] The use of longer wavelength photons to access low energy photooxgenation pathways results in improved product selectivity. In the case of *trans*-butene, where the hydrocarbon•O_2 complex is stabilized by *ca.* 1.5 eV in NaY, the sole product observed was the 3-hydroperoxybutene. The photooxidation is suggested to occur via deprotonation of the alkene to generate an allyl radical and a hydroperoxy radical. The hydroperoxide product is formed following cage recombination of these two radicals (Scheme 1.3).

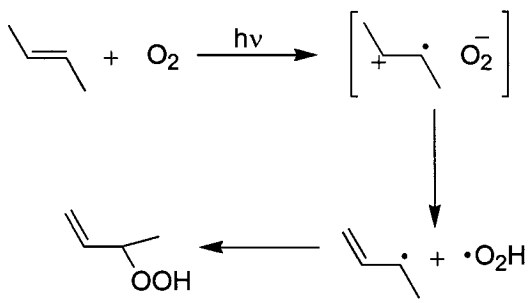

Scheme 1.3 Formation of the allylic hydroperoxide from photooxidation of *trans*-butene in zeolite NaY.

Electrostatic stabilization has also been used to improve selectivity in the partial photooxidation of cyclohexane to generate cyclohexanone.[83] Autooxidation of cyclohexane to form cyclohexanone is limited by an inherent lack of selectivity. Good selectivity is only achieved at low conversions, the major problem at high conversions being over-oxidation of the desired carbonyl products. In the cavities of zeolite NaY, the cyclohexane•O_2 charge-transfer absorption band is shifted from 275 nm to 500 nm, corresponding to a stabilization of *ca.* 2 eV.[83] Visible light oxidation of cyclohexane results in the formation of cyclohexanone and the thermal precursor, cyclohexyl hydroperoxide. Both positional restraints and absence of

secondary photochemistry contribute to the selectivity observed in this reaction, even at high conversions. The mechanism, given in Scheme 1.4, is presumed to be the same as shown above for the alkene. The initial proton transfer is favoured by the acidity of the hydrocarbon radical cation.

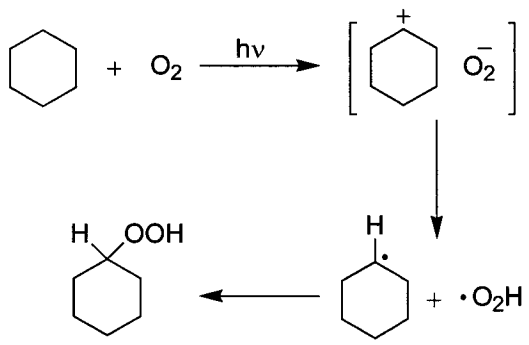

Scheme 1.4 Mechanism for the photooxygenation of cyclohexane in zeolite NaY.

Inclusion in zeolite cavities has also been used to control selectivity in the photooxidation of organic molecules by reaction with singlet molecular oxygen, a highly reactive form of oxygen. Singlet oxygen reacts rapidly with alkenes and aromatic hydrocarbons via cycloaddition and the *ene* reaction. The oxidation of organic sulfides also proceeds via reaction with singlet oxygen.

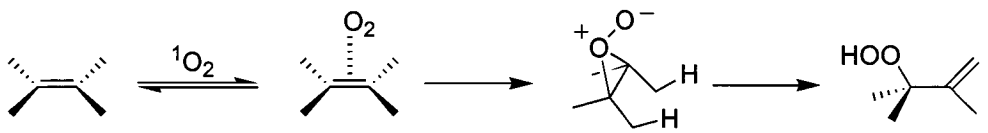

Scheme 1.5 Plausible mechanism for the singlet oxygen *ene* reaction showing the perepoxide intermediate.[84]

The main problem with singlet oxygen reactions is the lack of selectivity of this highly reactive species. Attempts to improve the diastereo- and enantioselectivity in these reactions have focused on control of both the substrate conformation and the geometry of singlet oxygen approach. In this context, supramolecular systems are an attractive reaction media due to their ability to organize and constrain reactants.[84] The use of zeolites is also convenient because the charge-balancing cations may be partially exchanged for the cationic sensitizers

used to generate singlet oxygen, such as methylene blue, methylene green, and thionin. In an early example of the intrazeolite singlet oxygen *ene* reaction, it was observed that both 2-methyl-2-pentene and β-myrcene were regioselectively photooxidized to a single allylic hydroperoxide product. This is in sharp contrast to the photooxidation in solution, where each hydroperoxide is formed in equal yield.[85] Further studies on the intrazeolite phootoxidation of a series of tetrasubstituted alkenes lead to the clarification of a model for the influence of the zeolite microenvironment on product regioselectivity.[86]

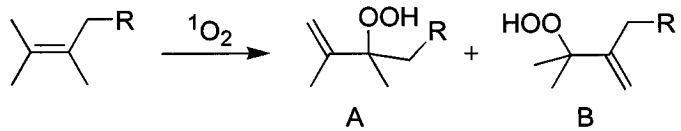

Scheme 1.6 Type II photooxidation of tetrasubstituted alkenes.

It was found that in solution, increasing the size of the allylic substituent R favoured formation of hydroperoxide B, shown in Scheme 1.6. The same trend was not observed in intrazeolitic photooxidation of these substrates, where the bulkiest R substituent was found to cause less of an effect than in solution. In order to rationalize the observed regioselectivity, Clennan *et al.* proposed that the alkene first forms a complex with the charge-balancing cation forcing the allylic substituent to occupy the face of the olefin approached by singlet oxygen. As the perepoxide intermediate forms, the cation shifts to eletrostatically stabilize this intermediate. Steric interactions in the countercation-perepoxide 'complex' control the population of each diastereomer. Electronic interactions that place more positive charge on the zeolite framework, dictate the regioselectivity of the perepoxide ring opening.[84, 86] This model was further supported by the study of a series of trisubstituted alkenes.[87] It should be mentioned that, despite the promising selectivities observed, intrazeolite photooxidations can still suffer from the same limitations as solution phase oxidations, including competition between Type I (electron or hydrogen

transfer initiated oxidation) and Type II (singlet oxygen mediated oxidation) processes and sensitizer bleaching.

1.4.2 Energy, Charge, and Electron Transfer in Zeolites

Energy transfer in zeolites has been studied both directly and indirectly in a number of cases. All of the singlet oxygen mediated photooxidations discussed in the previous section take advantage of an intrazeolite energy transfer in order to generate reactive singlet oxygen. The triplet states of zeolite encapsulated sensitizers, like methylene blue, undergo an energy transfer with the ground state triplet of molecular oxygen to generate singlet oxygen. These studies therefore, also indirectly probe intrazeolite energy transfer. In solution, the excited triplet state of xanthone undergoes a known energy transfer interaction with 1-methylnaphthalene due to the lower energy of the naphthalene triplet state.[75] In zeolites, this interaction has been used to probe the distance dependence for energy transfer within zeolite NaY. In order to determine the distance necessary for triplet energy transfer, xanthone and various amounts of methylnaphthalene were co-included within zeolite Y.[88] The presence of methylnaphthalene causes both a decrease in the signal intensity for the xanthone triplet, as well as a modulation of the triplet lifetime. The reduced signal intensity indicates an instantaneous interaction between molecules already in close proximity when promoted to the excited state surface. Consideration of the statistical distribution of quencher molecules surrounding the xanthone triplet led to the conclusion that intrazeolite energy transfer can occur between species sharing the same supercage as well as those occupying neighbouring cages.[88]

Intrazeolite energy transfer can also be used to perform sensitized photochemical reactions. Sensitization may bias the formation of triplet derived products, as was the case for the acenaphthylene example given in Section 1.2.2.5,[58] or zeolite-bound photosensitizers can be used to introduce an aspect of shape selectivity. An example of the latter is the sensitized isomerization of stilbene using

4-aminobenzophenone encapsulated in zeolite ZSM-5. Due to their molecular dimensions, only *trans*- and not *cis*-stilbenes are able to enter the channels of ZSM-5. Consequently, only *trans*-stilbene is able to contact the sensitizer and undergo isomerization resulting in a photostationary state enriched in *cis*-stilbene.[89]

Calzaferri *et al.* have contributed significantly to the study of energy transfer in zeolites as a part of their research devoted to the construction of artificial antenna systems.[90] In one example, a green-emitting pyronine dye was encapsulated in the channels of zeolite L crystals. The molecular restriction in the channels prevents the dye from stacking, instead forcing an end-to-end configuration. Each cylindrical zeolite microcrystal was capped with oxonine, a dye with red emission. Irradiation with the appropriate wavelength results in selective absorption by the pyronine dye. The excitation energy migrates along the column of pyronine molecules via energy transfer until it is eventually trapped by oxonine resulting in the observation of red emission.[91, 92]

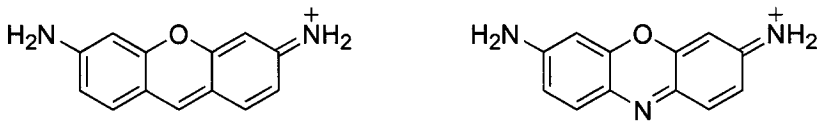

pyronine
λ_{abs} = 496 nm
λ_{em} = 510 nm

oxonine
λ_{abs} = 582 nm
λ_{em} = 597 nm

Scheme 1.7 Fluorescent dyes used to demonstrate energy transfer in zeolite L microcrystals.

As discussed in the previous section in the context of hydrocarbon•O_2 complexes, the polar and highly electrostatic environment of zeolite cavities can have a significantly stabilizing effect on included guests. This can have important consequences in terms of both charge transfer and electron transfer interactions. Zeolites can also support these interactions by disfavouring energy wasting back-reactions. In light of the tremendous advantages offered by the zeolite microenvironment, it is not surprising that there is a large volume of work relating to charge transfer (CT) and electron transfer (eT) in zeolites. The area of intrazeolite

charge transfer was pioneered by the work of Kochi and Yoon in their study of arene-pyridinium charge transfer complexes.[93-97] The formation of brightly coloured CT complexes was used as a diagnostic tool to determine the shape-selectivity of certain zeolite materials for guest uptake. Pyridinium cations were first introduced into the zeolite via ion-exchange, the zeolites were subsequently exposed to dichloromethane solutions of various arene electron-donors. Observation of the characteristic CT absorption band was indicative of inclusion of the arene guest into the supercage. In the case of methyl viologen-exchanged zeolite Y, co-inclusion of anthracene results in rapid formation of the purple CT complex while contact with a solution of 9-phenylanthracene leaves the zeolite colourless, demonstrating the size restraint for CT complex formation.[93] Yoon *et al.* also studied the retardation of back electron transfer (BeT) in ion pairs resulting from excitation of arene-pyridinium CT complexes.[95] Photoexcitation of methyl viologen-arene and other pyridinium-arene CT complexes in zeolite Y results in the formation of both the methyl viologen and arene radical ions as products of electron transfer. It was found that, despite complex decay kinetics, the rate of BeT was typically ten times slower than in acetonitrile solution. Several factors were proposed to account for these enhanced transient lifetimes, including the electrostatic and ionic environment as mentioned before. Coulombic interactions between the positively charged species and the negative zeolite framework were also implicated in the reduced BeT rate. The effect of the zeolite microenvironment on the redox potentials of the guest should also be considered.

Zeolites have since continued to attract considerable attention as hosts for photoinduced electron transfer (PeT) reactions due to their ability to extend the lifetime of the charge-separated state. This feature is important in the context of energy storage and artificial photosynthetic systems. Much of the research in this field has focused on eT between ruthenium (II) *tris*(bipyridyl) ($Ru(bpy)_3^{2+}$, bpy = bipyridine) and various electron acceptors. $Ru(bpy)_3^{2+}$ in its excited state is a good electron donor and, in the presence of electron acceptors, undergoes eT to form

$Ru(bpy)_3^{3+}$ as a relatively stable complex. In one example, it was shown that the use of zeolites to physically segregate the electron donor and acceptor lead to a much longer-lived charge separation. The spatial organization of $Ru(bpy)_3^{2+}$ on the external surface of the zeolite, and the electron acceptor within the voids, resulted in an extremely long-lived charge-separated state as compared to donor-acceptor pairs in solution or in neighbouring zeolite Y cages.[98]

In a more recent example, the $Ru(bpy)_3^{2+}$ electron donating moiety was prepared within the cavities of zeolite KY via ship-in-a-bottle synthesis and the electron accepting species, a dicyclohexyl derivative of viologen, was size-excluded from entering the pores.[99] This system was demonstrated to pump electrons from the zeolite framework to an externally located acceptor, under visible light irradiation. Electron transfer from the internal $[Ru(bpy)_3^{2+}]^*$ to the external viologen is mediated by migration of the charge-balancing cations, in order to maintain electroneutrality. When crown ethers were added to the solution to trap the ejected K^+ cations, BeT was retarded to such an extent that the viologen cation was detected by a conventional spectrometer. This light-fuelled, single direction electron-pumping is likely to be adapted by researchers working in the field of photocatalysis.

As demonstrated in the example above, the zeolite itself can participate in electron transfer reactions. The zeolite can also behave as an electron donor, as illustrated above, in the generation of methyl viologen radical cations in methyl viologen-exchanged Y zeolites.[100] Conversely, if an encapsulated guest molecule undergoes photoionization to generate a radical cation, the ejected electron may be trapped by the zeolite charge-balancing cations. The result is the formation of cationic clusters having characteristic absorptions in the red region of the spectrum; the exact maximum is dependent on factors such as co-included water. These clusters have been independently generated by γ-irradiation of alkali-exchanged zeolites and characterized spectroscopically.[101]

1.4.3 Supramolecular Control of Radical Reactions

The size and shape of zeolite cavities can be used to control the selectivity and reactivity of photogenerated radicals. The photochemistry of dibenzylketones (DBK) adsorbed onto or included in zeolites, has been used to probe the effect of zeolite-encapsulation on the fate of radical fragments.[1, 25, 102-104] In fluid solution, dibenzylketones undergo a Norrish I α-cleavage to generate a primary, geminate radical pair. A geminate pair refers to two radicals that were born together as opposed to a pair that has diffused together. The subsequent steps, for an unsymmetrical ketone ACOB, are given in Scheme 1.7. The primary, geminate pair may undergo radical-radical recombination or decarbonylation to generate the secondary, geminate radical pair. This secondary pair can itself undergo recombination or the two radicals can separate in the formation of a free radical pair.

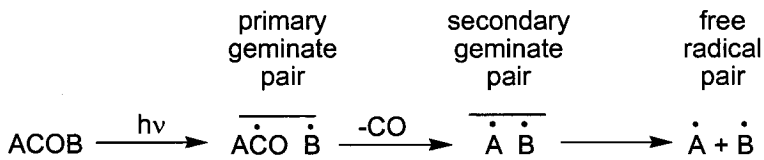

Scheme 1.8 Typical species formed following photolysis of unsymmetrical ketone ACOB.

In solution the free radicals undergo randomized radical-radical recombination reactions to give products AA, AB, and BB in a ratio of 1:2:1 respectively.[27] The photolysis of DBK in zeolites gives rise to stereochemically and regiochemically selective combination reactions of radical pairs.

The photochemistry of ketones adsorbed on pentasil type zeolites is a poignant example of the supramolecular control of secondary radical-radical recombination reactions. The photochemistry of unsymmetrical *ortho-* and *para-*substituted dibenzylketones, designated as *o*-ACOB and *p*-ACOB in Scheme 1.9, complexed with dry ZSM-5 zeolites was examined.[103] Due to the difference in molecular cross section between the two ketones, the chemistry of the

supramolecular complexes is expected to be distinct in each case. It was found that photolysis of either ketone adsorbed onto solventless ZSM-5 resulted in radical-radical combination of secondary radicals only. This indicates that under these circumstances decarbonylation to form the secondary pairs is much faster than recombination of the primary radical pairs.

In zeolites there are still three possible secondary radical recombination products; AA, AB, and BB. The population of each product can be discussed in the terms of the 'cage effect' or CE. Exclusive formation of the AB product, corresponding to total secondary, geminate pair recombination, is referred to as a positive cage effect. If the recombination products are formed in a random way, as in solution, the cage effect is zero. If the only observed products are AA and BB, this indicates a complete separation or sieving of the geminate radical pairs followed by combination of the separated radicals. This situation is termed a negative cage effect. The magnitude of the cage effect, CE, is given by Equation 1.1.[103]

Equation 1.1

$$\text{cage effect (CE)} = \frac{[AB] - [AA + BB]}{AA + AB + BB}$$

Examining the product ratios following photolysis of *p*-ACOB revealed the formation of only secondary, geminate recombination product *p*-AB. Since *p*-ACOB can be fully accommodated within the ZSM-5 channels, photolysis produces a radical pair that is constrained within the zeolite. The primary geminate pair has sufficient space to decarbonylate but once the secondary geminate pair is formed the constraint of the zeolite framework forces the formation of the geminate recombination product. This is illustrated pictorially in the right of Scheme 1.9.

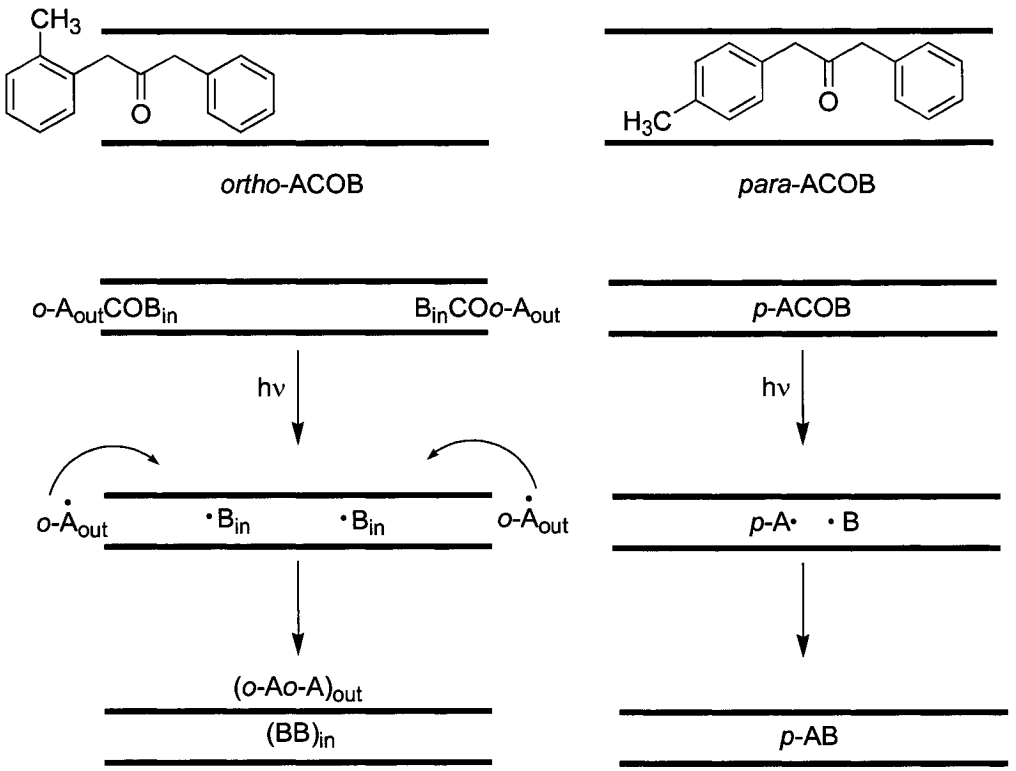

Scheme 1.9 Schematic representation of DBK photolysis in the channels of ZSM-5.

The geometry of *o*-ACOB does not allow for complete encapsulation within the zeolite micropores. As a result, the unsubstituted side of the ketone resides within the channel while the substituted ring is forced to remain outside. Photolysis of this complex results in the formation of two spatially distinct radicals. Following decarbonylation, the size-excluded *o*-A radicals are free to diffuse to the surface of the particle where they will encounter and recombine exclusively with other *o*-A radicals. The internally located B radicals will diffuse within the channel system until encountering and recombining with another B radical. This molecular sieving gives rise to exclusively AA and BB type products, a negative cage effect. Since there are a finite number of pore apertures on the external surface of the zeolite, ketone loading can have a significant effect on the observed product distributions. For example, in the case of the *ortho*-substituted ketone, once all of the channel openings have been filled any additional ketone molecules will be forced to occupy the particle surface. Radicals produced by the externally located

ketone are able to diffuse freely on the particle surface but are denied access to the internal space and no sieving is observed. The externally located radical pairs are free to recombine in a random fashion. Therefore, as the loading of ketone increases and more geminate radical pairs are formed on the zeolite exterior, the cage effect shifts from negative towards zero.

The photochemistry of DBK encapsulated in the spherical cavities of zeolites X and Y provides another example of supramolecular control over radical reactions.[102, 104] In this case, the free volume within the zeolite cavity has been manipulated in order control the regioselectivity of radical-radical recombination reactions. There are three possible products following photolysis of dibenzylketone in faujasite zeolites, the secondary radical coupling product 1,2-diphenylethane (DPE) and two regioisomers of the primary coupling product methyl-β-acetophenone (MAP).

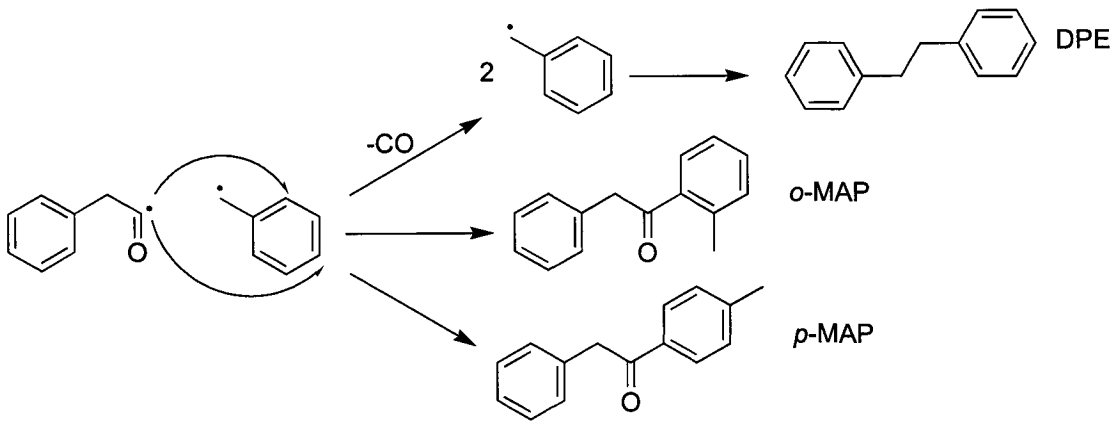

Scheme 1.10 Possible pathways following DBK photolysis: decarbonylation followed by secondary radical pair recombination (top) or primary radical pair recombination (middle, bottom).

In Y type zeolites the major product is DPE regardless of the charge-balancing cation (M). Zeolite Y has fewer cations than zeolite X so the size-reduction caused by introducing bulky cations is less for Y than for X. In zeolite X, therefore, changing the cation type will have noticeable effects on the product selectivity. For LiX the major product remains DPE but as larger cations are

introduced the regioisomers become more significant. In the less crowded zeolites, MY and LiX, diffusional separation and decarbonylation can occur and the secondary radicals can combine to form DPE. As the supercage becomes more crowded, diffusional and rotational motion are restricted, and the probability of primary, geminate radical recombination is increased. On going from LiX to NaX formation of the regioisomers increases from 20 to 40%. As steric constraints continue to increase the formation of the least motion regioisomer *o*-MAP begins to dominate over *p*-MAP. This study demonstrates the remarkable control that can be exerted by merely modifying the cavity size by simple cation-exchange.

1.4.4 Asymmetric Photoreactions using Zeolite Hosts

Stereoselective synthesis is an important facet of synthetic organic chemistry, particularly in the context of molecules with potential pharmaceutical applications. As such, enormous effort has been devoted to the development of general asymmetric methodologies for ground state reactions. Considerably less attention has been focused on asymmetric photochemical synthesis.[105, 106] This area has received increased consideration in recent years and one of the more successful methodologies has involved chiral induction in the solid or condensed state. Asymmetric photochemistry in the crystalline state requires that the achiral substrate crystallize in a chiral space group, providing the necessary environment for stereoselective reaction. Unfortunately, there are a limited number of useful compounds that will crystallize in a chiral fashion and so there are relatively few examples of induced asymmetric synthesis via this methodology.[107] A much more general strategy developed by Scheffer *et al.*, encourages the crystallization of achiral molecules into chiral space groups by forming a crystalline salt between a prochiral carboxylic acid-containing reactant and an optically pure, inert amine. Since the amine is optically pure, the salt is required to crystallize in a chiral space group. This is called the 'ionic chiral auxiliary approach'.[108, 109] This methodology

has lead to excellent optical yields in a wide variety of photochemical reactions, ranging from di-π-methane rearrangements to Yang photocyclization reactions.[109]

Zeolites have the ability to control and constrain included guest molecules making them a natural choice for attempts at stereocontrol in photochemical reactions. The use of zeolites as hosts for asymmetric induction takes two approaches. In the first, the achiral zeolite interior is rendered locally chiral by the inclusion of a chiral inductor such as (+)- or (-)-ephedrine.[110, 111] The first example of asymmetric induction in the cavity of a zeolite was reported for the Norrish II conversion of cyclohexyl ketones to the corresponding butanols.

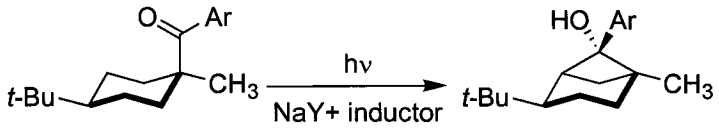

Scheme 1.11 Photocyclization of substituted cyclohexyl ketones to give the chiral cyclobutanol.

The enantiomeric excesses (**ee**) obtained were low to moderate, varying from 10 to 30% and it was observed that use of the (+)-inductor gave the optical antipode of the product from reaction using the (-)-inductor. While this method has the advantage that the chiral inductor and substrate are neither covalently nor ionically bonded, the **ee** is limited by the number of cavities in the zeolite that are occupied by both a substrate and inductor molecule. Nevertheless, there are examples of the chiral inductor method, such as the photocyclization of tropolone ethylphenyl ether, where **ee** of almost 80% were obtained.[112]

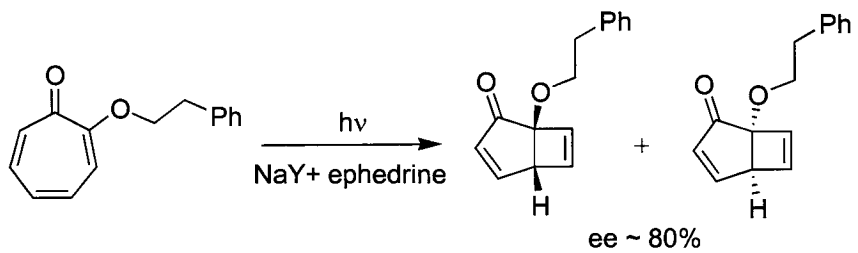

Scheme 1.12 Photocylization of tropolone ethylphenyl ether.

In order to improve selectivity the chiral auxiliary approach, often employed in solution phase reactions, was adapted for intrazeolite photochemical reactions. In this methodology, the chiral inductor is bonded directly to the achiral substrate so that each zeolite cavity will contain both substrate and inductor by default. This approach has worked very well in a number of cases and, together with the work on the chiral inductor method, has lead to some general observations.[23, 113, 114] Although these generalizations do not comprise a model with predictive power, they may be useful for the intelligent design of systems for asymmetric induction. It was observed that selectivity was dependent on the nature of the cation and was reduced in the presence of water. Selectivity was reliant on the number of cations present and when the photoreaction was carried out on silica gel (no cations) the induced selectivity was minimal. These observations lead to the conclusion that charge-balancing cations play an important role in intrazeolite asymmetric induction. The role of the cation is likely to immobilize the substrate either by cation-π interactions or by cation-dipolar interactions with nitro or carbonyl groups. The observation that using aryl rather than alkyl chiral inductors gave improved selectivity supports this idea, since the cation interaction will be stronger in the former case.[113] Work is still ongoing to improve both the generality and predictability of asymmetric induction in zeolites.

1.5 Concluding Remarks

Zeolite materials are remarkably versatile hosts for photochemical and photophysical processes. In addition to being available in a variety of morphologies, the specific properties of a zeolite host can be finely tuned by cation modification. The examples given in this chapter emphasize the efficacy of zeolite encapsulation for modification of guest photobehaviour. The unique properties of the zeolite cavity in terms of site isolation, compartmentalization, electrostatics, and acidity/basicity can result in behaviour that is very different from what is observed in solution. In the following chapters, the myriad uses of zeolite materials for the alteration of guest photochemistry and photophysics will be examined.

In the Chapter 3, the zeolite framework is used to spatially organize multi-component host/guest complexes and the effect of this compartmentalization on the photochemistry and photophysics is explored. The suitability of these new materials as visible-light photocatalysts is also examined. In Chapters 4 and 5, various zeolites are used to provide enhanced stability to both cationic and anionic species. Improving the stability allows the observation of excited states and chemical reactivity not normally observable for these species in solution. In Chapter 6, the use of fluorescence as a tool to explore both intra- and interzeolite reactivity will be considered. Finally, in Chapter 7, the use of zeolites as encapsulatory materials for a new class of *supramolecular sunscreens* will be discussed. An assessment of the photophysics, photostability, and biological impact of these new materials will be presented.

1.6 References

1. N. J. Turro, From boiling stones to smart crystals: supramolecular and magnetic isotope control of radical-radical reactions in zeolites, *Acc. Chem. Res.*, **2000**, *33*, 637-646.

2. H. van Bekkum, E. M. Flanigen, P. A. Jacobs and J. C. Jansen *Introduction to Zeolite Science and Practice;* Elsevier Science: Amsterdam, 2001.

3. D. W. Breck *Zeolite Molecular Seives;* John Wiley & Sons, Ltd.: New York, 1974.

4. L. Pauling, The structure of some sodium and calcium aluminosilicates, *Proc. Natl. Acad. Sci. USA*, **1930**, *16*, 453-459.

5. F. A. Mumpton, La roca magica: Uses of natural zeolites in agriculture and industry, *Proc. Natl. Acad. Sci. USA*, **1999**, *96*, 3463-3470.

6. S. M. Auerbach, K. A. Carrado and P. K. Dutta *Handbook of Zeolite Science and Technology;* Marcel Dekker, Inc.: New York, 2003.

7. A. Corma, State of the art and future challenges of zeolites as catalysts, *J. Catal.*, **2003**, *216*, 298-312.

8. A. Corma and H. García, A unified approach to zeolites as acid catalysts and as supramolecular hosts, *Dalton*, **2000**, *9*, 1381-1394.

9. W. F. Hoelderich and D. Heinz, Research and development of zeolite catalysis in the 80's and in the 90's as well as forthcoming trends, *Res. Chem. Intermed.*, **1998**, *24*, 337-348.

10. A. Corma, From microporous to mesoporous sieve materials and their use in catalysis, *Chem. Rev.*, **1997**, *97*, 2373-2419.

11. H. L. Casal and J. C. Scaiano, Intrazeolite photochemistry. I. Phosphorescence enhancement of aromatic ketones included in silicalite, *Can. J. Chem.*, **1984**, *62*, 628-629.

12. N. J. Turro and P. Wan, Photochemistry of phenyl alkyl ketones adsorbed on zeolite molecular sieves. Observation of pronounced effects on Type I/Type II photochemistry, *Tetrahedron Lett.*, **1984**, *25*, 3655-3658.

13. S. L. Suib and A. Kostapapas, Intermolecular pyrene excimer formation in zeolites. Decay parameters and ground-state association, *J. Am. Chem. Soc.*, **1984**, *106*, 7705-7710.

14. A. Corma and H. García, Zeolite-based photocatalysts, *Chem. Commun.*, **2004**, 1443-1459.

15. A. Corma and H. García, Supramolecular host-guest systems in zeolites prepared by ship-in-a-bottle synthesis, *Eur. J. Inorg. Chem.*, **2004**, 1143-1164.

16. A. Corma and H. García, Carbocations and organic radical cations inside zeolilte matrices. Generation, characterization, stability, and properties, *Top. Catal.*, **1998**, *6*, 127-140.

17. P. K. Dutta, Zeolite guest-host interactions: Implications in formation, catalysis, and photochemistry, *J. Incl. Phenom. Mol. Recog. Chem.*, **1995**, *21*, 215-237.

18. P. K. Dutta and Y. Kim, Photochemical processes in zeolites: New developments, *Curr. Opin. Solid State Mater. Sci.*, **2003**, *7*, 483-490.

19. S. Hashimoto, Zeolite photochemistry: Impact of zeolites on photochemistry and feedback from photochemistry to zeolite science, *J. Photochem. Photobiol. C*, **2003**, *4*, 19-49.

20. V. Ramamurthy, J. Shailaja, S. Kaanumalle, R. B. Sunoj and J. Chandrasekhar, Controlling chemistry with cations: Photochemistry within zeolites, *Chem. Commun.*, **2003**, 1987-1999.

21. V. Ramamurthy and N. J. Turro, Photochemistry of organic molecules within zeolites: Role of cations, *J. Incl. Phenom. Mol. Recog. Chem.*, **1995**, *21*, 239-282.

22. J. C. Scaiano and H. García, Intrazeolite photochemistry: Toward supramolecular control of molecular photochemistry, *Acc. Chem. Res.*, **1999**, *32*, 783-793.

23. J. Sivaguru, A. Natarajan, L. S. Kaanumalle, J. Shailaja, S. Uppili, A. Joy and V. Ramamurthy, Assymetric photoreactions within zeolites: Role of confinement and alkali metal ions, *Acc. Chem. Res.*, **2003**, *36*, 509-521.

24. C.-H. Tung, L.-Z. Wu, L.-P. Zhang and B. Chen, Supramolecular systems as microreactors: Control of product selectivity in organic phototransformation, *Acc. Chem. Res.*, **2003**, *36*, 39-47.

25. N. J. Turro, From molecular chemistry to supramolecular chemistry to superdupermolecular chemistry. Controlling covalent bond formation through non-covalent interactions, *Chem. Commun.*, **2002**, 2279-2292.

26. M. Anpo *Surface Photochemistry;* John Wiley & Sons, Ltd.: Chichester, 1996.

27. V. Ramamurthy *Photochemistry in Organized and Constrained Media;* VCH Publishers, Inc.: New York, 1991.

28. International Zeolite Association, Database of Zeolite Structures: http://www.iza-structure.org/databases/

29. W. M. Meier and D. H. Olson *Atlas of Zeolite Structure Types;* Butterworths: London, 1992.

30. R. Szostak *Molecular Seives. Principles of Synthesis and Identification;* Van Nostrand: New York, 1989.

31. J. S. Beck, J. C. Vartuli, W. J. Roth, M. E. Leonowicz, C. T. Kresge, K. D. Schmitt, C. T.-W. Chu, D. H. Olson, E. W. Sheppard, S. B. McCullen, J. B. Higgins and J. L. Schlenkert, A new family of mesoporous molecular sieves prepared with liquid crystal templates, *J. Am. Chem. Soc.*, **1992**, *114*, 10834-10843.

32. A. H. Heuer, D. J. Fink, V. J. Laraia, J. L. Arias, P. D. Calvert, K. Kendall, G. L. Messing, J. Blackwell, P. C. Rieke, D. H. Thompson, A. P. Wheeler, A. Veis and A. I. Caplan, Innovative materials processing strategies-A biomimetic approach, *Science*, **1992**, *255*, 1098-1105.

33. T. A. Konovalova, Y. Gao, R. Schad, L. D. Kispert, C. A. Saylor and L.-C. Brunel, Photooxidation of carotenoids in mesoporous MCM-41, Ni-MCM-41, and Al-MCM-41 molecular sieves, *J. Phys. Chem. B*, **2001**, *105*, 7459-7464.

34. Y. Gao, T. A. Konovalova, T. Xu and L. D. Kispert, Electron transfer of carotenoids imbedded in MCM-41 and Ti-MCM-41: EPR, ENDOR, and UV-Vis studies, *J. Phys. Chem. B*, **2002**, *106*, 10808-10815.

35. Y. Gao, T. A. Konovalova, J. N. Lawrence, M. A. Smith, J. Nunley, R. Schad and L. D. Kispert, Interaction of carotenoids and Cu^{2+} in Cu-MCM-41: Distance-dependent reversible electron transfer, *J. Phys. Chem. B*, **2003**, *107*, 2459-2465.

36. I. Casades, M. Alvaro, H. García and M. Narayana Pillai, Modified mesoporous MCM-41 as hosts for photochromic spirobenzopyrans, *Photochem. Photobiol. Sci.*, **2002**, *1*, 219-223.

37. E. G. Derouane and Z. Gabelica, A novel effect of shape selectivity: Molecular traffic control in zeolite ZSM-5, *J. Catal.*, **1980**, *65*, 486-489.

38. B. H. Baretz and N. J. Turro, Fluorescence studies of pyrenealdehyde adsorbed within zeolite supercages, *J. Photochem.*, **1984**, *24*, 201-205.

39. P. K. Dutta and W. Tubeville, Examination of the solventlike nature of zeolites based on solvatochromic indicator, *J. Phys. Chem.*, **1991**, *95*, 4087-4092.

40. S. Uppili, J. K. Thomas, E. M. Crompton and V. Ramamurthy, Probing zeolites with organic molecules: Supercages of X and Y zeolites are superpolar, *Langmuir*, **2000**, *16*, 265-274.

41. S. Corrent, P. Hahn, G. Pohlers, T. J. Connolly, J. C. Scaiano, V. Fornés and H. García, Intrazeolite photochemistry. 22. Acid-base properties of coumarin 6. Characterization in solution, the solid state, and incorporated into supramolecular systems, *J. Phys. Chem. B*, **1998**, *102*, 5852-5858.

42. R. A. Rao, D. L. Perlstein, R. J. Robbins, P. H. Lakshminarasimhan, H.-M. Kao, C. P. Grey and V. Ramamurthy, Detection of low levels of Brønsted acidity in Na^+Y and Na^+X zeolites, *Chem. Commun.*, **1998**, 269-270.

43. A. Corma, H. García, S. Iborra and J. Primo, Modified zeolite as catalysts in organic reactions - Esterification of carboxylic acids in the presence of HY zeolites, *J. Catal.*, **1989**, *120*, 78-87.

44. C. Walling, The acid strength of surfaces, *J. Am. Chem. Soc.*, **1950**, *72*, 1164-1168.

45. R. Ferwerda and J. H. van der Maas, Pyridine adsorbed on Na-faujasite. 2. An FT-Raman and DRIFT spectroscopic study, *J. Phys. Chem.*, **1995**, *99*, 14764-14770.

46. R. D. Place and P. K. Dutta, Quantification of acidic sites in faujasitic zeolites by resonance Raman spectroscopy, *Anal. Chem.*, **1991**, *63*, 348-351.

47. W. E. Farneth and R. J. Gorte, Methods for characterizing zeolite acidity, *Chem. Rev.*, **1995**, *95*, 615-635.

48. H.-M. Kao and C. P. Grey, Probing the Brønsted and Lewis acidity of zeolite HY: A $^{1}H/^{27}Al$ and $^{15}N/^{27}Al$ TRAPDOR NMR study of monomethylamine adsorbed on HY, *J. Phys. Chem.*, **1996**, *100*, 5105-5117.

49. Q. Zhao, W.-H. Chen, S.-J. Huang and S. B. Liu, Qualitative and quantitative determination of acid sites on solid acid catalysts, *Stud. Surf. Sci. Catal.*, **2003**, *145*, 205-210.

50. J. F. Haw, Zeolite acid strength and reaction mechanisms in catalysis, *Phys. Chem. Chem. Phys.*, **2002**, *4*, 5431-5441.

51. L. Peng, P. J. Chupas and C. P. Grey, Measuring Brønstead acid densities in zeolite HY with diphosphine molecules and solid state NMR spectroscopy, *J. Am. Chem. Soc.*, **2004**, *126*, 12254-12255.

52. J. K. Thomas and V. Ramamurthy, Detection and estimation of Brønsted acidities in alkali metal cation exchanged X and Y zeolites, *Langmuir*, **1998**, *14*, 6687-6692.

53. V. Ramamurthy, X.-G. Lei, N. J. Turro, T. J. Lewis and J. R. Scheffer, Photochemistry of macrocyclic ketones withing zeolites: Competition between Norrish Type I and Type II reactivity, *Tetrahedron Lett.*, **1991**, *32*, 7675-7678.

54. D. R. Corbin, D. F. Eaton and V. Ramamurthy, Modification of photochemical reactivity by zeolites: Norrish Type I and Type II reactions of benzoin derivatives, *J. Am. Chem. Soc.*, **1988**, *110*, 4848-4849.

55. V. Ramamurthy, D. R. Corbin, N. J. Turro and Y. Sato, Modification of photochemical reactivity by zeolites: Cation enhanced α-cleavage of aryl alkyl ketones included in faujasites, *Tetrahedron Lett.*, **1989**, *30*, 5829-5832.

56. P. Atkins *Concepts in Physical Chemistry;* W. H. Freeman and Company: New York, 1995.

57. V. Ramamurthy, J. V. Caspar, D. F. Eaton, E. W. Kuo and D. R. Corbin, Heavy-atom-induced phosphorescence of aromatics and olefins included within zeolites., *J. Am. Chem. Soc.*, **1992**, *114*, 3882-3892.

58. V. Ramamurthy, D. R. Corbin, C. V. Kumar and N. J. Turro, Modification of photochemical reactivity by zeolites: Cation controlled photodimerization of acenaphthylene within faujasites, *Tetrahedron Lett.*, **1990**, *31*, 47-50.

59. K. Pitchumani, M. Warrier, J. R. Scheffer and V. Ramamurthy, Novel approaches towards the generation of excited triplets of organic guest molecules within zeolites, *Chem. Commun.*, **1998**, 1197-1198.

60. F. L. Cozens, M. L. Cano, H. García and N. P. Schepp, Alkali metal cation control of oxidation reactions of radicals in zeolites, *J. Am. Chem. Soc.*, **1998**, *120*, 5667-5673.

61. N. Herron, A cobalt oxygen carrier in zeolite Y. A molecular "ship in a bottle", *Inorg. Chem.*, **1986**, *25*, 4714-4717.

62. W. DeWilde, G. Peeters and J. H. Lunsford, Synthesis and spectroscopic properties of tris(2,2'-bipyridine)ruthenium in zeolite Y, *J. Phys. Chem.*, **1980**, *84*, 2306-2310.

63. K. J. Balkus Jr., Zeolite encapsulated phthalocyanines, *Phthalocyanines*, **1996**, *4*, 285-305.

64. M. L. Cano, A. Corma, V. Fornés, H. García, M. A. Miranda, C. Baerlocher and C. Lengauer, Triarylmethylium cations encapsulated within zeolite supercages, *J. Am. Chem. Soc.*, **1996**, *118*, 11006-11013.

65. M. L. Cano, F. L. Cozens, V. Fornés, H. García and J. C. Scaiano, Intrazeolite photochemistry. 12. Ship-in-a-bottle synthesis and control of the photophysical properties of 9-(4-methoxyphenyl)xanthenium ion imprisoned in large-pore zeolites, *J. Phys. Chem.*, **1996**, *100*, 18145-18151.

66. J. Weitkamp, H. G. Karge, H. Pfeifer and W. Holderich *Zeolites and related microporous materials: State of the art 1994;* Elsevier: Amsterdam, 1994.

67. H. L. Casal and J. C. Scaiano, Intrazeolite photochemistry. 2. Evidence for site inhomegeneity from studies of aromatic ketone phosphorescence, *Can. J. Chem.*, **1985**, *63*, 1308-1314.

68. B. F. Chmelka, J. G. Pearson, S. B. Liu, R. Ryoo, L. C. De Menorval and A. Pines, NMR study of the distribution of aromatic molecules in NaY zeolite, *J. Phys. Chem.*, **1991**, *95*, 303-310.

69. H. Klein, H. Fuess and G. Schrimpf, Mobility of aromatic molecules in zeolite NaY by molecular dynamics simulation, *J. Phys. Chem.*, **1996**, *100*, 11101-11112.

70. H. Klein, C. Kirschhock and H. Fuess, Adsorption and diffusion of aromatic hydrocarbons in zeolite Y by molecular mechanics calculations and X-ray powder diffraction, *J. Phys. Chem.*, **1994**, *98*, 12345-12360.

71. J. A. Muller and W. C. Conner, Cyclohexane in ZSM-5. 1. FTIR and X-ray studies, *J. Phys. Chem.*, **1993**, *97*, 1451-1454.

72. V. Ramamurthy, D. R. Sanderson and D. F. Eaton, Distribution of organic molecules within zeolites as revealed by aromatic photophysical probes: Role of water and other coadsorbents, *J. Phys. Chem.*, **1993**, *97*, 13380-13386.

73. M. Sanchez-Sanchez and T. Blasco, Investigation on the nature of the adsorption sites of pyrrole in alkali-exchanged zeolite Y by nuclear magnetic resonance in combination with infrared spectroscopy, *J. Am. Chem. Soc.*, **2002**, *124*, 3443-3456.

74. A. Sayeed, S. Mitra, A. V. Anil Kumar, R. Mukhopadhyay, S. Yashonath and S. L. Chaplot, Diffusion of propane in zeolite NaY: A molecular dynamics and quasi-elastic neutron scattering study, *J. Phys. Chem. B*, **2003**, *107*, 527-533.

75. N. J. Turro *Modern Molecular Photochemistry;* University Science Books: Sausalito, 1991.

76. F. L. Cozens, M. Regimbald, H. García and J. C. Scaiano, Intrazeolite photochemistry. 15. Influence of aging, inert gases, and water on the mobility of pyrene molecules on the faujasite NaY, *J. Phys. Chem.*, **1996**, *100*, 18165-18172.

77. V. Ramamurthy, D. R. Sanderson and D. F. Eaton, Control of dye assembly within zeolites: Role of water, *J. Am. Chem. Soc.*, **1993**, *115*, 10438-10439.

78. J. M. Thomas and K. I. Zamaraev *Perspectives in Catalysis;* IUPAC/Blackwell Scientific Publications: London, 1992.

79. E. A. Gooding, K. R. Serak and P. R. Ogilby, Ground-state benzene-oxygen complex, *J. Phys. Chem.*, **1991**, *95*, 7868-7871.

80. F. Blatter and H. Frei, Very strong stabilization of alkene-O_2 charge-transfer state in zeolite NaY: Red-light-induced photooxidation of 2,3-dimethyl-2-butene, *J. Am. Chem. Soc.*, **1993**, *115*, 7501-7502.

81. F. Blatter and H. Frei, Selective photooxidation of small alkenes by O_2 with red light in zeolite Y, *J. Am. Chem. Soc.*, **1994**, *116*, 1812-1820.

82. H. Sun, F. Blatter and H. Frei, Selective oxidation of toluene to benzaldehyde by O_2 with visible light in barium (2+)- and calcium (2+)-exchanged zeolite Y, *J. Am. Chem. Soc.*, **1994**, *116*, 7951-7952.

83. H. Sun, F. Blatter and H. Frei, Cyclohexanone from cyclohexane and O_2 in a zeolite under visible light with complete selectivity, *J. Am. Chem. Soc.*, **1996**, *118*, 6873-6879.

84. E. L. Clennan, New mechanistic and synthetic aspects of singlet oxygen chemistry, *Tetrahedron*, **2000**, *56*, 9151-9179.

85. X. Li and V. Ramamurthy, Selective oxidation of olefins within organic dye cation-exchanged zeolites, *J. Am. Chem. Soc.*, **1996**, *118*, 10666-10667.

86. E. L. Clennan and J. P. Sram, Photooxidations in zeolites. Part 2. A new mechanistic model for reaction selectivity in singlet oxygen ene reactions in zeolitic media, *Tetrahedron Lett.*, **1999**, *40*, 5275-5278.

87. E. L. Clennan and J. P. Sram, Photochemical reactions in the interior of a zeolite. Part 5. The origin of the zeolite induced regioselectivity in the singlet oxygen ene reaction, *Tetrahedron*, **2000**, *56*, 6945-6950.

88. J. C. Scaiano, N. C. de Lucas, J. Andraos and H. García, Determination of the distance for triplet energy transfer in the faujasite NaY, *Chem. Phys. Lett.*, **1995**, *233*, 5-8.

89. M. V. Baldoví, A. Corma, H. García and V. Martí, Shape-selective photosensitized isomerization of stilbene using a benzophenone incorporated within acid zeolites, *Tetrahedron Lett.*, **1994**, *35*, 9447-9450.

90. N. Gfeller and G. Calzaferri, Energy migration in dye-loaded hexagonal microporous crystals, *J. Phys. Chem. B*, **1997**, *101*, 1396-1408.

91. N. Gfeller, S. Megelski and G. Calzaferri, Transfer of electronic excitation energy between dye molecules in the channels of zeolite L, *J. Phys. Chem. B*, **1998**, *102*, 2433-2436.

92. N. Gfeller, S. Megelski and G. Calzaferri, Fast energy migration in pyronine-loaded zeolite L microcrystals, *J. Phys. Chem. B*, **1999**, *103*, 3340-3351.

93. K. B. Yoon and J. K. Kochi, Shape-selective access to zeolite supercages. Arene charge-transfer complexes with viologens and visible probes, *J. Am. Chem. Soc.*, **1989**, *111*, 1128-1130.

94. K. B. Yoon and J. K. Kochi, Stepwise assembly of charge-transfer complexes within zeolite supercages as visual probes for shape selectivity, *J. Phys. Chem.*, **1991**, *95*, 3780-3790.

95. S. Sankararaman, K. B. Yoon, T. Yabe and J. K. Kochi, Control of back electron transfer from charge-transfer ion pairs by zeolite supercages, *J. Am. Chem. Soc.*, **1991**, *113*, 1419-1421.

96. K. B. Yoon, T. J. Huh, D. R. Corbin and J. K. Kochi, Shape-selective assemblage of charge-transfer complexes within channel-type zeolites, *J. Phys. Chem.*, **1993**, *97*, 6492-6499.

97. K. B. Yoon, Electron- and charge-transfer reactions within zeolites, *Chem. Rev.*, **1993**, *93*, 321-329.

98. T. E. Mallouk and Y. I. Kim, Dynamic electron-transfer quenching of the tris(2,2'-bipyridyl)ruthenium(II) MLCT excited state by intrazeolitic methylviologen ions, *J. Phys. Chem.*, **1992**, *96*, 2879-2885.

99. Y. S. Park, E. J. Lee, Y. S. Chun, Y. D. Yoon and K. B. Yoon, Long-lived charge-separation by retarding reverse flow of charge-balancing cation and zeolite-encapsulated $Ru(bpy)_3^{2+}$ as a photosensitized electron pump from zeolite framework to externally placed viologen, *J. Am. Chem. Soc.*, **2002**, *124*, 7123-7135.

100. M. Alvaro, H. García, S. García, F. Márquez and J. C. Scaiano, Intrazeolite photochemistry. 17. Zeolites as electron donors: Photolysis of methyl viologen incorporated within zeolites, *J. Phys. Chem. B*, **1997**, *101*, 3043-3051.

101. K. K. Iu, X. Liu and J. K. Thomas, Spectroscopic studies of electron trapping by sodium cationic clusters in zeolites, *J. Phys. Chem.*, **1993**, *97*, 8165-8170.

102. N. J. Turro, Photochemistry of organic molecules in microscopic reactors, *Pure Appl. Chem.*, **1986**, *58*, 1219-1228.

103. N. J. Turro, C.-C. Cheng, L. Abrams and D. R. Corbin, Size, shape, and site selectivities in the photochemical reactions of molecules adsorbed on pentasil zeolites. Effects of coadsorbed water, *J. Am. Chem. Soc.*, **1987**, *109*, 2449-2456.

104. N. J. Turro and Z. Zhang, Photochemistry of molecules adsorbed on alkali ion exchanged zeolites. A 'Lebensraum' effect on product formation, *Tetrahedron Lett.*, **1987**, *28*, 5637-5640.

105. Y. Inoue, Asymmetric photochemical reactions in solution, *Chem. Rev.*, **1992**, *92*, 741-770.

106. S. R. L. Everitt and Y. Inoue, Asymmetric photochemical reactions in solution In *Molecular and Supramolecular Photochemistry*; V. Ramamurthy and K. Schanze, Eds.; Marcell Dekker: New York, 1999; Vol. 3; 71-130.

107. M. Sakamoto, Asymmetric synthesis from achiral molecules in the chiral crystalline environment, *Chem. Eur. J.*, **1997**, *1997*, 684-689.

108. J. N. Gamlin, R. Jones, M. Leibovitch, B. Patrick, J. R. Scheffer and J. Trotter, The ionic chiral auxiliary concept in solid state organic photochemistry, *Acc. Chem. Res.*, **1996**, *29*, 203-209.

109. J. R. Scheffer, In the footsteps of Pasteur: Asymmetric induction in the photochemistry of crystalline ammonium carboxylate salts, *Can. J. Chem.*, **2001**, *79*, 349-357.

110. G. Sundarababu, M. Leibovitch, D. R. Corbin, J. R. Scheffer and V. Ramamurthy, Zeolite as a host for chiral induction, *Chem. Commun.*, **1996**, 2159-2160.

111. M. Leibovitch, G. Olovsson, G. Sundarababu, V. Ramamurthy, J. R. Scheffer and J. Trotter, Asymmetric induction in photochemical reactions conducted in zeolites and in the crystalline state, *J. Am. Chem. Soc.*, **1996**, *118*, 1219-1220.

112. A. Joy, J. R. Scheffer and V. Ramamurthy, Chirally modified zeolites as a reaction media: Photochemistry of an achiral tropolone ether, *Org. Lett.*, **2000**, *2*, 119-121.

113. L. S. Kaanumalle, J. Sivaguru, N. Arunkumar, S. Karthikeyan and V. Ramamurthy, Cation-π interation as a tool to enhance the power of a chiral auxiliary during asymmetric photoreactions within zeolites, *Chem. Commun.*, **2003**, 116-117.

114. S. Jayaraman, S. Uppili, A. Natarajan, A. Joy, K. C. W. Chong, M. R. Netherton, A. Zenova, J. R. Scheffer and V. Ramamurthy, The influence of chiral auxiliaries is enhanced within zeolites, *Tetrahedron Lett.*, **2000**, *41*, 8231-8235.

2. Time-Resolved Spectroscopic Techniques

2. Time-Resolved Spectroscopic Techniques 55

2.1 Introduction 56
2.2 Traditional Laser Flash Photolysis 57
2.2.1 Background 57
2.2.2 Laser Flash Photolysis Fundamentals 58
2.2.3 Absorption Detection for Transparent Samples 60
2.2.4 Diffuse Reflectance Detection for Opaque Samples 66
2.3 Time-Resolved Luminescence Techniques 72
2.3.1 Fluorescence Fundamentals 72
2.3.2 Experimental Set-up 74
2.4 Ultrafast Transient Absorption Techniques 78
2.4.1 Introduction 78
2.4.2 Experimental Set-up and Considerations 78
2.5 References 81

2.1 Introduction

This section is intended to give the reader an overview of time-resolved spectroscopic techniques, with specific emphasis on the conditions and instrumentation employed as part of this thesis. Time-resolved spectroscopy is an invaluable tool in the elucidation of the early events following absorption of a photon. The University of Ottawa laser lab has a variety of lasers available for excitation (Table 2.1) and the ability to monitor processes via absorption, diffuse reflectance, and photoluminenscence. Photoluminescence can be monitored on both the nanosecond and picosecond time scale.

Laser	Wavelength (nm)	Average Power ($pulse^{-1}$)	Average pulse duration
Surelite Nd:YAG (fourth harmonic)	266	≤ 20 mJ	~6 ns
Continuum PY-61 Nd:YAG	266	≤ 5 mJ	~35 ps
Lumonics EX-530 Excimer	308	50-100 mJ	~8 ns
Surelite Nd:YAG (third harmonic)	355	≤ 25 mJ	~6 ns
Continuum PY-61 Nd:YAG	355	≤ 5 mJ	~35 ps
Surelite Nd:YAG (second harmonic)	532	25 mJ	~6 ns

Table 2.1 Selected lasers available at the University of Ottawa with pulse energies and durations. YAG is Yttrium Aluminum Garnet.

Ultrafast transient absorption studies were carried out during a brief visit to the Central Laser Facility (CLF) at the Rutherford Appleton Laboratory (Didcot, Oxfordshire, UK). This work was done with the assistance of Drs. P. Matousek and M. Towrie, the CLF system is described in Section 2.4.

2.2 Traditional Laser Flash Photolysis

2.2.1 Background

Laser flash photolysis (LFP) is used to spectroscopically examine transients that have been generated following laser excitation of a suitable precursor. Flash photolysis employed in the microsecond to millisecond time scale, using a flash lamp for excitation, was first developed by Porter and Norrish; they later shared the 1967 Nobel prize for their work in this field.[1, 2] The development of LFP in the nanosecond time scale (nLFP) followed closely upon the heels of the discovery of the laser in 1960. This technique is an adaptation of the flash photolysis system developed by Porter and Norrish and first appeared in the mid to late 1960's. The use of laser excitation to generate and study reactive intermediates was reported nearly simultaneously by Porter,[3-5] Kosonocky,[6] and Lindqvist[7]. Interestingly, the design of most systems currently in use closely resemble the architecture of the Lindqvist system; his arrangement used a nitrogen laser (337 nm) to produce and detect the triplet state of acridine.[7] Many early laser flash photolysis systems used nitrogen or ruby lasers and the detection techniques were based on the more established technique of pulse radiolysis. The first computer-controlled laser flash photolysis system was developed in the late 1970's by Scaiano and Small at the University of Notre Dame.[8-10] This system represented a significant advancement with respect to data acquisition and processing and eventually became the prototype upon which many other systems were designed.

The main stipulation for studying photochemical events occurring on short time scales is that the duration of the excitation laser pulse must be both shorter than the monitored process and sufficiently intense to generate detectable transient populations. In the case of the lasers described in Table 2.1, this results in minimum time resolutions of approximately 15 ns for pulse durations of 5-8 ns and *ca.* 50 ps for 35 ps pulse widths. In essence, the LFP system is simply a very fast spectrometer coupled with a pulsed excitation source. The system employed in this

research can be used for the analysis of both transparent and opaque samples and can detect changes in both the absorption and emission properties of the samples. Although there are obviously differences in the detection systems and data treatments used for these very different samples, much of the general concept is the same and will be described below. Specifics of detectors, data treatment, and sample preparation for transparent and opaque samples will be discussed in subsequent sections.

2.2.2 Laser Flash Photolysis Fundamentals

Following laser excitation to generate the transient species of interest, the sample is interrogated with light from a monitoring light source. The geometry of the excitation and monitoring light sources is dependent upon the sample type. The use of a xenon lamp as the monitoring beam permits the acquisition of data from *ca.* 230 nm, and throughout the visible spectrum, up to 800 nm. In traditional LFP the monitoring beam is frequently pulsed, increasing the output intensity by a factor of 5-20 for several milliseconds, in order to improve the signal-to-noise ratio. This can be avoided by the use of new high-intensity ceramic lamps such as those employed in miniaturized nLFP systems (Luzchem Research Inc.). After interrogating the sample, the monitoring beam is subsequently focused onto the entrance slit of a high-intensity monochromator which selects the wavelength of light reaching the detector, located at the exit slit of the monochromator. The detector in the University of Ottawa system is a photomultiplier tube (PMT) operating on six dynodes. In the PMT, the optical signal generates a current that is terminated into a load resistor (typically 93 Ω depending on the signal cables) resulting in a voltage signal. The time-dependent voltage signal is captured by a Tektronix digitizing oscilliscope (equipped with pre-trigger capabilities) and the electrical signal is converted to a digital one. The oscilloscope is interfaced to a MacIntosh computer that provides experimental control through in-house software programmed in the LabView 5.1 environment from National Instruments. Each

component of the LFP system (laser, lamp, lamp pulser, shutters, etc.) is coordinated by a line synchronizer via a series of transistor-transistor linked (TTL) pulses that originate at the same point on a 60 Hz sine wave.

A schematic showing the timed sequence of the PMT output is given in Figure 2.1. Opening the monitoring beam shutter causes a sharp increase in the PMT output that is recorded as the pre-pulse baseline. The laser subsequently fires, striking a fiber optic cable that triggers the digitizer to start collecting data. The recorded signal is shown inside the box in Figure 2.1. The intensity of the monitoring beam itself is measured on a second channel and becomes the baseline from which changes in PMT voltage levels are determined. Kinetic information is obtained from the average of a set number of laser shots. The intensity data is plotted with respect to time in order to give a time-dependent decay trace. Spectral profiles of the transient are generated by compiling the kinetic data acquired at several different wavelengths and constructing a plot of intensity versus wavelength. In order to compare the signals from separate acquisitions, the intensity of the monitoring beam is maintained at a constant level through the use of a programmable power supply. The PMT output is set to a desired level and maintained throughout the duration of the experiment.

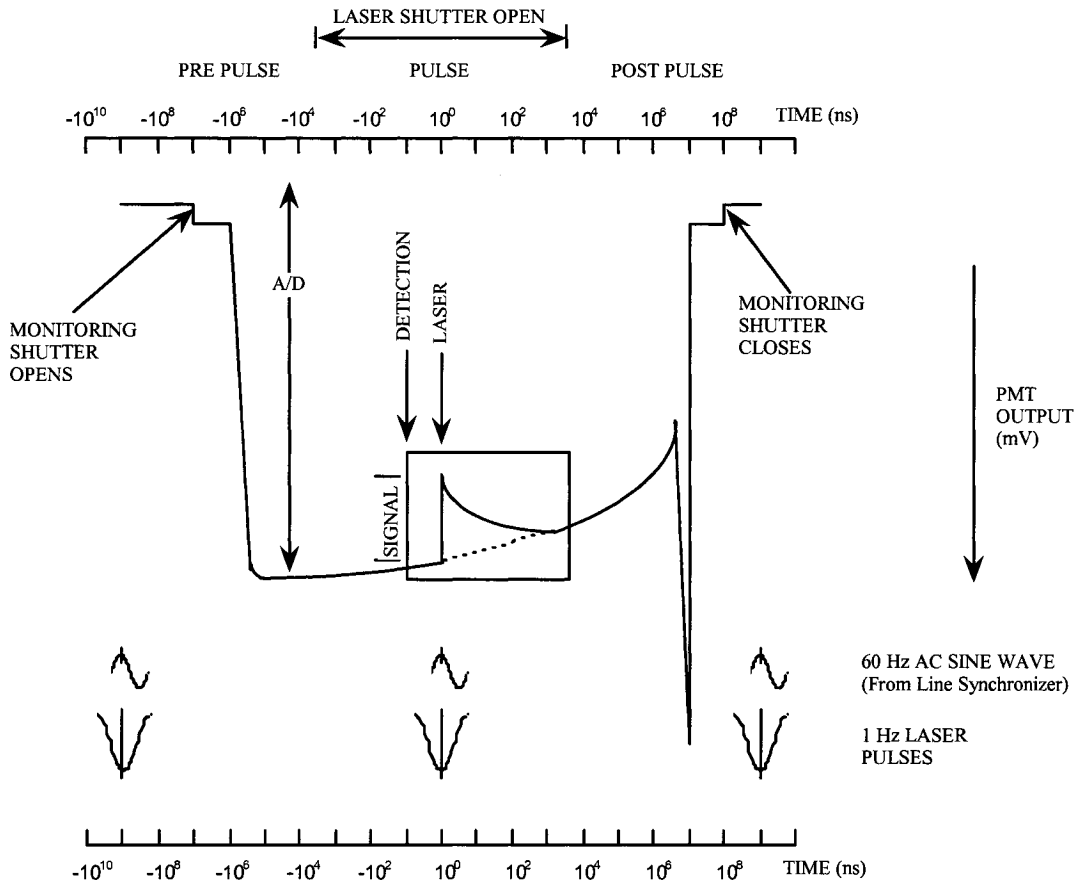

Figure 2.1 Plot of the PMT output versus time for a period before and after the laser pulse.

2.2.3 Absorption Detection for Transparent Samples

2.2.3.1 Detection and Data Treatment

When the sample of interest is transmissive, as is the case for the majority of solutions and films, the LFP experiment uses a detection mode based on changes in the transmission characteristics of the sample. This technique allows observation of both the formation of new species, as well as the disappearance of instantaneously formed transients. As mentioned in the previous section, following laser-induced formation of the excited state or reactive intermediate, the sample is interrogated by light from the monitoring lamp. The experimentally measured signal is converted (see below) to the change in absorbance, abbreviated ΔOD from the historical term

"optical density". The ΔOD reflects the change in the incident monitoring beam intensity ($I_{t=0}$ or I_0), following laser excitation ($I_{t=t}$ or I_t). A schematic of the LFP system showing the experimental geometry for transient absorption spectroscopy is given in Figure 2.2.

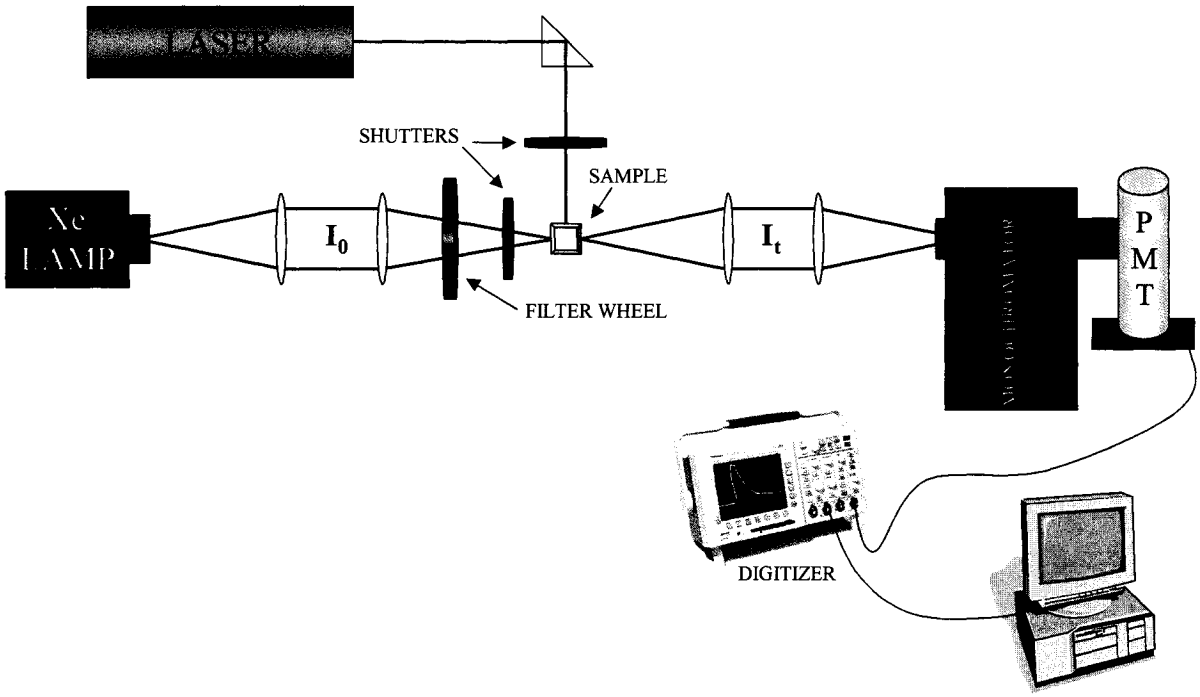

Figure 2.2 Schematic of the laser flash photolysis system for monitoring absorption changes in a transparent sample.

The transient absorption system uses a 150 W xenon lamp as the monitoring beam. The beam is concentrated and focused on a small 1-2 mm hole in the sample holder. The spectra are usually recorded on a point-by-point basis, where the time of data capture is preset before the acquisition, and the wavelength is changed over the course of the experiment. The resultant spectrum is called a difference spectrum (hence ΔOD), and represents from the difference between the molar absorption coefficient the ground state (ε_{GS}) and the transient (ε_T) at the probed wavelength. This is elaborated in Equations 2.1 to 2.6;

Equation 2.1 $OD_{t=0} = \varepsilon_{GS} \ell C_{GS}$ Absorbance at t = 0

Equation 2.2 $$OD_{t=t} = \varepsilon_{GS}\ell(C_{GS} - C_T) + \varepsilon_T \ell C_T$$ Absorbance at t = t

where $OD_{t=0}$ and $OD_{t=t}$ are the absorbances before and after excitation respectively; C_{GS} is the ground state concentration before excitation, C_T is the transient concentration produced following excitation, and ℓ is the optical path length. The change in absorbance following laser excitation can be obtained by combining Equations 2.1 and 2.2 to give the expression in Equation 2.3.

Equation 2.3 $$\Delta OD_{t=t} = (\varepsilon_T - \varepsilon_{GS})\ell C_T$$

Using the Beer-Lambert law we can describe the transmitted intensity of the probe beam (I_{PB}) before and after the laser excitation in terms of Equations 2.4 and 2.5.

Equation 2.4 $$I_{t=0} = I_{PB} \times 10^{(-\varepsilon_{GS}\ell C_{GS})}$$

Equation 2.5 $$I_{t=t} = I_{PB} \times 10^{(-\varepsilon_{GS}\ell C_{GS} + (\varepsilon_T - \varepsilon_{GS})\ell C_T)}$$

Amalgamating the previous three equations gives 2.6;

Equation 2.6 $$\Delta OD_{t=t} = -\log\left(\frac{I_{t=t}}{I_{t=0}}\right)$$

which can be rearranged to give ΔOD in terms of the experimentally observed quantity, i.e. the signal from the PMT.

Equation 2.7 $$\Delta OD_{t=t} = -\log\left(1 - \frac{signal_{t=t}}{I_{t=0}}\right)$$

The difference spectrum obtained by plotting the values of ΔOD at each wavelength is characteristic of the transient only when $\varepsilon_{GS}=0$; i.e. the ground state is transparent. In regions of the transient spectrum where the ground state also absorbs, the observed signal is precursor dependent; for example if $\varepsilon_{GS} > \varepsilon_T$ the

observed signal is negative and a bleaching is observed, if $\varepsilon_{GS} < \varepsilon_T$ the signal is positive, and similarly if $\varepsilon_{GS} = \varepsilon_T$ no signal is observed.

Using nanosecond laser flash photolysis, transients having lifetimes more than twice as long as the laser pulse duration can be easily studied. Consequently, this technique is ideally suited to the examination of a number of excited states and reactive intermediates such as excited triplet states, radicals, ions, and radical ions to name a few. In addition to providing spectral information, LFP can also be used to investigate reaction mechanisms by examining the kinetic behaviour of transients generated following laser excitation. By applying the appropriate kinetic equations, rate constants and reaction orders, data that can be very useful in the elucidation of mechanistic details, may be obtained. Additional information can be acquired by introduction of a quencher to the system providing an alternate mode for deactivation of the observed transient. Common quenchers may be energy acceptors, radical traps, molecular oxygen, hydrogen donors, and electron donors or acceptors, etc. The kinetic behaviour of the transient will be altered in the presence of a reactive quencher resulting in a change in the observed experimental first order rate constant (k_{exp}). A linear plot of the observed rate constant versus quencher concentration gives the quenching rate constant, k_q, according to Equation 2.8,

Equation 2.8 $$k_{exp} = k_0 + k_q[Q]$$

The observed value of k_q can be compared with literature values in order to aid in the assignment of the nature of the transient.

2.2.3.2 Experimental Considerations

A sample to be studied by LFP should have a ground state absorbance on the order of 0.3-0.5 at the wavelength of excitation in order to maximize the production of transients. This value is a compromise between the improved signals obtained from high transient concentrations and the exponential reduction in monitoring

beam intensity (I_0) as it passes through the sample volume as a function of the ground state absorption. The signal-to-noise ratio for weakly absorbing transients can also be improved through the use of a nearly parallel or "front-face" beam arrangement, contrary to the right angle configuration shown in Figure 2.2. This arrangement improves the signal by increasing the overlap volume between the pump and probe beams as illustrated in Figure 2.3.

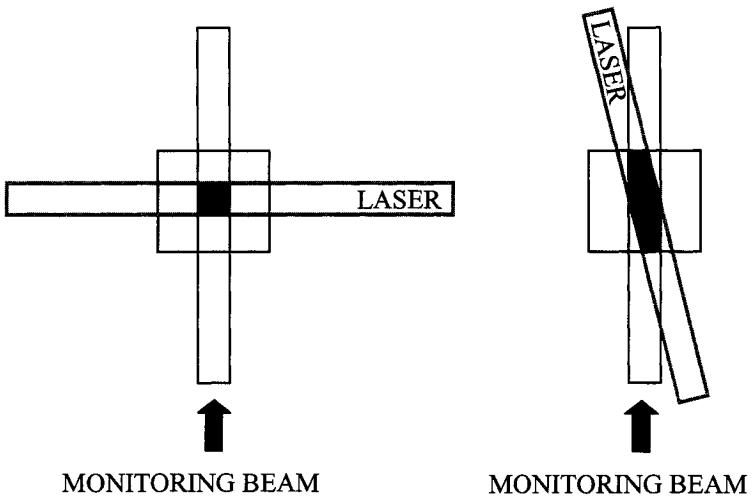

Figure 2.3 Top view of a stylized sample cell illustrating the increased overlap between the laser beam and the monitoring beam when using a front-face configuration (right) versus a side-on arrangement (left).

The limitations described above with respect to ground state absorbance do not apply when the laser beam and monitoring beam are oriented in a nearly parallel fashion. There are however, several additional reasons for preparing samples with low precursor absorbances as well as utilizing lasers with the minimum pulse energy to achieve decent signal-to-noise ratios. The following list highlights some of the most important considerations when designing a laser flash photolysis experiment:

1. *Sample concentration.* In addition to the general concerns mentioned above, highly absorbing samples can also result in the generation of "shock" or

acoustic waves leading to a repetitive signal superimposed on the time-dependent absorption signal of the transient. The frequency of the wave is determined by both the size of the sample cell and the speed of sound in the solution. Significant acoustic waves are generated when a large portion of the incident pulse energy is absorbed in a small volume of solution. Shock waves can also be the result of overly tight focusing of the laser beam, generation of highly absorbing intermediates, and defects on the surface of the sample cell.

2. *Laser power.* Intense signals will improve the signal to noise ratio in any experiment. Since a large signal is the result of high transient concentrations, which in turn are directly related to laser power, it might seem that the use of high laser power would be advantageous in all cases. This is not the case for several reasons, including the increased incidence of transient-transient interactions when high concentrations of transient are generated. Under the conditions of high transient concentration new mechanisms for transient decay may be introduced and the observed chemistry may be significantly different than that observed under low intensity irradiation. The use of high-energy laser pulses can also result in the observation of two-photon processes where, due to the photon density, a transient formed following absorption of a photon can absorb a second photon resulting in new chemistry and different reactive intermediates. Photo-ejection of an electron is a common process resulting from two-photon absorption. A plot of the signal magnitude versus laser power can be used to establish whether an observed transient was generated following the absorption of one or two photons. A monophotonic process will result in a linear dependence of signal intensity on laser power whereas a biphotonic process will display a non-linear relationship.
3. *Sample cell configuration.* Defect-free, high quality quartz or fused silica sample cells are mandatory for LFP experiments using excitation or

monitoring light sources in the UV. The material is chosen for its transparency in the spectral regions of interest and the unblemished surface is required to prevent light scattering and secondary effects such as the generation of shock waves (*vide supra*). The appropriate sample cell may be either a static container such as employed in traditional spectroscopy, or part of a larger system incorporating a reservoir where the sample solution is continually flowed through the sample cell during the experiment. There are advantages and disadvantages to the use of both static and flow cells. In general a flow system is preferred when the sample is to be subjected to multiple laser shots in order to avoid substrate depletion, the accumulation of a competitively absorbing photoproduct, and interference from a photoproduct that may participate in the transient photochemistry. The use of a static cell is recommended when acquiring transient kinetics since flow systems are more prone to air leakage as a result of the increased number of connections.

2.2.4 Diffuse Reflectance Detection for Opaque Samples

2.2.4.1 Detection and Data Treatment

When the sample of interest is opaque, the detection system described above must be modified. The study of heterogeneous systems requires an alteration of the traditional nLFP design such that light diffusely reflected from the sample surface is used as the analyzing light; as opposed to light transmitted through the sample. The technique of diffuse-reflectance laser flash photolysis (DR-LFP) was primarily developed by Wilkinson *et al* in the mid to late 1980's.[11-15] This technique allows the observation of both the growth and decay of transient species generated following laser excitation by monitoring changes in the reflected light intensity in an analogous fashion to that described above for conventional LFP.

Light reflected from a surface is comprised of both specular and diffuse reflectance components. Specular or normal reflectance is the light which is

returned from the surface at an angle equal to the angle of incidence with respect to the surface. Diffusely reflected light has penetrated the sample surface and returned to the surface following multiple scattering interactions with individual particles. This light may also be attenuated by absorption within the particles. Unlike specularly reflected light, diffusely reflected light is both symmetrically distributed and unpolarized regardless of the angle of incidence or the polarization of the incident beam. Since the specularly reflected light has merely bounced off of the sample surface, it contains no information and the DR-LFP detection system has been designed to avoid its detection (see Figure 2.4).

A mathematical approach has been developed in order to simplify the description of the interaction of light with diffusely reflecting samples. The Kubelka-Munk approach is applied to reflectance data in order to express the information in a format similar to the absorption spectrum plotted for translucent samples. This means, for example, that a plot of absorbance versus wavelength for a translucent glass will appear nearly identical to a plot of F(R) versus wavelength for the same material crushed to an opaque powder.

Equation 2.9

$$F(R) = \frac{K}{S} = \frac{(1-R)^2}{2R}$$

The Kubelka-Munk equation is given in 2.9, the reflectance data is expressed as a function of K and S where $K = 2\varepsilon C$ and ε is the extinction coefficient. R and S are the reflecting and scattering coefficients respectively and C is the concentration. For the examination of small to moderate changes in reflectance, as is the case for weakly absorbing samples, the Kubelka-Munk function is roughly linear with concentration. In this case the concentration of transients generated in DR-LFP are approximately proportional to the change in reflectance following laser excitation divided by the pre-pulse reflectance, $\Delta J/J$. The mathematical treatment of diffuse reflectance data has been described in detail by Wilkinson.[15]

The events in a DR-LFP experiment are completely analogous to those described for transient absorption spectroscopy in Section 2.2.3. The laser pulse induces formation of an excited state or reactive intermediate and the sample is interrogated by light from a water-cooled, 75 W xenon lamp oriented at a 45° angle to the sample surface. The diffusely reflected light is collected by a telescope and focused onto the entrance slit of the monochromator. The experimentally generated voltage signal is converted to a change in reflectance with respect to the pre-pulse reflectance, $\Delta J/J$. The $\Delta J/J$ value reflects any change to the pre-pulse monitoring beam intensity ($I_{t=0}$ or I_0), following laser excitation ($I_{t=t}$ or I_t). A schematic of the LFP system showing the experimental geometry for transient diffuse-reflectance spectroscopy is given in Figure 2.4. Spectra are recorded as described previously and the spectral profiles will have the same dependence on ground state and transient molar absorption coefficients.

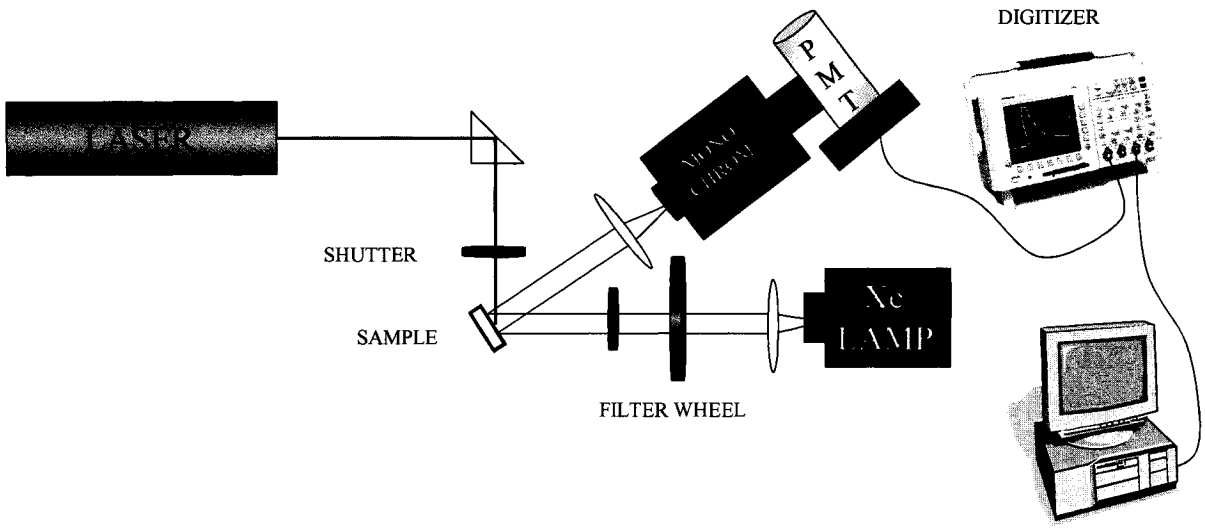

Figure 2.4 Schematic of the laser flash photolysis system for monitoring reflectance changes in opaque samples.

Time-dependent diffuse reflectance data can also be used to obtain mechanistic information. However, the data from heterogeneous systems must be treated with more care than that from homogeneous systems, where standard kinetic equations are easily applied. The non-homogeneous distribution of guest

molecules in supramolecular systems often results in decay traces that are not well described by single exponential decay kinetics. In addition, the values obtained from simple mono-exponential or bi-exponential treatments may in some cases be dependent on the time scale of observation.[16] A distribution analysis of the time-resolved data can more accurately reflect the site multiplicity available in the samples employed in this thesis.

Ideally, for this data treatment, decay traces are recorded at several different time scales and combined, resulting in a composite decay with closely spaced data points at short times and a lower density of points at longer times. The compiled decay trace is then evaluated using a fitting function containing 100 exponential terms with fixed, logarithmically spaced lifetimes from 10 ns to 10 ms and changeable pre-exponentials. The process is described in the scheme below for a sample of azaxanthone incorporated in zeolite NaY.[17] Transient decay traces were recorded over 20, 40, and 100 microseconds, compiled, and re-plotted versus log time. The combined date file is used as the input for exponential series method (ESM) software from Photon Technology Incorporated (PTI, Lawrenceville, NJ) that has been customized to process diffuse reflectance data. The inputted data is fitted using a function with 100 exponential terms as opposed to the one or two typically used for pure first and second order decay fittings. The output is plotted as abundance versus the logarithm of lifetime. This methodology clearly offers a more accurate representation of the multiplicity of sites available to zeolite-hosted guest molecules.

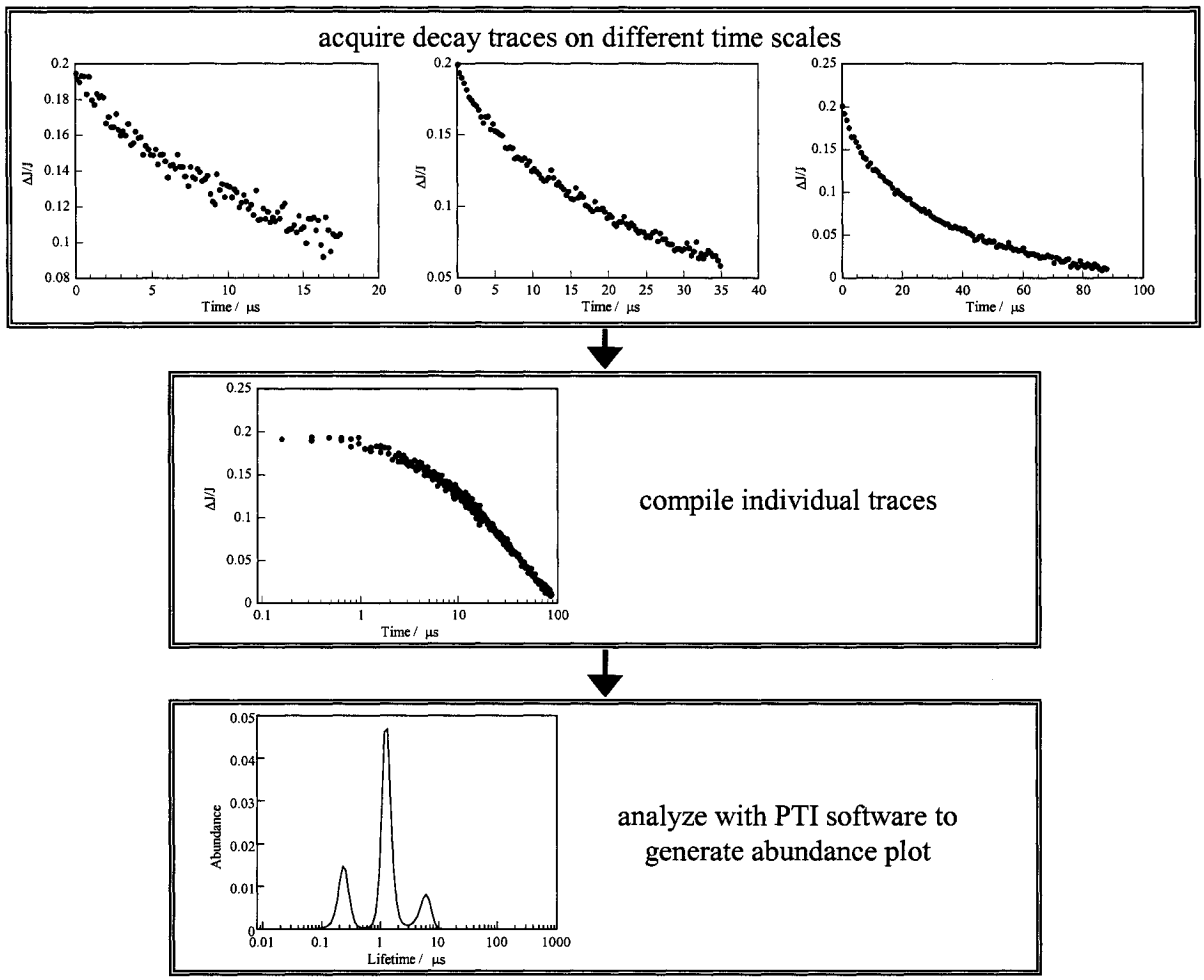

Scheme 2.1 Steps for performing a lifetime distribution analysis.

Although a distribution analysis best reflects the lack of homogeneity in the zeolite interior, it is important to point out that a detailed kinetic analysis is not always required. In many cases a qualitative comparison of transient behaviour within a series of samples is all that is necessary. However, when comparing transient lifetimes obtained from a single kinetic trace it is important to maintain the same observational time scale for all measurements.

2.2.4.2 Experimental Considerations

Many of the points raised in Section 2.2.3.2, with respect to laser power for example, are also valid when designing a DR-LFP experiment. As with solution or film samples, it is best if the absorption of the ground state is kept at the minimum

for which reasonable signals can be obtained. In addition to the problems mentioned in the previous section, the Kubelka-Munk approximation is no longer linear for highly absorbing samples. The typical sample cell employed in DR-LFP is a 3x7 mm^2 quartz or fused silica cell with minimal surface defects. Due to the impracticality of any sort of "flow system" for solid samples it is imperative that the surface exposed to the laser is moved after every one or two laser shots. The sample cells used in this thesis may be either sealed under vacuum or sealed with rubber septa and subsequently purged with oxygen, nitrogen, argon, etc.

2.3 Time-Resolved Luminescence Techniques

2.3.1 Fluorescence Fundamentals

Luminescence, the radiative relaxation of an electronically excited state, is subdivided into fluorescence and phosphorescence depending on whether or not relaxation of the excited state involves a change in multiplicity. The term fluorescence describes the emission of a photon during the relaxation of an excited state to a ground state of the same multiplicity; often the transition between an excited singlet and ground singlet state. This process is spin allowed and consequently occurs very rapidly; rate constants range from 10^6 s^{-1} up to 10^{12} s^{-1} with a typical fluorescence lifetime being on the order of 10 ns. Phosphorescence is the emission of light accompanying the transition between states of different multiplicity, for example the emission associated with relaxation of singlet oxygen to its triplet ground state. This process is spin forbidden and phosphorescence lifetimes are typically in the millisecond to second range, or longer. Phosphorescence is rarely observed in fluid solution at room temperature due to the presence of numerous competing deactivation pathways.

Time-resolved fluorescence spectroscopy is an important technique in the tool box of the physical organic chemist. Time-resolved data frequently contains information that cannot be obtained from steady-state fluorescence spectra; for example species with overlapping emission spectra can often be resolved on the basis of differences in their fluorescence lifetimes. However, unlike transient absorption spectroscopy, in fluorescence we are limited to the observation of only one type transient, i.e. the excited singlet state. Fortunately, fluorescence techniques are extremely sensitive, since the emitted photons are recorded against a baseline of zero emission whereas transient absorption spectroscopy measures small changes in transmitted light intensity. The fluorescence lifetime can provide important information about the environment being experienced by the species of interest. For example, fluorescence lifetimes have been used to determine DNA

damage by analysis of the different decay kinetics for nucleic acid dyes bound to double- versus single-stranded DNA.[18]

The experimental magnitude measured in a time-resolved fluorescence experiment is actually the lifetime of the excited singlet state, this value is commonly referred to as the *fluorescence lifetime* or τ_f. The fluorescence lifetime should be distinguished from the *radiative lifetime,* which is an intrinsic value and is not significantly affected by changes to the sample environment. One relevant relationship is given below in Equation 2.10 where k_{rad} is the inverse of the radiative lifetime and k_{nr} represents the rate of any non-radiative deactivation of the singlet state.[19]

Equation 2.10

$$\tau_f = \Phi \frac{1}{k_{rad}} = \frac{1}{k_{rad} + \Sigma k_{nr}}$$

It is useful to note that the observed lifetime is a statistical average calculated from the randomly emitting fluorophores in the sample. When the number of emitting species is large, some fluorophores will emit rapidly following excitation and a portion will emit at times longer than the average observed lifetime. The intensity decay is actually the time distribution of all emitted photons.

The addition of quenchers to induce changes in the observed lifetimes is one key way to expand the information gained by time-resolved emission spectroscopy. The lifetime behaviour will distinguish between the different modes of fluorescence quenching, i.e. static versus dynamic. Fluorescence quenching via the formation of a non-emissive ground state complex will reduce the overall fluorescence intensity. Formation of a ground state complex will have no effect on the observed decay times because, the only the unquenched fluorophores are observed in the experiment. Dynamic quenching is a process that affects the entire excited state population and so a decrease in the mean decay time of the excited state population is observed.

2.3.2 Experimental Set-up

There are two popular detection systems typically employed for time-resolved fluorescence measurements, single photon counting and streak camera detection; the University of Ottawa system is based on a streak camera. This section will describe the system and its components in detail, Figure 2.7 shows the geometry and major components. The laser used is a passively mode-locked Nd:YAG laser from Continuum producing a train of pulses at 1064 nm with a full width at half maximum of 35 ps. Before the laser pulse reaches the sample the series of events shown graphically in Figure 2.5 occurs. First, a single pulse from the original train is selected and amplified by a factor of ten to give the single 1064 nm pulse shown in 2.5-A. A small portion of this beam (< 1%) is directed towards a diode head generating the voltage pulse shown in B. The rising edge of this voltage pulse is used to trigger the streak camera to begin preparing to collect data; the rise time of the Hamamatsu streak camera is approximately 40 ns. While the streak camera is preparing to acquire data the laser pulse enters the optical delay unit or White cell and undergoes multiple reflections so that the arrival of the pulse at the sample coincides with the start of data acquisition by the streak camera (2.5-D and E). As a point of reference, the light pulse will travel approximately 30 cm in 1 ns. After exiting the delay unit the beam passes through the harmonic generators to give light at 532, 355, or 266 nm depending on whether the second, third, or fourth harmonic is used (2.5-F). This light is then used to excite the sample and the streak camera records the resulting emission.

There are some important differences between time-resolved spectroscopy on the picosecond time scale versus the nanosecond techniques described in the previous sections. One of these differences is illustrated in Figure 2.5-B and C where a delay is caused by the need to transmit an electrical signal via a fixed cable connection. The time evolution of events occurring in the picosecond or femtosecond regime is too fast to be captured by traditional digitizing methods and so the speed of light becomes the clock in the process. This limitation is an even

more important consideration in the femtosecond pump-probe techniques discussed in later sections. On the time scale of these experiments the speed of light can no longer be considered "instantaneous" and the acquisition times are varied by changing the distance traveled by the probe beam, before it interrogates the sample.

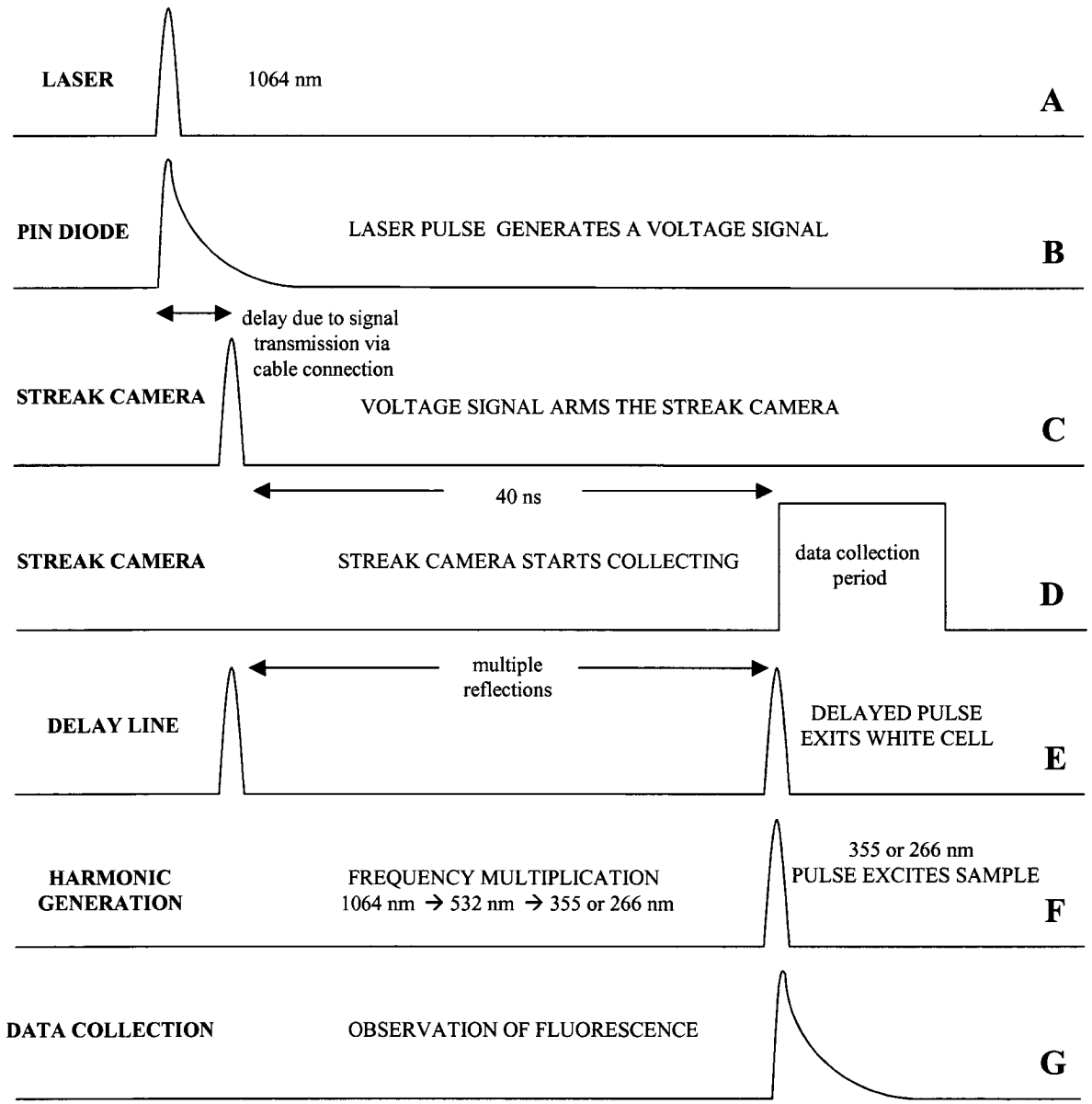

Figure 2.5 Pictorial representation of the early events of a time-resolved fluorescence experiment.

The streak camera is where the emitted photons are detected and converted into a manipulatable data format. The key component of the streak camera is the streak tube where the incident photons are converted to electrons after striking a photocathode. An applied voltage accelerates the electrons towards the microchannel plate (MCP) located at the opposite end of the device (see Figure 2.6 below). A sweep voltage is applied perpendicular to the path of the electrons. As a result the leading electrons are deflected to a lesser extent than the late electrons, striking the MCP at different locations, giving a time profile of the incident photons.[20] In the MCP the electrons are amplified by a factor of $\geq 10^3$ and subsequently strike a phosphor screen generating an image which is recorded by a CCD camera (CCD, charge capture device). In this way the electrical signal is converted back into an optical one.

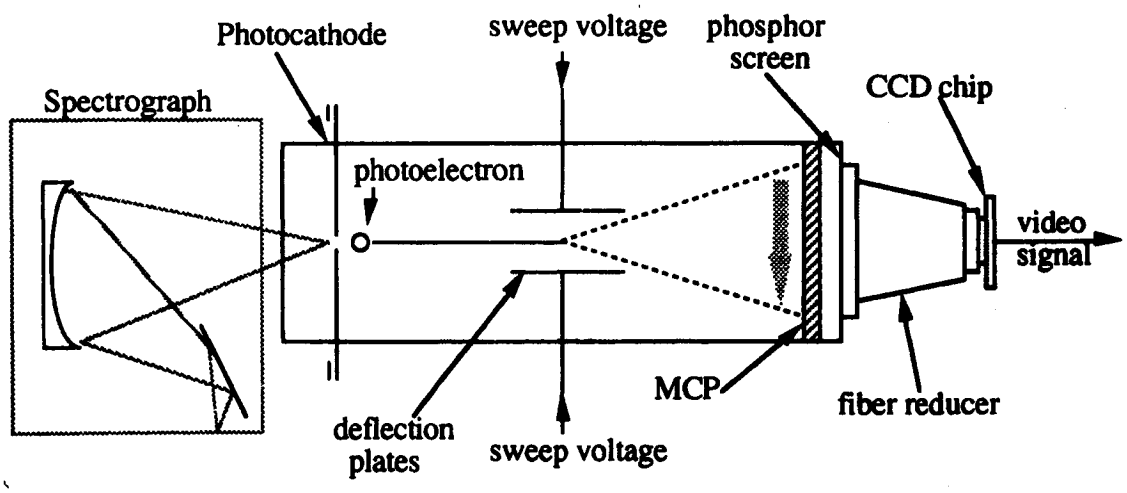

Figure 2.6 Schematic of an electronic streak camera. (Reproduced from reference 20)

In this system, a Chromex spectrograph is placed just before the streak camera so that the incident light reaching the streak tube is already resolved into its component wavelengths. With this arrangement it is possible to obtain an image in three dimensions where wavelength, time, and intensity are each acquired simultaneously. This is illustrated in Figure 2.7 below where the horizontal axis of the output plot represents wavelength and the vertical axis represents the time

domain. The signal intensity is indicated by the colour and brightness of each pixel in the recorded image.

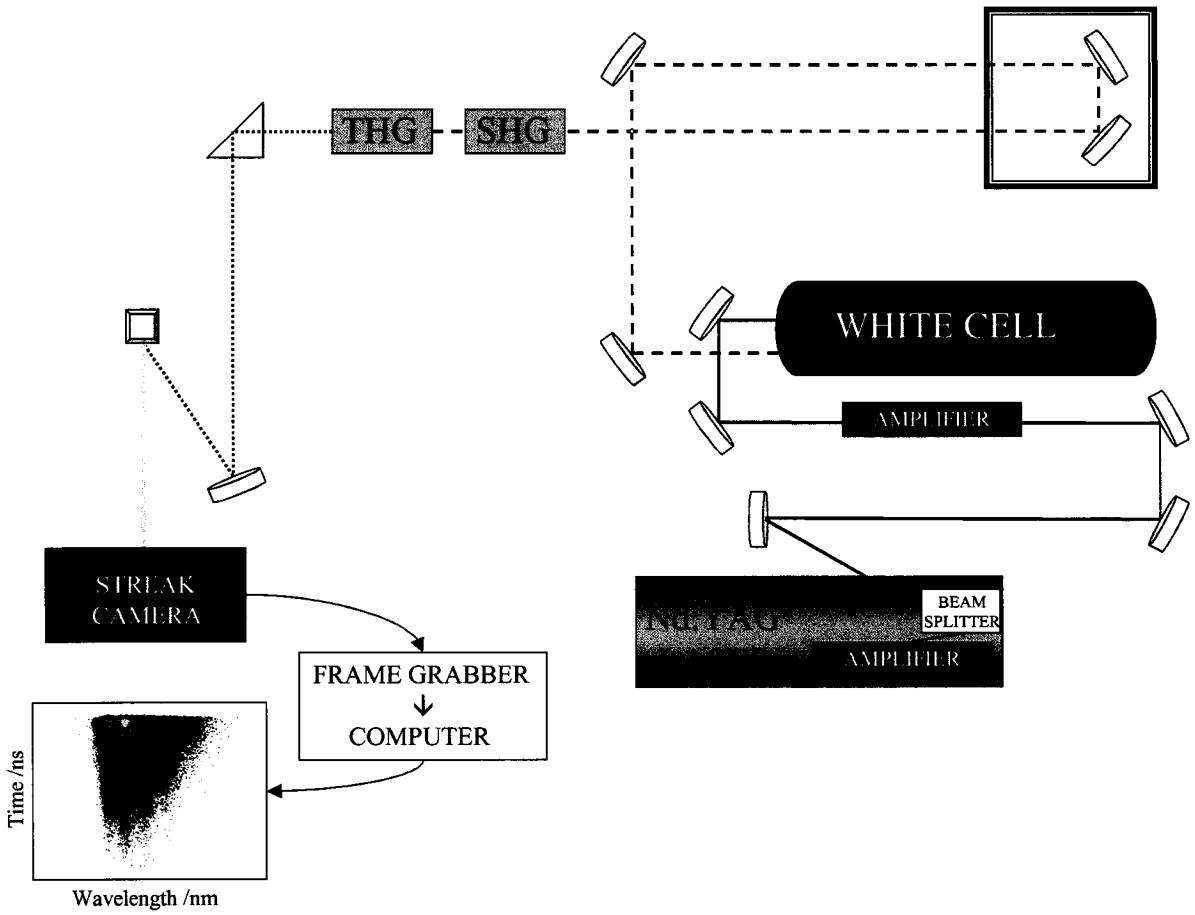

Figure 2.7 Schematic of the experimental set-up for time-resolved emission. SHG and THG stand for second and third harmonic generator respectively.

2.4 Ultrafast Transient Absorption Techniques

2.4.1 Introduction

Since the development of nLFP in the late 1960's, advances in lasers, optics, and electronics have paved the way for expansion of this technique to monitor phenomena on increasingly short time scales. The current state of the art employs femtosecond (fs, 10^{-15} s) laser pulses to monitor extremely fast processes. Although the basic concept is the same in both traditional and ultrafast LFP (uLFP) there are several key differences in the experimental design. The following section will attempt to give the reader some insight into the instrumental design and experimental considerations involved in uLFP work. This description is not intended to be exhaustive nor to represent an expert opinion but merely to provide an overview of the technique. The uLFP experiments performed as a part of this thesis were conducted at the Central Laser Facility of the Rutherford Appleton Laboratories (RAL) and emphasis will be given to the instrumental design employed in that facility. Although other time-resolved spectroscopic techniques have been more prominently employed in this work, ultrafast techniques are becoming an increasingly standard methodology for the study of photochemistry and photophysics. As such, a brief discussion of the technology is warranted here.

2.4.2 Experimental Set-up and Considerations

Ultrafast transient absorption spectroscopy uses a pump-probe technique where the pump beam generates the transient species of interest that are subsequently interrogated by the probe beam. In uLFP the traditional monitoring lamp is replaced by a white light continuum generated from the laser pulse in a 1 cm flowing water cell. The laser system at RAL is based on a Ti:sapphire oscillator and a Ti:sapphire regenerative amplifier pumped with a Nd:YLF (Yttrium Lithium Fluoride) laser. The fundamental output can be tuned from 770 to 840 nm and initial pulse energies are approximately 1 mJ at a frequency of 1 kHz. The pump

pulse for transient absorption measurements is further tunable to between 200 and 2000 nm through the use of a custom designed optical parametric amplifier (OPA).[21, 22] The OPA represents a significant advantage over the relatively narrow tuning range available with conventional dye laser technology. The OPA is designed to provide simple and efficient conversion of a pulsed pump laser to new frequencies with single passes through non-linear optical (NLO) crystals. A very simplified diagram of a generic experimental set-up for uLFP is shown below in Figure 2.8.

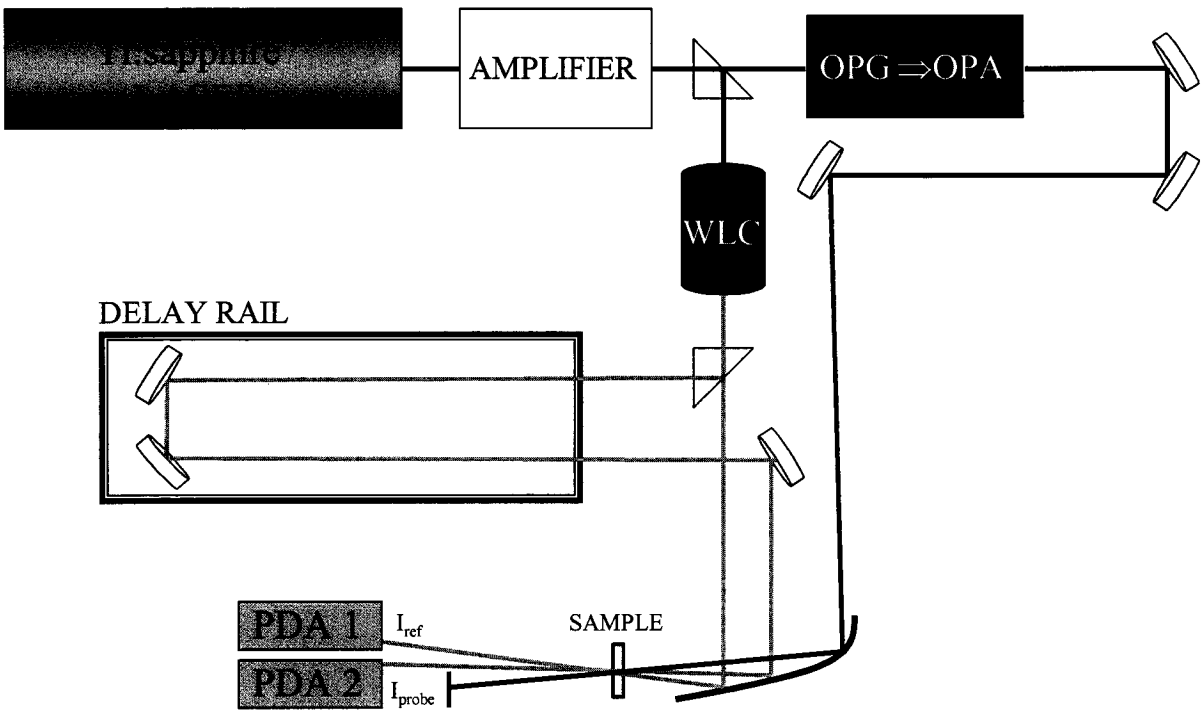

Figure 2.8 Simplified schematic of a system for ultrafast transient absorption spectroscopy. WLC represents the white light continuum generator.

The simplified sequence of events are as follows; the initial laser pulse is split to generate the white light continuum and the pump pulse of desired wavelength. The pump pulse is directed to the sample, generating the transient species of interest. The transient population is interrogated by the probe beam after a pre-selected delay time; the delay time is determined by the distance traveled along the delay rail. The pump and probe beams are overlapped in the cell through which

the sample solution is circulated via a peristaltic pump. The probe beam intensity is detected by a 512 pixel photodiode array camera (PDA). The portion of the white light continuum that is not directed towards the delay rail, is passed directly through the sample and detected by an identical PDA in order to provide a reference and reduce the pulse-to-pulse jitter. The pump pulse is chopped mechanically at *ca.* 2 kHz and the data are recorded by a lock-in amplifier. As with nLFP, the measured quantity is the change in absorbance, ΔOD, determined according to Equation 2.11. I_{probe} and I_{ref} are the intensities of the probe and reference beam respectively before (t=0) and after (t=t) the laser has fired. The instrument response function for this system is *ca.* 500 fs.

Equation 2.11

$$\Delta OD = -\log\left[\frac{(I^{\lambda}_{probe}/I^{\lambda}_{ref})_{t=0}}{(I^{\lambda}_{probe}/I^{\lambda}_{ref})_{t=t}}\right]$$

In contrast to nLFP, the detector in uLFP is a PDA and data is acquired as an entire spectral profile at each pre-selected delay time. In order to compile kinetic decay traces, the spectral profiles must be collected at a variety of delay times and then the ΔOD values at a chosen wavelength are plotted versus delay time. This process is the opposite of that which occurs in nLFP but, is analogous to data collection and processing in time-resolved emission where a streak camera and CCD comprise the detection system.

2.5 References

1. R. G. W. Norrish and G. Porter, Chemical reactions produced by very high light intensities, *Nature*, **1949**, *164*, 658.

2. G. Porter, The absorption spectroscopy of substances of short life, *Discuss. Faraday Soc.*, **1950**, *60*, 69-82.

3. G. Porter and J. I. Steinfeld, Giant-pulse-laser flash photolysis of phthalocyanine vapor, *J. Chem. Phys.*, **1966**, *45*, 3456-3457.

4. G. Porter and M. R. Topp, Nanosecond laser flash photolysis and the absorption spectra of excited singlet states, *Nature*, **1968**, *220*, 1228-1229.

5. G. Porter and M. R. Topp, Nanosecond laser flash photolysis, *Proc. Roy. Soc. Lond. A*, **1970**, *315*, 163-184.

6. W. F. Kosonocky, Observations of the triplet state in phthalocyanines, *J. Chem. Phys.*, **1965**, *43*, 831-833.

7. L. Lindqvist, Utilization of a laser with pulsed ultraviolet emission in flash photolysis. Triplet sate of acridine, *Hebd. Seances Acad. Sci. Ser. C*, **1966**, *263*, 852-854.

8. R. D. Small and J. C. Scaiano, Reaction of type II biradicals with paraquat ions. Measurement of biradical lifetimes, *J. Phys. Chem.*, **1977**, *81*, 828-832.

9. R. D. Small and J. C. Scaiano, Photochemistry of phenyl alkyl ketones. The lifetime of the intermediate biradicals, *J. Phys. Chem.*, **1977**, *81*, 2126-2131.

10. R. D. Small and J. C. Scaiano, The absolute rates of hydrogen abstraction by *tert*-butoxy radicals, *J. Am. Chem. Soc.*, **1978**, *100*, 296-298.

11. R. W. Kessler and F. Wilkinson, Diffuse Reflectance triplet-triplet absorption spectroscopy of aromatic hydrocarbons chemisorbed on γ–alumina, *J. Chem. Soc., Faraday Trans. 1*, **1981**, *77*, 309-320.

12. R. W. Kessler, D. Oelkrug and F. Wilkinson, Detection of transient spectra within polycrystalline samples using the new technique of diffuse reflectance flash photolysis, *Appl. Spectrosc.*, **1982**, *36*, 673-675.

13. F. Wilkinson, C. J. Willsher, P. Warwick, E. J. Land and F. A. P. Rushton, Diffuse reflectance pulse radiolysis of opaque samples, *Nature*, **1984**, *311*, 40-42.

14. F. Wilkinson and C. J. Willsher, Triplet-triplet absorption in microcrystalline benzil detected by diffuse reflectance laser flash photolysis, *Appl. Spectrosc.*, **1984**, *38*, 897-901.

15. F. Wilkinson and G. Kelly, Diffuse reflectance flash photolysis In *Handbook of Organic Photochemistry*; J. C. Scaiano, Ed.; CRC Press Inc.: Boca Raton, 1989; Vol. 1; 293-314.

16. G. Kelly, C. J. Willsher, F. Wilkinson, J. C. Netto-Ferreira, A. Olea, D. Weir, L. J. Johnston and J. C. Scaiano, Intrazeolite photochemistry. VI. Diffuse reflectance laser flash photolysis and product studies of diphenylmethyl radicals on solid supports, *Can. J. Chem.*, **1990**, *68*, 812-819.

17. S. Corrent, L. J. Martinez and J. C. Scaiano, Intrazeolite photochemistry. Photochemistry of 1-azaxanthone in zeolites in the presence of hydrogen donors, electron donors, and energy acceptors, *J. Phys. Chem. B*, **1999**, *103*, 8097-8103.

18. G. Cosa, K.-S. Focsaneanu, J. R. N. McLean and J. C. Scaiano, Direct determination of single to double stranded DNA ratio in solution applying time-resolved fluorescence measurements of dye-DNA complexes, *Chem. Commun.*, **2000**, 689-690.

19. J. R. Lakowicz *Principles of Fluorescence Spectroscopy;* Kluwer Academic/Plenum Publishers: New York, 1999.

20. M. Watanabe, M. Koishi and P. W. Roehrenbeck *The International Society for Optical Engineering;* SPIE: Los Angeles, 1993.

21. P. Matousek, A. W. Parker, P. F. Taday, W. T. Toner and M. Towrie, Two independently tunable and synchronised femtosecond pulses generated in the visible at the repetition rate 40 kHz using optical parametric amplifiers, *Opt. Commun.*, **1996**, *127*, 307-312.

22. M. Towrie, A. W. Parker, W. Shaikh and P. Matousek, Tunable picosecond optical parametric generator-amplifier system for time resolved resonance Raman, *Meas. Sci. Technol.*, **1998**, *9*, 816-823.

3. Multi-component Donor-Acceptor Systems in Zeolites

3. Multi-component Donor-Acceptor Systems in Zeolites 83

3.1 Background 84
3.2 Multi-component Photocatalytic Systems Based on TiO_2 90
3.2.1 Preparation of Titanium Dioxide-Sensitizer Combinations 90
3.2.2 Sample Characterization 92
3.2.3 Time-Resolved Studies 98
3.2.4 Photocatalytic Studies 107
3.3 Medium Effects in Multi-component Systems 115
3.3.1 Sample Preparation and Characterization 115
3.3.2 Photophysical Studies 119
3.4 Conclusions 125
3.5 Experimental 127
3.5.1 Sample Preparation 127
3.5.2 Steady-state Spectroscopy 129
3.5.3 Time-resolved Spectroscopy 130
3.5.4 Photocatalytic Studies 130
3.6 References 132

3.1 Background

The non-deformable internal cavities defined by the rigid crystal structure of zeolite materials provide an interesting host matrix for a variety of photophysical processes and photochemical transformations. Examples given in Chapter 1 demonstrated how zeolite encapsulation can affect excited state properties, such as lifetime, and exert an influence on the product distribution in chemical reactions. The ordered array of pores that comprise the zeolite structure can also be used to spatially organize guest molecules. This can be particularly attractive in the case of multi-component systems in which each constituent is spatially arranged with respect to the others. Following molecular level assembly of these materials, the system may remain ordered in a way reminiscent of the manner in which natural macromolecular structures are organized. The zeolite matrix embeds and confines each of the components, playing the role of the protein in natural systems. Noting this resemblance to biologically active macromolecules, the term *zeozymes* has been coined.[1] X and Y encapsulated metallophthalocyanines that catalyze the epoxidation of alkenes by hydroperoxides, in a way that mimics cytochrome P450, are an example of this similarity.[2]

The need for efficient and economical methodologies for the purification of drinking water is profoundly important at this time. In 2004, UNICEF estimated that over one billion people were still without access to sanitary drinking water.[3] The last 25 years have witnessed a growing awareness of the vulnerability of global fresh water resources.[4] The rates of natural biological remediation are surpassed in most parts of the world by the quantity of anthropogenic and other waste released into the system.[4] To cope with the increasing effects of pollution on the hydrosphere, the development of chemical treatments for wastewater has become increasingly important. In this context, treatment methodologies based on efficient catalytic materials are an attractive option. Thermal catalysts have been extensively investigated for this purpose; however, the achievable reaction rates in these

systems are slow compared to those using photocatalysts.[5] The main advantage of light activated catalysts is their reactivity at various temperatures, including room temperature, as opposed to thermal catalysts, which often require high temperatures for activation. Another advantage of photocatalytic systems is the ease with which they may be switched on or off in the presence or absence of light.

One of the most general methods for the degradation and mineralization of organic contaminants in aqueous solution is photocatalytic decomposition employing a sensitizer. Titanium dioxide is the most widely studied photosensitizer for this purpose because it is cheap, easily available, chemically robust, and has been shown to degrade a wide range of organic species.[4, 6, 7] Titanium dioxide is a semi-conductor oxide with a band gap of 3.2 eV in its anatase form. Photochemical excitation with light of the appropriate energy (3.2 eV ~ 380 nm) results in the promotion of one electron across the band gap from the valence band into the conduction band resulting in an electron/hole pair (e^-/h^+). This exciton may recombine and dissipate the pump energy or suitable chemical scavengers, i.e. electron acceptors or donors, may trap either species. The detailed mechanism for photocatalytic degradation of organic materials is a current topic of research, however, it is clear at this point that superoxide ($O_2^{-\bullet}$) and hydroxyl radicals ($^\bullet OH$) are active agents in the mineralization of organic compounds.[8, 9] These radicals are formed when the e^-/h^+ pair are scavenged by molecular oxygen and water respectively, according to the following scheme.

$$e^-_{CB} + O_2 \longrightarrow O_2^{\bullet -}$$

$$H_2O + h^+ \longrightarrow {}^\bullet OH + H^+$$

Scheme 3.1 Generation of reactive oxygen species (ROS) following scavenging of conduction band electrons and valence band holes by oxygen and water.

There are, however, disadvantages associated with the use of TiO_2 as a heterogeneous catalyst for the purification of aqueous systems: (1) complete removal of TiO_2 from treated water requires specialized micro-filtration techniques,

and (2) the active form (anatase) does not have significant absorption beyond 370 nm therefore requiring UV light for efficient photodegradation.[10] The desirability of alternative, environmentally-friendly photocatalytic systems able to operate under visible light illumination has prompted researchers to explore a variety of other heterogeneous systems.

The photochemical and photophysical properties of zeolite-encapsulated *tris*(2,2′-bipyridine)ruthenium(II) ($Ru^{2+}(bpy)_3$ in Figure 3.1 below) have been investigated by many researchers since its first preparation by ship-in-a-bottle synthesis in 1980.[11] Prior to the preparation of zeolite complexes, $Ru^{2+}(bpy)_3$ was observed to operate as an electron transfer reductant in solution. Electron transfer quenching of $Ru^{2+}(bpy)_3$ luminescence to generate $Ru^{3+}(bpy)_3$ in the presence of *trans*-2-bis(*N*-methyl-4-pyridyl)ethylene and 1,1′-dimethyl-4,4′-bipyridine^{2+} (methyl viologen cation, MV^{2+}) was observed in aqueous solution.[12, 13]

Lunsford *et al.* noted that that the excited state of $Ru^{2+}(bpy)_3$ encapsulated in zeolite Y is theoretically able to participate in the oxidation and reduction of water to ultimately produce H_2 and O_2.[11] These processes are likely to be inefficient in solution due to highly competitive back electron and energy transfer processes. The preparation of $Ru^{2+}(bpy)_3$@Y (recall that "@Y" indicates encapsulation in zeolite Y) was aimed at providing an environment that would favour formation of the $Ru^{2+}(bpy)_3$ excited charge-transfer state and the forward electron transfer while reducing the efficiency of energy wasting processes. Unfortunately, the production of H_2 and O_2 following irradiation were not observed in this case. The $Ru^{2+}(bpy)_3$@Y complex was, however, well characterized, and the diffuse reflectance spectra (DRS) of the orange-red solid was in excellent agreement with the aqueous solution absorption spectra. The emission spectrum and emission lifetime were also in agreement with those recorded in solution. $Ru^{2+}(bpy)_3$ luminescence was found to be quenched by O_2 and self-quenching was also observed at high loadings of the complex.[11]

As mentioned in Section 1.4.2, $Ru^{2+}(bpy)_3$@Y in combination with various electron acceptors (such as intrazeolitic MV^{2+}) has also been explored in the context of solar energy conversion and storage. In homogeneous solution the photoinduced electron transfer (PeT) from $Ru^{2+}(bpy)_3$ is followed by an efficient back reaction which can only be prevented by the presence of sacrificial electron donors.[14] The assembly of donor-acceptor pairs in heterogeneous support systems, such as zeolites, clays, and polymers, may provide the appropriate electrostatic and steric environment for the prevention of back electron transfer (BeT) thereby favouring the generation of a long-lived charge-separated state. The study of zeolites as supramolecular scaffolds for energy storage systems (via long-lived charge separation) has been pioneered largely by Dutta[15-22] *et al.* with significant contributions also from the groups of Kincaid[23, 24] and Mallouk.[25-27] Several examples were given in the preceding chapter, demonstrating how intelligent use of the zeolite framework, to spatially organize the donor and acceptor components, can result in the generation of extremely long-lived charge-separated states.

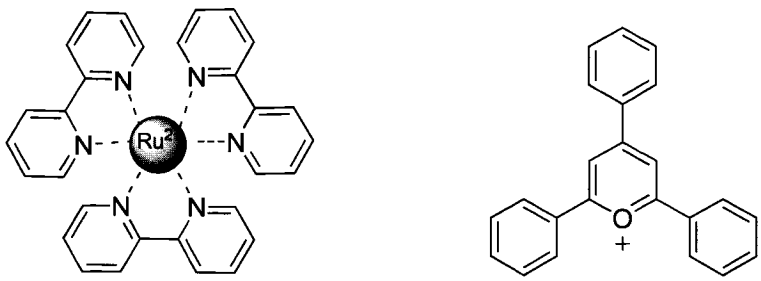

$Ru^{2+}(bpy)_3$ TP^+

Figure 3.1 Structures of *tris*(2,2′-bipyridine)ruthenium(II) ($Ru^{2+}(bpy)_3$) and 2,4,6-triphenylpyrylium cation, TP^+.

Triphenylpyrylium cation (TP^+ in Figure 3.1) is a well-established photoinduced electron transfer sensitizer in solution.[28] It possesses many desirable qualities with respect to eT sensitization, for example, visible wavelength absorption. In addition, since TP^+ is a cation there is no net charge separation associated with the electron transfer step; as a result, formation of the free ions is

enhanced and deactivation via BeT is reduced. It has been observed that PeT efficiency is generally higher for cationic sensitizers than for neutral sensitizers.[29] Irradiation of TP^+ does not produce singlet oxygen ($^1O_2$) or superoxide anion ($O_2^{-\bullet}$), another useful property in terms of photosensitization.[28] The triphenylpyrylium cation is typically not a good oxidant in its ground state, but becomes a powerful oxidizing agent in both its singlet and triplet excited states. The reduction potentials, therefore, are different depending on the spin multiplicity involved and have been measured versus a saturated calomel electrode (SCE). The measured reduction potentials are *ca.* 2.5 V for the singlet and *ca.* 2.0 V for the triplet, in the case of the tetrafluoroborate salt (these values incorporate the singlet and triplet excitation energies, E_S = 65 kcal mol^{-1} and E_T = 53 kcal mol^{-1}).[28] Despite these advantages, the major downfall to the use of TP^+ as a PeT photosensitizer in aqueous systems is its relatively rapid conversion to 1,3,5-triphenylpent-2-en-1,5-dione via nucleophilic addition of water (Scheme 3.2).

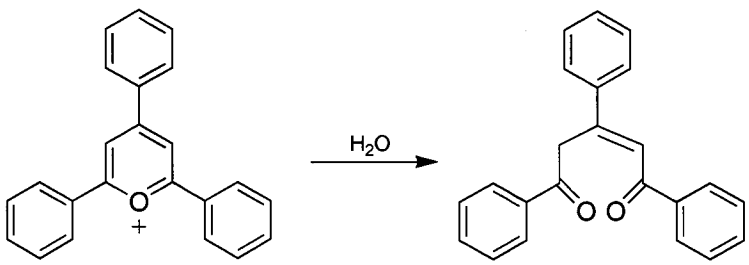

Scheme 3.2 Hydrolytic ring opening of TP^+ to give the 1,3,5-triphenylpent-2-en-1,5-dione.

TP^+ was prepared within the cavities of zeolite Y via ship-in-a-bottle synthesis by Corma *et al.* in order to give a photosensitizer which would be stable in aqueous solution.[30] Molecular modeling calculations showed that nucleophilic attack at the 2 or 4 position of the pyrylium ring would force the phenyl substituent attached to that carbon to move out of the ring plane. This motion would increase the molecular dimensions of the cation and would therefore be suppressed by the rigid walls of the zeolite supercage. Accordingly, stirred aqueous solutions of

TP^+@Y were found to undergo no spectroscopically observable changes for periods of up to 3000 hours.[31] This stability triggered the use of TP^+@Y as both a synthetic and degradative photocatalyst. TP^+@Y has been used as a sensitizer for the electron transfer induced isomerization of *cis*-stilbene and for the catalytic dihydroxylation of alkenes.[30, 32] The ability of TP^+@Y to generate hydroxyl radicals (•OH) upon irradiation in aqueous media[31] also resulted in its use as a photocatalyst for the degradation of impurities in aqueous systems, particularly pesticides.[10, 33, 34]

In the work presented in this chapter, we have attempted to take advantage of the supramolecular organization provided by the zeolite structure to tune the photocatalytic activity of the semiconductor oxide TiO_2 by combining the oxide with both electron donating and electron accepting sensitizer moieties. The combination of TiO_2 with electron transfer sensitizers may enable the efficient generation of ROS through the use of visible light irradiation. Our group and others have previously studied the preparation of TiO_2 nanoclusters within the cavities of medium- and large-pore zeolites in an effort to control photoactivity via quantum size effects.[35-40] Much of this research has been limited to time-resolved studies and a relatively small number of tests of the photocatalytic decomposition of NO_x and the reduction of CO_2.[37, 38] The potential of methodologies for tunable TiO_2 activity and the development of new catalytic systems, has yet to be fully realized. The preparation and characterization of multi-component systems constitutes a continued effort in this direction. In the last part of this work, the effect of the intrazeolitic media was briefly investigated. This work was carried out as part of a fruitful collaboration with Prof. H. García at the Instituto de Tecnologíca Química at the Universidad Politécnica de Valencia in Valencia, Spain. Selected samples were prepared with the assistance of Dr. M. S. Galletero and her help is gratefully acknowledged.

3.2 Multi-component Photocatalytic Systems Based on TiO_2

3.2.1 Preparation of Titanium Dioxide-Sensitizer Combinations

The ability of electron donating dyes, like $Ru^{2+}(bpy)_3$, to inject electrons into the conduction band of TiO_2 is well known and, as mentioned above, has been explored in the context of solar energy conversion. Preparation of the two-component photocatalytic system $Ru^{2+}(bpy)_3/TiO_2$@Y was accomplished via a step-wise procedure, preparing the encapsulated dye first, followed by incorporation of the semiconductor oxide nanoclusters. $Ru^{2+}(bpy)_3$@Y was prepared according to the procedure described by Lunsford *et al.* using commercial samples of zeolite NaY.[11] As shown in Scheme 3.3, the zeolite was first loaded with $Ru^{3+}(NH_3)_6$ by ion exchange from an aqueous solution of the chloride salt. The ruthenium-exchanged zeolite was dried in air and then reacted with 2,2′-bipyridine. The bipyridine-loaded zeolite was evacuated at room temperature for several hours followed by heating under vacuum. The resulting orange-red solid was then treated with exhaustive solid-liquid extraction.

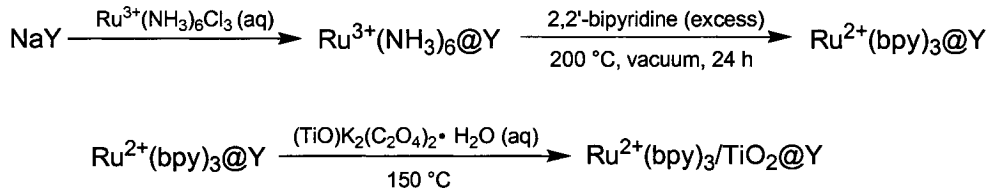

Scheme 3.3 Step-wise preparation of multi-component photocatalyst $Ru^{2+}(bpy)_3/TiO_2$@Y.

The semiconducting oxide nanoclusters were added by stirring a suspension of $Ru^{2+}(bpy)_3$@Y in an aqueous solution of a titanyl oxalate salt (ammonium or potassium) following by mild heating at 150°C; according to procedures reported for single component systems.[35, 39, 40] Encapsulation of the photosensitizer prior to the formation of TiO_2 clusters was preferred since the oxide clusters would be likely to block the pores, reducing the efficiency of sensitizer synthesis. Interestingly, in the course of research conducted concurrently by Bossman *et al.*, a similar complex

was prepared via ion-exchange with explosive $TiCl_3$.[5] This procedure requires a strictly inert atmosphere and the alternative methodology reported here represents a clear advantage with respect to both ease and safety.

The combination of TiO_2 with an electron-accepting moiety is much less documented. As mentioned above, TP^+ is a powerful electron acceptor in its triplet or singlet excited state. The measured redox potentials indicate that either TP^+ excited state should abstract an electron from the valence band of TiO_2 generating a positive hole (h^+).

TP^+/TiO_2@Y is also prepared in a step-wise fashion with formation of semiconductor nanoclusters following the ship-in-a-bottle synthesis of TP^+@Y. The 2,4,6-triphenylpyrylium cation was prepared by condensing acetophenone with two equivalents of 1,3-diphenyl-propenone (chalcone) in acidic zeolite HY, as reported.[30] TP^+@Y can also be prepared in NaY by the thermal condensation of 1,3,5-triphenylpent-2-en-1,5-dione, whose flexible structure is easily accommodated by the zeolite pore aperture. Recall that this dione is the product of TP^+ hydrolysis in aqueous solutions (Scheme 3.2).

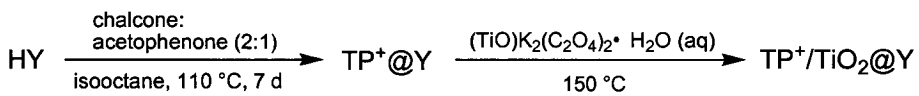

Scheme 3.4 Step-wise preparation of multi-component photocatalyst TP^+/TiO_2@Y.

Incorporation of TiO_2 was accomplished as described above. This procedure yields high loadings of TiO_2 clusters, filling the zeolite pore volume. The zeolite crystallinity is retained up to 75 % when the weight percent content of titanium is *ca.* 1.4% as shown by X-ray diffraction (XRD).[40] Thermogravimetric and spectroscopic studies have revealed that both TP^+ and $Ru^{2+}(bpy)_3$ are stable below 300 °C ensuring that the mild temperatures required for oligomerization are not high enough to result in significant decomposition of the dyes.

3.2.2 Sample Characterization

Spectroscopic characterization of the resulting two-component systems by UV and IR revealed characteristic features of either TP^+ or $Ru^{2+}(bpy)_3$ encapsulated in zeolite Y, accompanied by features corresponding to TiO_2. Selected analytical and spectroscopic data are summarized in Table 3.1.

Sample	Loading	DRS λ_{max} (nm)	IR ν (cm^{-1})
$Ru^{2+}(bpy)_3$@Y	~1 complex/6 supercages	300	1430
		440 (shoulder)	1450
		455	1467
			1610
$Ru^{2+}(bpy)_3/TiO_2$@Y[a]	~1.3 wt % Ti	250	1695
		300	
		440 (shoulder)	
		455	
TP^+@Y	~1 complex/3 supercages	290	1448, 1470
		365	1495, 1579
		410	1595, 1620
TP^+/TiO_2@Y[a]	~1.1 wt % Ti	250	1695
		290	
		365	
		410	

Table 3.1 Spectroscopic and analytical data for prepared samples. Loadings derived from combustion elemental analysis. Diffuse reflectance spectra (DRS) recorded of air equilibrated samples and IR spectra recorded of self-supported wafers after outgassing at 200 °C under 10^{-2} Pa for 1 h. [a]Prepared from 0.2 M aqueous solutions of $(NH_4)_2(Ti{=}O)(C_2O_4)_2{\cdot}H_2O$.

Figure 3.2 shows the IR spectra of TP^{+}@Y and $Ru^{2+}(bpy)_3$@Y before and after TiO_2incorporation. The characteristic bands for each of the dye molecules are seen in the 1800-1300 cm^{-1} region with the addition of a broad band at *ca.* 1700 cm^{-1} following the addition of TiO_2. The presence of TiO_2 clusters is further confirmed by an increase in the 200-250 nm region of the DRS that is not present in the absence of TiO_2 (Figure 3.3). The DRS of TiO_2 alone encapsulated in zeolite Y is shown in Figure 3.4. As reported, the absorption maxima is *ca.* 210 nm with the band tailing out to 300 nm.[40] Notably, the absorption maxima for TiO_2@Y represents a significant hypsochromic shift as compared to bulk TiO_2 in its anatase form (λ_{max} ~ 350 nm) corresponding to an increase in the band gap from 3.2 eV for anatase to *ca.* 4.7 eV for the encapsulated nanoclusters.[40] It was reported by Bossman *et al.* that an increased absorption in the 350-800 nm region of the spectrum was indicative of an interaction between $Ru^{2+}(bpy)_3$ and TiO_2 inside the zeolite cavity.[5] However, our samples do not exhibit significant absorption in the long wavelength region of the spectrum as seen in Figure 3.3.

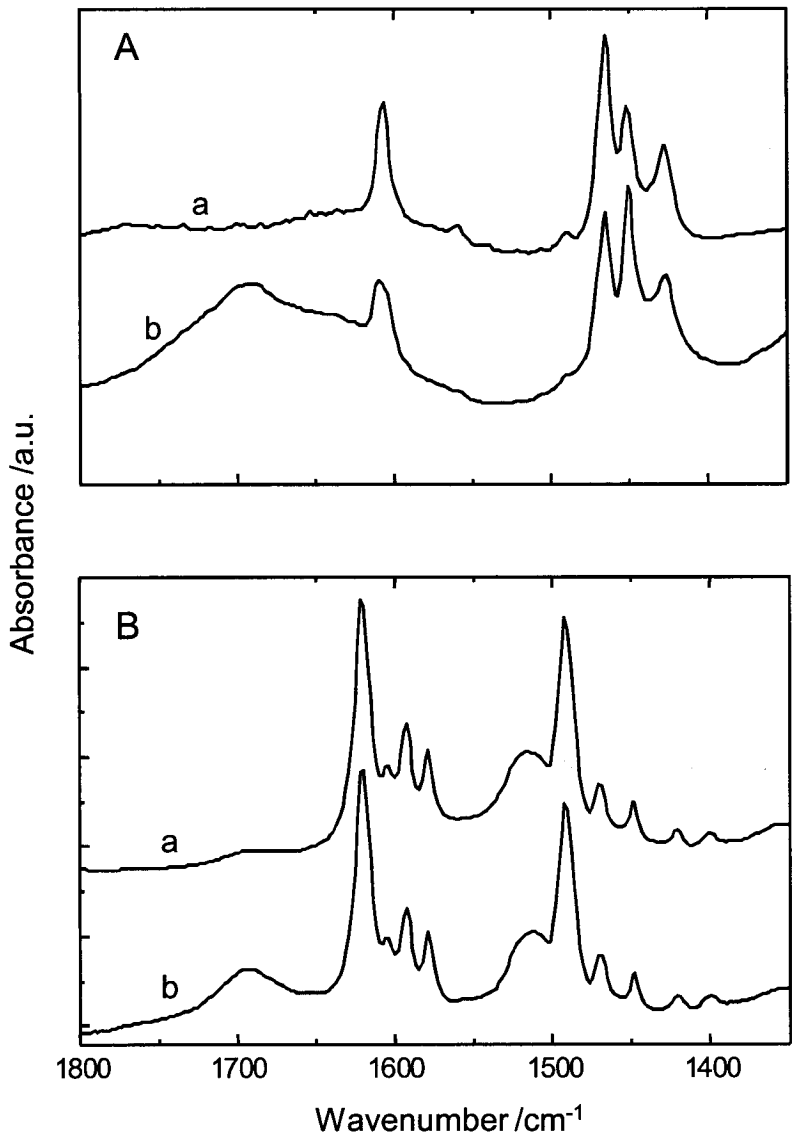

Figure 3.2 Aromatic region of the FT-IR spectra recorded of (A) $Ru^{2+}(bpy)_3$ and (B) TP^+ encapsulated in zeolite Y following outgassing at 200 °C under reduced pressure for 1 h before (a) and after (b) inclusion of TiO_2.

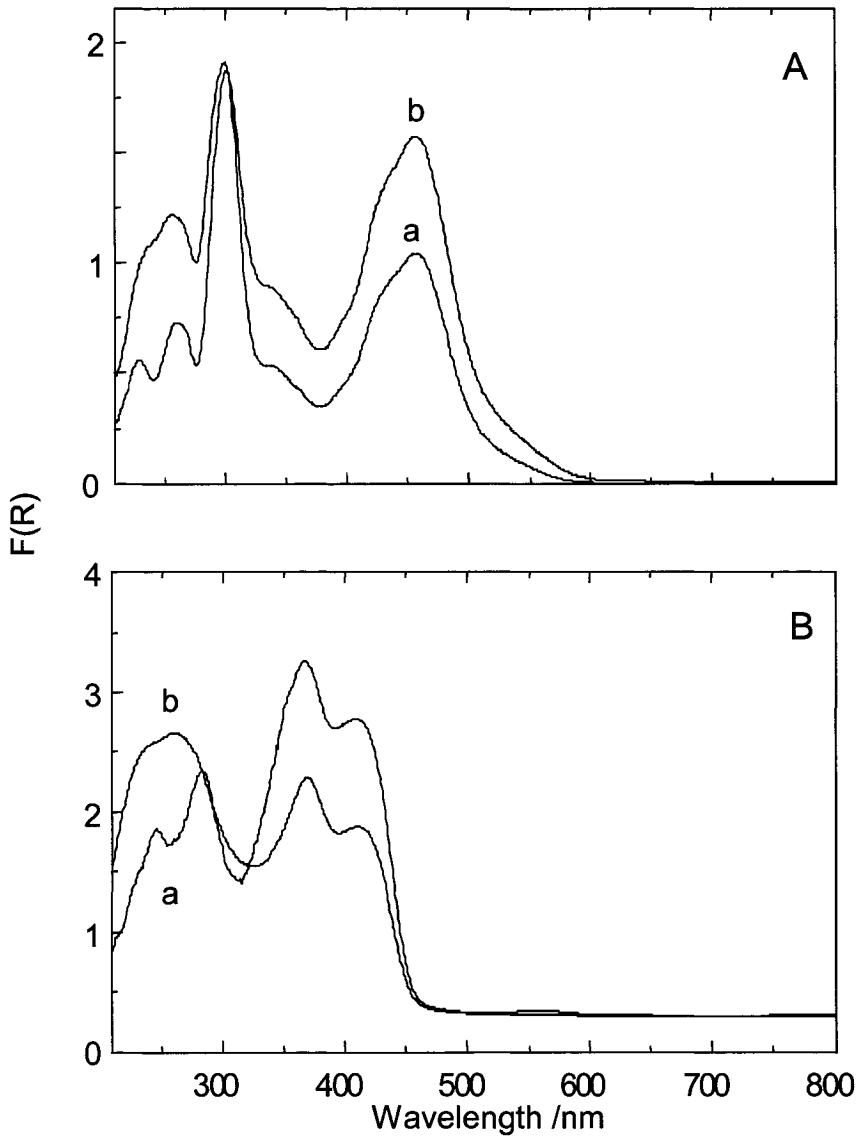

Figure 3.3 Diffuse reflectance spectra (plotted as the Kubelka-Munk function of the reflectance) of (A) $Ru^{2+}(bpy)_3$@Y and (B) TP^{+}@Y before (a) and after (b) incorporation of TiO_2.

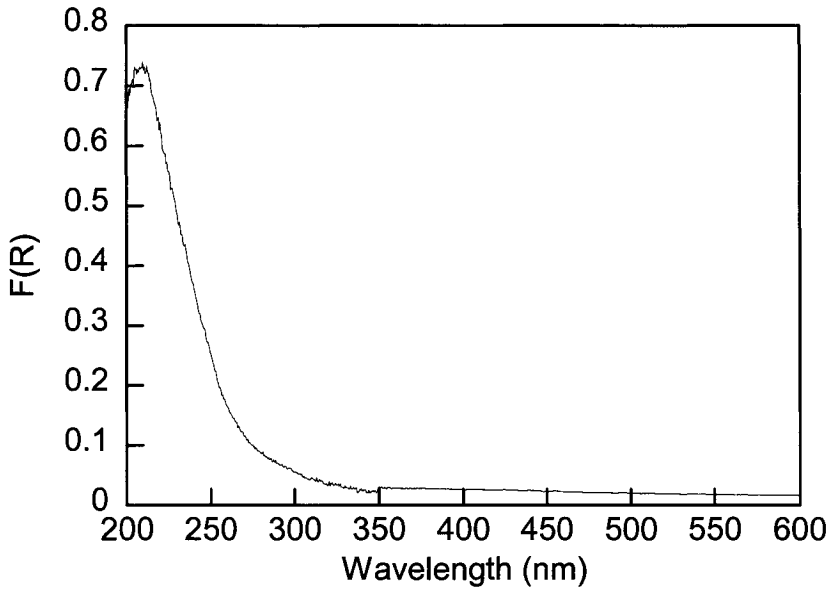

Figure 3.4 DRS of TiO_2@Y prepared according to the procedure described above. Ti content ca. 0.9% by combustion elemental analysis.

Both TP^+ and $Ru^{2+}(bpy)_3$ photosensitizers embedded within zeolite Y exhibit characteristic emission following excitation at the corresponding absorption maxima.[41, 42] In the case of $Ru^{2+}(bpy)_3$ encapsulated in zeolite Y, previous literature reports indicated that the intensity and emission lifetime are significantly influenced by the presence of quenchers. Several examples were given above, in particular the quenching of the $Ru^{2+}(bpy)_3$ excited state by methyl viologen cation has received considerable attention.

In this study, comparison of the steady-state emission of the single component $Ru^{2+}(bpy)_3$@Y sample with that of the same solid also containing TiO_2 revealed a *ca.* 25% decrease in the total emission intensity as calculated by the area of the average photoluminescence spectrum (Figure 3.5). As seen in Figure 3.6, the recorded emission spectrum of TP^+@Y is a superposition of the fluorescence (λ_{max} = 470 nm) and a small contribution from the phosphorescence (λ_{max} = 560 nm). Phosphorescence emission from the un-encapsulated cation, with a band centered at 560 nm, was previously observed in ethanol glasses at 77 K.[43]

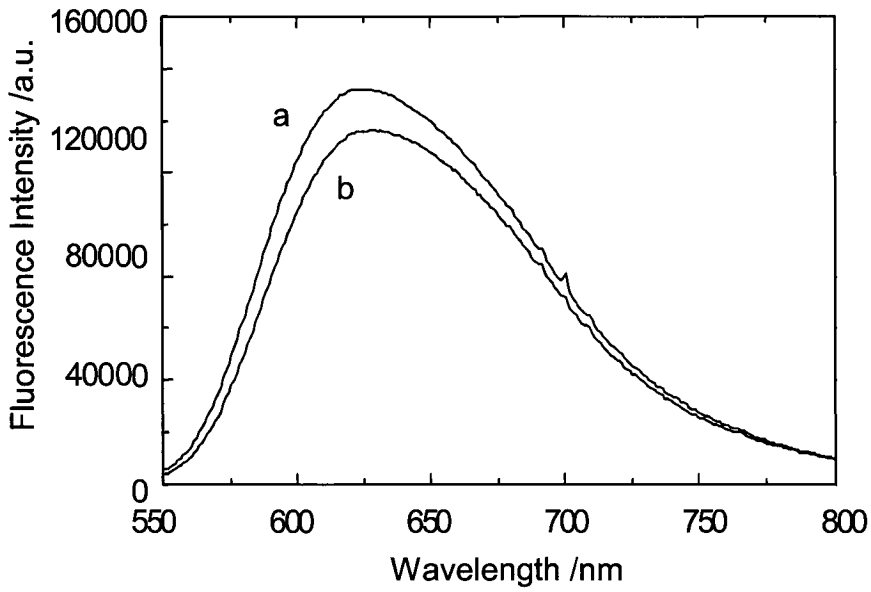

Figure 3.5 Emission spectrum of $Ru^{2+}(bpy)_3$@Y (a) and $Ru^{2+}(bpy)_3/TiO_2$@Y (b) following excitation at 466 nm. The area of the photoluminescence spectra determined as an average of 18 independent measurements was (2.3 ± 0.2) x 10^7 and (1.7 ± 0.1) x 10^7 for (a) and (b) respectively.

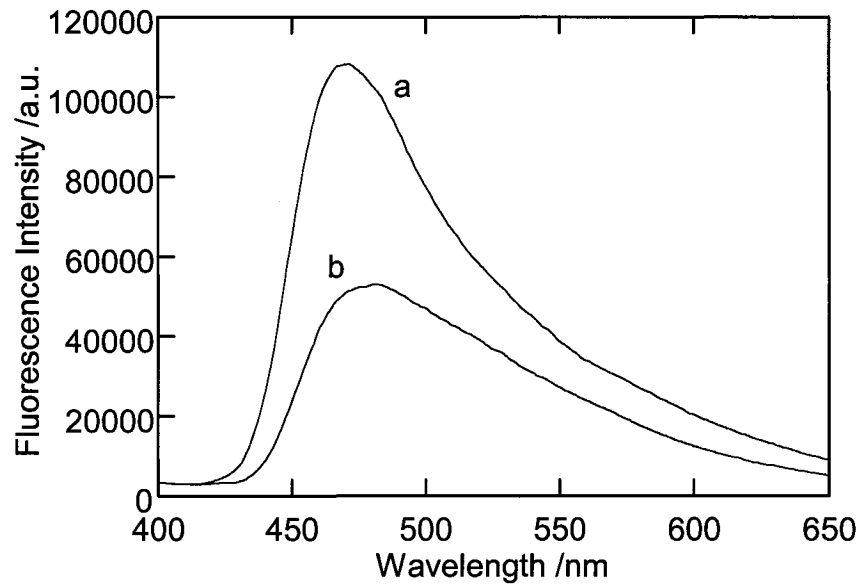

Figure 3.6 Emission spectrum of TP^+@Y (a) and TP^+/TiO_2@Y (b) following excitation at 420 nm. The area of the photoluminescence spectra determined as an average of 20 independent measurements was (1.0 ± 0.1) x 10^7 and (0.6 ± 0.1) x 10^7 for (a) and (b) respectively.

Simultaneous observation of emission from both the singlet and the triplet states is a consequence of the tight fit of the bulky cation within the zeolite cavity.[42] Considering the total area of the TP^+@Y photoluminescence spectrum, an overall intensity decrease of *ca.* 40% was observed in the presence of TiO_2. This number reflects both singlet and triplet quenching, as a result of the overlapping fluorescence and phosphorescence spectra, although it appears that the reduction in emission intensity is more pronounced in the spectral region corresponding to the singlet.

The spectroscopic data presented above indicate successful formation of both single- and multi-component materials incorporating photosensitizing dyes, TP^+ and $Ru^{2+}(bpy)_3$, and semiconductor oxide TiO_2. Steady-state photoluminescence studies indicate a quenching interaction in the multi-component systems where the emission from the dyes is reduced in the presence of TiO_2. The nature of this interaction was further investigated by employing time-resolved techniques.

3.2.3 Time-Resolved Studies

The nature of the interaction causing the overall decrease in emission yield was probed by time-resolved luminescence. The question of whether the quenching interaction is static or dynamic in nature was answered by examining the early events following pulsed laser excitation of the sample. The occurrence of dynamic quenching, i.e. an interaction occurring during the lifetime of the excited state, is reflected in the emission decay kinetics as well as in the overall emission intensity. In the systems under investigation, each component is essentially stationary. The photosensitizing dyes were prepared in-cage by ship-in-a-bottle synthesis and are permanently entrapped, being too large to escape the cavity through the *ca.* 7 Å windows. The TiO_2 nanoclusters prepared by oligomerization are also not mobile within the zeolite. If each component in the system is immobile within the lifetime of the excited state, the emission quenching should be predominantly static.

In the case of samples incorporating the electron accepting TP^+ dye, emission quenching was investigated using the picosecond time-resolved fluorescence setup described in Section 2.3.2. The use of a picosecond laser as the excitation source is required due to the relatively short fluorescence lifetime of the cation in zeolites. Samples of TP^+@Y and TP^+/TiO_2@Y were purged with nitrogen and the emission intensity was monitored following 355 nm excitation. The fluorescence decays are best fitted by a tri-exponential expression and a representative graph plotted versus the log of normalized intensity is shown in Figure 3.7. Although fitted with a tri-exponential expression, the data deviate only slightly (< 4%) from bi-exponential behaviour. The kinetic decay parameters for the data shown in Figure 3.7 are given in Table 3.2 below.

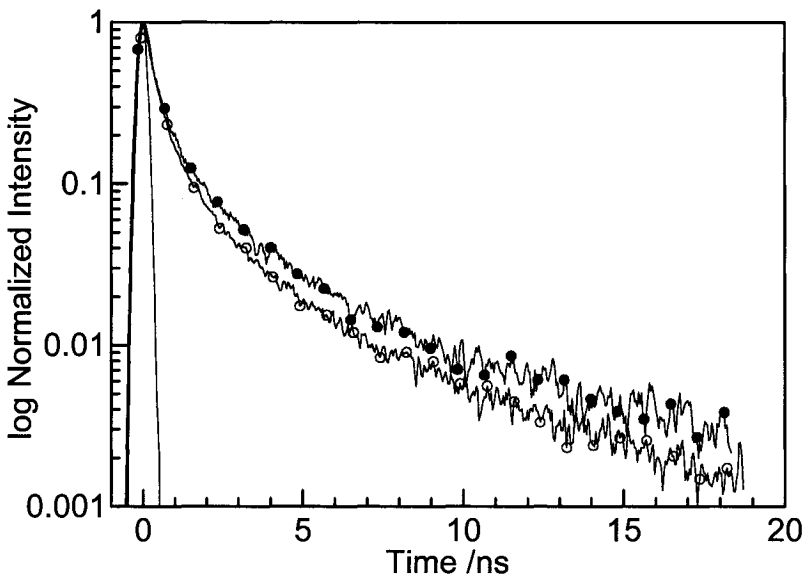

Figure 3.7 Fluorescence decay of TP^+@Y (●) and TP^+/TiO_2@Y (○) following pulsed irradiation at 355 nm under a N_2 atmosphere. Sample characteristics are given in Table 3.1. Instrument response (—).

Sample	k_1	A_1	k_2	A_2	k_3	A_3	k_{av}
TP^+@Y	3.00 ns^{-1}	0.74	0.70 ns^{-1}	0.23	0.16 ns^{-1}	0.04	2.39 ns^{-1}
TP^+/TiO_2@Y	3.26 ns^{-1}	0.92	0.70 ns^{-1}	0.21	0.16 ns^{-1}	0.03	3.15 ns^{-1}
$Ru^{2+}(bpy)_3$@Y	2.73 μs^{-1}	0.42	1.14 μs^{-1}	0.56			1.79 μs^{-1}
$Ru^{2+}(bpy)_3/TiO_2$@Y	2.31 μs^{-1}	0.47	1.05 μs^{-1}	0.56			1.67 μs^{-1}

Table 3.2 Fluorescence decay parameters determined for selected samples studied. k_x is the rate constant and A_x the pre-exponential factor.

As seen in Table 3.2, there is a marginal variation in the measured rate constants for the samples that were loaded with TiO_2. This difference is primarily observed for the fast decay component. This component represents lifetimes of 0.33 ns for TP^+@Y and 0.31 ns for TP^+/TiO_2@Y, which are close to the 100 ps resolution of the system. Significant changes in the decay rate constants were not observed for samples containing higher loadings of TiO_2. Small changes in the observed kinetics may reflect the heterogeneity of the system in terms of imperfect degassing and subtle sample differences resulting from their preparation via one-step or two-step procedures. For example, samples prepared with higher loadings of TiO_2, achieved by consecutive aqueous loadings of the oxalate salt, may contain slightly larger amounts of trapped water. In any case, it seems that the reduced steady-state emission intensity is due to a decrease in the number of dye molecules undergoing radiative decay. Since the excited state and the quencher are essentially immobile (except for small in-cage motions), the dye molecules that are at an appropriate distance from the quencher when the excited state is formed, will be "instantaneously" deactivated. The resulting effect is a reduction in emission intensity with no effect on the emission lifetime. Although quenching of TP^+ by TiO_2 that occurs within 100 ps or less cannot be resolved with the technique used, a dynamic quenching model cannot be logically applied to this system. The reduced emission observed in these cases can be reasonably ascribed to static quenching.

In the case of samples containing $Ru^{2+}(bpy)_3$, the emission lifetime is sufficiently long (up to *ca.* 1 μs) for time-resolved fluorescence techniques employing nanosecond pulsed laser excitation. Samples of $Ru^{2+}(bpy)_3$@Y and $Ru^{2+}(bpy)_3/TiO_2$@Y were purged with nitrogen and the emission decay following excitation at 355 nm was recorded. A representative plot (Figure 3.8) shows the fitted bi-exponential decays for both samples. No change in the emission lifetime was observed when comparing samples before and after TiO_2 incorporation. Figure 3.8, along with the kinetic parameters given in Table 3.2, clearly indicate the absence of any significant dynamic quenching in these systems.

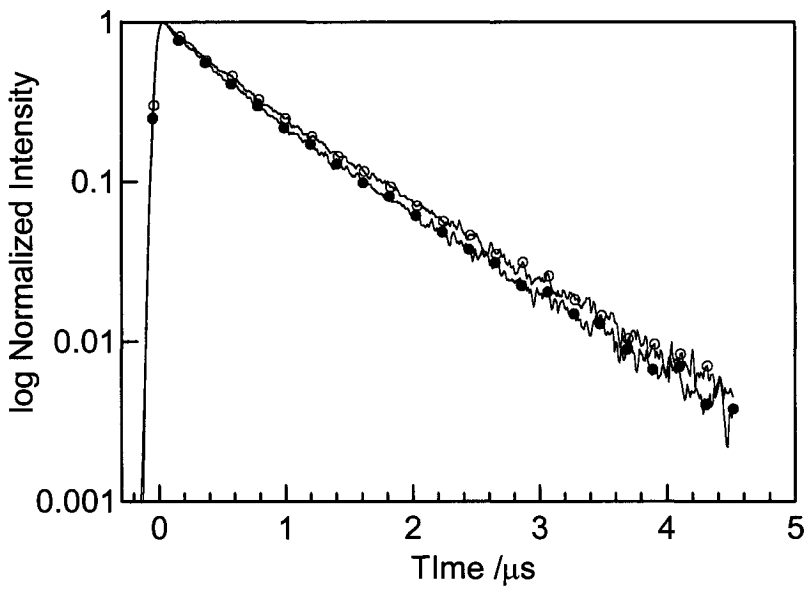

Figure 3.8 Fluorescence decay of $Ru^{2+}(bpy)_3$@Y (●) and $Ru^{2+}(bpy)_3/TiO_2$@Y (○) following pulsed irradiation at 355 nm under a N_2 atmosphere. Sample characteristics are given in Table 3.1.

Previous photoluminescence quenching studies of excited $Ru^{2+}(bpy)_3$, by zeolite-encapsulated methylviologen cations, established the occurrence of both static and dynamic processes. The different quenching processes depended on the extra- or intrazeolitic location of $Ru^{2+}(bpy)_3$.[25, 41] The dynamic component in these systems is due to the ability of the relatively small methylviologen molecules to diffuse throughout the zeolite structure and interact with the, reasonably long-

lived, $Ru^{2+}(bpy)_3$ excited-state. The data presented above indicate the absence of any significant dynamic component for the quenching of TP^+ and $Ru^{2+}(bpy)_3$ by TiO_2 within zeolites. This is consistent with the expected limited diffusion of the dye and the TiO_2 clusters within the zeolite micropores. In light of the data presented above, we concluded that excited-state deactivation proceeds predominantly through static quenching. 'Instantaneous' or static quenching of the excited state occurs within the instrument response time, resulting in the observation of non-emissive relaxation of the excited state.

Static $Ru^{2+}(bpy)_3$* quenching seems appropriate in view of the well-known, fast interfacial electron injection observed for related $Ru^{2+}(bpy)_3$ complexes bound to the surface of TiO_2 particles. However, the interaction between TiO_2 and an electron-accepting moiety, such as TP^+, is unprecedented. Such an interaction should occur by a mechanism that is similar but opposite, to the one observed for TiO_2 and $Ru^{2+}(bpy)_3$. Instead of electron injection, the excited-state electron-acceptor would abstract an electron from the valence band in the semiconductor to generate a positive "hole". In order to assign the nature of the interaction between TiO_2 and the dye excited states, diffuse-reflectance laser flash photolysis (DR-LFP) studies were carried out. This technique allows excited states and reactive intermediates, that have an absorption in the UV-Vis portion of the spectrum, to be detected. If the quenching interaction occurs via electron transfer, as suspected, then the $Ru^{3+}(bpy)_3$ and 2,4,6-triphenylpyranyl radical ($TP^{\bullet}$) products should be observed by DR-LFP (Scheme 3.5).

$$Ru^{2+}(bpy)_3 + TiO_2 \xrightarrow{h\nu} Ru^{3+}(bpy)_3 + TiO_2/e^-_{CB}$$

$$TP^+ + TiO_2 \xrightarrow{h\nu} TP^{\bullet} + TiO_2/h^+_{VB}$$

Scheme 3.5 The products of photoinduced electron transfer between TiO_2 and the two dyes.

Previous work from our group has demonstrated that laser flash photolysis of TP^+ encapsulated in zeolite Y generates the TP^+ triplet excited state (in the

absence of quencher). The TP^+ triplet appears as a band at *ca.* 450 nm which decays with a lifetime on the order of microseconds.[42] This behaviour was also observed for the TP^+@Y samples prepared in this work. DR-LFP of nitrogen purged samples of TP^+@Y following excitation at 308 or 355 nm showed a moderately intense peak at *ca.* 450 nm that decayed with the expected kinetics (Figure 3.9). However, the transient spectrum recorded following co-inclusion of TiO_2 was distinctly different. The triplet absorption at 450 nm was significantly quenched and this was accompanied by the appearance of a band at *ca.* 570 nm. This absorption was assigned to the 2,4,6-triphenylpyranyl radical ($TP^•$).[43, 44] In Figure 3.10, the pyranyl radical spectrum is overlaid with the spectrum of the TP^+ triplet acquired under the same instrumental conditions.

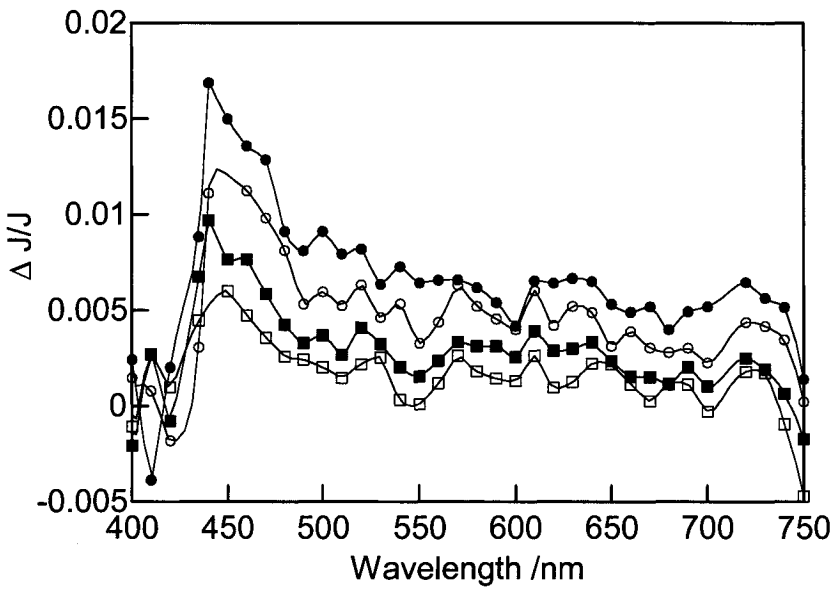

Figure 3.9 Transient DRS recorded (●) 3.2 μs, (○) 18.4 μs, (■) 59.2 μs, and (□) 140 μs after 355 nm laser excitation of N_2 purged TP^+@Y.

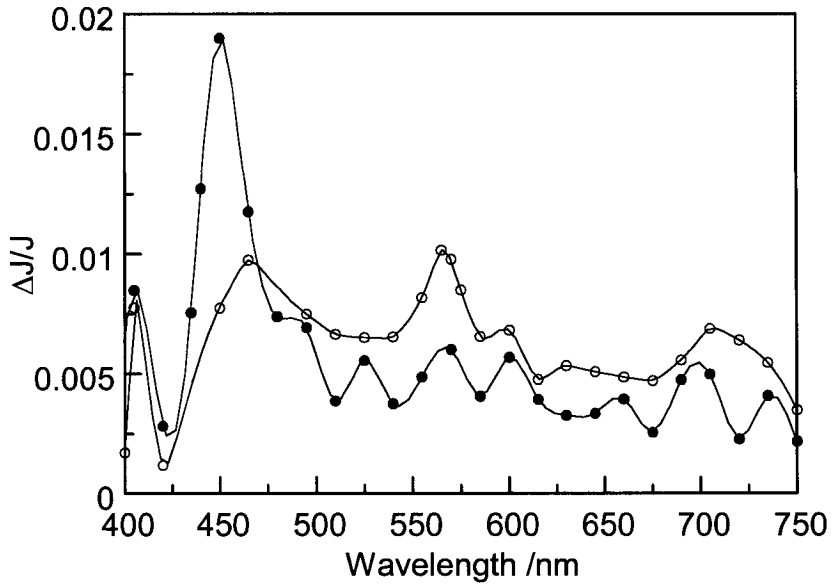

Figure 3.10 Transient DRS of TP^+@Y (●) and TP^+/TiO_2@Y (○) recorded ~6 μs after 355 nm laser excitation. The TP^+ triplet can be seen at ca. 450 nm and the $TP^\bullet$ radical at 570 nm.

Notably, the residual triplet excited-state lifetime remains unchanged in the presence of co-encapsulated TiO_2. Monitoring the decay of the triplet at 450 nm in the presence and absence of TiO_2 revealed only a decrease in the maximum absorption at that wavelength and no change in the time profile. Fitting both decays with a single exponential gives $k_T = 1.0 \times 10^6\ s^{-1}$ for the triplet in the absence of TiO_2 and $k_T = 9.3 \times 10^5\ s^{-1}$ after TiO_2 incorporation. The single exponential fitting of these data is to give a basis for comparison only and is not meant to assign the process as truly first order. Figure 3.11 shows the time profile of the absorption at 450 nm and at 570 nm (inset) illustrating the lack of significant change. The observed $TP^\bullet$ radical is excellent evidence for the photoinduced electron transfer from TiO_2 to the excited state of TP^+. Similar decay kinetics at 450 nm, before and after TiO_2 inclusion, indicate that the triplet quenching mechanism is static rather than dynamic. A static interaction mechanism for $TP^\bullet$ radical formation is also supported by the fact that no growth is observed in the signal at 570 nm within the recorded time scale (Figure 3.11 inset).

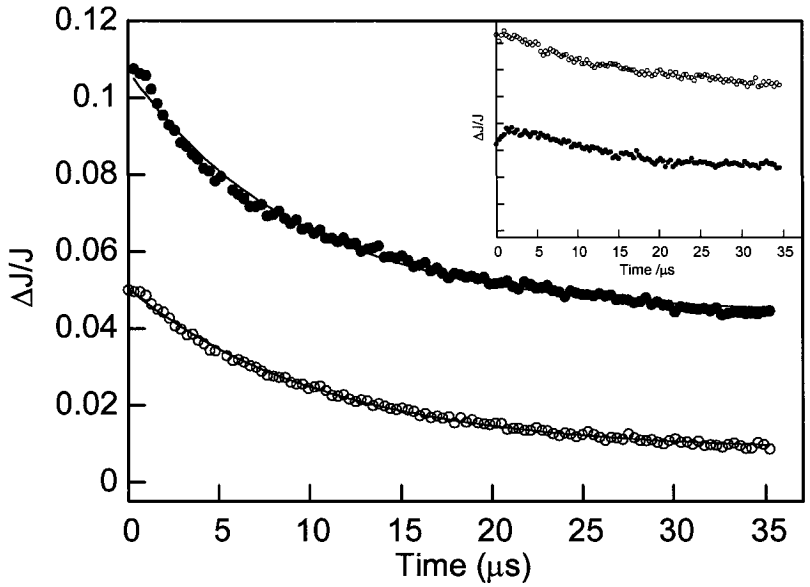

Figure 3.11 Transient decay traces for TP^+@Y (●) and TP^+/TiO_2@Y (O) recorded at 450 nm following 355 nm laser excitation. Inset: decay traces for the same samples recorded at 570 nm.

Assignment of TiO_2 as the electron donor is based on the presence of TiO_2 nanoclusters in TP^+/TiO_2@Y, where electron transfer is observed, and not in TP^+@Y. This behaviour is exactly the reverse of the well-established electron injection observed for the $Ru^{2+}(bpy)_3/TiO_2$ couple. Electrochemical measurements on zeolite-modified electrodes gave a reduction potential of -0.28 V vs SCE in acetonitrile, for TP^+ encapsulated within the interior of zeolite Y.[10, 45] This is in agreement with values measured for other soluble TP^+ salts in solution.[28] Electrochemical measurements for a TiO_2@Y modified zeolite electrode yielded an oxidation potential of 1.2 V vs SCE.[46] Considering the energy of the singlet excited-state, estimated as 272 $kJmol^{-1}$ or *ca.* 2.8 eV, the proposed oxidation is clearly thermodynamically feasible according to the Rehm-Weller equation (Equation 3.1).[47] Note that the Coulombic term is negligible; this is in part because of the absence of electrostatic attraction when the electron transfer occurs between a charged and a neutral species, as mentioned previously.

Equation 3.1 $$\Delta G_{eT} = E_{ox}^{D/D+} - E_{red}^{A-/A} - E_{Coulombic} - \Delta E_{0,0}$$

In contrast to TP^+, the photochemistry and photophysics of $Ru^{2+}(bpy)_3$ in solution and in zeolites have been extensively examined. The DRS shown in Figure 3.3, similar to the absorption spectrum in aqueous solution, has a band at *ca.* 300 nm that was assigned to ligand centered (LC) transitions. The broad band at *ca.* 450 nm is due to metal-to-ligand charge transfer (MLCT) transitions; specifically an electron from a Ru^{2+} *d*-orbital is promoted to a π^* orbital on the ligand. The lowest energy excited state of $Ru^{2+}(bpy)_3$ is generally considered to be a triplet charge transfer state (CT^3), $Ru^{2+}(bpy)_3^*$. This state is characterized by an intense and long-lived emission between 600-650 nm. The transient absorption spectrum of $Ru^{2+}(bpy)_3$ is characterized by a bleaching of the MLCT band at 450 nm and the appearance of a weak band at *ca.* 370 nm. This band is coincident with the absorption band of the radical anion of the free ligand in solution; 2,2'-bipyridine$^{-\bullet}$ λ_{max} = 360 nm.[48] In the presence of an electron acceptor, in this case TiO_2, laser excitation gives rise to the formation of $Ru^{3+}(bpy)_3$ as a long-lived intermediate. The spectrum recorded following 532 nm excitation shows the slightly blue-shifted LC band as well as a band at *ca.* 650 nm. The 650 nm band may be due to the reduced ligand, i.e. the bipyridine radical anion, or the Ru^{3+} LMCT (ligand-to-metal charge transfer) transition. Notably, the MLCT band for the Ru^{2+} species at 450 nm was completely quenched (Figure 3.12).

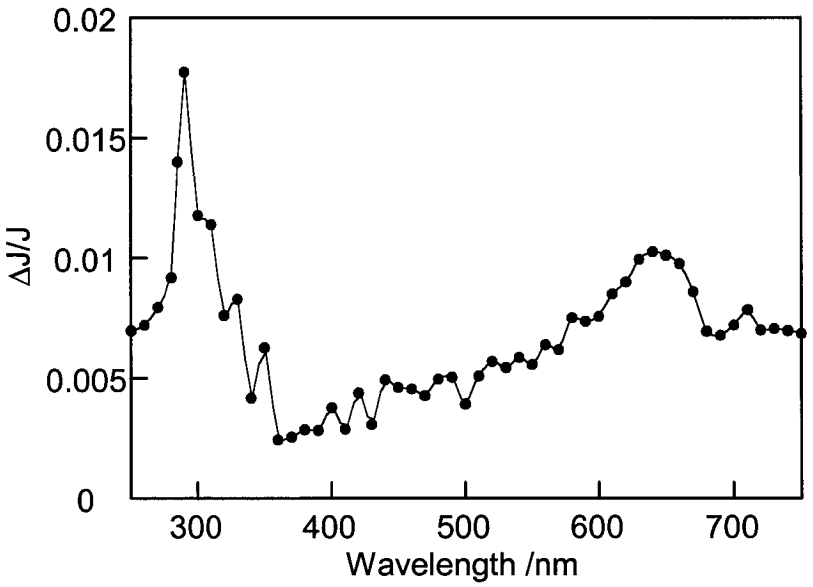

Figure 3.12 Transient DRS recorded 6.4 μs after 532 nm excitation of a nitrogen purged sample of $Ru^{2+}(bpy)_3/TiO_2$@Y.

Elucidation of the early events following the laser pulse was not possible due to interference from the intense and long-lived emission.

3.2.4 Photocatalytic Studies

The photocatalytic activity of TiO_2 has been previously studied with respect to its action on biologically relevant substrates in aqueous solution. These studies, most notably by Serpone *et al.*, have indicated that UVA irradiation of amino acids and nucleotides in the presence of TiO_2 results in the catalyzed degradation of these biomolecules.[49-52] A simple test reaction was required in order to compare the relative photocatalytic efficiencies of the two-component systems with those for the analogous single-component samples relative to commercial TiO_2 anatase. The selected test reaction was the photodeactivation of the enzymatic activity of horseradish peroxidase (HRP). Horseradish peroxidase is one of a large family of peroxidases that catalyzes the decomposition of H_2O_2 to water in the presence of a suitable hydrogen donor. The choice of HRP as a model substrate is a reflection of the cost and commercial availability of this enzyme as well as its relatively simple

spectrophotometric activity assay.[53] The assay is based on the capability of HRP to decompose hydrogen peroxide in the presence of a sacrificial hydrogen donor, such as 2,2'-azino-bis(3-ethylbenzthiazoline-6-sulfonic acid) diammonium salt (ABTS). Peroxide reduction by the enzyme is accompanied by formation of the ABTS radical cation (Scheme 3.6). The radical cation has a distinctive green colour and its formation can be easily monitored spectroscopically (Figure 3.13).

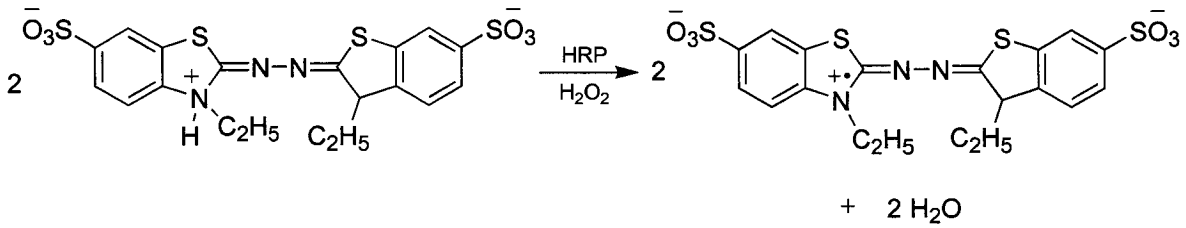

Scheme 3.6 HRP catalyzed decomposition of H_2O_2 concomitant with oxidation of ABTS to its radical cation.

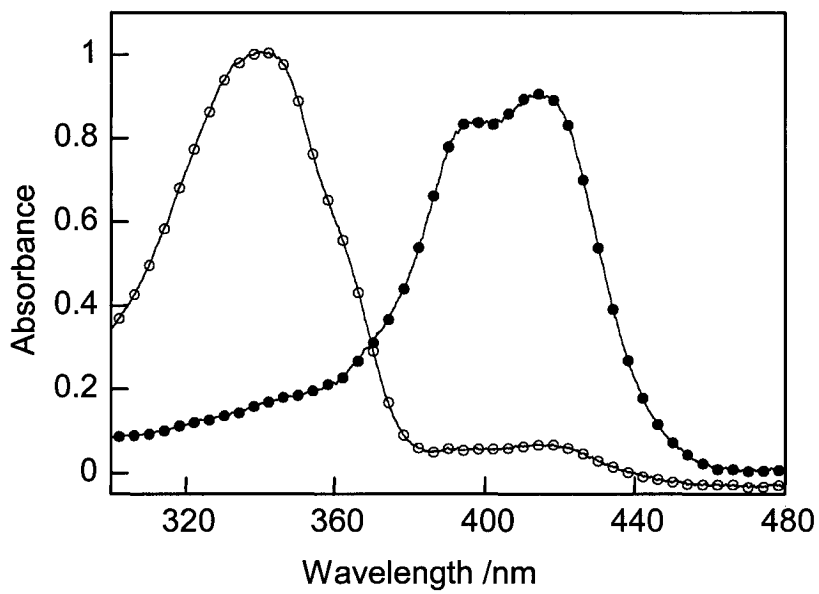

Figure 3.13 Absorption spectra of ABTS (O) and ABTS radical cation (●) in acetate buffer at pH 4.4.

Previous studies in our group have shown that HRP is efficiently deactivated in illuminated suspensions of TiO_2 particles.[54] The deactivation process occurs both under anaerobic and aerobic conditions, but is far more effective in the latter case.

The photocatalytic behaviour of the two-component zeolite systems (TP^+/TiO_2@Y and $Ru^{2+}(bpy)_3/TiO_2$@Y) in aqueous suspensions of HRP was examined. The collected results were compared with the results from the single-component systems (TP^+@Y, $Ru^{2+}(bpy)_3$@Y, and TiO_2@Y) and bulk TiO_2 (anatase). Each suspension was irradiated at ~360 nm in order to avoid light absorption by the protein that would lead to radiation-induced enzyme deactivation. Analysis of the photocatalytic behaviour was accomplished by comparing irradiated samples to un-irradiated samples having the same composition. Following irradiation/incubation, a small aliquot of the solution was added to a buffered solution containing ABTS and H_2O_2. The enzymatic activity was assessed by monitoring the absorbance increase, due to the ABTS radical cation, occurring immediately after mixing. The radical cation is formed as the enzyme catalyzes the reduction of hydrogen peroxide. Representative curves showing the absorbance increase due to the ABTS radical cation (monitored at 412 nm) for irradiated and un-irradiated samples containing TiO_2 anatase, TiO_2@Y, or no photocatalyst are shown in Figure 3.14.

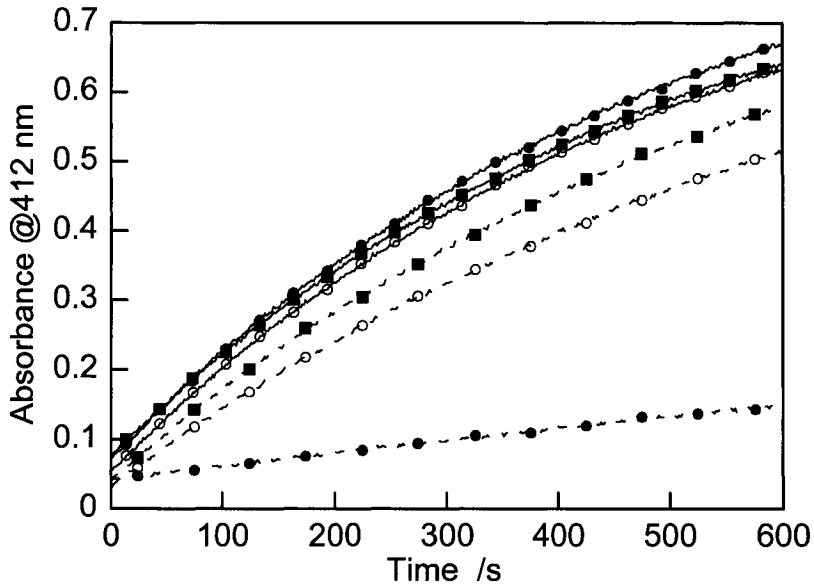

Figure 3.14 Representative curves showing the HRP catalyzed oxidation of ABTS as a function of time for samples containing TiO_2 (●), TiO_2@Y (○), and no catalyst (■). Data fitted with dotted lines were exposed to UVA radiation. Data fitted with solid lines were not irradiated.

In order to visualize the data collected from each assay, the kinetic traces were fitted with a second order polynomial expression;

Equation 3.2
$$A_{412nm} = a + bt + ct^2$$

where A is the absorbance and t is the time. The coefficients a, b, and c are fitting parameters. The derivative of this expression with respect to t is given by:

Equation 3.3
$$\frac{dA_{412nm}}{dt} = b + 2ct$$

which corresponds to b at $t = 0$. Specifically, the first coefficient of the quadratic fit, b, is the calculated initial slope. This slope, often referred to as the initial velocity or v_0, is a commonly used parameter for defining enzymatic activity.

Representative data from two single experiments are shown below in Figures 3.15 and 3.16. The enzyme activity, in the form of the calculated initial

slope, is plotted for each of the samples. From these single experiments, it is obvious that HRP deactivation occurs upon irradiation in samples containing suspended TiO_2 anatase. Encapsulation of TiO_2 in zeolite Y was seen to reduce its efficiency as a photocatalyst. This modulated catalytic activity has been previously observed and is related in part to the reduced UVA absorption of TiO_2@Y due the hypsochromic shift in its absorption maxima, relative to TiO_2 anatase.[40] Multi-component photocatalytic systems provide the opposite effect, where the catalytic ability of the material is increased depending on the electron-accepting and electron-donating character of the co-included moieties.

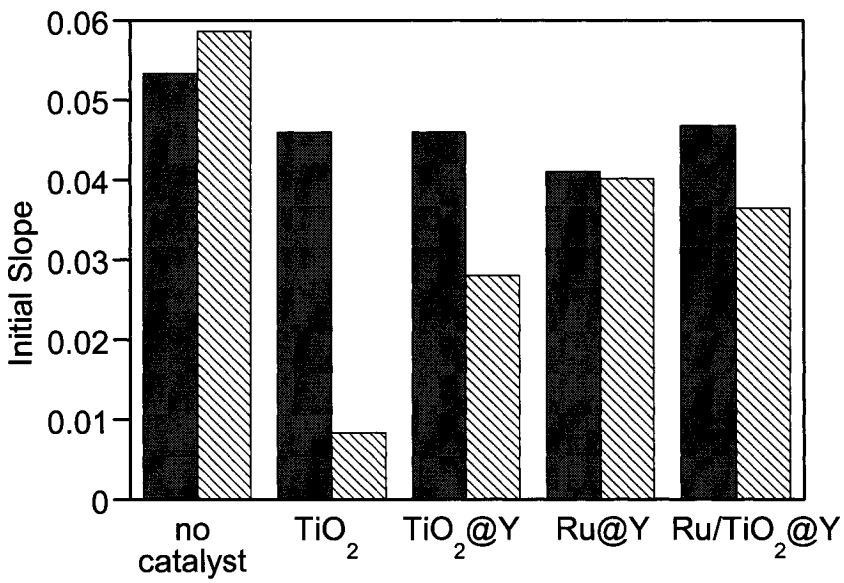

Figure 3.15 Calculated initial slopes for irradiated (striped bars) and un-irradiated (solid bars) samples, where Ru = $Ru^{2+}(bpy)_3$.

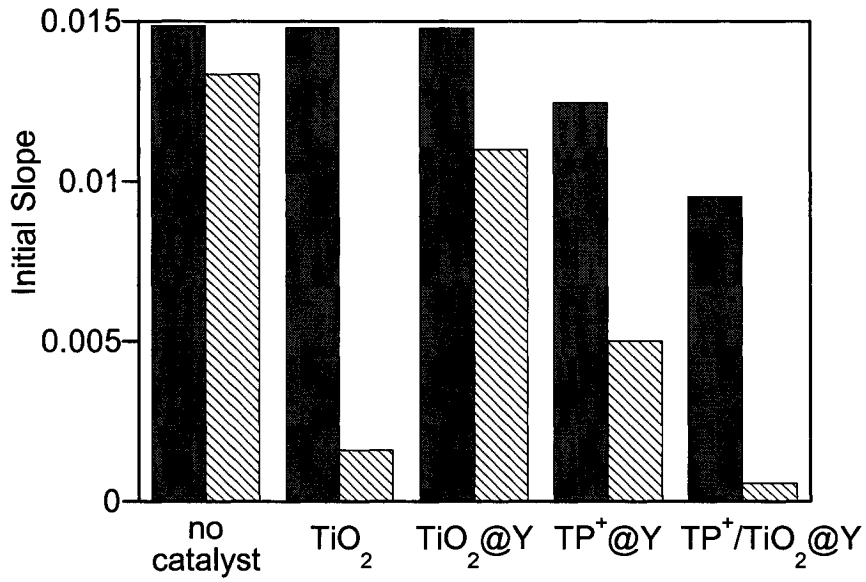

Figure 3.16 Calculated initial slopes for irradiated (striped bars) and un-irradiated (solid bars) samples.

These single trials were each repeated (n = 3, each sample assayed in triplicate) in order to confirm a general trend. The trend in photocatalytic activity is convincingly seen in Figures 3.17 and 3.18 where the enzyme activities for multiple trials are compiled and plotted as the ratio of activity in the irradiated samples as compared to the un-irradiated, control samples.

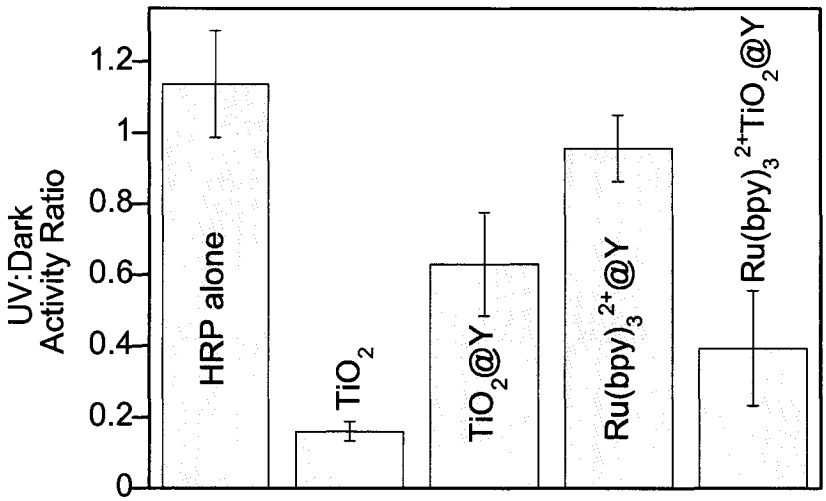

Figure 3.17 Relative enzymatic activities for HRP in the presence of various photocatalysts.

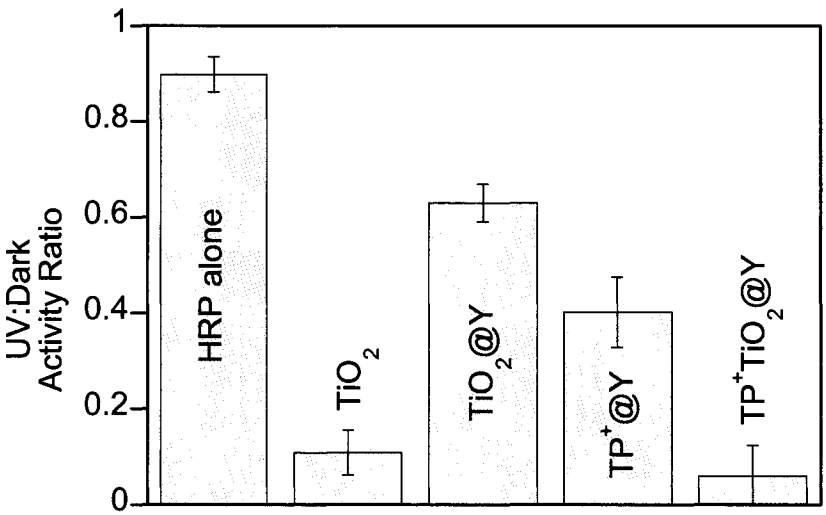

Figure 3.18 Relative enzymatic activities for HRP in the presence of various photocatalysts.

From the combined data it is clear that the zeolite photocatalysts simultaneously incorporating both a photosensitizer and TiO_2 nanoclusters are more active than any of the single component materials. It is also clear that the TP^+-based photocatalysts are more active than those based on the $Ru^{2+}(bpy)_3$ photosensitizer. The reduced activity of the $Ru^{2+}(bpy)_3$ photocatalysts may be explained by considering the possible reactive species that are produced upon

excitation. The interaction between the $Ru^{2+}(bpy)_3$ excited-state and TiO_2 results in the promotion of an electron into the conduction band. The TiO_2/e^-_{CB} species generates a superoxide radical anion via reaction with molecular oxygen, whereas the TiO_2/h^+ species, generated via electron abstraction by TP^+, results in the formation of a hydroxyl radical. This species is likely to be more reactive in the deactivation of HRP.

Remarkably, the photocatalytic activity of the TP^+/TiO_2@Y combination is observed to be equal to or slightly better than TiO_2 anatase itself, under the conditions studied. This result is significant since it implies that TP^+/TiO_2@Y, due to its absorption at wavelengths >400 nm, may be used to achieve efficient photocatalysis with visible light, i.e. under the conditions of solar illumination. The high photocatalytic activity of TP^+/TiO_2@Y can be attributed to the synergistic interaction between the two components as well as the capability of the individual components to generate reactive hydroxyl radicals.

$$e^-_{CB} + O_2 \longrightarrow O_2^{\bullet -}$$

$$H_2O + h^+ \longrightarrow \bullet OH + H^+$$

$$O_2^{\bullet -} + H^+ \longrightarrow HO_2^{\bullet}$$

$$HO_2^{\bullet} + HO_2^{\bullet} \longrightarrow H_2O_2 + O_2$$

$$H_2O_2 + O_2^{\bullet -} \longrightarrow {}^-OH + \bullet OH + O_2$$

$$h^+ + {}^-OH \longrightarrow \bullet OH$$

$$H_2O_2 + e^- \longrightarrow {}^-OH + \bullet OH$$

Scheme 3.7 Possible reactive oxygen species generated in an aqueous aerobic environment.

3.3 Medium Effects in Multi-component Systems

3.3.1 Sample Preparation and Characterization

It was shown in the previous section that TiO_2, encapsulated in zeolite Y in the form of nanoclusters, behaves as an electron relay capable of promoting the effective electron transport necessary for directed electron transfer. The presence of embedded electron relays improves the light-harvesting capability of zeolite-based photocatalysts based on entrapped photosensitizers. In this work, we have examined the through-space electron transfer between species that are irreversibly segregated in separate zeolite cavities. Samples were prepared that incorporated both an electron-donating species and an electron-accepting species within the same particle. The intrazeolite space between the sensitizers was in this case filled by semiconducting nanoparticles of TiO_2, intrazeolite polyethyne, or co-adsorbed water molecules. The samples were prepared analogously to the samples studied in the previous section. The electron-donating sensitizer $Ru^{2+}(bpy)_3$ was included first due to the high temperatures required for its formation. The inclusion of the electron-accepting TP^+ cation was accomplished by the thermal cyclization of zeolite-encapsulated 1,3,5-triphenylpenten-1,5-dione. Based on the calculated sizes of each species, it is reasonable to assume that each occupies its own individual cavity within the zeolite particle. The closest distance between the two dyes therefore corresponds to neighbouring cavities. The space-filling TiO_2 nanoparticles were also prepared in the same fashion as described above, i.e. thermal oligomerization following ion exchange with a titanyl oxalate salt. The preparation sequence is shown below in Scheme 3.8.

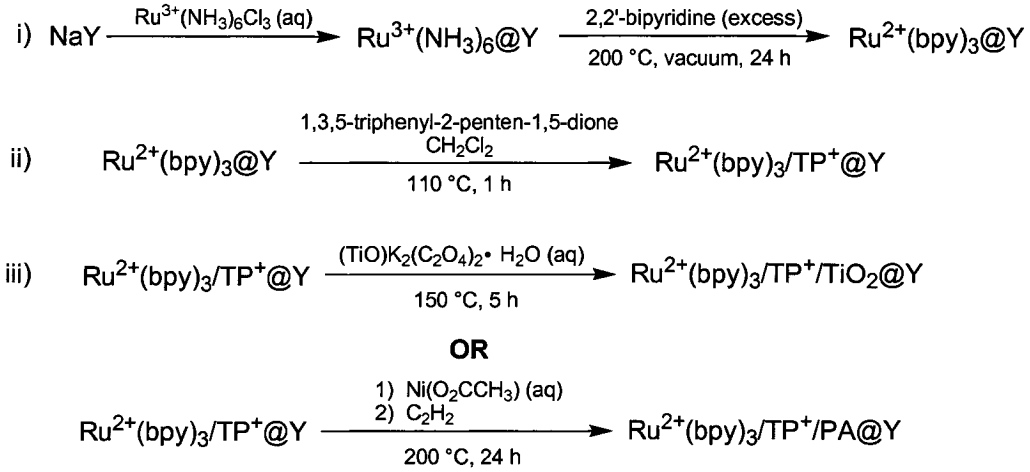

Scheme 3.8 Stepwise preparation of $Ru^{2+}(bpy)_3/TP^+@Y$ containing either TiO_2 nanoparticles or co-included polyacetylene (PA).

Polyethyne (polyacetylene, PA), a structurally simple conducting polymer, was prepared according to reported techniques by nickel-catalyzed polymerization of ethyne.[55, 56] Samples of $Ru^{2+}(bpy)_3@Y$ and $Ru^{2+}(bpy)_3/TP^+@Y$ were prepared first according to the procedures outlined above. Due to the space-filling nature of the intrazeolitic polymer, the polyacetylene was included last, despite the high temperatures required for its preparation as compared to $TP^+@Y$. The dye-loaded zeolites were first submitted to ion exchange with aqueous solutions of nickel acetate. The nickel-exchanged zeolites were dehydrated by heating under reduced pressure, cooled to room temperature, and exposed to ethyne gas at atmospheric pressure for three minutes. The sample was isolated and heated at 200°C for 24 hours. All samples were characterized by combustion analysis and relevant data are given in Table 3.3. Diffuse reflectance and infrared spectra of the two-dye material are shown below. The diffuse reflectance spectrum shows a broad envelope of absorption for the two chromophores whose individual peaks are at ~300 and 460 nm for $Ru^{2+}(bpy)_3$ and 290, 370, and 420 nm for TP^+ (see Figure 3.3). The aromatic region of the IR spectrum more clearly indicates the simultaneous presence of both species. The characteristic bands of each component are indicated in Figure 3.20 (see Figure 3.2 for IR of individually encapsulated species).

Sample	Combustion analysis	DRS λ_{max} (nm)	IR ν (cm^{-1})
$Ru^{2+}(bpy)_3/TP^+/TiO_2@Y^a$	Ti: 0.9		
0.9	N: 2.82	230	
	C: 11.27	285	
	H: 2.35	390 (broad)	TP^+: 1626, 1576, 1491,
$Ru^{2+}(bpy)_3/TP^+/TiO_2@Y^b$	Ti: 1.8	450 (shoulder)	
1.8	N: 2.92	500-800	
	C: 12.27		$Ru^{2+}(bpy)_3$: 1607, 1465, 1450, 1427
	H: 2.45		
$Ru^{2+}(bpy)_3/PA@Y$	N: 0.70		PA: 1583, 1450. 1423, 1340
	C: 14.81	285	
	H: 2.17	350 (shoulder)	
$Ru^{2+}(bpy)_3/TP^+/PA@Y$	N: 0.83	400 (broad)	
	C: 17.12	450-800	
	H: 1.84		

Table 3.3 Analytical data for selected samples. [a] Prepared using a 0.2 M titanyl oxalate solution. [b] Prepared using a 0.4 M titanyl oxalate solution.

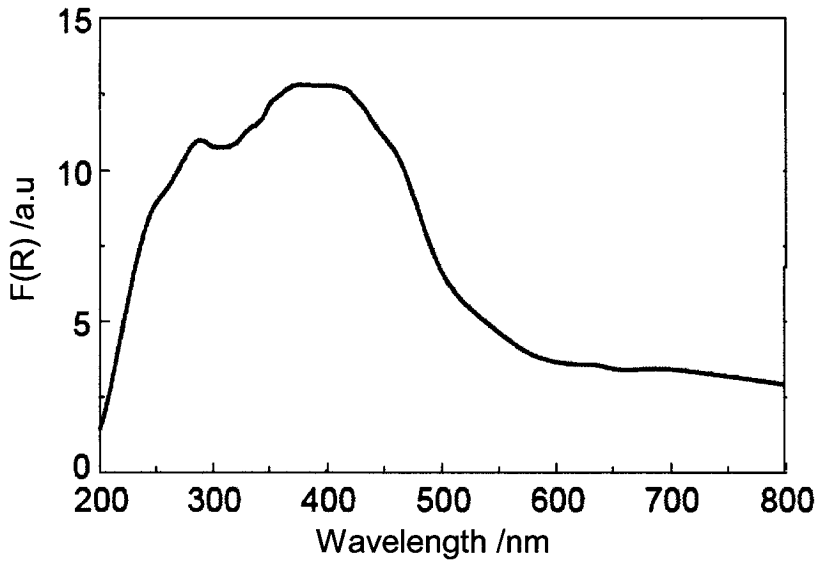

Figure 3.19 Diffuse reflectance spectrum of $Ru^{2+}(bpy)_3/TP^+$@Y showing a broad absorption envelope for the two chromophores.

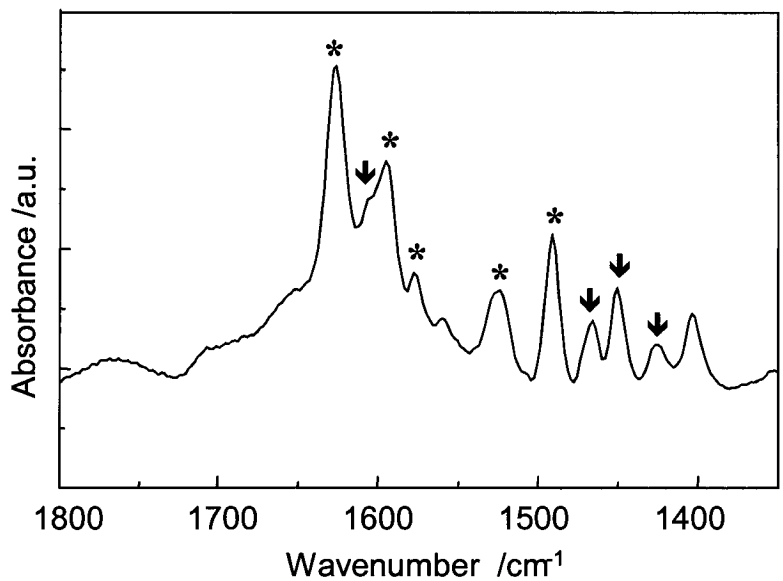

Figure 3.20 Aromatic region of the FT-IR spectrum of $Ru^{2+}(bpy)_3/TP^+$@Y recorded following outgassing at 200 °C for 1 h. The characteristic peaks for $Ru^{2+}(bpy)_3$ (⬇) and TP^+ (*) are labeled.

3.3.2 Photophysical Studies

The effect of the intrazeolite medium on the electron transfer interaction between encapsulated donor and acceptor were examined by DR-LFP and emission spectroscopies. In the previous section, it was shown that electron transfer from $Ru^{2+}(bpy)_3$ results in emission quenching and the formation of the oxidized species, $Ru^{3+}(bpy)_3$. A map of the emission spectra as a function of the excitation wavelength for $Ru^{2+}(bpy)_3/TP^{+}@Y$ shows how the contribution of each species to the total emission spectrum varies depending on excitation wavelength. These data demonstrate that the emission from either component can be preferentially observed by using the appropriate excitation wavelength; for example, excitation above *ca.* 470 nm results in emission from $Ru^{2+}(bpy)_3$* almost exclusively.

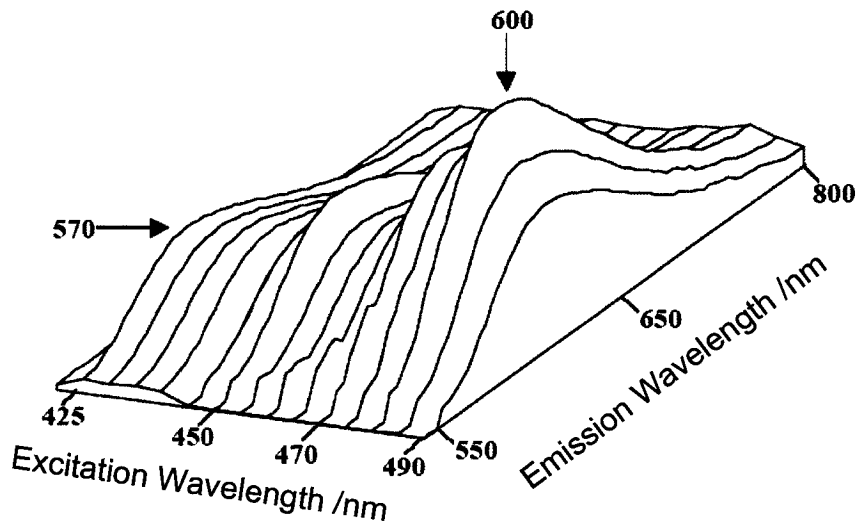

Figure 3.21 Map of the emission spectrum as a function of excitation wavelength for $Ru^{2+}(bpy)_3/TP^{+}@Y$ recorded under N_2.

The DR-LFP spectrum of $Ru^{2+}(bpy)_3/TP^{+}@Y$ following excitation at 532 nm is very complicated due to the number of transients present. The excitation wavelength was chosen in order to have preferential absorption of the laser light by the ruthenium complex. Some of the features present in the spectrum include the bleaching due to the $Ru^{2+}(bpy)_3$ ground state, which partly overlaps with the band

for the TP^+ triplet state in the 450 nm region, and the absorption of the $Ru^{2+}(bpy)_3$* excited state seen at ~380 nm. The sharp LC transition and the broad MLCT transition for the $Ru^{3+}(bpy)_3$ species are also clearly seen at 310 and 650 nm respectively. The relatively weak absorption due to the $TP^{\bullet}$ cannot be resolved.

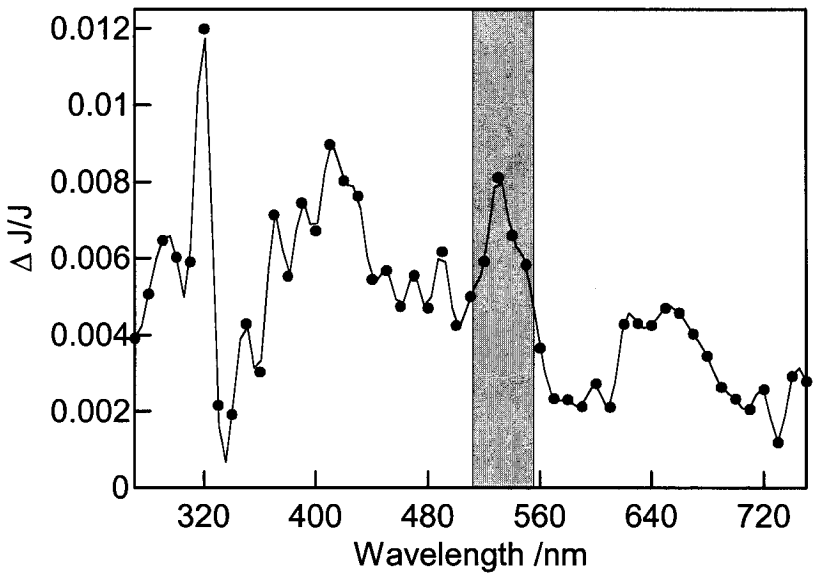

Figure 3.22 DRS spectrum of $Ru^{2+}(bpy)_3/TP^+$@Y recorded 13.2 μs after the 532 nm laser pulse. The shaded area indicates a region where artifacts are present as a result of the 532 nm laser line.

At shorter time-scales, the transient DRS spectrum of this sample is dominated by the residual emission from the $Ru^{2+}(bpy)_3$ excited state (Figure 3.23). As previously stated, the shaded section indicates an artifact from the laser. The emission spectrum of $Ru^{2+}(bpy)_3$@Y (λ_{ex} = 466 nm) recorded before and after incorporation of TP^+ clearly indicates an interaction that quenches the emission at *ca.* 650 nm (curves a and d in Figure 3.24). The transient DRS was recorded again following co-inclusion of TiO_2. At longer times after the laser pulse (*ca.* 3-13 μs), the spectral profile is much the same as for $Ru^{2+}(bpy)_3/TP^+$@Y indicating that electron transfer still occurs. At short time scales, the negative signal in the 650 nm region of the spectrum appears to be slightly more intense, i.e. there is less quenching of the $Ru^{2+}(bpy)_3$ excited state. This suggests that the presence of TiO_2 is interfering with

the electron transfer interaction between $Ru^{2+}(bpy)_3$ and TP^+. To confirm this, the steady-state emission spectra of each sample was recorded and compared.

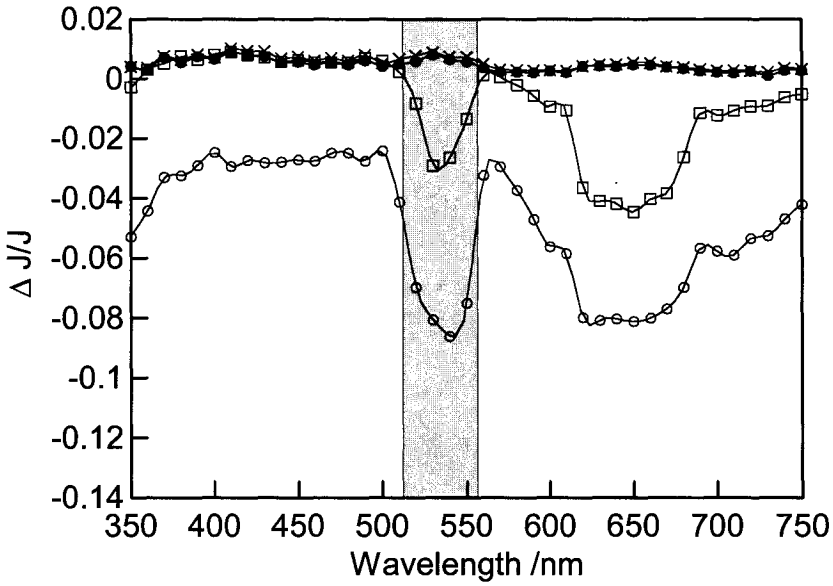

Figure 3.23 Transient DRS spectrum of $Ru^{2+}(bpy)_3/TP^+$@Y (same sample as Figure 3.22) recorded 0.40 μs (○), 0.88 μs (□), 3.44 μs (5), and 13.2 μs (●) after the 532 nm laser pulse.

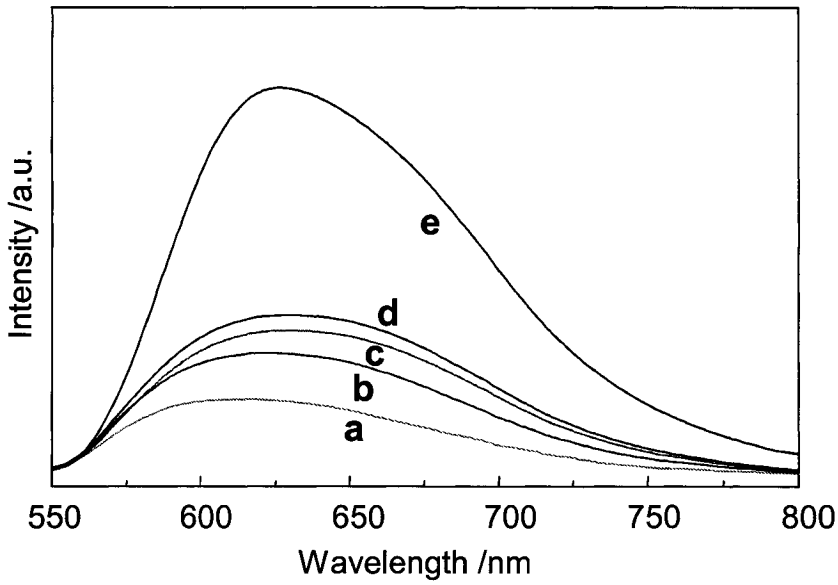

Figure 3.24 Emission spectra recorded of (a) $Ru^{2+}(bpy)_3/TP^+$@Y, (b) $Ru^{2+}(bpy)_3/TP^+/TiO_2$@Y (0.9% Ti w/w), (c) $Ru^{2+}(bpy)_3/TP^+/TiO_2$@Y (1.8% Ti w/w), (d) $Ru^{2+}(bpy)_3/TiO_2$@Y, and (e) $Ru^{2+}(bpy)_3$@Y as an average of 9 independent measurements. λ_{ex} = 466 nm.

As can be seen in Figure 3.24, *ca.* 70% of the emission from $Ru^{2+}(bpy)_3$ is quenched in the presence of intrazeolitic TP^+. The co-inclusion of TiO_2 at two different loading levels causes a partial restoration of the emission that is proportional to the titanium content. This result indicates that the presence of TiO_2 is an impediment to the electron transfer interaction between $Ru^{2+}(bpy)_3$ and TP^+. Curve d in Figure 3.24 represents the extreme case where no interaction with TP^+ is possible because the system contains only $Ru^{2+}(bpy)_3$ and TiO_2. If TiO_2 were acting as an efficient molecular wire, relaying electrons from $Ru^{2+}(bpy)_3$ to TP^+, the emission quenching would be more efficient in the presence of TiO_2. Since the quenching in $Ru^{2+}(bpy)_3/TP^+/TiO_2$@Y is greater than for the system containing only the dye and TiO_2 but less than for the system containing both donor and acceptor with no medium interposed, we can conclude that TiO_2 behaves as a semi-conductor in this case. That is, TiO_2 nanoclusters between $Ru^{2+}(bpy)_3$ and TP^+ act as partial insulators against the electron transfer between the two species.

In the case of samples containing PA interposed in the intrazeolite space between the donor and acceptor, emission spectra were also recorded in order to determine the effect of the polymer media.

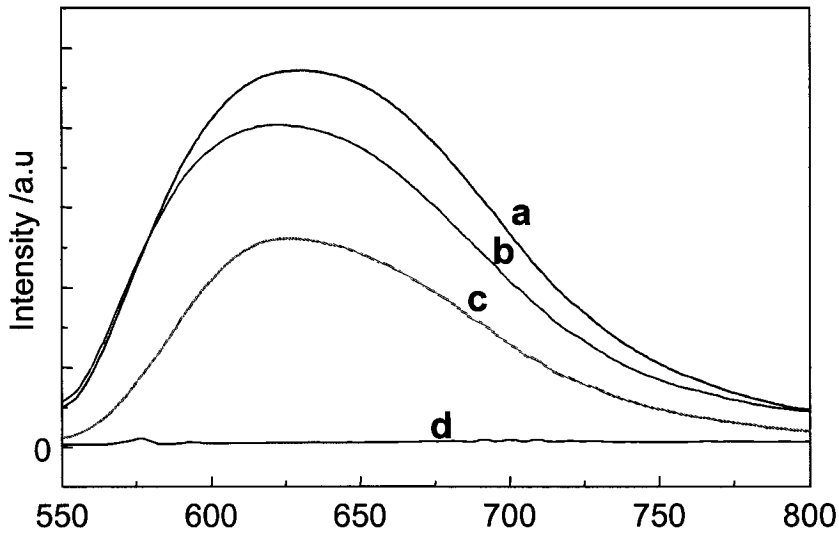

Figure 3.25 Emission spectra recorded of (a) $Ru(bpy)_3^{2+}$/ TP^+/TiO_2@Y (1.8% Ti w/w), (b) $Ru(bpy)_3^{2+}/TP^+/TiO_2$@Y (0.9% Ti w/w), (c) $Ru(bpy)_3^{2+}/TP^+$@Y, and (d) $Ru(bpy)_3^{2+}/TP^+$/PA@Y as an average of 9 independent measurements. λ_{ex} = 466 nm.

Figure 3.25 shows that, in contrast to the samples incorporating TiO_2, the PA-containing sample (curve d) shows complete quenching of the $Ru(bpy)_3^{2+*}$ emission. At first glance, this would seem to indicate that, due to its conductive properties, PA acts as an extremely efficient electron relay material, shuttling electrons from $Ru(bpy)_3^{2+}$ to TP^+ which results in $Ru(bpy)_3^{2+}$ excited-state emission quenching. Unfortunately, the control sample containing only $Ru(bpy)_3^{2+}$ and PA, in the absence of TP^+, also showed complete quenching of $Ru(bpy)_3^{2+}$ emission at *ca.* 650 nm. It was initially believed that PA itself was participating in electron transfer quenching of the $Ru(bpy)_3^{2+}$ excited-state, but this was eventually ruled out. Transient DRS spectra recorded following 532 nm excitation of $Ru(bpy)_3^{2+}/TP^+$/PA@Y shows no absorption band at *ca.* 640 nm, indicating the absence of the electron transfer product, $Ru(bpy)_3^{3+}$. In fact, it was determined that

PA is not at all responsible for the observed emission quenching in the PA-containing sample. Spectroscopic examination of a sample of $Ru(bpy)_3^{2+}$@Y following Ni^{2+} exchange, but prior to addition of acetylene, revealed that the presence of the cation itself is responsible for the observed emission quenching in this system. This is perhaps not unexpected in light of the observed quenching of $Ru(bpy)_3^{2+}$ emission by other paramagnetic metal cations such as Cu^{2+} and Fe^{3+}.[57, 58]

3.4 Conclusions

Multi-component zeolite systems incorporating electron-donating and accepting photosensitizers were prepared and their photophysical and photocatalytic properties studied. When TiO_2 nanoclusters were co-incorporated within the zeolite void space the semiconductor was capable of acting as both an electron donor and acceptor. This behaviour resulted in the generation of reactive oxygen species that deactivated a model biological substrate, HRP, in aqueous suspension. Time-resolved spectroscopic studies demonstrated that the interaction between the two species, manifested as emission quenching, is static and instantaneous on the observed time scale. The intermediates, such as $Ru^{3+}(bpy)_3$ and the $TP^{\bullet}$ radical, observed by DR-LFP confirm that the interaction is an electron transfer to or from TiO_2, depending on the nature of the dye.

Studies of the photocatalytic efficiency of the prepared materials confirmed that the encapsulation of TiO_2 caused a reduction in its catalytic activity with respect to the un-encapsulated material. The single-component zeolite systems were each capable of catalyzing HRP degradation to different extents. Neither system was as active as TiO_2 anatase, while $Ru^{2+}(bpy)_3$@Y was less active than TiO_2@Y. However, TP^+@Y was a more effective catalyst than TiO_2@Y and, when combined with TiO_2 nanoclusters, was a more active catalyst than TiO_2 itself. This is a significant result in light of the relatively simple preparation of TP^+/TiO_2@Y and the long wavelength absorption of the material. Absorption in the visible region of the spectrum suggests that this catalyst may be used under solar irradiation.

$Ru^{2+}(bpy)_3/TP^+$@Y was prepared as a test material to observe intrazeolite electron transfer between two moieties segregated in separate zeolite cavities. The electron transfer interaction was observed as a quenching of the $Ru^{2+}(bpy)_3$ emission in the presence of co-incorporated TP^+. Transient DRS, which were too complicated to interpret completely, did show the presence of the electron transfer

product $Ru^{3+}(bpy)_3$. It was determined that the electron transfer interaction between the two moieties was most efficient in the case where only absorbed water molecules were interposed between them. Filling of the intrazeolite void space with TiO_2 nanoclusters reduced the efficiency of electron transfer indicating that TiO_2 does not shuttle the electrons from $Ru^{2+}(bpy)_3$ to TP^+. $Ru^{2+}(bpy)_3$ emission was, however, quenched more in the case of $Ru^{2+}(bpy)_3/TP^+/TiO_2@Y$ than in the case of $Ru^{2+}(bpy)_3/TiO_2@Y$. This indicates that TiO_2 most likely acts as an electron acceptor, relaying some electrons to TP^+ as a secondary acceptor and the rest to other secondary acceptors such as water or oxygen. The overall result is that TiO_2 behaves as a semi-conductor in this system. The effect of an interposed conducting polymer could not be evaluated due the emission quenching caused by the presence of transition metal cations necessary for its efficient preparation.

3.5 Experimental

3.5.1 Sample Preparation

All chemicals used for sample preparation were obtained form Aldrich in their highest available purity and used as received, unless otherwise indicated.

3.5.1.1 $Ru^{2+}(bpy)_3$@Y

$Ru^{2+}(bpy)_3$@Y was prepared according to the method originally reported by Lunsford *et al.*[11] A sample of NaY was activated at 480°C in an oven overnight. The zeolite was subjected to ion-exchange with an aqueous solution of $[Ru(NH_3)_6]Cl_3$ \(0.1 M) at pH ~ 5 to obtain $Ru^{3+}(NH_3)_6$@Y. Following ion-exchange the sample was washed with deionized water (Millipore MilliQ) and dried at room temperature. Bipyridine (2,2′-dipyridyl) was introduced into the $Ru^{3+}(NH_3)_6$@Y zeolite from an ethanol slurry containing an excess of bipyridine. The bipyridine loaded $Ru(bpy)_3^{2+}$@Y was evacuated at room temperature for several hours and then sealed under vacuum and heated at 200°C for 24 h. The resulting red-orange powder was subjected to exhaustive solid-liquid extraction (Soxhlet) with dichloromethane (DCM) for two weeks.

3.5.1.2 TP^+@Y

Acidic zeolite HY was prepared at ITQ starting from commercial NaY and subjecting it to three consecutive Na^+-to-NH_4^+ ion-exchange cycles followed by steam calcination at 500°C for 2 h. TP^+@Y was prepared in two ways. Firstly, according to the reported procedure, TP^+@Y was prepared by heating an isooctane slurry of 2:1 acetophenone (410 mg, 1.9 mmol) and 1,3-diphenylpropenone (Fluka, recrystallized) (120 mg, 1.0 mmol) containing *ca.* 1.0 g of zeolite HY at 110 °C for one week. The canary yellow solid was subsequently subjected to solid-liquid extraction with DCM. Alternatively, TP^+@Y was prepared by refluxing a slurry containing 1,3,5-triphenyl-2-penten-1,5-dione (prepared by isolation from the aqueous photolysis of 2,4,6-triphenylpyrylium cation tetrafluoroborate salt) (50 mg,

0.15 mmol) and zeolite NaY (*ca.* 1.0 g) for 2 h. The solid was collected by filtration and baked at 110°C for 2 h resulting in the formation of a bright yellow powder containing the 2,4,6-triphenylpyrylium cation.

3.5.1.3 $Ru^{2+}(bpy)_3/TiO_2$@Y and TP^+/TiO_2@Y

TiO_2 nanoclusters were introduced into the single-dye systems according to a previously reported procedure for the incorporation of semiconductor nanoclusters.[35] $Ru^{2+}(bpy)_3/TiO_2$@Y and TP^+/TiO_2@Y were prepared by stirring 1.0 g of the single-component zeolites in aqueous suspensions containing $K_2(Ti{=}O)(C_2O_4)_2{\cdot}H_2O$ (0.2 M) for 5 h at room temperature in a solid-liquid ratio of 0.1. The solids were collected by filtration, washed thoroughly with deionized water, and baked in an oven at 150°C for 5 h.

3.5.1.4 $Ru^{2+}(bpy)_3/TP^+$@Y

This sample was prepared stepwise. $Ru^{2+}(bpy)_3$Y was first prepared according to the procedure described above. A sample of $Ru^{2+}(bpy)_3$@Y was dehydrated at 110°C for 4 h and then added to a DCM solution of 1,3,5-triphenyl-2-penen-1,5,-dione (52 mg, 0.16 mmol). This suspension was refluxed with stirring for 2 h. After this time, the solid was collected by filtration and baked in an oven at 100°C for 2 h.

3.5.1.5 $Ru^{2+}(bpy)_3/TP^+/TiO_2$@Y

This material was prepared by stirring a sample of $Ru^{2+}(bpy)_3/TP^+$@Y, prepared as described in Section 3.5.3.4, in an aqueous solution of $(NH_4)(Ti{=}O)(C_2O_4)_2{\cdot}H_2O$ at room temperature for 5 h. The solid to liquid ratio in the suspension was 0.1. The concentration of the titanyl oxalate solution was either 0.2 M or 0.4 M, yielding samples with % titanium contents of 0.9 and 1.8 respectively, as determined by combustion elemental analysis.

3.5.1.6 $Ru^{2+}(bpy)_3$/TP^+/PA@Y

This sample was prepared by subjecting $Ru^{2+}(bpy)_3$@Y (prepared as described in Section 3.5.3.1) to ion-exchange in order to replace Na^+ charge-balancing cations with Ni^{2+}. This was accomplished by two consecutive ion-exchange treatments; $Ru^{2+}(bpy)_3$@Y was stirred in an aqueous solution of nickel acetate (0.6 M) for 12 h, filtered and subjected to a second ion-exchange cycle in a more concentrated nickel acetate solution (1.0 M). The Ni^{2+}-exchanged solid was collected by filtration and washed with deionized water. Prior to polymerization, $Ru^{2+}(bpy)_3$@(Ni^{2+})Y was dehydrated at 200°C under 0.1 Torr for 3 h. The sample was cooled to room temperature and, while being "stirred", was exposed to acetylene gas at atmospheric pressure for 3 min. The sample was then sealed and heated in an oil bath at 200°C for 24 h. This sample was prepared with the assistance of Dr. M. S. Galletero.

3.5.2 Steady-state Spectroscopy

Absorption and DR spectra were recorded at room temperature on either a Cary 5G or 1E spectrophotometer from Varian with a Diffuse Reflectance Attachment (DRA), also from Varian. Spectralon or $BaSO_4$ were used as reflectance standards. Steady-state emission spectra were recorded at room temperature on either a Perkin-Elmer LS-50 or Edinburgh FL900 spectrofluorimeter. Emission spectra have been reported as an average of multiple measurements made of the same sample in random order and orientation. Spectra were recorded under nitrogen where indicated, liquid samples were typically contained in Suprasil quartz cells from Hellma and solid samples were recorded in cells made in-house from clear fused quartz (Friedrich & Dimmock).

FT-IR spectra were obtained using a Nicolet 710 FT spectrophotometer. Self-supported wafers (*ca.* 10 mg) were compressed at 1 ton cm^{-2} for 3 min and placed in sealed, greaseless cells with CaF_2 windows. The cells were outgassed at 200°C

under 10^{-2} Pa for 1 h before recording the spectra at room temperature. These spectra were recorded at ITQ, Valencia, Spain.

3.5.3 Time-resolved Spectroscopy

Diffuse-reflectance laser flash photolysis experiments were carried out using the system described in detail in Section 2.2 of this thesis. Samples were typically contained in 3 x 7 mm^2 quartz cells and were purged with nitrogen as indicated. Pulsed laser excitation was achieved using the second (532 nm) or third (355 nm) harmonic of a Surelite Nd-YAG laser. The average pulse width was 6 ns with a typical power output of *ca.* 25 mJ $pulse^{-1}$.

Time-resolved emission spectra were recorded using the streak camera system described in detail in Section 2.3 of this thesis. Samples were contained in 3 x 7 mm^2 quartz cells and were purged with nitrogen as indicated. For monitoring emission from samples with short fluorescence lifetimes (e.g. in the case of TP^+), the sample was excited with pulses from a Continuum PY-61 Nd-YAG laser with an average pulse width of 35 ps and a typical power output at 355 nm of *ca.* 5 mJ $pulse^{-1}$. Samples with longer emissive lifetimes were excited with nanosecond pulses from the Surelite Nd-YAG laser described above. All time-resolved data were manipulated and kinetic parameters extracted using the Kaleidagraph program from Synergy software.

3.5.4 Photocatalytic Studies

Titanium dioxide used for comparison was pure anatase with a particle size of *ca.* 32 nm (Alfa Aeser). High purity horseradish peroxidase type VI-A was purchased from Sigma and stored at 4°C. 2,2'-Azino-bis(3-ethylbenzthiazoline-6-sulfonic acid) diammonium salt (ABTS) was also purchased from Sigma in high purity and used as received. Buffers were prepared in house using reagent grade chemicals and distilled, deionized water (Millipore, MilliQ). Buffers and distilled water used for assays and irradiation were also treated with a chelating resin to remove dissolved metal ions.

Irradiations were performed in an irradiation chamber fitted with 6 x 8 W LZC-UVA lamps from Luzchem Research Inc.. The maximum wavelength in the emission profile of these lamps is at 366 nm and each lamp contributes approximately 0.1 mW cm^{-2} at the sample. Each sample contained 0.033 mg mL^{-1} HRP, and 0.033 mg mL^{-1} TiO_2, 0.33 mg mL^{-1} zeolite catalyst, or no catalyst suspended in 3.0 mL of distilled, deionized water. Samples were irradiated in air for 30 to 90 min (depending on the experiment) in Pyrex tubes with 1.0 cm i.d. Each sample was placed on a rotating carousel to ensure even light exposure and was agitated every 5 min during the irradiation to avoid settling of the suspension. In each experiment, dark control samples with the same composition were covered in aluminum foil and placed in the irradiation chamber for the duration of the irradiation. The chamber temperature was maintained at *ca.* 28 °C by a cooling fan.

After irradiation, all samples were centrifuged to remove the suspended catalyst. An aliquot of each sample was diluted in acetate buffer at pH 4.4. For the assay, an aliquot of the diluted enzyme solution was added to a freshly prepared buffered solution containing 250 μM hydrogen peroxide and 25 μM ABTS co-factor. The final enzyme concentration was *ca.* 10 ng mL^{-1}. The absorbance at 412 nm immediately after mixing was then monitored versus time using a Cary 1E spectrophotometer operating in Kinetics mode. Data were plotted using Kaleidagraph software and fitted with a second order polynomial in order to obtain the initial slope.

3.6 References

1. J. Weitkamp, H. G. Karge, H. Pfeifer and W. Holderich *Zeolites and Related Materials: State of the Art 1994;* Elsevier: Amsterdam, 1994.

2. S. Seelan, A. K. Sinha, D. Srinivas and S. Sivasanker, Spectroscopic investigation and catalytic activity of copper(II) phthalocyanine encapsulated in zeolite Y, *J. Mol. Catal. A*, **2000**, *157*, 163-171.

3. UNICEF Water, Environment, and Sanitation: www.unicef.org/wes

4. O. Legrini, E. Oliveros and A. M. Braun, Photochemical processes for water treatment, *Chem. Rev.*, **1993**, *93*, 671-698.

5. S. H. Bossman, C. Turro, C. Schnabel, M. R. Pokhrel, L. M. Payaman Jr, B. Baumeister and M. Wörner, $Ru(bpy)_3^{2+}/TiO_2$-codoped zeolites: Synthesis, characterization, and the role of TiO_2 in electron transfer photocatalysis, *J. Phys. Chem. B*, **2001**, *105*, 5374-5382.

6. M. Abdullah, G. K. C. Low and R. W. Matthews, Effects of common inorganic anions on rates of photocatalytic oxidation of organic-carbon over illuminated titanium dioxide, *J. Phys. Chem.*, **1990**, *94*, 6820-6825.

7. R. W. Matthews, Purification of water with near-UV illuminated suspensions of titanium dioxide, *Water Res.*, **1990**, *24*, 653-660.

8. J. Fan and J. T. Yates, Mechanism of photooxidation of trichloroethylene on TiO_2: Detection of intermediates by infrared spectroscopy, *J. Am. Chem. Soc.*, **1996**, *118*, 4686-4692.

9. T. L. Villarreal, R. Gomez, M. Gonzalez and P. Salvador, A kinetic model for distinguishing between direct and indirect interfacial hole transfer in the heterogeneous photooxidation of dissolved organics on TiO_2 nanoparticle suspensions, *J. Phys. Chem. B*, **2004**, *108*, 20278-20290.

10. A. Sanjuán, G. Aguirre, M. Álvaro and H. García, 2,4,6-Triphenylpyrylium ion encapsulated within Y zeolite as photocatalyst for the degradation of methyl parathion, *Water Res.*, **2000**, *34*, 320-326.

11. W. DeWilde, G. Peeters and J. H. Lunsford, Synthesis and spectroscopic properties of tris(2,2'-bipyridine)ruthenium(II) in zeolite Y, *J. Phys. Chem.*, **1980**, *84*, 2306-2310.

12. C. R. Bock, T. J. Meyer and D. G. Whitten, Electron transfer quenching of the luminescent excited state of tris(2,2'-bipyridine)ruthenium(II). A laser flash photolysis relaxation technique for measuring the rates of very rapid electron transfer reactions, *J. Am. Chem. Soc.*, **1974**, *96*, 4710-4712.

13. H. D. Gafney and A. W. Adamson, Excited state $Ru(bipyr)_3^{2+}$ as an electron-transfer reductant, *J. Am. Chem. Soc.*, **1972**, *94*, 8238-8239.

14. K. Kalyanasundaram, Photophysics, photochemistry and solar energy conversion with tris(bipyridyl)ruthenium(II) and its analogues, *Coord. Chem. Rev.*, **1982**, *46*, 159-244.

15. P. K. Dutta and J. A. Incavo, Photoelectron transfer from tris(2,2'-bipyridine)ruthenium(II) to methylviologen in zeolite cages: A resonance Raman spectroscopic study, *J. Phys. Chem.*, **1987**, *91*, 4443-4446.

16. J. A. Incavo and P. K. Dutta, Zeolite host-guest interactions: Optical spectroscopic properties of tris(bipyridine) ruthenium(II) in zeolite Y cages, *J. Phys. Chem.*, **1990**, *94*, 3075-3081.

17. P. K. Dutta and W. Turbeville, Intrazeolitic photoinduced redox reactions between $Ru(bpy)_3^{2+}$ and methylviologen, *J. Phys. Chem.*, **1992**, *96*, 9410-9416.

18. P. K. Dutta, Zeolite guest-host interaction: Implications in formation, catalysis, and photochemistry, *J. Inclusion Phenom. Mol. Recog. Chem.*, **1995**, *21*, 215-237.

19. M. Sykora, J. R. Kincaid, P. K. Dutta and N. B. Castagnola, On the nature and extent of intermolecular interactions between entrapped complexes of $Ru(bpy)_3^{2+}$ in zeolite Y, *J. Phys. Chem. B*, **1999**, *103*, 309-320.

20. M. Vitale, N. B. Castagnola, N. J. Ortins, J. A. Brooke, A. Vaidyalingam and P. K. Dutta, Intrazeolitic photochemical charge separation for $Ru(bpy)_3^{2+}$-bipyridinium system: Role of the zeolite structure, *J. Phys. Chem. B*, **1999**, *103*, 2408-2416.

21. Y. Kim, H. Lee, P. K. Dutta and A. Das, Zeolite-mediated photochemical charge separation using a surface-entrapped ruthenium-polypyridyl complex, *Inorg. Chem.*, **2003**, *42*, 4215-4222.

22. M. Borja and P. K. Dutta, Storage of light energy by photoelectron transfer across a sensitized zeolite-solution interface, *Nature*, **1993**, *362*, 43-45.

23. M. Sykora and J. R. Kincaid, Photochemical energy storage in a spatially organized zeolite-based photoredox system, *Nature*, **1997**, *387*, 162-164.

24. K. Maruszewski, D. P. Strommen and J. R. Kincaid, Zeolite-entrapped ruthenium(II) complexes with bipyridine and related ligands. Elimination of the ligand-field-state deactivation and increase in ^{3}MLCT state lifetimes, *J. Am. Chem. Soc.*, **1993**, *115*, 8345-8350.

25. Y. I. Kim and T. E. Mallouk, Dynamic electron-transfer quenching of the tris(2,2'-bipyridyl)ruthenium(II) MLCT excited state by intrazeolitic methylviologen ions, *J. Phys. Chem.*, **1992**, *96*, 2879-2885.

26. E. H. Yonemoto, Y. I. Kim, R. H. Schmehl, J. O. Wallin, B. A. Shoulders, B. R. Richardson, J. F. Haw and T. E. Mallouk, Photoinduced electron transfer reactions in zeolite-based donor-acceptor and donor-donor-acceptor diads and triads, *J. Am. Chem. Soc.*, **1994**, *116*, 10557-10563.

27. Y. I. Kim, S. W. Keller, J. S. Krueger, E. H. Yonemoto, G. B. Saupe and T. E. Mallouk, Photochemical charge transfer and hydrogen evolution mediated by oxide semiconductor particles in zeolite-based molecular assemblies, *J. Phys. Chem. B*, **1997**, *101*, 2491-2500.

28. M. A. Miranda and H. García, 2,4,6-Triphenylpyrillium tetrafluoroborate as an electron-transfer photosensitizer, *Chem. Rev.*, **1994**, *94*, 1063-1089.

29. W. P. Todd, J. P. Dinnocenzo, S. Farid, J. L. Goodman and I. R. Gould, Efficient photoinduced generation of radical cations in solvents of medium and low polarity, *J. Am. Chem. Soc.*, **1991**, *113*, 3601-3602.

30. A. Corma, V. Fornés, H. García, M. A. Miranda, J. Primo and M.-J. Sabater, Photoinduced electron transfer within zeolite cavities: *cis*-Stilbene isomerization photosensitized by 2,4,6-triphenylpyrylium cation imprisoned inside zeolite Y, *J. Am. Chem. Soc.*, **1994**, *116*, 2276-2280.

31. A. Sanjuán, M. Álvaro, G. Aguirre, H. García and J. C. Scaiano, Intrazeolite photochemistry. 21. 2,4,6-Triphenylpyrylium encapsulated inside zeolite Y supercages as a heterogeneous photocatalyst for the generation of hydroxyl radical, *J. Am. Chem. Soc.*, **1998**, *120*, 7351-7352.

32. A. Sanjuán, M. Álvaro, A. Corma and H. García, An organic sensitizer within Ti-zeolites as photocatalyst for the selective oxidation of olefins using oxygen and water as reagents, *Chem. Commun.*, **1999**, 1641-1642.

33. A. Sanjuán, G. Aguirre, M. Álvaro, H. García and J. C. Scaiano, Degradation of propoxur in water using 2,4,6-triphenylpyrylium-zeolite Y as photocatalyst. Product study and laser flash photolysis, *Appl. Catal. B*, **2000**, *25*, 257-265.

34. A. Sanjuán, G. Aguirre, M. Álvaro, H. García, J. C. Scaiano, M. N. Chrétien and K.-S. Focsaneanu, Product studies and laser flash photolysis of direct and 2,4,6-triphenylpyrylium-zeolite Y photocatalyzed degradation of fenvalerate, *Photochem. Photobiol. Sci.*, **2002**, *1*, 955-959.

35. X. Liu, K.-K. Iu and J. K. Thomas, Preparation, characterization and photoreactivity of titanium(IV) oxide encapsulated in zeolites, *J. Chem. Soc. Faraday Trans.*, **1993**, *89*, 1861-1865.

36. Y. Xu and C. H. Langford, Enhanced photoactivity of a titanium(IV) oxide supported on ZSM-5 and zeolite A at low coverage, *J. Phys. Chem.*, **1995**, *99*, 11501-11507.

37. H. Yamashita, Y. Ichihashi and M. Anpo, Photocatalytic decomposition of NO at 275 K on titanium oxides included within Y-zeolite cavities: The structure and role of the active sites, *J. Phys. Chem.*, **1996**, *100*, 16041-16044.

38. M. Anpo, H. Yamashita, Y. Ichihashi, Y. Fujii and M. Honda, Photocatalytic reduction of CO_2 with H_2O on titanium oxides anchored within micropores of zeolites: Effects of the structure of the active sites and the addition of Pt, *J. Phys. Chem. B*, **1997**, *101*, 2632-2636.

39. S. Corrent, G. Cosa, J. C. Scaiano, M. S. Galletero, M. Álvaro and H. García, Intrazeolite photochemistry. 26. Photophysical properties of nanosized TiO_2 clusters included in zeolites Y, β, and mordenite, *Chem. Mater.*, **2001**, *13*, 715-722.

40. G. Cosa, M. S. Galletero, L. Fernández, F. Márquez, H. García and J. C. Scaiano, Tuning the photocatalytic activity of titanium dioxide by encapsulation inside zeolites exemplified by the cases of thianthrene photooxygenation and horseradish peroxidase photodeactivation, *New. J. Chem.*, **2002**, *26*, 1448-1455.

41. W. Turbeville, D. S. Robins and P. K. Dutta, Zeolite-entrapped $Ru(bpy)_3^{2+}$: Intermolecular structural and dynamic effects, *J. Phys. Chem.*, **1992**, *96*, 5024-5029.

42. M. L. Cano, F. L. Cozens, H. García, V. Martí and J. C. Scaiano, Intrazeolite photochemistry. 13. Photophysical properties of bulky 2,4,6-triphenylpyrylium and tritylium cations within large- and extra-large-pore zeolites, *J. Phys. Chem.*, **1996**, *100*, 18152-18157.

43. V. Wintgens, J. Pouliquen and J. Kossanyi, Emission properties of charge-transfer complexes formed by pyrylium ions with electron donors, *Nouv. J. Chim.*, **1985**, *9*, 229-234.

44. S. Niizuma, N. Sato, H. Kawata, Y. Suzuki, T. Toda and H. Kokubun, Free-radicals from the derivatives of pyrylium-salts in solution by photoillumination, *Bull. Chem. Soc. Jpn.*, **1985**, *58*, 2600-2607.

45. A. Sanjuán, G. Aguirre, M. Álvaro and H. García, 2,4,6-Triphenylpyrylium ion encapsulated in Y zeolite as photocatalyst. A co-operative contribution of the zeolite host to the photodegradation of 4-chlorophenoxyacetic acid using solar light, *Appl. Catal. B*, **1998**, *15*, 247-257.

46. M. S. Galletero and H. García, *unpublished results*,

47. D. Rehm and A. Weller, Kinetics of fluorescence quenching by electron transfer and H-atom transfer, *Isr. J. Chem.*, **1970**, *8*, 258-271.

48. C. Bremard, G. Buntinx, G. Coustillier and G. Ginestet, A time-resolved diffuse reflectance study of the photo-reduction of 2,2'-bipyridine in faujasitic zeolites, *J. Mol. Struc.*, **1997**, *410/411*, 81-84.

49. S. Horikoshi, N. Serpone, J. C. Zhao and H. Hidaka, Towards a better understanding of the initial steps in the photocatalyzed mineralization of amino acids at the titania/water interface. An experimental and theoretical examination of L-alanine, L-serine, and L-phenylalanine, *J. Photochem. Photobiol. A*, **1998**, *118*, 123-129.

50. H. Hidaka, S. Horikoshi, N. Serpone and J. Knowland, *In vitro* photochemical damage to DNA, RNA and their bases by an inorganic sunscreen agent on exposure to UVA and UVB radiation., *J. Photochem. Photobiol. A*, **1997**, *111*, 205-213.

51. R. Dunford, A. Salinaro, L. Z. Cai, N. Serpone, S. Horikoshi, H. Hidaka and J. Knowland, Chemical oxidation and DNA damage catalyzed by inorganic sunscreen ingredients, *FEBS Lett.*, **1997**, *418*, 87-90.

52. H. Hidaka, S. Horikoshi, K. Ajisaka, J. C. Zhao and N. Serpone, Fate of amino acids upon exposure to aqueous titania irradiated with UVA and UVB radiation - Photocatalyzed formation of NH_3, NO_3^- and CO_2, *J. Photochem. Photobiol. A*, **1997**, *108*, 197-205.

53. B. Porstmann, T. Porstmann and E. Nugel, Comparison of chromogens for the determination of horseradish peroxidase as a marker in enzyme immunoassay, *J. Clin. Chem. Clin. Bio.*, **1981**, *19*, 435-439.

54. T. Hancock-Chen and J. C. Scaiano, Enzyme inactivation by TiO_2 photosensitization, *J. Photochem. Photobiol. B*, **2000**, *57*, 193-196.

55. D. J. Cardin, S. P. Constantine, A. Gilbert, A. K. Lay, M. Álvaro, M. S. Galletero, H. García and F. Marquez, Polymerization of alkynes in the channels of mesoporous materials containing Ni and Zn cations: Almost complete filling of the voids, *J. Am. Chem. Soc.*, **2001**, *123*, 3141-3142.

56. M. S. Galletero, M. Álvaro, H. García, C. J. Gómez-García and A. K. Lay, Spontaneous doping and magnetic properties of polyacetylene synthesized *in situ* in Ni-exchanged mordenite and mesoporous MCM-41, *Phys. Chem. Chem. Phys.*, **2002**, *4*, 115-120.

57. B. H. Milosavlijevic and J. K. Thomas, Photochemistry of compounds adsorbed into cellulose. Part 4. Diffusion-controlled mechanism of tris(2,2'-bipyridine)ruthenium^{2+} luminescence quenching by copper(II), *J. Chem. Soc. Faraday Trans.*, **1985**, *81*, 735-744.

58. W. Shi and H. D. Gafney, Distribution of metal ions cation exchanged onto porous Vycor glass and its effect on the emission quenching of coadsorbed tris(bipyridyl)ruthenium^{2+}, *J. Phys. Chem.*, **1988**, *92*, 2329-2333.

4. Photophysical Properties of Dibenzotropylium Cation

4. Photophysical Properties of Dibenzotropylium Cation 137

4.1 Background 138
4.2 Sample Preparation and Characterization 140
4.3 Photophysical Studies 144
4.3.1 Fluorescence Spectroscopy 144
4.3.2 Laser Flash Photolysis of Dibenzotropylium Cation 146
4.3.3 Quenching Studies 148
4.3.4 Electron Transfer Interactions 150
4.4 Conclusions 154
4.5 Experimental 155
4.5.1 Sample Preparation 155
4.5.2 Steady-state Spectroscopy 156
4.5.3 Time-resolved Spectroscopy 157
4.6 References 158

4.1 Background

In Chapter 1 the various properties of zeolite aluminosilicates were reviewed and it was noted that, due to the different valence between Si and Al, each Al atom present in the framework generates a negative charge in the lattice. The presence of a charge-balancing cation within the internal voids is required in order to ensure the electroneutrality of the solid. The ionic nature of the interaction between these countercations and the zeolite framework allows for the selective exchange of the original cations with other positively charged species (organic or inorganic) without any alteration in the crystalline structure of the host. The fact that the negatively charged lattice provides a convenient microenvironment for positively charged species, has led to the use of zeolites for the study and control of the physical and chemical properties of organic cations in an inert environment. The preparation and observed stability of zeolite Y-encapsulated 2,4,6-triphenylpyrylium cation, discussed in the previous chapter, constitutes an early example.[1] The ability of zeolites and clays to stabilize cationic species has been taken advantage of for the preparation of a variety of encapsulated organic cations including xanthylium, fluorenylium and its 9-substituted analogues, and various triarylmethyliums.[2-5] The simple preparation of these stabilized carbenium ions allows their excited state behaviour to be examined.

In contrast to the volume of data available on the formation, stability, structure, and chemical reactivity of carbenium ions in the ground state, much less information is available concerning the characterization and behaviour of these species in the excited state.[6] This is due, in part, to the difficulty of performing these studies in solution where the cations must be generated as transient species or in the presence of strong acids.[7-12] The preponderance of photochemical studies involving transient carbocations have been directed towards their generation and detection in media where their lifetime is limited by a fast reaction with the media.[7] Studies of the photochemistry and photophysics of carbenium excited states

specifically, were not reported until the mid-1990's. The best characterized systems in solution are xanthenium cations and their 9-substituted analogues.[8, 10, 12, 13] The xanthenium singlet and triplet excited states have also been well characterized in zeolites.[3]

In this work we have investigated the cation derived from 10,11-dihydro-5*H*-dibenzo[*a*,*d*]cycloheptatriene (dibenzosuberene, DBH). The dibenzosuberenyl cation has an internal cyclic array and possesses six π-electrons. The cyclic nature of the cation, along with the 4n+2 π-electrons and the vacant *p*-orbital on the trivalent carbon, all contribute to the aromatic nature of this carbenium ion. The aromaticity contributes to the observed stability of this cation, especially as compared to the structurally related fluorenylium cation whose central five-membered ring is anti-aromatic.

4.2 Sample Preparation and Characterization

Dibenzotropylium cation was first prepared as a stable species within the pores of acidic zeolites during a study of the involvement of the zeolite framework in electron-transfer reactions. In this study 9*H*-xanthene (XH), 9*H*-fluorene (FH), and dibenzosuberene (DBH) were adsorbed into the pores of acidic zeolites possessing both Lewis and Brønstead acid sites.[2] Spontaneous formation of the corresponding cations via a formal hydride loss was observed in the case of both the xanthylium (X^+) and dibenzotropylium (DB^+) cations. Inclusion of fluorene in acidic zeolites results in the formation of both the cationic fluorenylium species (F^+) and the radical cation ($F^{\bullet+}$). This observation prompted the authors to conclude that carbenium ion formation proceeds through the radical cation as a precursor.[2] Predominant observation of the radical cation is likely related to cation instability, resulting from the anti-aromatic character of the cyclic four π-electron carbenium ion.[2]

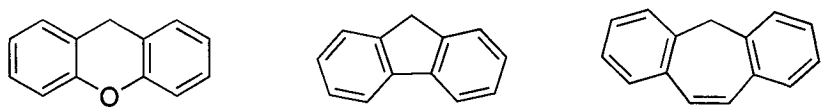

XH FH DBH

Figure 4.1 Structures of the parent hydrides included in acidic zeolites in the study discussed above.

In order to minimize any interference from radical cation formation, the stabilized DB^+-containing samples used in this work were prepared from the parent alcohol. Cation formation from the alcohol has been proposed to proceed by protonation and subsequent dehydration. This procedure has been used for the preparation of related carbocations, including xanthenium cations in zeolites and the 9-phenyl-9-fluorenyl cation in clays, from the parent alcohols.[3, 5] A series of related cations (xanthenium, thioxanthenium, and analogues) have been similarly prepared in acidic solution, typically moderate concentrations of H_2SO_4 or trifluoroacetic acid (TFAA).[8, 10, 12] In this work DB^+ was prepared by incorporation of

the parent alcohol into the channels of H^+-exchanged, mono-directional zeolite ZSM-5. The structures of ZSM-5 type zeolites were given in Figures 1.3 and 1.4.

Scheme 4.1 Preparation of DB^+ cation in acidic zeolite HZSM-5.

To prepare DB^+@HZSM-5, a sample of thermally dehydrated HZSM-5 was added to a dichloromethane solution of 5*H*-dibenzo[*a,d*]cyclohepten-5-ol (DBOH). The slurry was refluxed for one hour, after which the bright red-pink solid was collected by filtration and subjected to solid-liquid (Soxhlet) extraction with DCM. The diffuse reflectance spectrum of the prepared solid (Figure 4.2) is perfectly coincident with the absorption spectrum of an authentic sample of DB^+ obtained by dissolving DBOH in acetonitrile containing 0.3 M trifluoroacetic acid. The recorded DRS is also in agreement with the reported spectrum of DB^+@Hβ and the transient absorption spectrum obtained by Johnston *et al.* following photodehydroxylation of DBOH in trifluoroethanol.[2,9]

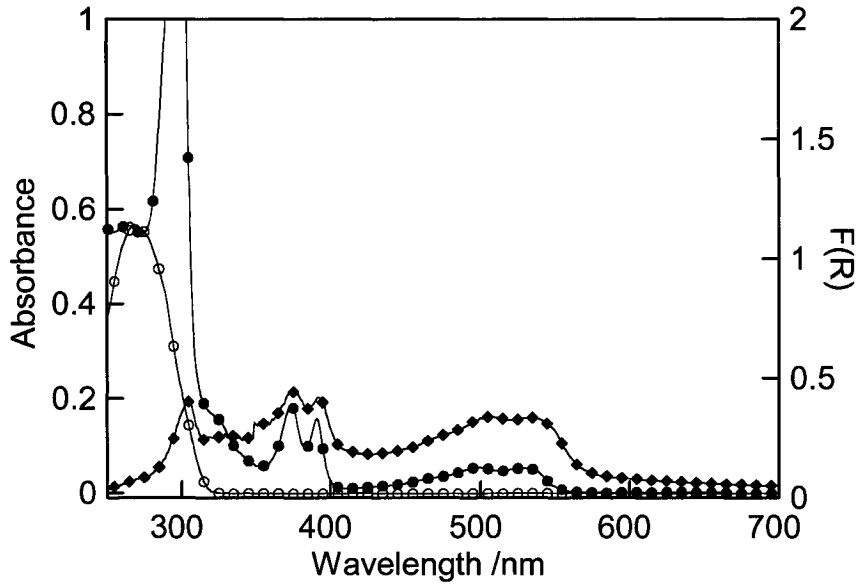

Figure 4.2 UV-vis absorption spectrum of DBOH (○) in acetonitrile, DB^+ (●) prepared by dissolving DBOH in acetonitrile containing 0.3 M TFAA, and the DRS of DB^+@ZSM-5 (◆) plotted as a function of the reflectance.

The IR spectrum of DB^+@HZSM-5 was recorded and compared with the IR spectra of DBOH and DB^+ obtained by dissolving DBOH in H_2SO_4. Figure 4.3 shows the aromatic region of the IR spectra for each sample. The spectra of the two cationic samples are in excellent agreement, while the IR spectrum of DBOH is distinctly different in this region, given that the central cycloheptatriene ring of parent alcohol is not aromatic. These observations indicate that DB^+ is the predominant species present in the zeolite sample. It is of interest to observe the photochemical and photophysical behaviour of the cation in the absence of interference from the parent alcohol.

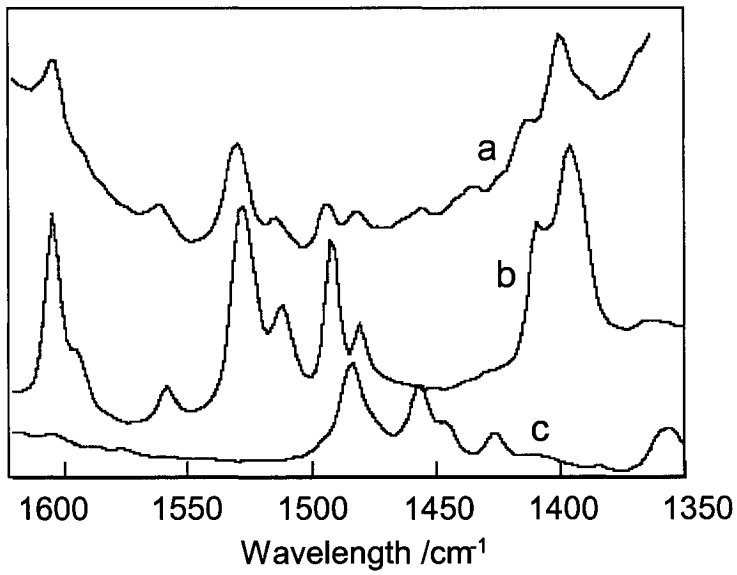

Figure 4.3 Aromatic region of the IR spectra of (a) DB^+ in HZSM-5, (b) DB^+ obtained by dissolving DBOH in H_2SO_4, and (c) DBOH.

4.3 Photophysical Studies

4.3.1 Fluorescence Spectroscopy

DB^+@HZSM-5 was further characterized by emission spectroscopy. The fluorescence spectrum was recorded following 355 nm excitation. The emission spectrum, given in Figure 4.4, is a reasonable mirror image of the lowest energy absorption band. This emission spectrum is in agreement with previously reported spectra obtained by generating the cation in acidic solutions or by photodehydroxylation in polar solvents.[8, 9, 11] It was originally suggested that the fluorescence observed in these cases resulted from an adiabatic dehydroxylation of the parent alcohol, i.e. the cation is generated in its singlet excited-state and subsequently undergoes radiative relaxation.[11] However, Johnston *et al.* later showed that, under the conditions of laser excitation, a significant portion of the emission is due to the excited singlet generated by non-adiabatic formation of the cation followed by re-excitation within the laser pulse.[9] The short lifetime of the singlet excited-state of the alcohol (*ca.* 5 ns) is certainly consistent with rapid formation of the ground state cation and subsequent re-excitation within the same laser pulse.

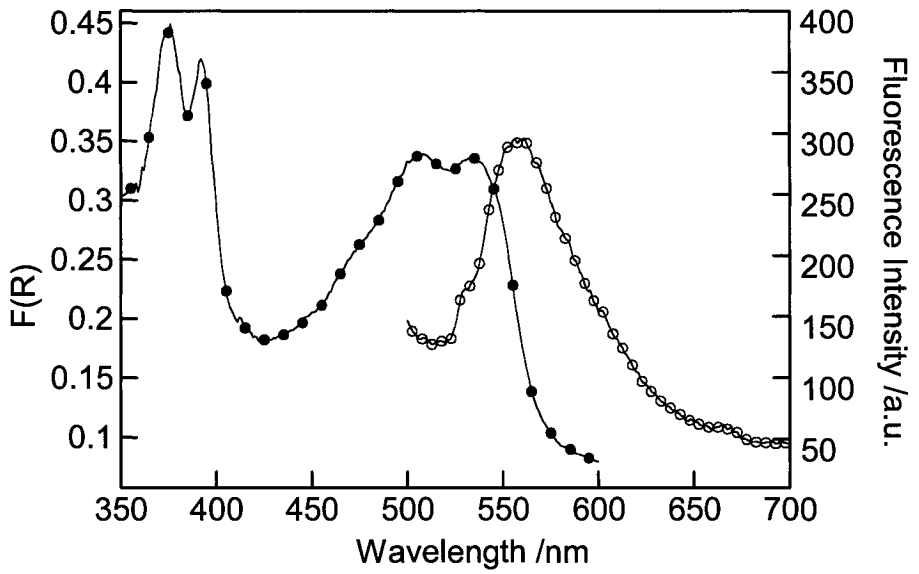

Figure 4.4 DRS (●) and emission spectra (○) of nitrogen purged DB^+@HZSM-5. The excitation wavelength was 355 nm.

The observed emission decayed with first-order kinetics (Figure 4.5) and had an average lifetime of 55 ns. This value is similar to the 40 ns reported for the cation generated in acidic solution (H_2SO_4 or TFAA).[8, 11] The slightly longer lifetime may be attributed to spatial restriction or to the more efficient exclusion of ubiquitous singlet quenchers, such as oxygen, in the zeolite matrix.

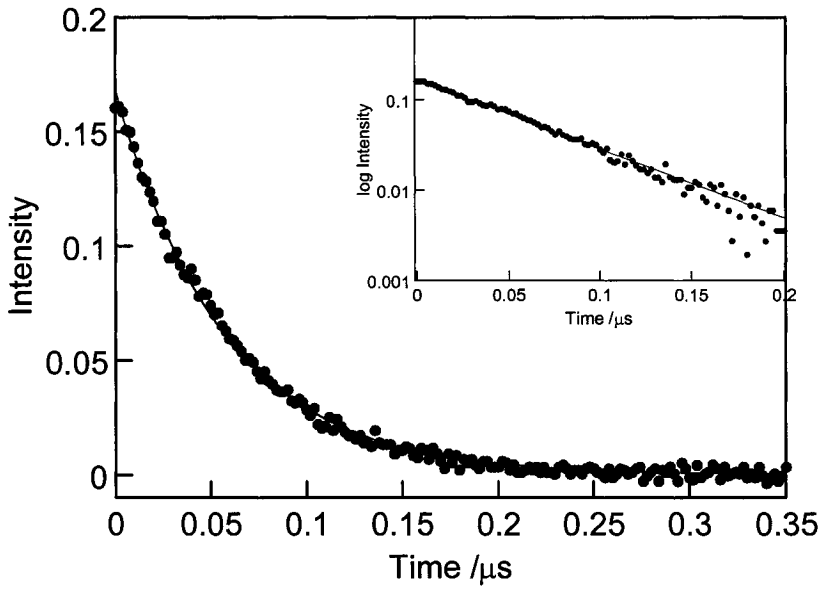

Figure 4.5 Emission decay monitored at 580 nm following 355 nm pulsed excitation (ns Nd-YAG laser) of DB^+@HZSM-5.

4.3.2 Laser Flash Photolysis of Dibenzotropylium Cation

The cation excited-state was further investigated using time-resolved DR-LFP techniques. The time-resolved DRS recorded following excitation of a nitrogen purged sample of DB^+@HZSM-5, shows a transient with two distinct absorption bands, a narrow band at *ca.* 300 nm and a broad band at *ca.* 440 nm (Figure 4.6). Decay profiles measured across the spectral range are similar, suggesting that these spectroscopic features are due to a single transient with a lifetime on the order of 30-40 μs. The triplet-triplet absorption spectrum of this cation has not been previously reported, but the band structure is similar to that reported for zeolite-encapsulated xanthenium cations, which have a narrow band at 275 nm and a broad absorption at 550 nm in the case of HZSM-5.[3]

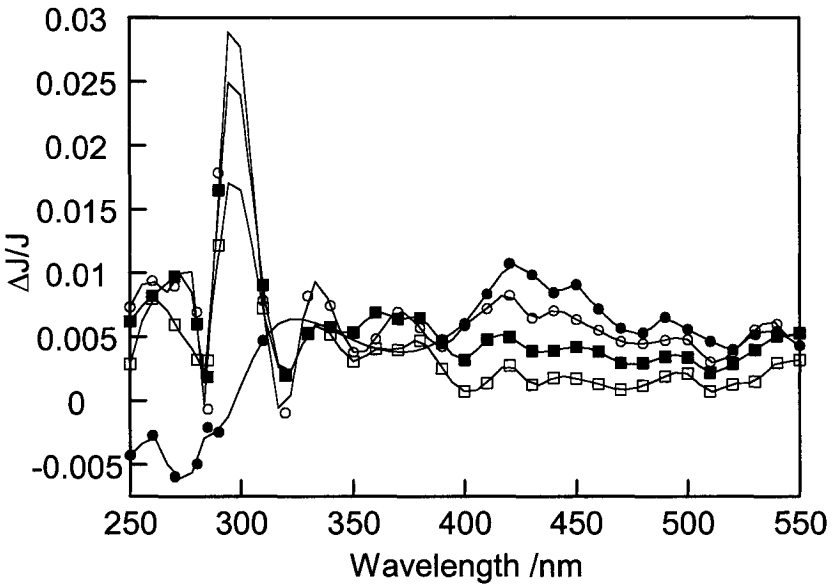

Figure 4.6 Transient DRS recorded (●) 0.96 μs, (○) 2.56 μs, (■) 9.60 μs, and (□) 29.9 μs after 355 nm laser excitation of a nitrogen purged sample of DB^+@HZSM-5.

The assignment of photochemically generated transients within zeolites is typically supported by their coincidence with the spectra recorded in solution. However, in the case of DB^+, previous laser flash photolysis studies failed to observe any transient which could be assigned to the triplet state.[8] The lifetime of the cation triplet excited-state is expected to be short in solution. The failure to observe the triplet may have been because the transient spectrum in solution is complicated, at short times, by the intense bleaching of the highly coloured ground state. Despite this anticipated complication, LFP experiments were carried out with DB^+ generated by dissolving DBOH in trifluoroethanol solutions containing TFAA (see UV-vis absorption spectrum in Figure 4.2). This solution was excited with the second harmonic of a Nd-YAG laser (532 nm) in order to ensure selective excitation of the cation. In control experiments, no transients were observed when TFE solutions of DBOH were excited at this wavelength. The transient absorption spectrum recorded following 532 nm excitation of the DB^+ cation in acidic solution is shown below in Figure 4.7. At short times, the spectrum is dominated by an

intense negative signal due to bleaching of the DB^+ ground state, but a short-lived transient with absorption at *ca.* 320 and 420 nm was observed.

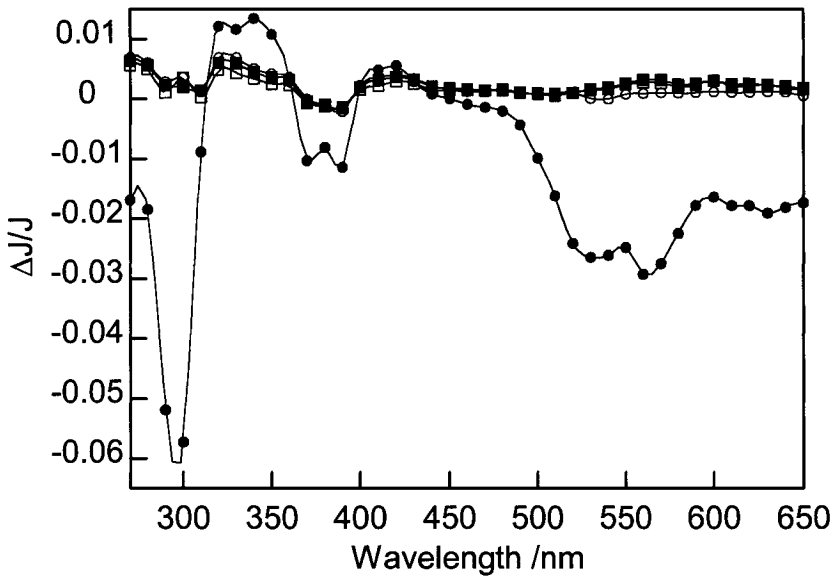

Figure 4.7 Transient UV-vis spectrum recorded (●) 0.16 μs, (○) 0.96 μs, (■) 6.88 μs, and (□) 15.2 μs after 532 nm excitation of a 6.9 x 10^{-5} M solution of DBOH in deaerated TFE containing TFAA to generate the DB^+ cation.

It is reasonable to assume that this transient species, generated upon excitation of DB^+ in TFE solution, is the same as that observed upon excitation of DB^+ encapsulated in HZSM-5, and corresponds to the triplet excited-state of the cation. This behaviour is consistent with the photochemical behaviour of structurally related aromatic carbenium ions, xanthylium for example, for which triplet excited states have been observed.[7] The minor shift in the absorption maxima likely reflects a solvatochromatic effect, while the remarkable increase in the triplet excited-state lifetime, upon zeolite incorporation, has been observed for other zeolite-bound ions.[3, 14-16]

4.3.3 Quenching Studies

Further evidence for the triplet nature of the transient resulting from excitation of DB^+, was obtained by quenching studies using a known triplet

quencher, 1,3-cyclohexadiene (1,3-CHD). 1,3-CHD is an energy transfer acceptor and is capable of quenching excited-states with energies greater than 240 kJ mol^{-1}.[17-19] Upon addition of 1,3-CHD to the DB^+@HZSM-5 sample, complete quenching of the transient signals was observed. Quenching by 1,3-CHD is excellent evidence for the triplet nature of the observed transient. The observed quenching was extremely efficient and the dynamic effect of 1,3-CHD on the triplet lifetime was not resolved. In some instances, the observation of static or instantaneous quenching can indicate that the quencher interacts with the transient precursor rather than the transient itself. However, although the interaction appears instantaneous in nature, quenching cannot be attributed to an interaction with the singlet excited-state precursor in this case. The singlet energy of DB^+ has been estimated as 217 kJ mol^{-1} based on its fluorescence spectrum, since the singlet energy of 1,3-CHD is *ca.* 460 kJ mol^{-1} quenching of the DB^+ singlet state by 1,3-CHD is thermodynamically unfeasible. Therefore, we conclude that the observed reduction in signal intensity is due to an ET interaction between 1,3-CHD and the DB^+ triplet excited-state.

When the zeolite sample was purged with oxygen, a known quencher of triplet states as well as many free radicals, a reduction in transient signal intensity was observed. The decrease in absorption intensity across the spectral range was not accompanied by a decrease in the observed transient lifetime, as seen in the representative decay traces in Figure 4.8. There are several possible explanations for this slightly unexpected result. It is possible that the quenching appears static due to the tight fit of the cation within the zeolite channels (diameter 5.2 x 5.7 $Å^2$) and the low solubility of oxygen in water (the zeolite samples are hydrophilic and are not dehydrated prior to LFP experiments). The lower concentration of oxygen (as compared to 1,3-CHD) and the restricted environment in the water-saturated zeolite may reduce the contribution of dynamic quenching by oxygen. It is also possible that there is a partial quenching of the transient precursor, i.e. the singlet state, resulting in reduced formation of the triplet state via intersystem crossing. Although a contribution from singlet state quenching cannot be ruled out, this

interaction will not be favoured by the short lifetime of the DB^+ singlet excited-state. In addition, oxygen-induced emission quenching was not observed during fluorescence studies.

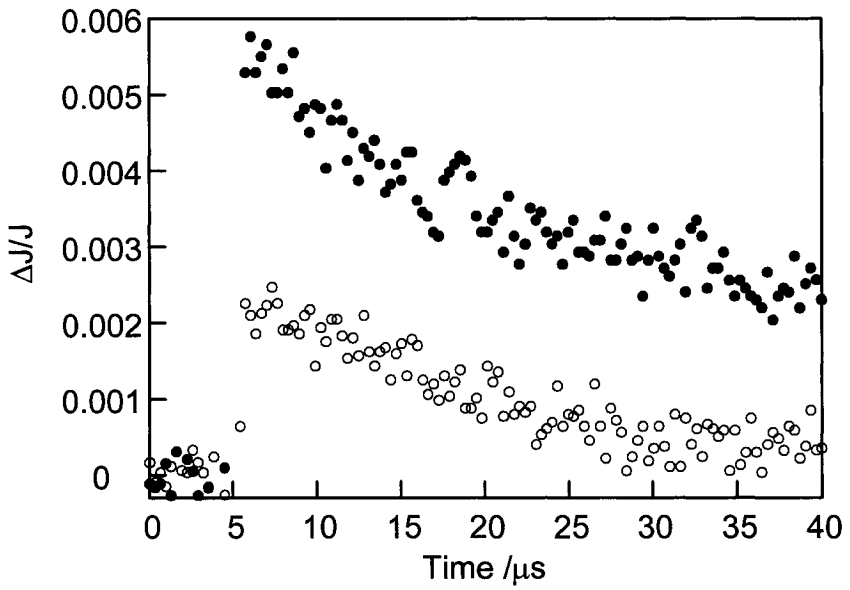

Figure 4.8 Decay profile monitored at 500 nm following 355 nm laser excitation of a nitrogen purged (●) and an oxygen purged (○) sample of DB^+@HZSM-5.

4.3.4 Electron Transfer Interactions

The triplet excited-states of aromatic carbenium ions are expected to be good electron acceptors and should, therefore, undergo efficient electron transfer with a good electron donor. This was explored by addition of a volatile amine (triethylamine, TEA) as an intrazeolitic electron donor. A reasonably volatile quencher will experience more facile distribution throughout the zeolite pore structure. In solution, this type of reaction is complicated by the fact that amines are also strong nucleophiles and will readily react with the carbenium ion ground state. In the channels of ZSM-5 zeolite nucleophilic addition will be sterically prohibited by the tight fit of the cation within the pore and the electron transfer interaction should predominate. When triethylamine is co-adsorbed in the DB^+@HZSM-5 sample, the transient diffuse reflectance spectrum recorded

following 532 nm excitation is distinctly different. As seen in Figure 4.9, the absorption bands at 300 and 440 nm, assigned to the triplet, were quenched accompanied by the appearance of peaks at ca. 275 and 350 nm.

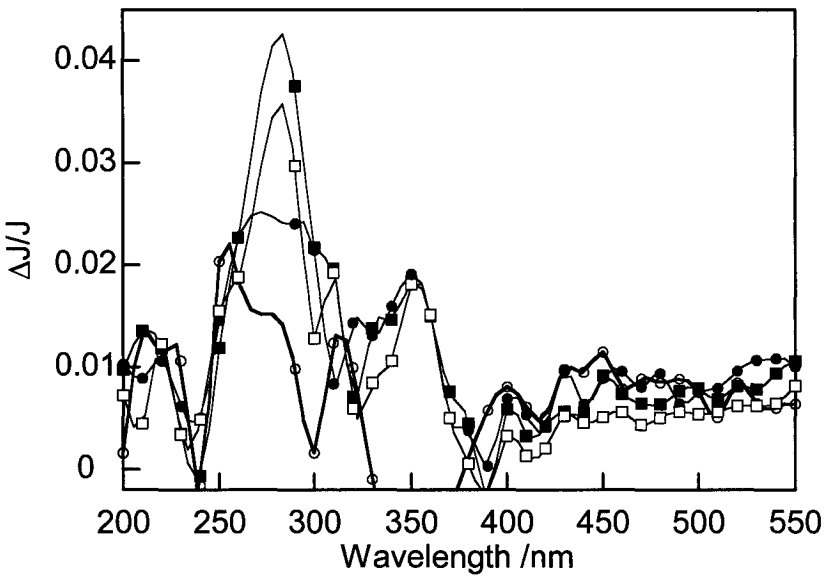

Figure 4.9 Transient DRS recorded (○) 0.96 μs, (●) 2.56 μs, (■) 9.60 μs, and (□) 29.9 μs after 532 nm laser excitation of a nitrogen purged sample of DB^+@HZSM-5 containing TEA.

These two new absorption bands were tentatively assigned to the dibenzosuberenyl radical ($DB^•$). This radical is the product of an electron transfer reaction between DB^+ and TEA, the electron donor. To confirm the assignment of these absorption bands, these data were compared with an authentic spectrum of this radical. The $DB^•$ radical was alternately generated by photolysis of 5-chloro-5*H*-dibenzo[*a*,*d*]cycloheptene (DBCl). Photoexcitation of DBCl in a non-polar solvent results in homolytic cleavage of the C-Cl bond to give the corresponding carbon-centered radical. DBCl was prepared from the parent alcohol by reaction with thionyl chloride (Scheme 4.2). The UV-vis absorption spectrum of DBCl is given in Figure 4.12.

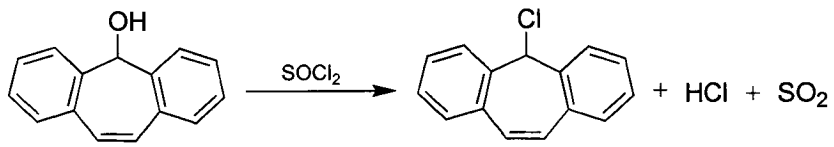

Scheme 4.2 Preparation of DBCl from DBOH and thionyl chloride.

The laser flash photolysis of DBCl in deaerated hexane gave the transient absorption spectrum shown in Figure 4.10. This spectrum has three main features; a sharp band at 275 nm that overlaps with the ground state bleaching at 300 nm, a smaller band at *ca.* 350 nm, and a broad band centered at 420 nm. The first two bands were assigned to the radical resulting from homolysis of the C-Cl bond in DBCl, and are coincident with the spectrum recorded in the zeolite sample containing TEA. The band at 420 nm was assigned to the triplet excited-state of the chloride. Purging with oxygen decreased the signal intensity of all three bands, but while the radical signals were only partially quenched, the signal at 420 nm was almost entirely quenched (Figure 4.11). The assignment of this band to the DBCl triplet excited-state is consistent with the triplet-triplet absorption spectra of the alcohol (DBOH) and the parent hydrocarbon (DBH); both have an absorption band at *ca.* 420 nm as well.[9, 20]

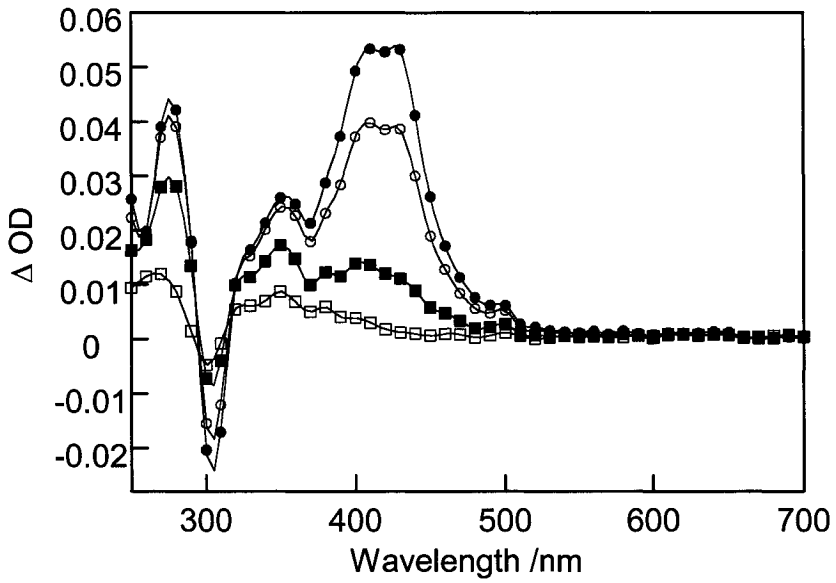

Figure 4.10 Transient absorption spectrum recorded (●) 0.40 μs, (○) 1.04 μs, (■) 3.84 μs, and (□) 14.4 μs after 308 nm excitation of a 5.3 x 10^{-5} M solution of DBCl in nitrogen purged hexane.

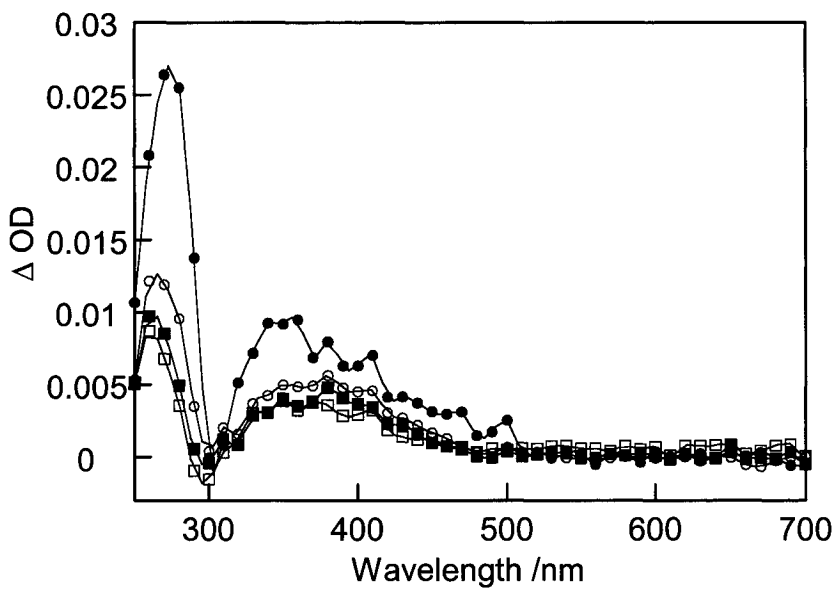

Figure 4.11 Transient absorption spectrum recorded (●) 0.24 μs, (○) 0.72 μs, (■) 3.04 μs, and (□) 14.6 μs after 308 nm excitation of a 5.3 x 10^{-5} M solution of DBCl in oxygen purged hexane.

4.4 Conclusions

Zeolites have, once again, proved to be convenient solid matrices for the generation and stabilization of organic cations. This extra stability has enabled the study of the photophysical and photochemical properties of a carbenium ion, DB^+, that is not easily examined in solution. Medium-pore sized zeolite ZSM-5 is particularly well-suited to the stabilization of the dibenzotropylium cation due to the close match between the diameter of the internal channels and the molecular dimensions of the cation. The DB^+ sample used in this work was prepared in high purity by inclusion of DBOH in acidic HZSM-5. The cation was observed to be an extremely persistent species, in fact no spectroscopic change was observed for this sample over a period of more than five years. This persistence allowed us to perform DR laser flash photolysis studies and the observed transient diffuse reflectance spectrum was attributed to the triplet excited-state of this cation. Electron transfer quenching of the triplet excited-state was observed and the dibenzosuberenyl radical product was characterized. In solution, the photochemistry of DB^+ is complicated by the short excited-state lifetime as well as the reactivity of this cation with nucleophiles.

4.5 Experimental

4.5.1 Sample Preparation

All chemicals used for sample preparation were obtained form Aldrich in their highest available purity, unless otherwise indicated.

4.5.1.1 DB^+@HZSM-5

HZSM-5 with a Si/Al ratio of 34 was prepared using tetrapropylammonium as the structure directing agent according to the method described in the literature and was a generous gift from the Instituto Tecnología Química, Valencia, Spain.[21] DB^+@HZSM-5 was prepared by adding a sample of HZSM-5 (1.0 g), that had been thermally dehydrated at 500°C overnight, to a solution of 5*H*-dibenzo[*a,d*]cyclohepten-5-ol (50 mg, 0.24 mmol) in DCM (20 mL). The slurry was stirred at reflux temperature for 1 h before the red-pink solid was collected by filtration. The collected solid was subjected to exhaustive solid-liquid extraction with fresh DCM until no organic material was recovered from the filtrate. GC-MS analysis of the extraction solutions revealed only unreacted DBOH (Fisons 8000/8060 series equipped with a J&W DBS 30 m x 0.32 mm fused silica column).

4.5.1.2 5-Chloro-5*H*-dibenzo[*a,d*]cycloheptene (DBCl) [18506-04-2]

5*H*-dibenzo[*a,d*]cyclohepten-5-ol (0.6 g, 2.88 mmol) was placed in a 50 mL round bottom flasked equipped with a nitrogen bubbler. Thionyl chloride (5.0 mL, 68.5 mmol) was added by syringe, the solution immediately turned red accompanied by the evolution of gas. The solution was stirred at room temperature for 1 h, after which the resulting mixture was subjected to rotary evaporation to remove the unreacted thionyl chloride. The light pink solid was washed with water and dried under flowing nitrogen overnight and finally under vacuum, also overnight. 5-Chloro-5*H*-dibenzo[*a,d*]cycloheptene was obtained as a faintly pink solid in quantitative yield and was not further purified: ^{1}H NMR (200 MHz, $CDCl_3$)

δ 7.55 - 7.30 (m, 8H), 7.15 (s, 2H), 6.28 (s, 1H); IR (Nujol mull) 1462, 1377, 805, 724, 681, 620 cm^{-1}; UV-vis (acetonitrile) 223, 291 nm.

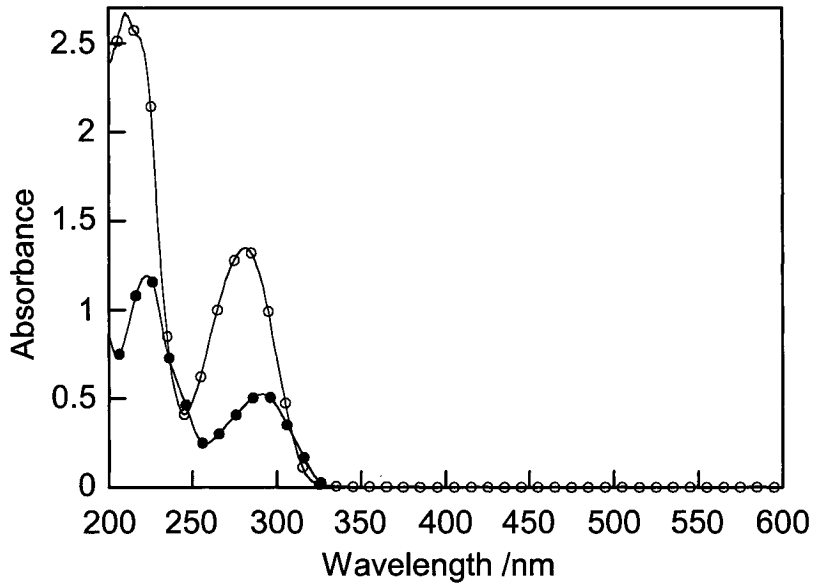

Figure 4.12 UV-vis absorption spectrum of DBOH (O, 1.1 x 10^{-4} M) and DBCl (●, 4.7 x 10^{-5} M) in acetonitrile solution.

4.5.2 Steady-state Spectroscopy

Absorption and DR spectra were recorded at room temperature on a Cary 1E spectrophotometer from Varian with a Varian DRA for reflectance measurements. Spectralon was used as a reflectance standard. Steady-state emission spectra were recorded at room temperature on a Perkin-Elmer LS-50 spectrofluorimeter. Spectra were recorded under nitrogen where indicated, liquid samples were typically contained in Suprasil quartz cells from Hellma and solid samples were recorded in cells made from clear fused quartz (Friedrich & Dimmock).

FT-IR spectra were obtained using a Nicolet 710 FT spectrophotometer. Self-supported wafers (*ca.* 10 mg) were compressed at 1 ton cm^{-2} for 3 min and placed in sealed, greaseless cells with CaF_2 windows. The cells were outgassed at 200°C under 10^{-2} Pa for 1 h before recording the spectra at room temperature. These spectra were recorded at ITQ, Valencia, Spain.

4.5.3 Time-resolved Spectroscopy

Laser flash photolysis experiments with zeolite samples were carried out using the diffuse reflectance system described in detail in Section 2.2.4 of this thesis. Solid samples were typically contained in 3 x 7 mm^2 quartz cells and were purged with nitrogen or oxygen as indicated. Quenchers (30 μL 1,3-CHD and 500 μL TEA) were added to nitrogen purged samples (250 mg) as neat liquids and allowed to diffuse through the zeolite at room temperature for 2-4 h prior to LFP experiments. Pulsed laser excitation was achieved using the second (532 nm) or third (355 nm) harmonic of a Surelite Nd-YAG laser. The average pulse width was 6 ns with a typical power output of *ca.* 25 and 15 mJ $pulse^{-1}$ at 532 and 355 nm respectively. Laser flash photolysis experiments with DBCl and DBOH in solution were carried out in spectroscopic grade hexane (OmniSolv) and trifluoroethanol (Fluka, distilled) respectively. Solutions were purged with O_2 or N_2 for 30 min prior to the experiment and were flowed through a 7 x 7 mm^2 quartz sample cell for the duration of the experiment in order to avoid interference from photoproducts. Samples were excited with 308 nm pulses from a Lumonics EX-530 excimer laser using a Xe/HCl/Ne mixture. Typical pulse widths were 6 ns with an average power of *ca.* 85 mJ $pulse^{-1}$.

Time-resolved emission data were recorded using the DR-LFP set-up described previously with the Xenon monitoring lamp turned off. Samples were excited with nanosecond pulses from the Surelite Nd-YAG laser described above (355 nm) and the fluorescence signal was detected using the PMT. Samples were contained in 3 x 7 mm^2 quartz cells and deaerated as indicated. All time-resolved data were manipulated and kinetic parameters extracted using the Kaleidagraph program from Synergy software.

4.6 References

1. A. Corma, V. Fornés, H. García, M. A. Miranda, J. Primo and M.-J. Sabater, Photoinduced electron transfer within zeolite cavities: *cis*-Stilbene isomerization photosensitized by 2,4,6-triphenylpyrylium cation imprisoned inside zeolite Y, *J. Am. Chem. Soc.*, **1994**, *116*, 2276-2280.

2. M. L. Cano, A. Corma, V. Fornés and H. García, Acid zeolites as electron acceptors. Generation of xanthylium, dibenzotropylium, and fluorenylium cations from their corresponding hydrides though an electron-transfer mechanism, *J. Phys. Chem.*, **1995**, *99*, 4241-4246.

3. F. L. Cozens, H. García and J. C. Scaiano, Intrazeolite photochemistry. 9. Laser flash photolysis of xanthenium ion generated by the adsorption of 9-xanthenol within acid zeolites, *Langmuir*, **1994**, *10*, 2246-2249.

4. M. L. Cano, A. Corma, V. Fornés, H. García, M. A. Miranda, C. Baerlocher and C. Lengauer, Triarylmethylium cations encapsulated within zeolite supercages, *J. Am. Chem. Soc.*, **1996**, *118*, 11006-11013.

5. F. L. Cozens, F. Gessner and J. C. Scaiano, Spontaneous carbocation generation on clays, *Langmuir*, **1993**, *9*, 874-876.

6. G. A. Olah and P. Scheleyer *Carbenium Ions;* Wiley: New York, 1968-1976.

7. P. K. Das, Transient carbocations and carbanions generated by laser flash photolysis and pulse radiolysis, *Chem. Rev.*, **1993**, *93*, 119-144.

8. A. Azarani, A. B. Berinstain, L. J. Johnston and S. Kazanis, Electron transfer reactions between excited diarylmethyl and triarylmethyl carbocations and aromatic donors, *J. Photochem. Photobiol. A*, **1991**, *57*, 175-189.

9. L. J. Johnston, J. Lobaugh and V. Wintgens, Laser flash photolysis studies of dibenzosuberenyl cations and radical cations, *J. Phys. Chem.*, **1989**, *93*, 7370-7374.

10. L. J. Johnston and D. F. Wong, Characterization of the triplet excited state of the phenylxanthenium carbocation, *Can. J. Chem.*, **1992**, *70*, 280-282.

11. M. R. Feldman and N. G. Thame, Stabilities of trivalent carbon species. 5. Equilibria of excited singlet alcohols and carbocations, *J. Org. Chem.*, **1979**, *44*, 1863-1865.

12. A. Samanta, K. R. Gopidas and P. K. Das, Carbocationic fluorescence and its efficient electron-transfer quenching, *J. Phys. Chem.*, **1993**, *97*, 1583-1588.

13. L. J. Johnston and D. F. Wong, Electron transfer reactions of triplet 9-arylxanthenium and 9-arylthioxanthenium cations, *J. Phys. Chem.*, **1993**, *97*, 1589-1595.

14. M. L. Cano, F. L. Cozens, V. Fornés, H. García and J. C. Scaiano, Intrazeolite photochemistry. 12. Ship-in-a-bottle synthesis and control of the photophysical properties of 9-(4-

methoxyphenyl)xanthenium ion imprisoned into large-pore zeolites, *J. Phys. Chem.*, **1996**, *100*, 18145-18151.

15. M. L. Cano, F. L. Cozens, H. García, V. Martí and J. C. Scaiano, Intrazeolite photochemistry. 13. Photophysical properties of bulky 2,4,6-triphenylpyrylium and tritylium cations within large- and extra-large-pore zeolites, *J. Phys. Chem.*, **1996**, *100*, 18152-18157.

16. A. Sanjuán, M. Álvaro, G. Aguirre, H. García and J. C. Scaiano, Intrazeolite photochemistry. 21. 2,4,6-Triphenylpyrylium encapsulated inside zeolite Y supercages as heterogeneous photocatalyst for the generation of hydroxyl radical, *J. Am. Chem. Soc.*, **1998**, *120*, 7351-7352.

17. L. J. Martínez and J. C. Scaiano, Characterization of the transient intermediates generated from the photoexcitation of nabumetone: A comparison with naproxen, *Photochem. Photobiol.*, **1998**, *68*, 646-651.

18. G. Cosa, L. J. Martínez and J. C. Scaiano, Influence of solvent polarity and base concentration on the photochemistry of ketoprofen: Independent singlet and triplet pathways, *Phys. Chem. Chem. Phys.*, **1999**, *1*, 3533-3537.

19. G. Cosa, Photodegradation and photosensitization in pharmaceutical products: Assessing drug phototoxicity, *Pure Appl. Chem.*, **2004**, *76*, 263-275.

20. A. R. Watkins and F. Bayrakceken, Excited state properties of 5H-dibenzo[*a,d*]cycloheptene, *J. Luminescence*, **1980**, *21*, 239-246.

21. R. J. Argauer, D. H. Olson and G. R. Landlolt, *Brit. Pat.*, **1969**, pat. no.1161974.

5. Stabilization and Reactivity of a Ketoprofen Derived Carbanion

5. Stabilization and Reactivity of a Ketoprofen Derived Carbanion 160

5.1 Background 161
5.2 Nature of the Ketoprofenate Excited State 165
5.2.1 Solvent Dependent Observation of Reactive Intermediates 165
5.2.2 Suggested Mechanism for Solvent Dependence 166
5.2.3 Photophysics of a Ketoprofen Analogue 169
5.2.4 Conclusions to this Section 174
5.3 Reactivity of the Carbanion Intermediate 176
5.3.1 Preparation of KP@Y 176
5.3.2 Intrazeolite Decarboxylation 179
5.3.3 Intrazeolite Carbanion Reactivity 182
5.3.4 Conclusions to this Section 191
5.4 Experimental 193
5.4.1 Sample Preparation 193
5.4.2 Steady-state Spectroscopy 194
5.4.3 Time-Resolved Spectroscopy 194
5.4.4 Product Studies 196
5.5 References 198

5.1 Background

This project was inspired by previous work in this research group related to the fascinating photochemistry of the non-steroidal anti-inflamatory drug (NSAID) ketoprofen (2-(3-benzoyl-phenyl)-propionic acid, KP). The photochemistry of NSAIDs in general has a been a topic of considerable interest.[1-3] This attention has been stimulated, in part, by questions relating to the problems of photostability and potential photosensitization associated with many of these drugs. Photosensitization in biological systems is the process by which radiation-induced abnormal reactions are mediated by exogenous chemicals (for example pharmaceuticals, cosmetics, and industrial chemicals).[1] Ketoprofen in particular has been implicated in both *in vitro* and *in vivo* phototoxicity and there are a number of reports in the literature describing its photobiological effects. Examples of these studies include investigations into photohemolysis[4-7] and DNA damage,[8-11] as well as epidemiological and animal studies of contact dermatitis.[12-15] Studies of ketoprofen photodegradation report that an efficient photodecarboxylation (quantum yield *ca.* 0.75) is the primary photochemical reaction pathway.[4, 16]

Structurally, ketoprofen (KP) is a simple substituted benzophenone (BP) (see structure in Scheme 5.1) with an absorption spectrum that is very similar to that of benzophenone itself. However, despite its structural similarity to benzophenone, KP displays some unconventional photochemistry making it a fascinating molecule to study. One example of ketoprofen's unique behaviour, is its unusual pH dependent photochemistry.[3, 6, 16-20] In its acidic form, ketoprofen behaves as a conventional benzophenone derivative, exhibiting high intersystem crossing yields and the expected n,π^* triplet, alkoxyl radical-like behaviour (i.e. hydrogen atom abstraction).[17, 18] In contrast, the carboxylate form of ketoprofen has been shown to undergo rapid decarboxylation, ultimately resulting in the formation of 3-ethylbenzophenone (EB) under anaerobic conditions (Scheme 5.1). This is an

important mechanistic pathway considering that the pK_a of KP is 4.7, implying that the carboxylate form of the drug will be predominant at physiological pH.[4, 16]

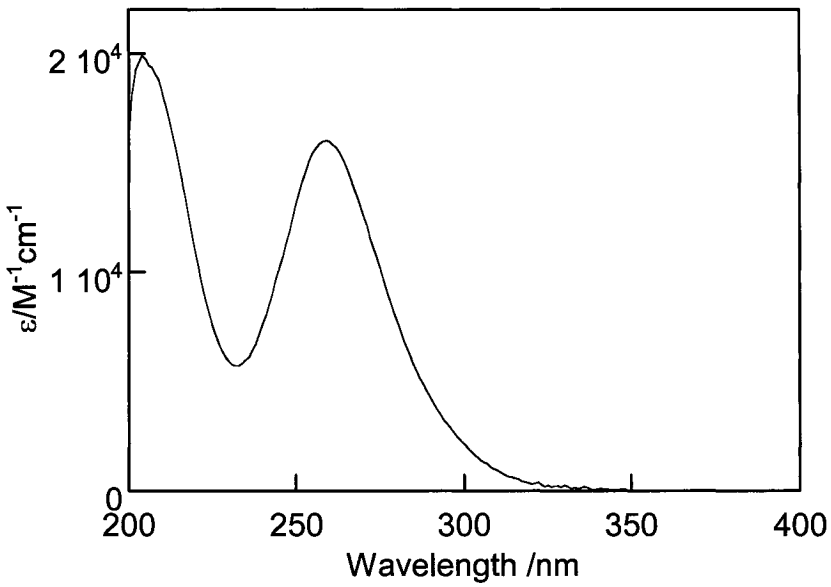

Figure 5.1 Molar absorptivity of ketoprofen in phosphate buffer solution (pH 7.4).

Laser flash photolysis of ketoprofenate (KP^-) in solution reveals a transient species with an absorption at around 580 nm having a lifetime of *ca.* 210 ns in aqueous systems.[17] There has been some debate in the literature regarding the assignment of this transient and the nature of its precursor. In one model, the visible absorbing transient was postulated to form following an electron transfer in the triplet manifold from the carboxyl group to the carbonyl group. The resulting biradicaloid species was assumed to decay via adiabatic decarboxylation to give the triplet carbanion.[18] This mechanism was later discarded in favour of one involving a prompt decarboxylation occurring within the nanosecond laser pulse, based on both the Arrhenius parameters of the transient decay (which did not support a bond-fragmentation process) and the associated volume changes in solution as measured by laser-induced optoacoustic spectroscopy (LIOAS).[20, 21] The transient is now generally agreed to be the carbanion shown in Scheme 5.1 and some researchers suggest contributions from the structure given in Scheme 5.2 below. In

the literature this biradical species is often shown to be in resonance with the carbanion structure, however this species is not strictly a resonance contributor.

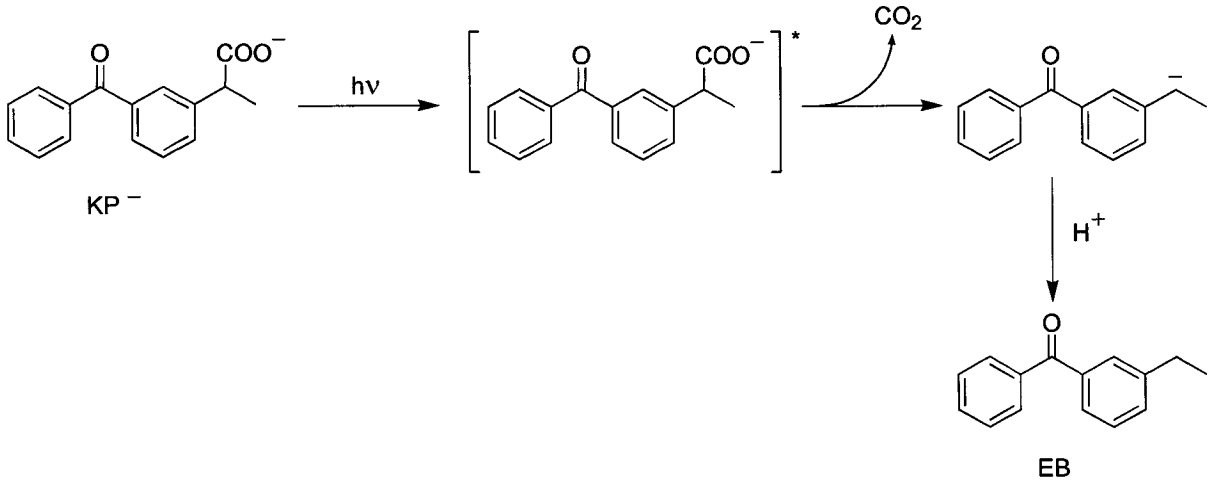

Scheme 5.1 Proposed mechanism of ketoprofen decarboxylation.[17, 20]

Both the singlet excited-state of the carboxylate and a short-lived triplet state have been proposed as precursors to this transient. In a recent investigation into the nature of the carbanion precursor, Cosa *et al.* succeeded in finding experimental conditions where both the benzophenone-like triplet state and the carbanionic species could be simultaneously detected.[20] Through the use of an appropriate solvent system, both species were monitored in a single experiment and it was determined that these species are formed independently and, therefore, not mechanistically linked.[20] Assignment of the precursor as a singlet excited-state also makes sense from the point of view of the direct generation of a ground state carbanion in a spin-allowed process.

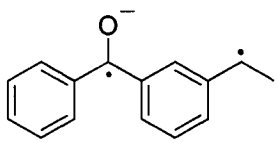

Scheme 5.2 Alternate structure of the transient resulting from ketoprofenate photolysis.

The assignment of the transient generated following decarboxylation of ketoprofenate as carbanionic is also supported by subsequent studies of the

reactivity of this species, including the results presented later in this chapter. In a contemporaneous series of examples, ketoprofenate derivatives having long alkyl chains capped with a labile leaving group were prepared and the competition between protonation of the carbanion and the intramolecular S_N2 reaction was studied.[22-24]

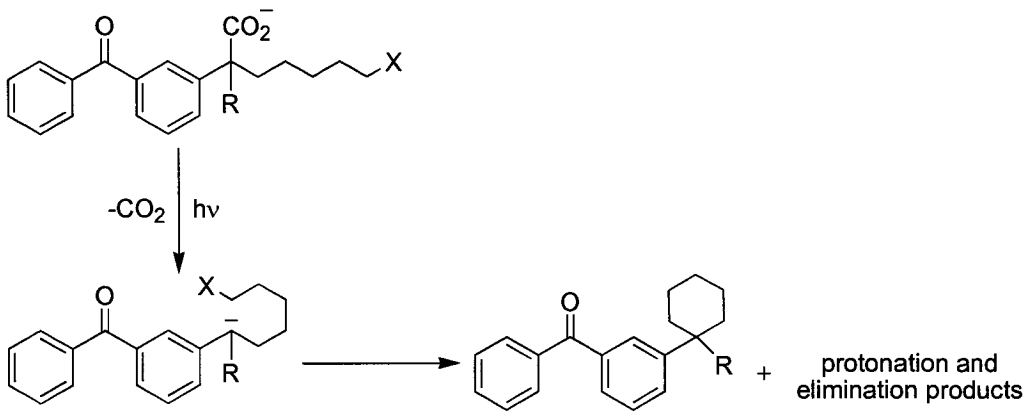

Scheme 5.3 Intramolecular S_N2 reaction of modified ketoprofen.[22-24]

Another clever exploitation of ketoprofen photochemistry, which further demonstrates the carbanionic nature of the transient, involves the use of modified ketoprofens for the photorelease of selected moieties.[25] In this work, a leaving group was substituted α to the benzylic position on ketoprofen. Upon irradiation, the carbanion is generated and rapidly undergoes an elimination reaction, liberating the appended substituent. The elimination reaction competes with protonation of the carbanion and its success rate is determined by the nature of the leaving group. This chemistry is currently being exploited for the development of photocages for the photorelease of biologically relevant molecules.[25]

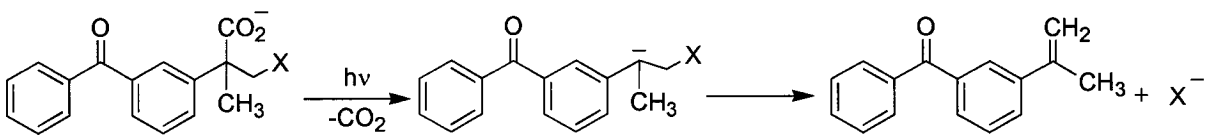

Scheme 5.4 Photorelease of X^- from a modified ketoprofen.[25]

5.2 Nature of the Ketoprofenate Excited State

5.2.1 Solvent Dependent Observation of Reactive Intermediates

As mentioned in the previous section, there exists a solvent system where both the triplet state and the carbanion intermediate derived from KP can be simultaneously observed. In buffered aqueous solutions, laser flash photolysis of ketoprofen gives rise to a relatively short-lived transient absorbing at *ca.* 580 nm which has been assigned to the benzylic carbanion resulting from decarboxylation (Scheme 5.1).[17] In 95% acetonitrile (ACN) solutions (5% water v/v) containing sufficient base to fully deprotonate the carboxylic acid, the transient absorption spectrum shows two distinct species both appearing within the laser pulse.[20] The transient species absorbing at *ca.* 600 nm had a lifetime of 25-30 ns and was spectroscopically similar to that obtained in aqueous buffered solutions. The absorption at *ca.* 525 nm was longer lived and was efficiently quenched by both 1,3-cyclohexadiene and biphenyl, confirming its triplet nature. The yield and lifetime of the 600 nm transient were not affected by the presence of triplet quenchers and this absorption was assigned to the carbanion.

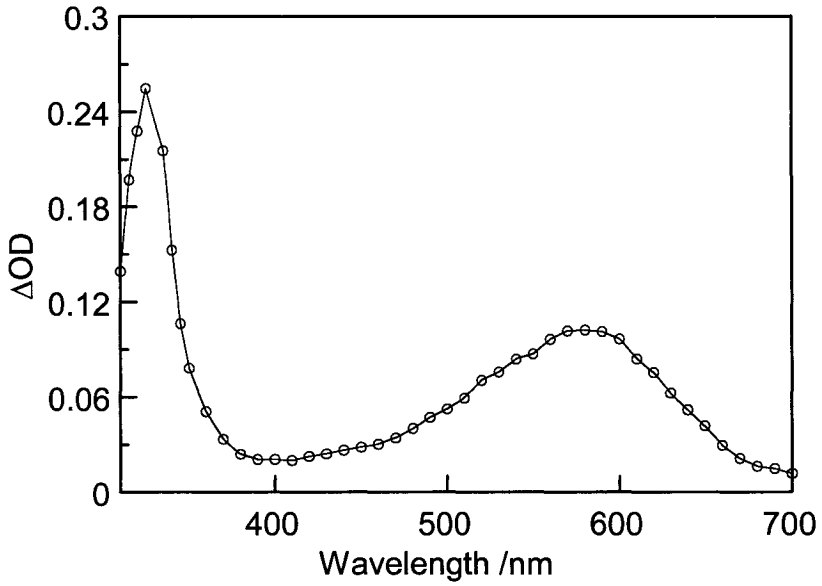

Figure 5.2 Transient absorption spectrum recorded 55 ns after 308 nm laser excitation of a 4.0×10^{-4} M methanol solution of KP containing 10 mM sodium methoxide.

These results confirm that the carbanion and the triplet species are not mechanistically linked however, they also raise the question of why the triplet is not observed in basic solutions of higher polarity? In the following sections, we propose a possible explanation for this behaviour and present the results of preliminary studies aimed at understanding the interesting results described above. The instrumentation available in the time-resolved spectroscopy laboratory at the University of Ottawa is not capable of the time resolution necessary to investigate the proposed hypotheses and so these preliminary studies were made possible by the generous and serendipitous donation of instrument time by the Central Laser Facility at the Rutherford Appleton Laboratories in Didcot, United Kingdom. Thanks to Drs. Anthony Parker, Pavel Matousek, and Michael Towrie for their assistance during this brief visit.

5.2.2 Suggested Mechanism for Solvent Dependence

Assuming that the precursor to the carbanion is the ketoprofenate singlet excited-state, and based on the reported observations, we hypothesize that, in fully

aqueous systems the decarboxylation of ketoprofenate occurs exclusively, with the complete suppression of intersystem crossing. In other words the rate constant for decarboxylation would be greater than the rate constant for intersystem crossing (ISC), $k_{-CO2} > k_{ISC}$. In more apolar solvent systems (95% acetonitrile), both the triplet excited-state and the singlet-derived carbanion are observed, indicating that the rate constant for ISC has become competitive with the rate constant for decarboxylation, $k_{-CO2} \approx k_{ISC}$. Product studies revealed no difference in the quantum yield of photodegradation for KP^- studied in buffered aqueous solutions versus basic acetonitrile solutions (5% water v/v) suggesting that k_{-CO2} has not changed. A higher rate constant for ISC in ACN than in water, $k_{ISC}(ACN) > k_{ISC}(H_2O)$ may explain the observed results.

In benzophenone itself, population of the triplet state is generally accepted to occur via a fast ($k \sim 10^{11}$ s^{-1}) intersystem crossing from the lowest singlet excited-state, which is n,π^* in nature, to a close lying upper triplet excited-state with π,π^* character.[26] Rapid internal conversion follows, populating the lowest triplet excited-state. The T_1 state in benzophenone is n,π^*, giving rise to the well-known alkoxyl radical-like behaviour of benzophenone triplet states.[26] The configuration of the lowest triplet excited-state in BP is n,π^* in both polar and non-polar solvents; only the presence of strongly electron-donating groups have made it possible to observe an induced inversion of configuration.[27-29]

The extremely rapid and efficient ISC observed in benzophenone (Figure 5.3) can be ascribed to both the energetic proximity between the singlet and the triplet states as well as the change in orbital symmetry on going from the S_1 (n,π^*) to T_2 (π,π^*). This can be understood in terms of selection rules (also called El-Sayed's rules) which emphasize that the transition to a state having the same orbital symmetry as the originating state is "forbidden", in part due to an absence of spin-orbit coupling.[26, 30-32] All other considerations being equal, a forbidden transition will proceed more slowly than an allowed transition according to these rules.

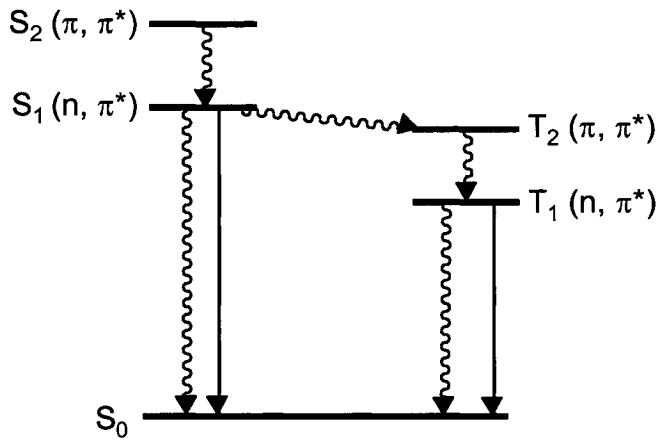

Figure 5.3 State diagram for benzophenone showing approximate energy levels (not to scale). Wavy lines indicate radiationless transitions.

Based on this information, we suggest that solvent dependent formation of the KP^- triplet may be caused by a solvent-induced state inversion. If the intersystem crossing process in KP^- switches from an allowed transition in organic solvents to a forbidden transition in aqueous systems, this may explain the observation of the triplet state in 95% ACN but not in phosphate buffer solution (PBS). Assuming that the state diagram for KP^- in acetonitrile is similar to that given for BP in Figure 5.3, ISC would be an allowed transition proceeding from S_1 (n,π^*) to T_2 (π,π^*) and undergoing internal conversion to populate T_1 (n,π^*). In water, a change or inversion in the triplet energy levels could result in the n,π^* triplet energy being higher than or equal to the energy of the π,π^* triplet. Increased solvent polarity stabilizes polar π,π^* states and causes a hypsochromic shift in the energy of n,π^* transitions.[26] A state inversion or increased state mixing would cause the ISC process in water to become less allowed, consequently, the ISC rate constant would decrease. This behaviour would be similar to that observed for 4-methoxybenzophenone, where the nature of the lowest triplet excited-state state was found to be π,π^* in water.[29]

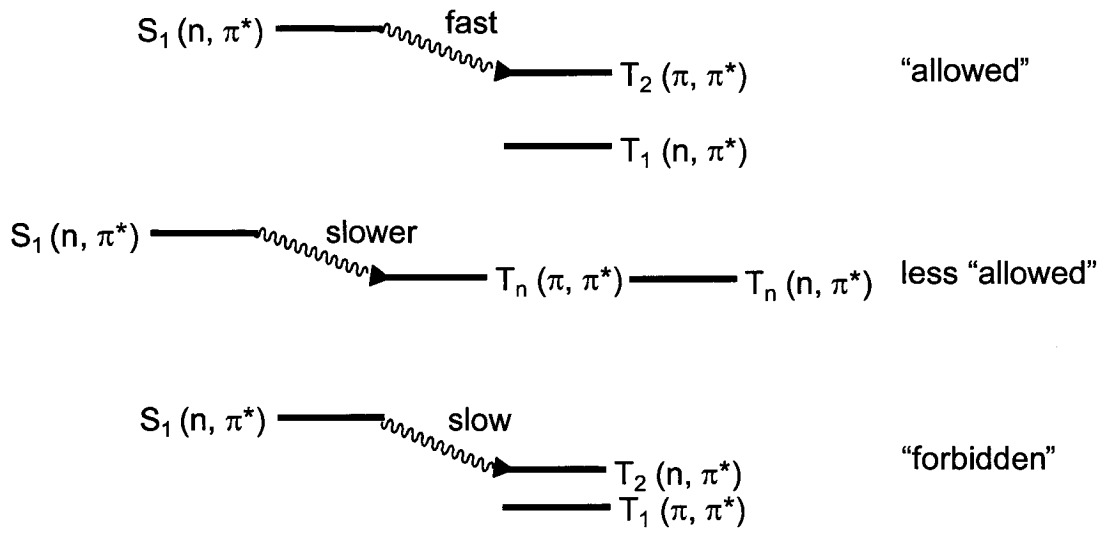

Figure 5.4 Pictorial description of the implications of triplet energy level changes.

As alluded to above, a slower ISC rate in water would allow decarboxylation from the singlet manifold to compete more effectively, ultimately suppressing the ISC mode. In a KP^- analogue, not having a pathway of chemical reactivity from the singlet manifold, this process should manifest itself as an increased quantum yield for emission and a slower rise time for the triplet as the competing mode for singlet depletion (i.e. ISC) becomes less efficient. In order to test this hypothesis, the photophysical properties of a ketoprofen analogue (3-methylbenzophenone, MB) were investigated in a series of solvents with varying polarities.

5.2.3 Photophysics of a Ketoprofen Analogue

One of the implications of a reduced intersystem crossing rate constant may be an increase in the radiative deactivation of the singlet excited-state. Most simple, substituted benzophenones exhibit extremely efficient ISC and, therefore, little to no fluorescence. However, if k_{ISC} is decreased in aqueous systems, this may be accompanied by a measurable increase in fluorescence. The emission spectra of optically matched solutions of MB in deaerated hexane, acetonitrile, and 96% water (4% ACN v/v) are shown below in Figure 5.5. It should be noted that the π,π* absorption band of MB shows a bathochromic shift in the absorption maximum as

well as broadening on going from hexane (λ_{max} = 246 nm), to acetonitrile (λ_{max} = 251 nm), to 96% water (λ_{max} = 265 nm).

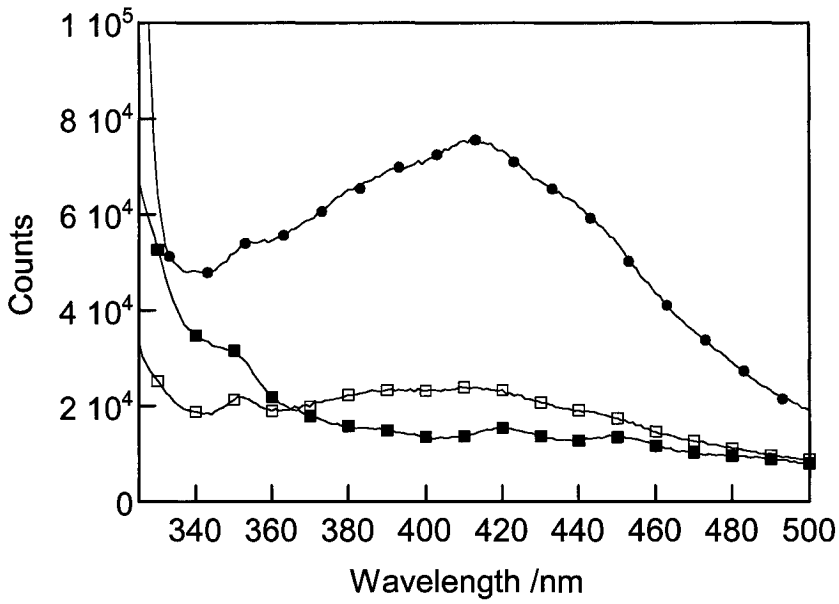

Figure 5.5 Emission spectra of 3-methylbenzophenone in 96% water (●), acetonitrile (□), and hexane (■). Solutions were optically matched at the excitation wavelength (288 nm) with an absorbance of 0.1.

The relative quantum yields can be calculated using the following equation:[33]

Equation 5.1

$$\frac{\Phi_a}{\Phi_b} = \frac{I_a OD_b \eta_a^2}{I_b OD_a \eta_b^2}$$

giving values of Φ_{hexane}/Φ_{H2O} = 0.022 and Φ_{ACN}/Φ_{H2O} = 0.14. As can be seen from Figure 5.5 and by the relative quantum yields, there is a small increase in the fluorescence yield with increasing solvent polarity. This preliminary result encouraged us to pursue the measurement of triplet rise times for our substrate in solvents of different polarity.

Measurements of k_{growth} for the triplet-triplet absorption of MB were recorded using the pump-probe technique describe in Section 2.4 of this thesis. Solutions were excited with 267 nm pulses from a femtosecond laser and the

changes in absorbance were detected with a 512-pixel diode array camera. Due to the nature of the detection system, a full spectral profile is obtained at several pre-selected time delays and the ΔOD values at a selected wavelength are subsequently plotted versus delay time to construct a kinetic trace. Figure 5.6 below shows the spectral profiles obtained in each of the four solvent systems, 200 ps after the laser pulse.

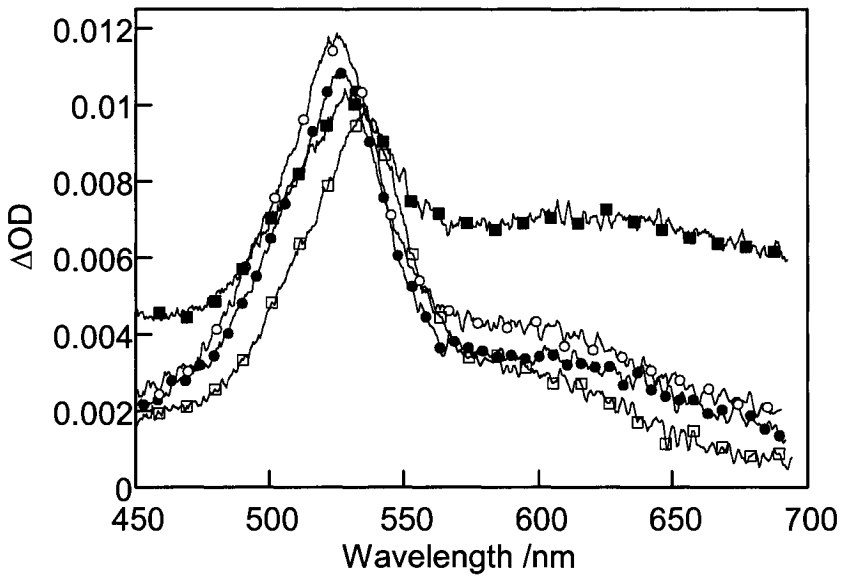

Figure 5.6 Transient absorption spectrum recorded 200 ps after 267 nm excitation of 3-methylbenzophenone in hexane (□, 9.9 x 10^{-4} M), acetonitrile (●, 7.3 x 10^{-4} M), ethanol (○, 4.4 x 10^{-4} M), and 90% water (■, 4.7x 10^{-4} M).

The peak, which appears over time, at *ca.* 525 nm is assigned to the triplet-triplet absorption spectrum of MB. The broad absorption observed at long wavelengths, in aqueous solution is assigned to the solvated electron resulting from photoionization. Photoionization is not expected to be significant in solvents of lower polarity.[17] The spectrum recorded in acetonitrile (Figure 5.7) is in excellent agreement with the published spectra of benzophenone recorded following irradiation with ultrashort laser pulses at 355-360 nm.[34, 35] Immediately after excitation, the spectrum has a maximum at *ca.* 575 nm, with increasing delay time the profile changes as the peak at 525 nm grows in. The 575 nm band has been

previously assigned to the benzophenone $S_1 \rightarrow S_n$ transition and it seems reasonable to also assign it as such in this case.[34]

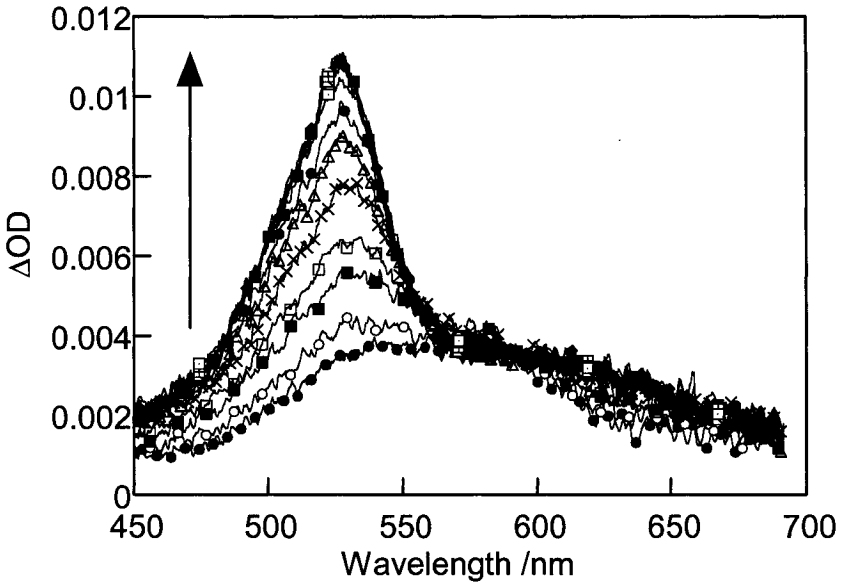

Figure 5.7 Transient absorption spectrum of 7.3 x 10^{-4} M 3-methylbenzophenone in acetonitrile 2 to 500 ps after 267 nm excitation.

The rise time of the triplet signal was calculated by averaging the ΔOD values between 520 and 530 nm and plotting the averaged values versus the delay time (Figure 5.8). The data were fitted with a first order growth expression giving the formation times for the triplet in each solvent τ_{growth} or $\tau_{formation}$ (Table 5.1).

Equation 5.2

$$\tau_{growth} = k_{obs}^{-1} = \left(k_{ISC} + k_{IC} + k_f\right)^{-1}$$

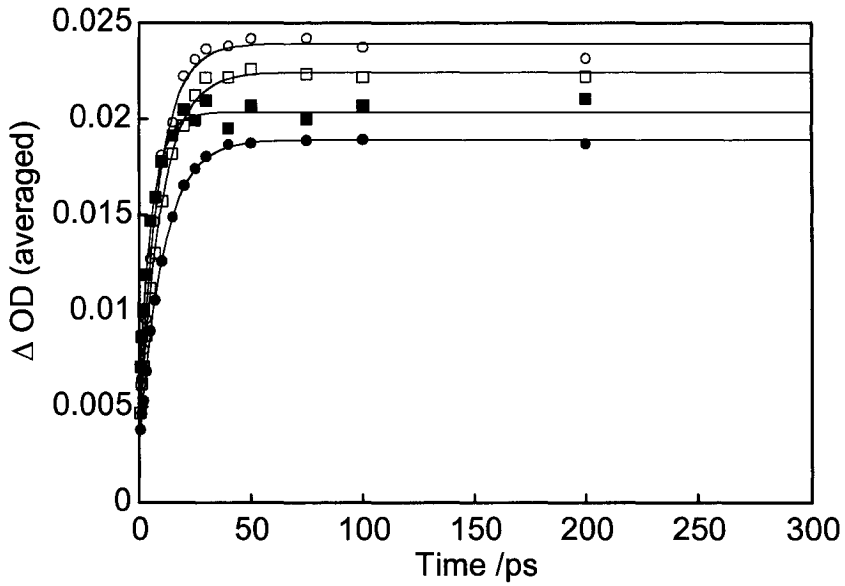

Figure 5.8 Change in absorbance following 267 nm excitation of 3-methylbenzophenone in hexane (●, 9.9 x 10^{-4} M), acetonitrile (□, 7.3 x 10^{-4} M), ethanol (○, 4.4 x 10^{-4} M), and 90% water (■, 4.7x 10^{-4} M).

Solvent	$E_T(30)$	α_H	k_{obs}	τ_{growth}
n-hexane	31.0	0.0	9.3 x 10^{10} s^{-1}	10.8 ps
acetonitrile	45.6	0.19	1.0 x 10^{10} s^{-1}	10 ps
ethanol	51.9	0.86	1.1 x 10^{11} s^{-1}	8.9 ps
90% water[a]	~ 63.1	~ 1.17	1.7 x 10^{11} s^{-1}	5.7 ps

Table 5.1 $E_T(30)$, H-bond donor ability (α_H), and photophysical data for the solvents measured.[36] [a]10% acetonitrile v/v.

As can be seen in Table 5.1 and Figure 5.9 there is a small solvent dependence for the rate constant of triplet formation. The trend is generally one of decreasing formation time for the triplet with increasing solvent polarity (as described by $E_T(30)$ values and hydrogen-bond donating ability, α_H).[36] This observation is contrary to the proposed explanation for the solvent dependent photochemistry of ketoprofen. However, the trend does agree with earlier studies

of benzophenone photophysics using picosecond laser flash photolysis[37] and xanthones examined with femtosecond laser flash photolysis.[38]

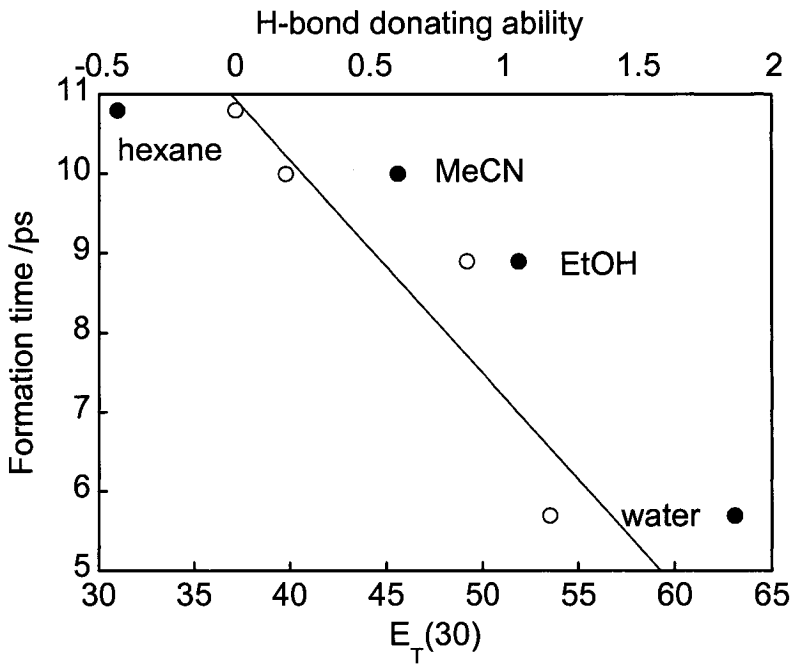

Figure 5.9 Plot of k_{growth} versus $E_T(30)$ (●) and H-bond donating ability (○) for the solvents studied.

5.2.4 Conclusions to this Section

The original hypothesis was that observation of the KP^- triplet state in acetonitrile was the result of an improved rate constant for intersystem crossing in this solvent. The measurement of triplet growth kinetics for a KP analogue indicate that this is not the case, k_{obs} is actually slightly larger in polar, hydroxylic solvents. This indicates that the appearance of the triplet signal in basic acetonitrile is probably not the result of a faster intersystem crossing in this solvent. The unexpected increase in fluorescence, which is measurable but modest, may be attributed to an increase in the π,π* character of the S_1 state in polar solvents. Polar solvents have a stabilizing effect on the polar π,π* state and, to a lesser extent, a destabilizing effect on the apolar n,π* state, these effects may combine to increase

the contribtution from an upper $S_n(\pi,\pi^*)$ state to the $S_1(n,\pi^*)$ state.[26] The oscillator strength for $S_0 \leftrightarrow S_n$ transitions is much higher for π,π^* states causing the observed increase in the fluorescence.[26] An S_1 state with more π,π^* character may explain the increased fluorescence but it does not explain the observed increase in k_{obs}. The value of k_{obs} increases by a factor of two on going from hexane to aqueous acetonitrile. Assuming an upper value of $k_f = 10^8$ in hexane, the increase in the fluorescence rate constant in water would have to be greater than three orders of magnitude to cause the observed increase in k_{obs}. This leads us to suggest that the increase in k_{obs} may be largely due to an increase in k_{ISC}. The observed trend can perhaps be explained by comparison with similar behaviour observed for xanthone. Cavaleri *et al.* have suggested that solvent dependence in k_{ISC} may be due to an "inverse gap effect".[38] Increased solvent polarity may increase the singlet-triplet energy gap (ΔE_{ST}) without resulting in a change in the ordering of states. One might expect that a larger energy gap would decrease the ISC rate constant, however, the coupling between singlet and triplet manifolds is closely related to the density of triplet vibronic states isoenergetic with the singlet state. As a result, an increase in ΔE_{ST} may cause there to be more triplet vibronic levels at the same energy as the singlet, thereby increasing the intersystem crossing rate constant. This explanation has also been invoked to explain the intersystem crossing kinetics in diphenylcarbenes.[39] Ultimately, there is no way to confirm or exclude the suggested explanations based on the preliminary data collected here.

In conclusion, based on the behaviour of MB, it has been determined that formation of the KP^- triplet excited-state in acetonitrile, but not in water, is unrelated to the relative rates of intersystem crossing in these two solvents. Ultimately, it should be noted that MB is only a simple analogue of KP and its behaviour cannot account for all of the reactive modes available in KP itself. In the course of these studies the interesting solvent dependent photobehaviour of MB has been observed and the increase in k_{ISC} with solvent polarity has been attributed to the "inverse gap effect" in analogy to similar behaviour observed for xanthone.

5.3 Reactivity of the Carbanion Intermediate

The intermediate formed following ketoprofenate photolysis in basic solution has the properties of a ground state carbanion, undergoing rapid protonation to give 3-ethylbenzophenone as the primary photoproduct.[4, 16] The fast protonation reaction precludes the observation of other carbanion-like chemistry. If the carbanion could be further stabilized or generated in the absence of a proton source it may then be possible to observe other reactive pathways.

As demonstrated in Chapters 3 and 4 of this thesis, zeolites can be convenient matrices for the stabilization of reactive species, such as cations. It has been demonstrated that some carbocations, having a submillisecond lifetime in solution, become indefinitely persistent when incorporated inside the rigid framework of a zeolite; for example dibenzotropylium cation in HZSM-5. Considering the overall negative framework charge for all aluminum containing zeolites, the incorporation and stabilization of positively charged species is intuitive. By this same reasoning, zeolites as negatively charged, solid polyelectrolytes, could be expected to impede the absorption and diffusion of negative ions by electrostatic repulsion. There is a general belief that zeolites cannot incorporate and/or stabilize carbanions and as a result very little effort has been devoted to the study of the properties of reactive carbanions absorbed in zeolites.[40, 41] The results presented herein disabuse the widely accepted notion that zeolites are ineffective hosts for reactive, negatively charged species.

5.3.1 Preparation of KP@Y

Despite the fact that the negative zeolite framework may not provide the best electrostatic environment for the incorporation of a negatively charged species, it was reasoned that if the carboxylate form of KP could be generated within the zeolite, the matrix might provide a convenient environment for generation of the carbanion intermediate in the absence of water or other proton sources. If protonation is suppressed, other modes of reaction may be observed. The inclusion

complex, KP@Y, was prepared by two methods. In the first, KP was included directly by contacting a DCM solution of KP with a sample of thermally dehydrated zeolite NaY. It has been reported that xanthene-9-carboxylic acid incorporated in various alkali-metal exchanged zeolites undergoes spontaneous deprotonation to a degree that depends on the Brønstead basicity of the host. In Na^+-exchanged zeolites the IR spectra had bands for both the carboxylate and the acid, while in the more basic Cs^+-exchanged zeolite only the carboxylate ion band was observed.[42] In analogy with this system, the ketoprofenate ion may be expected to form spontaneously upon inclusion of the acid in zeolite NaY.

In the second preparation method, ketoprofen was dissolved in methanol with an excess of sodium methoxide base. This basic solution, where the deprotonated form of KP should predominate, was contacted with a thermally dehydrated sample of NaY and the slurry stirred for several hours. In both methods, as result of high the quantum yield of decarboxylation, it is imperative to avoid exposure of the slurries to light, both during the preparation and up to the time of intended experimental use. In both cases the objective is to prepare a material where the ketoprofenate species is encapsulated within the zeolite and water has been completely excluded. For this reason, following stirring of the slurries, solvent was removed by drying under vacuum (> 50 mTorr) resulting in a dehydrated and solvent-free sample. Samples were either used immediately or stored for short periods of time under vacuum and protected from light.

Surprisingly, in spite of the negative framework, both preparations yielded the desired material, as indicated by spectroscopic analysis. The diffuse reflectance spectrum recorded of the prepared material KP@Y (either preparation) is in very good agreement with the spectrum of KP recorded in PBS at pH 7.4 (Figure 5.10 below). The slight shift in maxima is commonly observed for benzophenone and its derivatives with increasing polarity of the environment. The IR spectrum recorded of an outgassed, self-supported wafer of the sample prepared by the first method, is similar to the spectrum of KP in a KBr disc except that the band at 1716 cm^{-1},

consistent with the carbonyl stretching of the acid group, is much weaker. The carbonyl of benzophenone is conjugated to two benzene rings and will appear at lower frequencies (*ca.* 1650 cm^{-1}) as will the signal for the asymmetric stretching of the partially double bonded C-O groups in the carboxylate ion. The sample from the second preparation method also has a weak band at 1716 cm^{-1}, indicating that the acid is largely deprotonated. Unfortunately the O-H stretching region is not a useful diagnostic region for zeolite samples due to the possible presence of water and surface silanol groups.

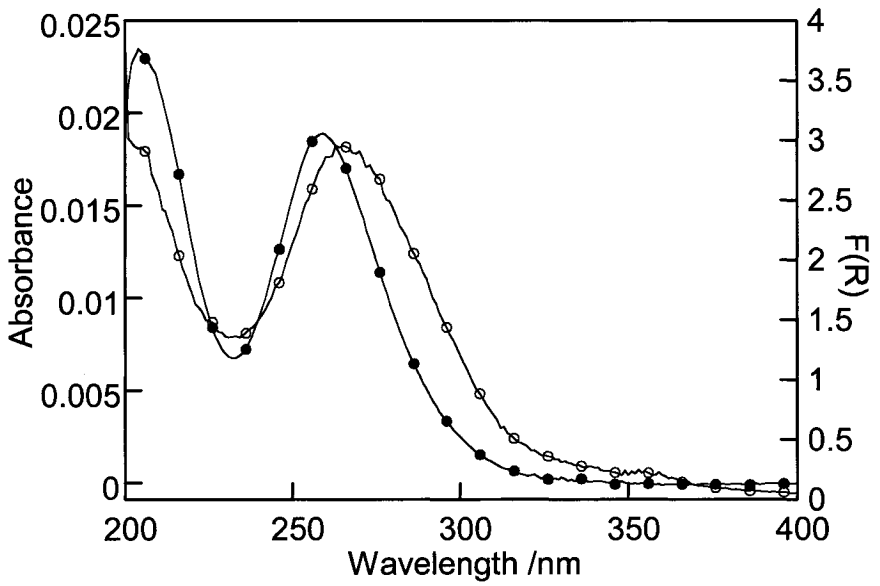

Figure 5.10 UV-vis absorption spectrum of 1.2 x 10^{-5} M KP in PBS (pH 7.4) (●) and diffuse reflectance spectrum of KP@Y under vacuum (O) plotted as the Kubelka-Munk function of the reflectance.

The first preparation methodology was simple and efficient in terms of zeolite loading, presumably since it involved the inclusion of a neutral species. This methodology had the advantage that the inclusion solvent is much more volatile and less likely to be contaminated with water. However, in deprotonating the acid outside of the zeolite micropores, the second preparation method avoids contaminating the zeolite interior with excess protons. The products from treating KP with sodium methoxide in methanol are simply methanol and sodium

ketoprofenate, methanol should be removed under vacuum and sodium ions are already present within the zeolite as charge-balancing cations. Early preparative studies and time-resolved experiments were carried out with samples prepared by the first method. Later, in light of difficulties encountered, *vide infra*, product studies were conducted using samples prepared by the second method in hopes that fewer in-cage protons would improve the results. When sealed under vacuum and not exposed to light, these samples showed no variation in spectroscopic properties for periods of weeks.

5.3.2 Intrazeolite Decarboxylation

Having successfully included KP^- in the cavities of zeolite NaY, it remained to be seen whether or not the photochemistry observed in solution would occur intrazeolitically. The solvent-free solid was sealed under vacuum and the transient diffuse reflectance spectrum was recorded (Figure 5.11). As can be seen by comparing Figure 5.11 with the transient absorption spectrum recorded in basic solution (Figure 5.2), formation of the same transient is observed upon photolysis of KP@Y. Irradiation of ketoprofenate encapsulated in zeolite NaY results in photodecarboxylation of the carboxylate to generate the benzylic carbanion, exactly as seen in solution.

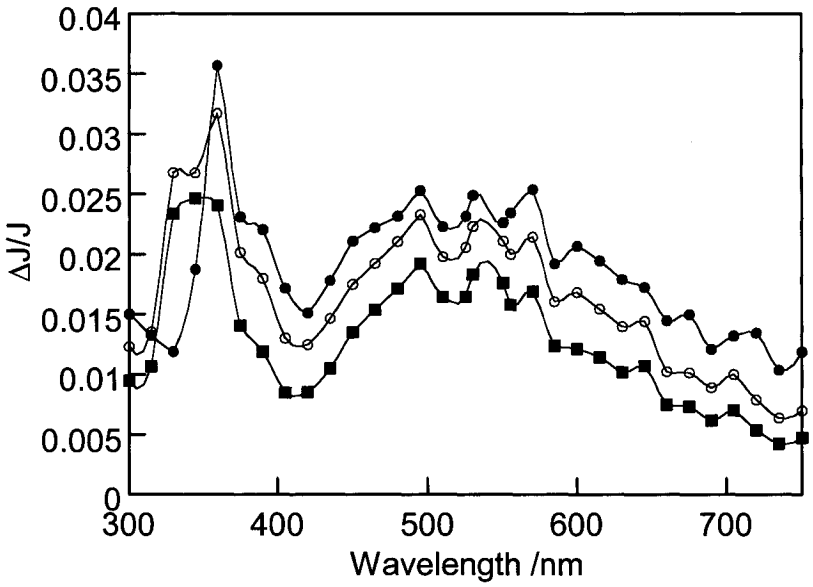

Figure 5.11 Transient DRS recorded 1.36 μs (●), 4.72 μs (○), and 14.5 μs (■) after 266 nm laser excitation of a vacuum sealed sample of KP@Y.

While observation of the intrazeolite photodecarboxylation is itself interesting, more remarkable is the lifetime of the carbanion generated within the zeolite cavities. The observed transient decays much more slowly than the corresponding species in solution ($\tau \sim 210$ ns in aqueous systems) and its disappearance no longer follows pseudo-monoexponential kinetics. In zeolites the carbanion now decays with complex kinetics and lifetime distribution analysis reveals three modes of decay. The results of a distribution analysis (described in Section 2.2.4) are given in Figure 5.12. The longest lifetime component ($\tau = 9.5$ μs) represents an increase of approximately fifty times compared to values measured in buffered solution, and is experienced by more than half of the transients. The values obtained vary slightly depending on unavoidable exposure to ambient moisture during sample handling but are reproducible within ± 100 ns for the short-lived components and ± 2 μs for the longer lifetime. The distributions are remarkably narrow suggesting the presence of discrete, well-defined sites.

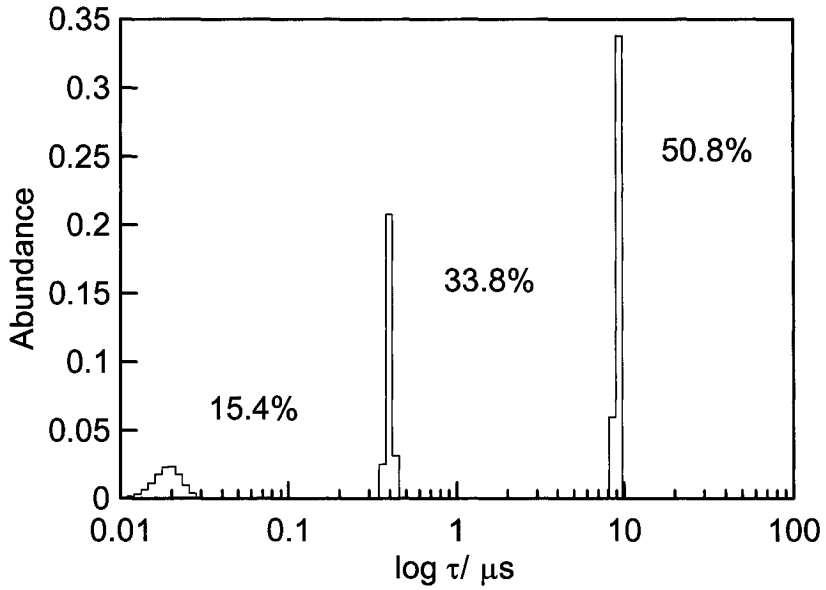

Figure 5.12 Lifetime distribution analysis compiled from kinetic data acquired at 600 nm at various times after 266 nm excitation of KP@Y under vacuum.

The multi-exponential behaviour observed suggests that the carbanion experiences more than one environment within the zeolite cavities. This is not an uncommon situation in zeolites where a distribution of sites frequently results in the observation of multi-modal behaviour. In the case of the encapsulated carbanion, while each individual NaY supercage must have the same structure, the water content or distribution of acids sites may vary from cage to cage. The shorter lifetimes may indicate locations within the zeolite where protonation is easy and does not require extensive migration. In fact, the shortest lifetimes (*ca.* 20 ns) may reflect the behaviour of carbanions generated adjacent to water molecules and protonated with very little barrier. Extremely long-lived carbanions may owe their longevity to the lack of nearby water molecules and/or a stabilizing interaction with the zeolite charge-balancing cations. This interaction can be imagined as analogous to the stabilization observed in Grignard reagents or organosodium species in the Wurtz reaction. The observed lifetime enhancements provided the

exciting possibility of novel nucleophilic addition chemistry; essentially Grignard-like chemistry triggered photochemically, in supramolecular systems.

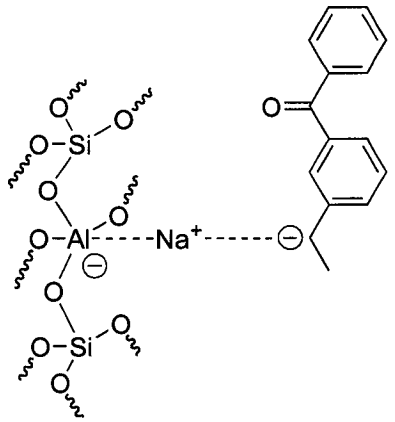

Scheme 5.5 Schematic representation of a possible carbanion stabilization mode in NaY.

5.3.3 Intrazeolite Carbanion Reactivity

The lifetimes given above were measured using a sample sealed under vacuum and with care taken to exclude water. If water is re-introduced into the system, the observed signal should be quenched as the carbanion is protonated to give 3-ethylbenzophenone. The signal following laser excitation was monitored at 600 nm for a sample prepared in the same manner as above (i.e. dry and in vacuo) and this sample was then exposed to water saturated nitrogen and the signal at 600 nm re-measured. Faujasitic zeolite NaY is hydrophilic and will absorb water readily. The data given in Figure 5.13 were fitted bi-exponentially as an approximation for the purposes of comparison. It is obvious from Figure 5.13 that co-inclusion of water in the zeolite results in a marked decrease in the lifetime of the observed transient, as expected. The long lifetime component of the decay, as estimated by the bi-exponential fitting, decreased from 8.4 μs to 3.4 μs and the shorter component from 650 ns to 450 ns.

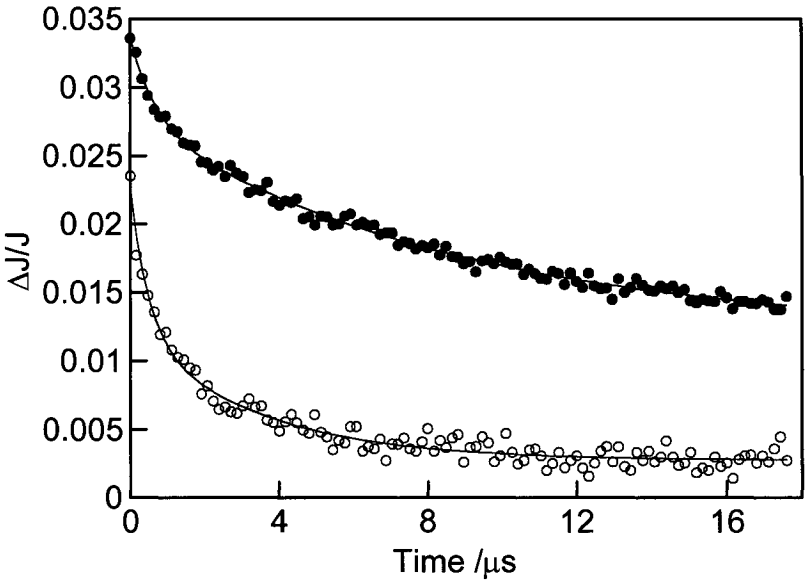

Figure 5.13 Signal recorded at 600 nm following 266 nm excitation of a sample of KP@Y under vacuum (●) and after exposure to moisture (○).

When a water-saturated sample was irradiated in a steady-state fashion and subjected to solid-liquid extraction with organic solvent (DCM or ethyl acetate), EB was recovered almost exclusively. This product confirms that the reduced lifetime in the presence of moisture, results from water-mediated protonation of the carbanion. The encapsulated system containing water clearly behaves in much the same way as the system in aqueous or alcoholic media. However, in the supramolecular system, there is the option of excluding water and introducing other electrophilic scavengers enabling the observation of novel intrazeolitic addition reactions.

In order to observe lifetime reductions associated with reaction of the carbanion with various electrophiles, a special cell for time-resolved diffuse reflectance studies was devised. The cell was constructed of quartz with the typical 3 x 7 mm^2 rectangular portion to contain the solid sample, and a long neck allowing the cell to be evacuated and sealed. Built into the neck was a side-arm permitting a liquid quencher to be added and frozen to a solid, before the zeolite sample is placed in the main part of the cell and the entire system placed under vacuum (see

Figure 5.14). This arrangement allows the experiment to be conducted with the minimum possible exposure to ambient moisture prior to photolysis.

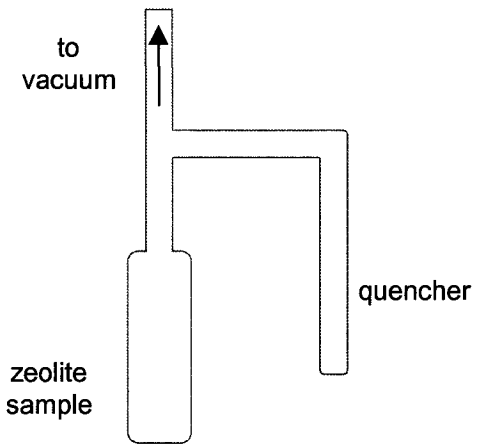

Figure 5.14 Schematic of the laser cell used for examining quencher effects on carbanion lifetime in the absence of moisture.

In analogy with Grignard-type chemistry, the reactivity of the carbanion transient with alkylhalides was investigated. We chose to investigate the reaction with bromoalkanes, reasoning that they would be more reactive than the chloro-analogues and avoid the possible photolability of iodoalkanes. 1-Bromoethane was placed in the cell side-arm and frozen by immersion in liquid nitrogen. KP@Y was added to the main part of the cell with efforts made to minimize exposure to ambient moisture. The cell was evacuated at *ca.* 50 mTorr with the quencher kept frozen. After evacuation, the laser cell was flame sealed and the DR-LFP experiment was conducted. The decay was monitored at 600 nm following 266 nm excitation of the zeolite, while the quencher was still frozen, and re-recorded after the quencher had thawed and diffused into the zeolite. The results of this experiment for 1-bromoethane are shown in Figure 5.15.

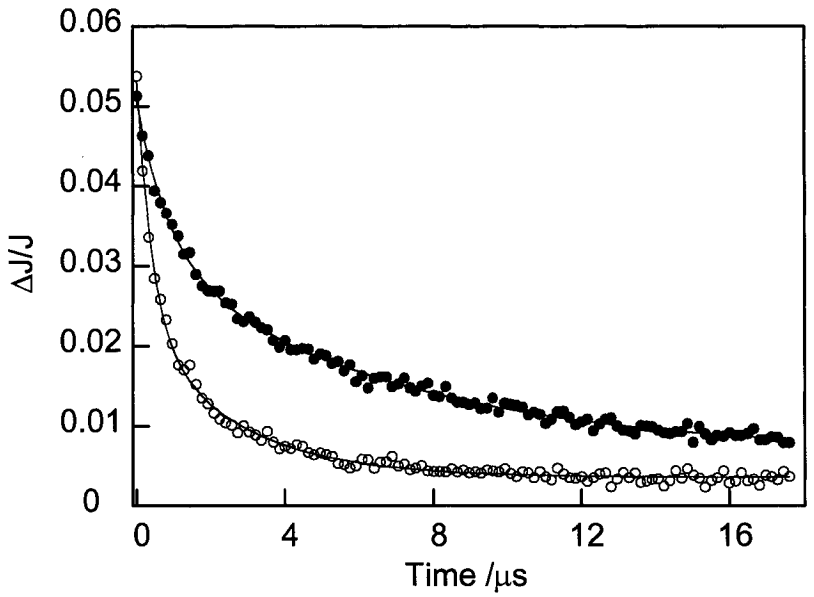

Figure 5.15 Signal recorded at 600 nm following 266 nm excitation of a sample of KP@Y under vacuum in the presence of frozen (●) and thawed (○) 1-bromoethane, <S> ~ 2.

There is a distinct decrease in the observed lifetime after exposure of KP@Y to the alkylhalide. Fitting the data bi-exponentially gives τ_1 = 6.5 μs and τ_2 = 860 ns prior to the start of quencher thawing and τ_1 = 3.1 μs and τ_2 = 580 ns one minute after the start of thawing. Given that the system is sealed under vacuum it is reasonable to attribute the observed lifetime reduction to an interaction between the carbanion and the bromoalkane to yield the butyl-substituted benzophenone.

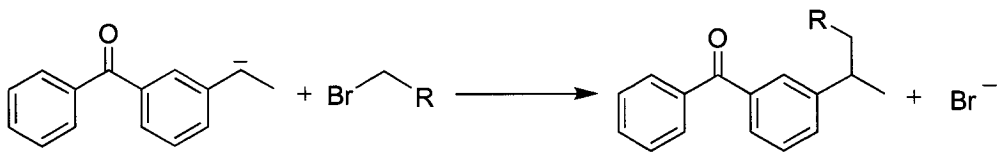

Scheme 5.6 Reaction of KP-derived carbanion with a 1-bromoalkane.

Product studies were conducted in order to confirm that the modified transient kinetics were due to a nucleophilic addition-type reaction. For these studies KP@Y was first prepared and subsequently loaded with the substrate of choice (loadings of <S> ~ 1-2 were achieved). The solid was irradiated with a lamp

for several hours and then subjected to Soxhlet extraction to collect the reaction products. Products were analyzed and identified by gas chromatography with flame ionization detection (GC-FID) or mass spectrometric detection (GC-MS) and comparison with authentic samples.

In the course of these studies it became obvious that extreme care must be taken to exclude water from the zeolite sample. Numerous experimental protocols were investigated before arriving at the procedure described in detail in Section 5.4.3. One interesting facet of the final protocol was the use of perfluorohexane as the slurry solvent for irradiation. Irradiation of zeolite powders as dry solids has the disadvantage of non-homogenous exposure and, as a result, zeolite samples are often irradiated as slurries in organic solvents. Although exposure is improved in a stirred slurry, the disadvantage is that many organic solvents are not chemically inert and any substrate exhibiting low affinity for the zeolite interior may be "washed" out of the zeolite cavity by the slurry solvent. Perfluorous solvents have no reported intrazeolite reactivity and the reduced solubility of most organic compounds in fluorinated as compared to hydrocarbon solvents should reduce the likelihood of substrate migration out of the cage.[43] For this application, perfluorinated solvents also have the advantage of low water solubility and high volatility for easy removal. To our knowledge this example, along with the clever use of perfluorinated solvents for investigating intrazeolite photooxidation reactions, are the first reported uses of perfluorinated solvents in intrazeolite photochemistry.[44]

When a perfluorohexane slurry of KP@Y loaded with 1-bromoethane was irradiated at 254 nm in a quartz vessel with stirring, analysis of the extracted material revealed that 3-ethylbenzophenone was the overwhelmingly major product (*m/z* 211, 210(M^+), 181, 133(100), 105, 77). This was the case for samples co-incorporating 1-bromoethane, 1-bromobutane, and 1-bromopentane. Despite intense efforts to exclude water and oxygen, EB remained the major product. In the case of 1-bromoethane and 1-bromobutane, comparison with authentic samples of

the product resulting from reaction between the carbanion and the bromoalkane, revealed that these products are formed, but are present in the zeolite extraction solution in minute amounts. A small amount of a product having *m/z* 209 was also observed in each case and will be discussed later. Irradiations were also performed using 300 nm lamps and/or a Pyrex filter in order to avoid potential complications arising from irradiation of the alkyl halide. Neither modification had a significant impact on the results.

In order to determine the reason behind the lack of significant product formation, it was necessary to confirm that the EB recovered from the extraction solution was formed during the irradiation and not as a result of accidental light-exposure prior to the experiment. Ketoprofen has a weak absorption in the UVA that tails into the visible. Although the molar absorption coefficient is on the order of *ca.* 10^2 M^{-1} cm^{-1}, the photodecarboxylation chemistry is so efficient that significant photolysis by ambient light is possible. If encapsulated KP^- was unintentionally photolyzed prior to addition of the bromoalkane, low yields of the addition product may be attributed to the presence of EB within the zeolite cavities at the time of irradiation instead of KP^-. To confirm that the carboxylate species was still present at the time of irradiation, the above experiment was repeated in the presence of deuterium oxide (D_2O) instead of bromoalkane. Analysis of the extraction solution by GC-MS showed an enhancement at *m/z* 211 (3-ethylbenzophenone-*d*) as well as a new peak at *m/z* 212 (M+1) indicating that ketoprofenate was indeed present at the time of the photolysis and underwent the expected decarboxylation followed by deuteration of the carbanion by D_2O to give the deuterated product (*m/z* 212, 211(M^+), 210, 181, 134(100), 106, 105, 77). An un-irradiated sample of KP@Y was subjected to the same extraction protocol and the recovered yield of EB was > 100 times less (by GC-FID) than in a sample which had been irradiated, supporting the idea that significant quantities of encapsulated KP^- survive the sample handling and the majority of EB is produced during the intended photolysis period.

One other possible explanation for the low yields of addition products in the case of bromoethane may be that the carbanion undergoes an unexpected elimination type reaction at the expense of the substitution reaction. If the carbanion underwent a reaction of the type shown in Scheme 5.7 the end result would be formation of EB as well as ethene and HBr, both undetectable by the analytical techniques used. To rule out this possibility the experiment was repeated, this time substituting bromoethane-d_5 (CD_3CD_2Br) for bromoethane (<S> ~ 2). The products of this reaction showed no evidence of deuterium incorporation, ruling out the mechanism for EB formation given in Scheme 5.7.

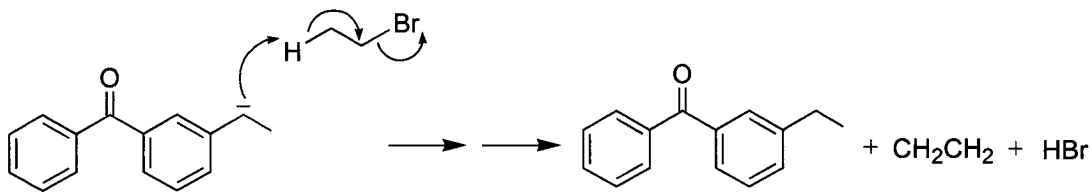

Scheme 5.7 Alternate formation of EB in the presence of 1-bromoethane.

Given these results, it was concluded that the most likely reason for observation of only the protonation product (EB) is that, despite efforts to exclude moisture, the zeolite must contain sufficient water such that the extremely efficient protonation reaction dominates over the addition reaction. The interaction can be observed by time-resolved spectroscopy because the samples prepared for these measurements were exposed to ambient moisture for much shorter periods of time and were analyzed in sealed containers under vacuum. Unfortunately the sample sizes in these cases were too small for product analysis. Despite many protocol modifications and attempts to perform the irradiations in vacuo, instrumental limitations and the size of the sample that must be used in order to obtain sufficient material for analysis precluded the exclusion of water to the point that the reaction between bromoethane and the carbanion became dominant.

In order to circumvent the problem, we chose to continue with a different substrate. The intrazeolite carbanion should be very reactive towards the

electrophilic carbon of a carbonyl group and so the experiments described above were repeated using acetaldehyde as the substrate. In addition to its improved electrophilicity, acetaldehyde also has the advantage of being smaller in size and more volatile. These two attributes should favour its incorporation into, and mobility within, the zeolite cavity. In fact, zeolites containing up to seven times more acetaldehyde than bromoalkane were obtainable ($\langle S \rangle \geq 15$).

Initially, time-resolved diffuse reflectance experiments were undertaken to monitor changes in the carbanion lifetime. The carbanion signal was monitored at 600 nm, following 266 nm laser excitation of a sample of KP@Y with acetaldehyde frozen in the laser cell side-arm. The DR-LFP results are given in Figure 5.16.

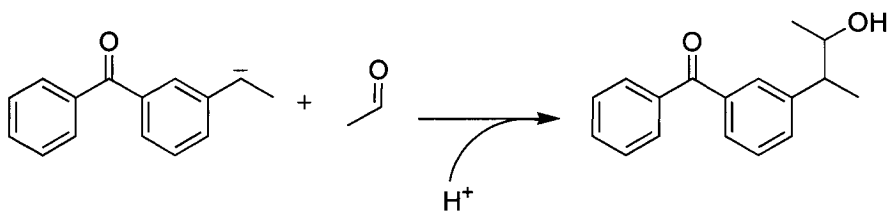

Scheme 5.8 Reaction of the carbanion with acetaldehyde.

The data show a very efficient quenching of the carbanion signal one minute after the acetaldyde has been allowed to thaw. The large decrease in $\Delta J/J$ indicates a static quenching interaction, i.e. one that is very rapid and appears instantaneous on the time scale of observation. The observed reduction in signal lifetime and intensity was attributed to an addition reaction between the carbanion and the co-included ketone (Scheme 5.8). Approximate fitting of the data with a bi-exponential expression gives τ_1 = 8.8 μs and τ_2 = 780 ns for the sample prior to incorporation of acetaldehyde and τ_1 = 3.9 μs and τ_2 = 320 ns afterwards. The time-resolved results indicate that acetaldehyde is a very reactive quencher and it was anticipated that this would translate into higher yields of the addition reaction product.

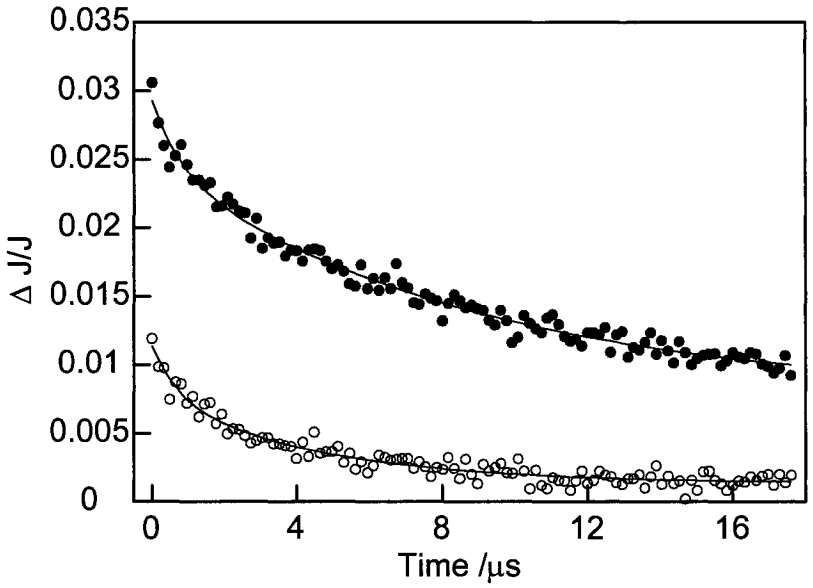

Figure 5.16 Signal recorded at 600 nm following 266 nm laser excitation of a sample of KP@Y under vacuum in the presence of frozen (●) and thawed (○) acetaldehyde, <S> ~ 15.

Product studies were undertaken using the protocol optimized during the bromoalkane experiments. The major difference was the increased loading of acetaldehyde as compared to the akylhalide substrates. KP@Y samples containing acetaldehyde were irradiated in perflurohexane at 300 nm in quartz vessels, under a nitrogen atmosphere. After irradiation, the reaction products were collected by Soxhlet extraction and analyzed by GC-MS. In this case, unlike the inefficient reaction observed with bromoethane, the alcohol product shown in Scheme 5.8 was obtained cleanly in an approximate yield (by GC) of 80% (*m/z* 254(M^+), 209, 177, 105, 77(100)). Protonation to give EB was almost completely suppressed in the presence of acetaldehyde, accounting for only *ca.* 10% of the products. A third unidentified chromatographic peak accounted for < 10% of the products formed. In light of this success, quenching with acetone was also attempted but the problem of contamination with water returns. Acetone is incorporated to a lesser extent than acetaldehyde and it was also difficult to prepare acetone that was sufficiently dry. It might also be expected that the increased steric hindrance would disfavour the

reaction. Whether due to one or all of these factors, the alcohol product from reaction with acetone was only obtained in very minor amounts with EB being the dominant reaction product.

As mentioned above, in the case of both bromoalkanes and acetaldehyde, there was a minor product identified by GC-MS having *m/z* 209. This chromatographic peak was tentatively assigned to a dimer of the benzylic radical produced by electron loss from the carbanion. The ability of the zeolite framework to behave as both an electron donor and acceptor in electron transfer reactions has been well established and it is conceivable that NaY may participate as an electron acceptor in this case.[40] Formation of a dimer following electron transfer from the carbanion could possibly be confirmed by isolation of dimer products following irradiation of KP^- in the presence of a good electron acceptor in solution. 1,4-Dicyanobenzene (DCB) was chosen as the electron acceptor and the bimolecular rate constant for quenching of the carbanion signal by DCB was determined by LFP to be $k_q = 9.5 \times 10^7\ M^{-1}s^{-1}$. Given this value of k_q, the relatively high concentration of DCB required for efficient quenching of the carbanion could not be co-dissolved in a solvent where the carbanion itself was generated efficiently. Although this experimental limitation precludes the observation of electron transfer products in solution, it does not disqualify the occurrence of electron transfer in the zeolite cavity where the lifetime of the carbanion is significantly longer and the electron-acceptor, i.e. the zeolite framework, is present at infinite concentration for practical purposes.

5.3.4 Conclusions to this Section

The nonsteroidal anti-inflamatory drug, ketoprofen, has been successfully incorporated within the cavities of faujasite zeolite NaY. Ketoprofen has been shown to undergo spontaneous deprotonation in NaY to generate the carboxlyate form of the drug. Diffuse reflectance laser flash photolysis studies revealed that ketoprofenate encapsulated in the zeolite cavity undergoes efficient

decarboxylation to generate an extremely long-lived carbanion. The photochemistry is the same as that observed in basic solution, but in the relatively anhydrous and aprotic zeolite environment, the carbanion lifetime is *ca.* 50 longer than in aqueous solution. The observed carbanion decay in zeolites is multimodal, suggesting more than one stabilization mechanism. We propose that the long lifetime is due to the absence of a proton source and a stabilizing interaction between the carbanion and the zeolite charge-balancing cations.

We have demonstrated that, if the zeolite is sufficiently dry, it is possible to observe intermolecular alkylation reactions via S_N2-type chemistry within the zeolite cavity. More reactive electrophiles allow nucleophilic substitution to compete more effectively with protonation by adventitious water. As a result, the reaction with acetaldehyde proceeds in good yield while reaction with bromoalkanes is inefficient.

This work is one of few examples of the stabilization of a carbanionic species by incorporation in a zeolite. The extended lifetime of the encapsulated carbanion is observed to decrease in a water-saturated sample (from *ca.* 8 μs to *ca.* 3 μs), although the shorter lifetime is still an order of magnitude longer than observed in water or methanol. This suggests an extra mode of stabilization by the zeolite framework in addition to provision of an anhydrous environment. These results have prompted other researchers to explore the behaviour of other zeolite-stabilized carbanionic species, such as the Meisenheimer complex.[41]

5.4 Experimental

5.4.1 Sample Preparation

All chemicals used for sample preparation were obtained from Aldrich in their highest available purity and used as received, unless otherwise indicated.

5.4.1.1 KP@Y by Method I

Zeolite NaY (*ca.* 1 g) was thermally dehydrated at 480°C overnight and added directly from the furnace to a foil-wrapped round bottom flask containing a solution of ketoprofen (Sigma) (50 mg, 0.19 mmol) in 15 mL of dry, deaerated DCM. The slurry was transferred to a nitrogen atmosphere and stirred at room temperature for 5 h. After this time the solvent was removed by flowing nitrogen. The solid was further dried under vacuum (< 50 mTorr) for several hours and was either used immediately or stored in a vacuum desicator for no more than 72 h. At each step in the preparation, efforts were made to minimize exposure to light and moisture.

5.4.1.2 KP@Y by Method II

Ketoprofen (Sigma) (50 mg, 0.19 mmol) was dissolved in 15 mL of dry, deaerated methanol containing $NaOCH_3$ (16 mg, 30 mmol) in a foil-wrapped round bottom flask. This solution was stirred for 0.5 h after which NaY (*ca.* 1 g), that had been thermally dehydrated at 480°C overnight, was added directly from the furnace. The slurry was transferred to a nitrogen atmosphere and stirred at room temperature for 5 h. After this time, the solid was collected by filtration and washed once with dry methanol. The solid was further dried under vacuum (< 50 mTorr) and either used immediately or stored in a vacuum desicator for no more than 72 h. At each step in the preparation, efforts were made to minimize exposure to light and moisture

5.4.2 Steady-state Spectroscopy

Absorption and DR spectra were recorded at room temperature on a Cary 1E spectrophotometer from Varian with a Varian DRA for reflectance measurements and Spectralon as the reflectance standard. Liquid samples were typically contained in Suprasil quartz cells from Hellma and solid samples in cells made of clear fused quartz (Friedrich & Dimmock).

FT-IR spectra were obtained using a Nicolet 710 FT spectrophotometer. Self-supported wafers (*ca.* 10 mg) were compressed at 1 ton cm^{-2} for 3 min and placed in sealed, greaseless cells with CaF_2 windows. The cells were outgassed at 200°C under 10^{-2} Pa for 1 h before recording the spectra at room temperature. These spectra were recorded at ITQ, Valencia, Spain.

Fluorescence spectra of MB were recorded using a v.1.2 X luminescence spectrometer from Photon Technology International. Optically matched solutions of 3-methylbenzophenone were prepared in spectroscopic grade solvents (OmniSolv) and deaerated by purging with nitrogen.

5.4.3 Time-Resolved Spectroscopy

5.4.3.1 Ultrafast Laser Flash Photolysis

Femtosecond LFP experiments were conducted at the Central Laser Facility of the Rutherford Appleton Laboratories (Didcot, United Kingdom) as described in Section 2.4 of this thesis. Solutions of 3-methylbenzophenone were prepared in spectroscopic grade solvents (BDH) at the concentrations indicated. The sample solution was contained in a 250 mL reservoir and was flowed rapidly through a quartz cell with 2 mm path length via a peristaltic pump. Samples were excited with 267 nm pulses from a Spitfire Ti-sapphire laser (coupled to a custom designed OPA as described in Chapter 2). Typical pulse energies were *ca* 3 μJ with a frequency of 600 Hz. The changes in absorption before and after the laser pulse were detected by a 512 photodiode array camera.

5.4.3.2 Nanosecond Laser Flash Photolysis

The LFP system for transient absorbance and diffuse-reflectance was described in detail in Section 2.2. The transient absorption spectrum of KP^- was recorded in deaerated spectroscopic grade methanol (OmniSolv) containing 10 mM $NaOCH_3$. The spectrum was recorded using a flow cell to avoid interference from photoproduct accumulation. The solution was excited with 308 nm pulses from a Lumonics EX-530 laser and the average power was *ca.* 90 mJ per pulse.

The rate constant for quenching of the carbanion signal with DCB was calculated by recording the decay at 600 nm for four separate solutions containing increasing amounts of DCB. The solutions were contained in static quartz cells and deaerated by purging with nitrogen. The samples were shaken after each laser shot and exposed to a minimum of laser pulses.

For transient DRS measurements of KP@Y alone, samples were contained in typical 3 x 7 mm^2 quartz cells and flame sealed under vacuum (< 50 mTorr). Pulsed laser excitation was from the fourth harmonic (266 nm) of a Surelite Nd-YAG laser. Pulse widths were typically 6 ns with an average power of *ca.* 20 mJ per pulse. To measure the effect of added water, a sealed sample of KP@Y was opened in a nitrogen atmosphere and then purged with water-saturated nitrogen in order to avoid the complication of adding oxygen to the system in addition to moisture.

To measure the effect of added quenchers on the lifetime of the carbanion the cell described in Figure 5.14 was used. 500 μL of the substrate, 1-bromoethane or acetaldehyde were placed into the side-arm of the cell and the side-arm was immersed in a dewar containing liquid nitrogen. When the liquid was completely frozen, *ca.* 250 mg of KP@Y was carefully added to the main part of the cell. The cell was then evacuated for 1 h with the liquid in the side arm still frozen. After 1 h, the cell was flame sealed under vacuum. The zeolite sample was excited with 266 nm laser pulses as described above. The signal variation with time was recorded while the side-arm was still immersed in liquid nitrogen and then again after the liquid nitrogen was removed and the quencher began to liquefy. Maximum

quenching was achieved within approximately one minute from the beginning of thawing.

Synergy Kaleidagraph software was used for all data manipulation and the ESM program from PTI used to perform lifetime distribution analysis.

5.4.4 Product Studies

The experimental protocol for product studies was modified extensively while trying to optimize the methodology in order to observe products from the reaction with bromoalkanes. The protocols ultimately used are described below and are a compromise of experimental efficiency and conditions that favour product formation.

To prepare the samples co-incorporating KP and the quencher of choice, KP@Y was prepared first as described in Section 5.4.1 and dried under vacuum. Gentle heating of the prepared KP@Y under dynamic vacuum to remove any absorbed water was attempted but had no impact on the observed products. After drying the zeolite sample was transferred to a nitrogen atmosphere and the quencher was included in one of two ways. An emulsion of *ca.* 100 μL of the quencher (1-bromoethane, 1-bromobutane, 1-bromopentane, acetone) was prepared in 5 mL of deaerated perfluorohexane and *ca.* 1 g of KP@Y were added to the solution and the slurry was stirred for 0.5 h at room temperature. Alternatively, a sample of KP@Y (*ca.* 1 g) was placed in a large vial and the vial was placed in a jar containing several milliliters of the quencher (acetaldehyde, acetone, 1-bromoethane). The jar was sealed and the system was left to equilibrate for approximately 1 h. The amount of incorporation was easily determined in this case by determining the difference in mass of the zeolite sample before and after exposure to the quencher.

Samples were photolyzed under nitrogen in Pyrex or fused quartz round bottom flasks with one 8 W lamp from Luzchem Research Inc. (LZC-UVC λ_{max} ~ 254 nm or LZC-UVB λ_{max} ~ 300 nm). The zeolites were irradiated for 1-4 hours as

slurries in 5 mL of perfluorohexane and were magnetically stirred throughout the irradiation. No increase in desired products was observed for irradiation times longer than 2 hours. Following irradiation, the solid was collected by gravity filtration and dried under nitrogen. Perfluorohexane is very volatile and was easily removed. The irradiated solids were subjected to solid-liquid extraction with 200 mL of DCM or ethylacetate for a period of 24 h. The extraction solution was concentrated by rotary evaporation and analyzed by GC-FID (Fisons 8000 series equipped with a J&W DBS 30 m x 0.32 mm fused silica column) and GC-MS (Fisons 8000/8060 series equipped with the same column as above). Authentic samples for comparison were prepared by Dr. G. Cosa.[23]

5.5 References

1. F. Boscá and M. A. Miranda, Photosensitizing drugs containing the benzophenone chromophore, *J. Photochem. Photobiol. B*, **1998**, *43*, 1-26.

2. F. Boscá, M. L. Marín and M. A. Miranda, Photoreactivity of the nonsteroidal anti-inflammatory 2-arylpropionic acids with photosensitizing side effects, *Photochem. Photobiol.*, **2001**, *74*, 637-655.

3. D. de la Peña, C. Martí, S. Nonell, L. J. Martínez and M. A. Miranda, Time-resolved near infrared studies on singlet oxygen production by the photosensitizing 2-arylpropionic acids, *Photochem. Photobiol.*, **1997**, *65*, 828-832.

4. L. L. Constanzo, G. De Guidi, G. Condorelli, A. Cambria and M. Fama, Molecular mechanism of drug photosensitization II. Photohemolysis sensitized by ketoprofen, *Photochem. Photobiol.*, **1989**, *50*, 359-365.

5. C. F. Chignell and R. H. Sik, Magnetic field effects on the photohemolysis of human erythrocytes by ketoprofen and protoporphyrin IX, *Photochem. Photobiol.*, **1995**, *62*, 205-207.

6. C. F. Chignell and R. H. Sik, The effect of static magnetic fields on the photohemolysis of human erythrocytes by ketoprofen, *Photochem. Photobiol.*, **1998**, *67*, 591-595.

7. G. De Guidi, S. Ragusa, M. T. Cambria, A. Belvedere, A. Catalfo and A. Cambria, Photosensitizing effect of some nonsteroidal anti-inflammatory drugs on natural and artificial membranes: Dependence on phospholipid composition, *Chem. Res. Toxicol.*, **2005**, *18*, 204-212.

8. T. Artuso, J. Bernadou, B. Meunier, J. Piette and N. Paillous, Mechanism of DNA cleavage mediated by photoexcited nonsteroidal anti-inflammatory drugs, *Photochem. Photobiol.*, **1991**, *54*, 205-213.

9. M. C. Maguery, N. Chouini-Lalanne and J. C. Ader, Comparison of the DNA damage photoinduced by fenofibrate and ketoprofen, two phototoxic drugs of parent structure, *Photochem. Photobiol.*, **1998**, *68*, 679-684.

10. V. Lhiaubet, N. Paillous and N. Chouini-Lalanne, Comparison of DNA damage photoinduced by ketoprofen, fenofibric acid, and benzophenone by electron and energy transfer, *Photochem. Photobiol.*, **2001**, *74*, 670-678.

11. A. L. Vinette, J. P. McNamee, P. V. Bellier, J. R. N. McLean and J. C. Scaiano, Prompt and delayed nonsteroidal anti-inflammatory drug-induced DNA damage in peripheral blood mononuclear cells measured with the comet assay, *Photochem. Photobiol.*, **2003**, *77*, 390-396.

12. A. Alomar, Ketoprofen photodermatitis, *Contact Dermatitis*, **1985**, *12*, 112-113.

13. H. Bagheri, V. Lhiaubet, J. L. Montastruc and N. Chouini-Lalanne, Photosensitivity to ketoprofen: Mechanisms and pharmacoepidemiological data, *Drug Safety*, **2000**, *22*, 339-349.

14. L. Matthieu, L. Meuleman, E. Van Hecke, A. Blondeel, B. Dezfoulian, L. Constandt and A. Goossens, Contact and photocontact allergy to ketoprofen. The Belgian experience, *Contact Dermatitis*, **2004**, *50*, 238-241.

15. M. Sugiura, R. Hayakawa, Z. Xie, K. Sugiura, K. Hiramoto and M. Shamoto, Experimental study on phototoxicity and the photosensitization potential of ketoprofen, suprofen, tiaprofenic acid, and benzophenone and the cross-reactivity in guinea pigs, *Photodermatol. Photoimmunol. Photomed.*, **2002**, *18*, 82-89.

16. F. Boscá, M. A. Miranda, G. Carganico and D. Mauleón, Photochemical and photobiological properties of ketoprofen associated with the benzophenone chromophore, *Photochem. Photobiol.*, **1994**, *60*, 96-101.

17. L. J. Martínez and J. C. Scaiano, Transient intermediates in the laser flash photolysis of ketoprofen in aqueous solutions: Unusual photochemistry for the benzophenone chromophore, *J. Am. Chem. Soc.*, **1997**, *119*, 11066-11070.

18. S. Monti, S. Sortino, G. De Guidi and G. Marconi, Photochemistry of 2-(3-benzoylmethyl)propionic acid (ketoprofen). 1. A picosecond and nanosecond time resolved study in aqueous solution, *J. Chem. Soc., Faraday Trans.*, **1997**, *93*, 2269-2275.

19. S. Monti, S. Sortino, G. De Guidi and G. Marconi, Supramolecular photochemistry of 2-(3-benzoylphenyl)propionic acid (ketoprofen). A study in the beta-cyclodextrin cavity, *New J. Chem.*, **1998**, *22*, 599-604.

20. G. Cosa, L. J. Martínez and J. C. Scaiano, Influence of solvent polarity and base concentration on the photochemistry of ketoprofen: Independent singlet and triplet pathways, *Phys. Chem. Chem. Phys.*, **1999**, *1*, 3533-3537.

21. C. D. Borsarelli, S. E. Braslavsky, S. Sortino, G. Marconi and S. Monti, Photodecarboxylation of ketoprofen in aqueous solution. A time-resolved optoacoustic study, *Photochem. Photobiol.*, **2000**, *72*, 163-171.

22. G. Cosa, L. Llauger, J. C. Scaiano and M. A. Miranda, Absolute rate constants for water protonation of 1-(3-benzoylphenyl)alkyl carbanions, *Org. Lett.*, **2002**, *4*, 3083-3085.

23. L. Llauger, G. Cosa and J. C. Scaiano, First determination of absolution rate constants for the reaction of aroyl-substituted benzyl carbanions in water and DMSO, *J. Am. Chem. Soc.*, **2002**, *124*, 15308-15312.

24. L. Llauger, M. A. Miranda, G. Cosa and J. C. Scaiano, Comparative study of the reactivities of substituted 3-(benzoyl)benzyl carbanions in water and DMSO, *J. Org. Chem.*, **2004**, *69*, 7066-7071.

25. M. Lukeman and J. C. Scaiano, Carbanion-mediated photocages: Rapid and efficient photorelease with aqueous compatibility, *J. Am. Chem. Soc.*, **2005**, *127*, 7698-7699.

26. N. J. Turro *Modern Molecular Photochemistry;* University Science Books: Sausalito, 1991.

27. A. K. Singh, A. C. Bhasikuttan, D. K. Palit, A. V. Sapre and J. P. Mittal, Excited-state dynamics and photophysical properties of *para*-aminobenzophenone, *J. Phys. Chem. A*, **1998**, *104*, 7002-7009.

28. A. K. Singh, D. K. Palit and J. P. Mittal, Excite-state dynamics of Michler's ketone: A laser flash photolysis study, *Res. Chem. Intermed.*, **2001**, *27*, 125-136.

29. F. Boscá, G. Cosa, M. A. Miranda and J. C. Scaiano, Inversion of 4-methoxybenzophenone triplet in aqueous solution, *Photochem. Photobiol. Sci.*, **2002**, *9*, 704-708.

30. M. A. El-Sayed, The radiationless processes involving change of multiplicity in the diazenes, *J. Chem. Phys.*, **1962**, *36*, 573-574.

31. M. A. El-Sayed, Spin-orbit coupling and the radiationless processes in nitrogen heterocycles, *J. Chem. Phys.*, **1963**, *38*, 2834-2838.

32. M. A. El-Sayed, Vanishing first- and second-order intramolecular heavy-atom effects on the (π^*–>n) phosphorescence in carbonyls, *J. Chem. Phys.*, **1964**, *41*, 2462-2467.

33. J. R. Lakowicz *Principles of Fluorescence Spectroscopy;* Kluwer Academic/Plenum Publishers: New York, 1999.

34. H. Miyasaka, K. Morita, K. Kamada and N. Mataga, Femtosecond-picosecond laser photolysis studies on photoreduction process of excited benzophenone with *N,N*-dimethylaniliine in acetonitrile solution, *Bull. Chem. Soc. Jpn.*, **1990**, *63*, 3385-3397.

35. N. Tamai, T. Asahi and H. Masuhara, Intersystem crossing of benzophenone by femtosecond transient grating spectroscopy, *Chem. Phys. Lett.*, **1992**, *198*, 413-418.

36. Y. Marcus, The properties of organic liquids that are relevant to to their use as solvating solvents, *Chem. Soc. Rev.*, **1993**, *22*, 409-416.

37. P. F. McGarry, C. E. Doubleday Jr., C.-H. Wu, H. A. Staab and N. J. Turro, UV-vis absorption studies of singlet to triplet intersystem crossing rates of aromatic ketones: Effects of molecular geometry, *J. Photochem. Photobiol. A*, **1994**, *77*, 109-117.

38. J. J. Cavaleri, K. Prater and R. M. Bowman, An investigation of the solvent dependence on the ultrafast intersystem crossing kinetics of xanthone, *Chem. Phys. Lett.*, **1996**, *259*, 495-502.

39. E. V. Sitzmann, J. G. Langan, D. Griller and K. B. Eisenthal, Effects of solvent polarity and structure on intersystem crossing in diphenylcarbenes. A picosecond laser study on dimesitylcarbene, *Chem. Phys. Lett.*, **1989**, *161*, 353-360.

40. H. García and H. D. Roth, Generation and reactions of organic radical cations in zeolites, *Chem. Rev.*, **2002**, *102*, 3947-4008.

41. J. R. Herance, J. Marquet, J. L. Bourdelande and H. García, Stabilization of an anionic guest adsorbed on sodium faujasites through enhanced Coulombic interactions, *Chem. Phys. Lett.*, **2004**, *395*, 49-52.

42. F. L. Cozens, M. L. Cano, H. García and N. P. Schepp, Alkali metal cation control of oxidation reactions of radicals in zeolites, *J. Am. Chem. Soc.*, **1998**, *120*, 5667-5673.

43. I. T. Horváth, Fluorous biphase chemistry, *Acc. Chem. Res.*, **1998**, *31*, 641-650.

44. A. Pace and E. L. Clennan, A new experimental protocol for intrazeolite photooxidations. The first product-based estimate of an upper limit for the intrazeolite singlet oxygen lifetime, *J. Am. Chem. Soc.*, **2002**, *124*, 11236-11237.

6. Fluorescent Sensors for Intra- and Interzeolite Interactions

6. Fluorescent Sensors for Intra- and Interzeolite Interactions 202

6.1 Background 203
6.2 Zeolite-Incorporated Sensor for Monitoring In-cage Interactions 206
6.2.1 Sample Preparation and Characterization 206
6.2.2 Intrazeolite Radical Detection by DT@NaY 210
6.2.3 Intrazeolite Hydrogen-atom Abstraction by DT@NaY 215
6.2.4 Conclusions to this Section 217
6.3 Fluorescently Labeled Zeolites for Imaging 219
6.3.1 Preparation and Characterization 219
6.3.2 Photophysical Studies 225
6.3.3 Microscopy Studies 229
6.3.4 Conclusions to this Section 235
6.4 Experimental 236
6.4.1 Sample Preparation 236
6.4.2 Steady-state Spectroscopy 237
6.4.3 Time-Resolved Spectroscopy 237
6.4.4 Intrazeolite Reactivity of DT@NaY 238
6.4.5 Fluorescence Microscopy 239
6.5 References 241

6.1 Background

This chapter explores the innovative use of fluorescence spectroscopy as a tool to monitor interactions within zeolite particles, as well as between zeolite particles and other substrates. The first part of this chapter describes the development and utilization of a zeolite-bound pre-fluorescent probe for monitoring radicals and hydrogen-atom donors (H-donors) within the zeolite pore structure. This project is part of a fruitful collaboration with Dr. A. Ricci. The second section deals with a material that was prepared and characterized for the study of zeolite interactions with skin cells. Fluorescence is a powerful technique in terms of its use as a sensor in heterogeneous systems, due to the high sensitivity with which it can be detected and the multidirectional nature of emission. Fluorescence techniques are very sensitive because the emitted photons are recorded against a baseline of zero emission compared to other techniques (such as transient DR spectroscopy) where small changes in light intensity are measured. The difference is akin to distinguishing the lighting of a match in a dark room versus the extinguishing of a match in a well-lit room.

In Section 6.2, the use of intrazeolite pre-fluorescent probes to examine the intra-particle dynamics of selected radicals and hydrogen-atom donors is examined. The use of pre-fluorescent probes for the facile and sensitive monitoring of various species is a topic of current interest. Originally reported by Blough and co-workers, a pre-fluorescent probe is a molecular dyad consisting of a fluorophoric unit tethered to a stable nitroxyl radical (such as 2,2,6,6-tetramethyl-piperidine-1-oxyl, TEMPO).[1, 2] In its paramagnetic form (Scheme 6.1) the excited singlet state of the fluorophore is efficiently quenched by the tethered nitroxide moiety corresponding to a free or "off" state. The mechanism of excited-state quenching is dependent on the particular chromophore-nitroxide pair and may comprise contributions from several mechanisms, including electron-exchange induced intersystem crossing or internal conversion, energy transfer by electron exchange (Dexter), resonance

energy transfer (Förster), and electron transfer.[2] There are examples in the literature where the mechanism has been elucidated for specific fluorophore-nitroxide pairs.[1-4]

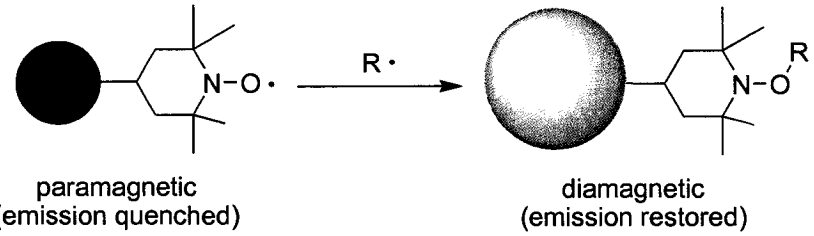

Scheme 6.1 Mechanism of radical detection by pre-fluorescent probes.

Persistent nitroxides are active scavengers of carbon-centered radicals and when the oxygen of the nitroxide probe couples with a carbon-centered radical (R• in Scheme 6.1) the resulting species is a diamagnetic alkoxyamine.[5-8] After radical trapping, the fluorescence-quenching mode operative in the paramagnetic probe is no longer available and the fluorophore emission is restored. This corresponds to a trapped or "on" state. The radical detection capability of the pre-fluorescent probe is a consequence of the different fluorescence quantum yields for the paramagnetic and diamagnetic forms. By measuring the time-evolution of the fluorescence intensity, pre-fluorescent probes have been employed to obtain kinetic information for reactions involving carbon-centered radicals.[9-12]

Nitroxides have also been reported to undergo hydrogen abstraction reactions with phenolic antioxidants in aqueous media.[13, 14] This has lead to the use of pre-fluorescent probes to study the antioxidant capability of a number of phenolic species.[15, 16] For example, a pre-fluorescent probe methodology has been used in solution to determine the experimental rate constants for hydrogen transfer from several phenolic compounds to a nitroxide probe.[15]

In Section 6.3, ship-in-a-bottle techniques were used to prepare a new fluorescent-labeled zeolite material. The advantage of ship-in-a-bottle synthesis in this case is that the fluorophore is permanently entrapped within the zeolite matrix with no possibility of escape to the bulk media. This is especially important for

experiments where the zeolite is suspended in aqueous media and the extreme affinity of water for the zeolite interior may cause internally located guests to be displaced to the particle exterior.[17] This probe was developed in order to study the interaction between zeolite particles and skin cells.

6.2 Zeolite-Incorporated Sensor for Monitoring In-cage Interactions

6.2.1 Sample Preparation and Characterization

Over the last several years, our research group has been active in the design of new pre-fluorescent probes, as well as in the investigation of novel applications for fluorescence-based sensor methodologies. Many studies have been carried out with quinoline-TEMPO or QT (4-(3-hydroxy-2-methyl-4-quinolinoyloxy)-2,2,6,6-tetramethylpiperidine-1-oxyl), a pre-fluorescent probe containing a quinoline fluorophore. QT has been successfully applied to study a variety of complex systems including the thermal[18] and photochemical[19] generation of carbon-centered radicals in polymer films and the radical-mediated photodegradation of micelles (see Chapter 7). Similarly, a coumarin-based pre-fluorescent probe has been employed to monitor the end-cap cleavage in TEMPO-mediated living free radical polymerization.[20]

In this work, a zeolite-entrapped pre-fluorescent probe based on the dansyl amide fluorophore was prepared by ship-in-a-bottle synthesis. Dansyl chloride was developed as a probe by Weber and has been used extensively to study the N-terminal, amino acid residues of proteins and to prepare fluorescent derivatives of drugs, amino acids, oligonucleotides and proteins for detection by a variety of chromatographic methods.[21, 22] Non-fluorescent dansyl chloride reacts with amines to form fluorescent dansylamides exhibiting large Stokes shifts. The sulfonylamido linkage in dansyl-TEMPO (see structure in Scheme 6.2) plays the same role as the reaction with amines in biological labeling experiments. Dansyl-TEMPO or DT (4-(5-(dimethylamino)-1-naphthalenesulfonylamido)-2,2,6,6-tetramethylpiperidine-1-oxyl) has been previously employed by Likhtenshtein *et al.* for the quantitative analysis of vitamin C in commercial fruit juices.[16] The fluorescence increase in this case was the result of a hydrogen-atom transfer from vitamin C, a polyhydroxylic hydrogen donor, to the nitroxide moiety of the probe, yielding the corresponding diamagnetic hydroxylamine (Scheme 6.2).

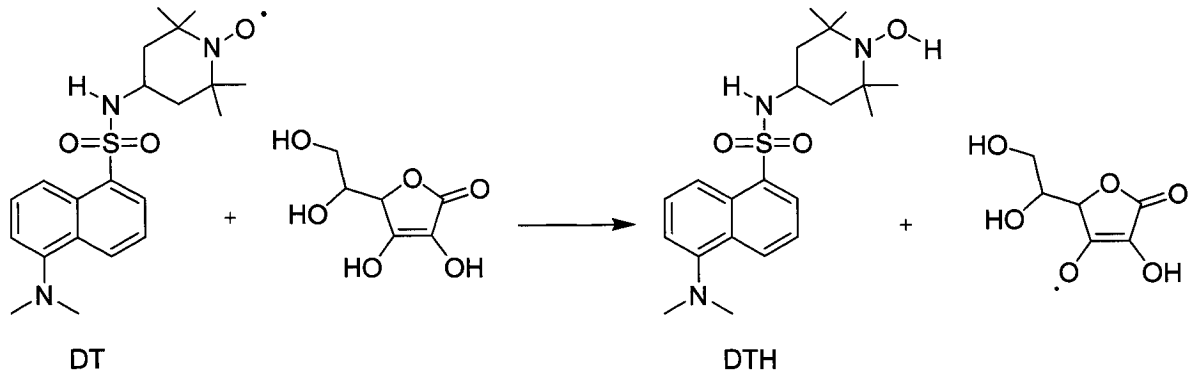

Scheme 6.2 Reaction of the DT probe with vitamin C.

The high fluorescence quantum yield of dansylamides is not completely quenched by the unpaired spin of the nitroxide moiety. The paramagnetic form of DT exhibits a measurable fluorescence emission and the intensity difference between the diamagnetic and paramagnetic forms was reported to be a factor of *ca.* two.[16] For applications in solution, it is normally desirable to have a large difference in quantum yield between the free, versus the trapped, probe (usually 30- to 60-fold).[1, 3, 18-20] From this perspective DT seems less than ideal, however, DT was suitable for this study because the weak fluorescence from the paramagnetic form provides a direct and convenient tool to establish the formation of the probe within the zeolite cavities.

As mentioned above, DT was prepared within the supercages of faujasite zeolite NaY via ship-in-a-bottle synthesis. As described in Section 1.3, this methodology allows the preparation of compounds that can be accommodated by the zeolite supercage but cannot pass through the pore aperture; DT cannot be directly encapsulated but its building blocks are easily accommodated. For probing the diffusion of hydrogen donors and organic radicals within the zeolite pore structure it was important to use an immobilized probe to avoid complications arising from diffusion of the probe itself. Probe immobilization is especially important in experiments where radicals are generated in the solution phase of a zeolite-solvent slurry. In this case, DT is also held in place by the electrostatic

interaction between the zeolite interior and the polar or "sticky" moieties in DT, such as the amino and sulfonyl groups.

In the literature synthesis, DT was obtained by treatment of 4-amino TEMPO with dansyl chloride under anyhydrous conditions in either pure pyridine or pyridine/DCM mixtures. These same building blocks, 4-amino TEMPO and dansyl chloride, were employed for the synthesis in NaY. In order to perform a base-catalyzed reaction in NaY it was first necessary to neutralize any intra-cavity acid sites. It has been established that organic bases are able to bind to the acidic sites in zeolite cavities, inducing pH modifications.[23, 24] With this in mind, the zeolite was pretreated with an excess of pyridine (<S> ~ 1) prior to incorporation of the reactants. 4-Amino TEMPO and dansyl chloride were added sequentially from a hexane slurry to a final loading of <S> ~ 0.5 each. The resulting slurry was stirred under nitrogen for several days. The solid was collected, washed with hexane, and subjected to solid-liquid extraction to remove pyridine and un-reacted starting materials. A small amount of dansyl-TEMPO was also recovered from the extraction solution, as determined by comparison with an authentic sample. To the best of our knowledge, this base-catalyzed, ship-in-a-bottle synthesis is unique in the literature. Typical synthetic methodologies are acid catalyzed,[25] as is the case for TP^+@Y discussed in Chapter 3, or metal-ion templated, as for encapsulated metallophthalocyanines and $Ru^{2+}(bpy)_3$@Y from Chapter 3.[26]

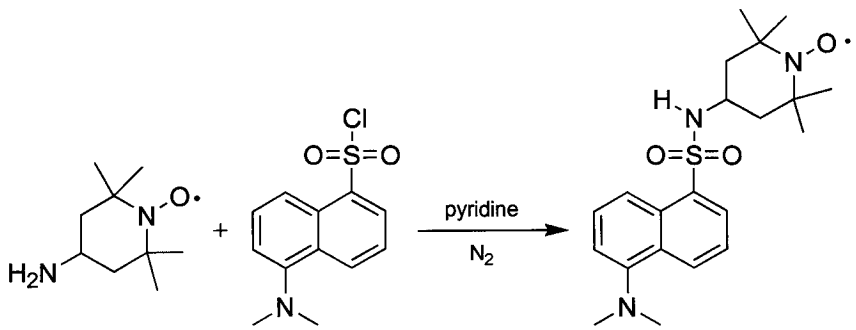

Scheme 6.3 Synthesis of dansyl-TEMPO.

The ground state DRS of DT@NaY matches well with the spectrum of DT recorded in acetonitrile (Figure 6.1). Compounds prepared by ship-in-a-bottle synthesis can sometimes be characterized directly, if they can be recovered by liquid-liquid extraction following degradation of the zeolite framework. Unfortunately, degradation requires treatment of the complex with strong acid and many compounds, including DT and others described in this thesis, are not stable under strongly acidic conditions. In these cases, the prepared materials must be characterized indirectly by spectroscopic methods. The ^{13}C CP/MAS (cross polarization/magic angle spinning) solid state NMR of DT@NaY showed only a broad, weak signal in the aromatic region, as would be expected for a paramagnetic species.

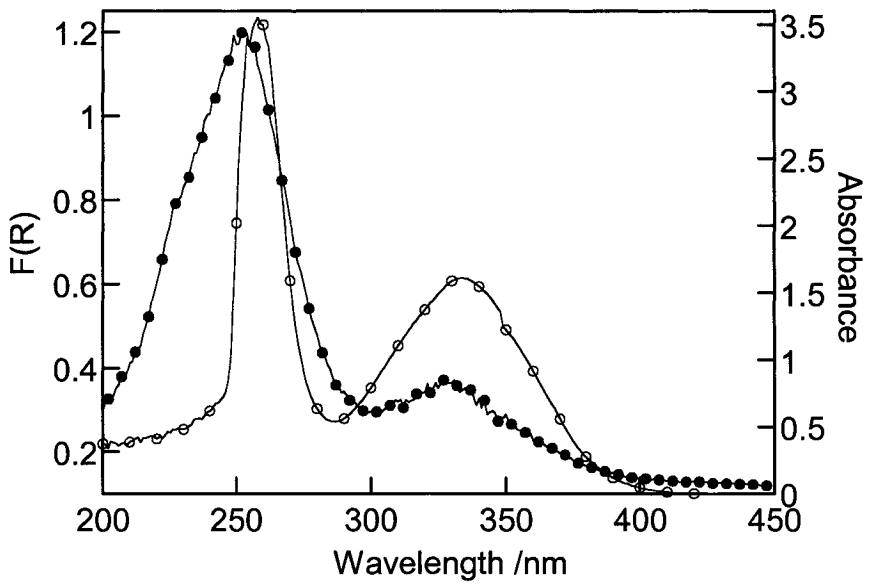

Figure 6.1 Ground state DRS of DT@NaY (●) and UV-vis absorption spectrum of DT in ACN, 5.0 x 10 M (O).

The fluorescence emission spectra of DT@NaY and a benzene solution of DT were recorded and compared. When excited at 330 nm, both samples had a moderate fluorescence emission in the same region of the spectrum. The maximum in the emission spectrum was at 470 nm for the benzene solution and 500 nm for

DT@NaY. The bathochromic shift may be due to stabilizing electrostatic interactions experienced by the probe within the zeolite cavity. Accordingly, when DT@NaY was suspended in benzene and the fluorescence spectrum re-recorded, the maximum had shifted to 490 nm, closer to the value in benzene solution. The presence of benzene within the cage disrupts the interaction between the guest and the framework causing the environment to be more solution-like. Neither dansyl chloride nor 4-amino TEMPO are fluorescent.

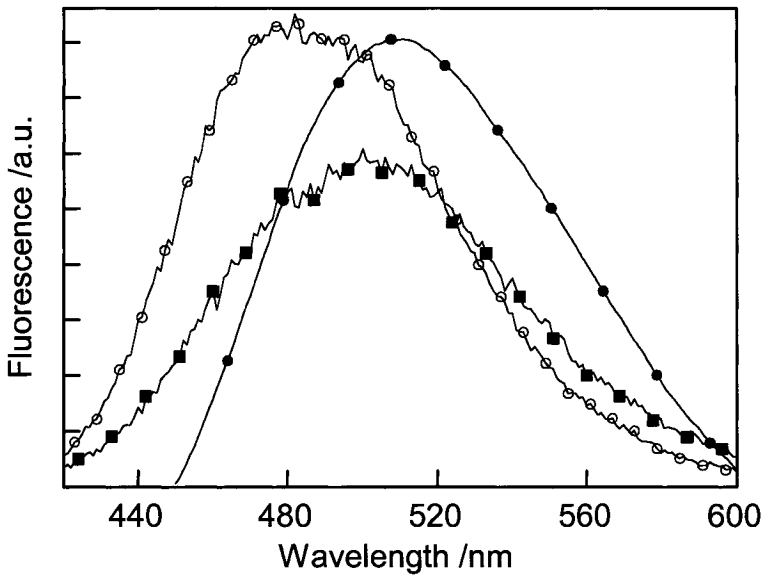

Figure 6.2 Emission spectra (λ_{ex} = 330 nm) of a benzene solution of DT (1.0 x 10^{-4} M, O), a solid sample of DT@NaY (●), and a benzene slurry of DT@NaY (1.0 mg mL^{-1}, ■).

The spectral data given above support the conclusion that DT was successfully prepared, via a base-catalyzed reaction, within the cavities of zeolite NaY. Combustion elemental analysis of a rigorously dried sample gave an occupancy of <S> ~ 0.1 corresponding to a reaction yield of approximately 20%.

6.2.2 Intrazeolite Radical Detection by DT@NaY

The radical-detection capability of DT@NaY was first investigated in a system where the radical precursor was co-incorporated in the zeolite supercages. 2,2'-Azo*bis*isobutyronitrile (AIBN), a well-known thermal and photochemical

precursor for carbon-centered radicals, is commonly used as an initiator in free radical polymerization.[27] In solution, heat or light induced homolysis of the two C-N single bonds in AIBN results in the liberation of a stable nitrogen molecule and the formation of two isobutyronitrile radicals. AIBN was co-included in DT@NaY from a hexane slurry to a final loading of <S> ~ 0.5. The thermal decomposition of AIBN at 70°C was examined by monitoring the time-evolution of the fluorescence emission at 550 nm.

A solventless sample of DT@NaY was heated to 70°C and then cooled to room temperature before the start of fluorescence monitoring. Figure 6.3 shows the normalized fluorescence increase with time. The fluorescence growth begins to plateau after approximately 200 minutes, indicating the end of coupling reactions between the nitroxyl moiety of the probe and the carbon-centered radicals. In solution, the half-life of isobutyronitrile radicals is *ca.* five hours at 70°C, becoming shorter at higher temperatures.[27] As reported for the previous use of this probe in solution, the final increase in fluorescence intensity is approximately a factor of two.[16] The intramolecular quenching of fluorophore emission by the nitroxide should be relatively insensitive to zeolite encapsulation and therefore the quantum yield of the paramagnetic species should remain largely unchanged. Some species exhibit an increased emission quantum yield upon encapsulation due to the suppression of non-radiative modes (such as bond rotations or other molecular motions) but this should affect the diamagnetic and paramagnetic species equally. A reference sample of DT@NaY, containing no AIBN, was treated with the same heating and cooling did not exhibit a fluorescence increase.

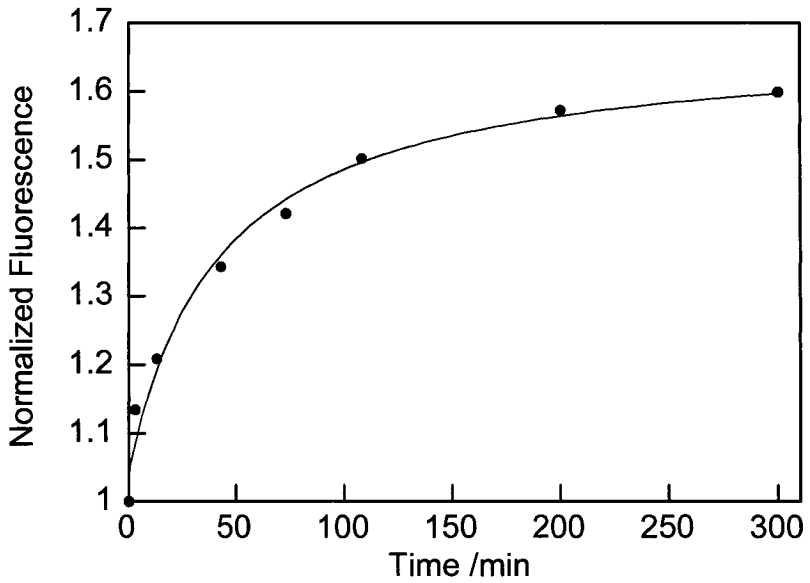

Figure 6.3 Fluorescence increase (normalized to 1.0 at t = 0 min) recorded after heating (70°C) a solid sample of DT@NaY with co-included AIBN ($\langle S \rangle_{DT} \sim 0.1$, $\langle S \rangle_{AIBN} \sim 0.5$). $\lambda_{ex} = 305$ nm, $\lambda_{em} = 550$ nm.

The results with AIBN demonstrate the ability of DT@NaY to trap radicals generated within the zeolite pore structure. In this case, the thermolysis of AIBN was complete (the sample was returned to room temperature) at the time of measurement, so the time-dependence of the fluorescence increase reflects the percolation of radicals though the zeolite lattice.

The behaviour of carbon-centered radicals generated exterior to the zeolite particle was also investigated. The zeolite-bound radical sensor, DT@NaY, was used to examine the penetration, and subsequent percolation, of radicals through the zeolite microarray. The radical precursor used was 3,3'-diphenyl-3*H*,3*H*'-[3,3']*bis*benzofuranyl-2,2'-dione (PC-PC, structure given in Scheme 6.4). The ability of this compound to yield 3-phenyl-2-coumaranone radicals upon heating, via homolytic C-C bond cleavage, and the subsequent behaviour of these radicals is well documented.[28-32] Depending on the solvent and temperature, the favoured process is either recombination to form the starting dimer,[29] coupling affording

head-to-tail dimers and tetramers,[30] or hydrogen-atom abstraction from a donor, such as a phenol, to yield 3-phenyl-2-coumaranone (Scheme 6.4).[29, 31]

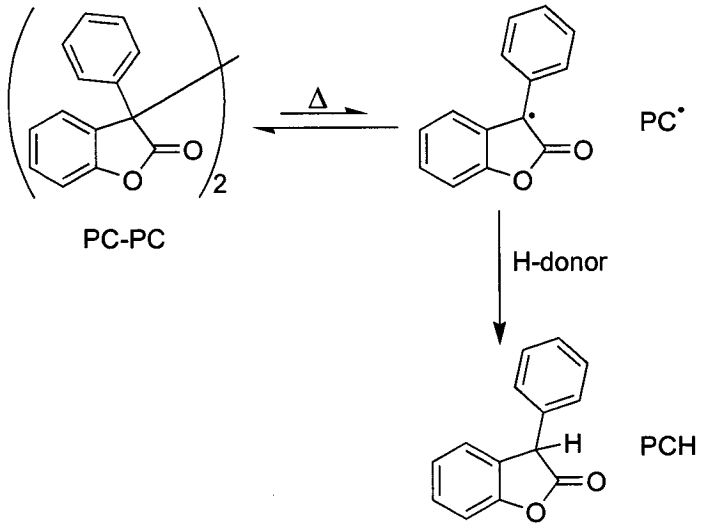

Scheme 6.4 Reactivity of 3,3'-diphenyl-3*H*,3*H*'-[3,3']*bis*benzofuranyl-2,2'-dione.

The 3-phenyl-2-coumaranone radical dimer, PC-PC, was particularly suitable for this study because only the 3-phenyl-2-coumaranone radicals (PC•) are small enough to diffuse through the NaY cavity windows. The molecular dimensions of the dimer prevent its direct inclusion in the zeolite and therefore radicals are exclusively formed outside of the particle. The documented persistency of 3-phenyl-2-coumaranone radicals ensures that they will endure long enough to migrate through the zeolite pore structure.[31, 32] A fluorescence increase over time was expected as PC• radicals penetrate the zeolite pores, and encounter and couple with the embedded pre-flourescent probe. The resulting product would be bulky but should be comfortably accommodated between two adjacent supercages.

PC-PC was dissolved in hexane and this solution was used to prepare a slurry with DT@NaY. The slurry was purged with nitrogen and heated to 50°C, the fluorescence emission at 550 nm was recorded during heating and after reaching the desired temperature. Figure 6.5 shows the fluorescence evolution recorded during heating. In the absence of PC-PC (i.e. DT@NaY in hexane only) the fluorescence was observed to initially decrease until reaching a plateau after

approximately 600 seconds. It was determined that this is the time required for the sample to reach 50°C, suggesting that the fluorescence quantum yield of DT decreases with increasing temperature. When the slurry was heated with the radical precursor present in the slurry solution, the initial emission decrease persisted for only 300 seconds. During this time PC$^{\bullet}$ radicals are formed in solution, diffuse into the zeolite pores, and subsequently encounter and couple with the embedded probe molecules. After the initial decrease, a fluorescence growth was observed. This growth began to plateau after approximately 1500 seconds. Measurements beyond the time shown in Figure 6.4 were not practical due to the elevated temperature and the small solvent volume (2 mL).

The observed fluorescence increase over time shows that, at this temperature and concentration of the dimeric radical precursor, radical penetration into the zeolite pores occurs within minutes. As expected, TLC analysis of the solution at the end of the experiment did not indicate the presence of DT, confirming its entrapment. The rate-determining step for the overall process cannot be unequivocally assigned based on these experiments; possible candidates are the initial penetration into the zeolite particle (i.e. a surface process), diffusion within the zeolite pore structure, or the reaction between the radical and the nitroxide, although this is the least likely explanation. The elevated temperature likely plays a role in increasing the rate of percolation, as well as the rate of the inherently fast radical recombination reaction.

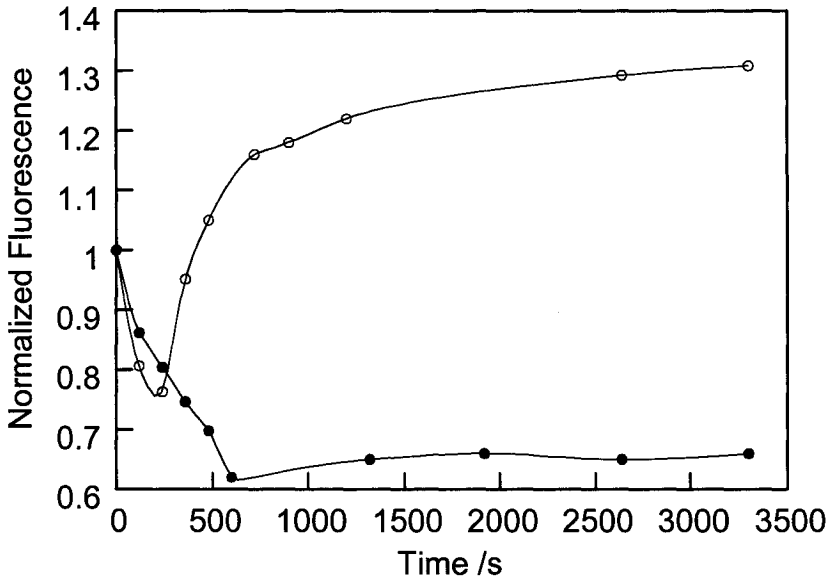

Figure 6.4 Fluorescence growth (normalized to 1.0 at t = 0 s) for a hexane slurry of 1.0 mg mL^{-1} DT@NaY in the absence (●) and presence (○) of 1.3 x 10^{-3} M PC-PC. λ_{ex} = 330 nm and λ_{em} = 550 nm.

6.2.3 Intrazeolite Hydrogen-atom Abstraction by DT@NaY

As a further demonstration of the utility of matrix-immobilized pre-fluorescent probes, hydrogen-atom transfer in microheterogeneous systems was briefly examined. As mentioned in Section 6.1, the nitroxide moiety of a pre-fluorescent probe is susceptible to reduction by good hydrogen-atom donors such as antioxidants, as in the reaction given in Scheme 6.2.[14-16] By monitoring the fluorescence increase resulting from hydroxylamine formation in the presence of an excess of the antioxidant in question (pseudo first-order conditions) the rate constants of hydrogen-atom transfer (k_{HT}) have been calculated for a number of compounds. For example, Likhtenshtein *et al.* reported a value of k_{HT} = 7 M^{-1} s^{-1} for vitamin C in commercial fruit juice.[16]

Hydrogen-atom transfer from synthetic antioxidant 3-phenyl-2-coumaranone (PC) was investigated using DT@NaY to track the behaviour of the antioxidant as it penetrates the particle, diffuses through the zeolite pores,

encounters the pre-fluorescent probe and consequently forms carbon-centered radicals and fluorescent DTH within the cavities (Scheme 6.5). 3-Phenyl-2-coumaranone is an analogue of the synthetic antioxidant HP-136, marketed by CIBA as a polymer stabilizer.

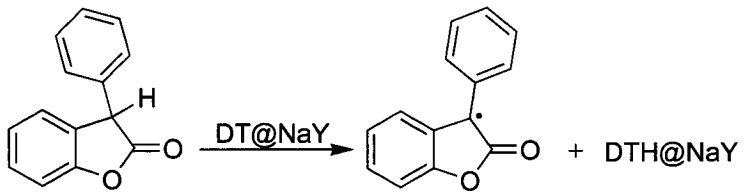

Scheme 6.5 Intracavity reaction between 3-phenyl-2-coumaranone and DT.

PC was dissolved in nitrogen-saturated benzene and the resulting solution was used to make a slurry with DT@NaY. The fluorescence increase was monitored at 550 nm while the solution was stirred at room temperature. As before, no DT was recovered from the solution at the end of the experiment indicating that there is no leaching of the entrapped probe. As seen in Figure 6.5, the fluorescence intensity increases rapidly at first and begins to decelerate after approximately 150 minutes. As in the previous example, the rate-determining step in this process is unlikely to be the hydrogen abstraction reaction and is more likely related to the percolation of the molecule though the pore structure, prior to encountering a nitroxide. In this experiment PC is present in large excess, as a result the most likely fate of the carbon-centered radicals generated by hydrogen abstraction, is reaction with another molecule of the relatively ubiquitous 3-phenyl-2-coumaranone. This process would effectively result in radical center migration. This experiment was conducted at room temperature and so the slow rate of fluorescence increase after 150 minutes may indicate a situation of "molecular gridlock" where all of the easily accessible DT has reacted and the remaining DT molecules are more difficult to reach. More pronounced congestion was expected in this case, as compared to the previous example, due to the higher concentration of coumaranone and the lower temperature. At lower temperatures the dimer-

radical equilibrium is shifted towards coupling products. In addition, any in-cage dimer formation will increase steric restrictions.

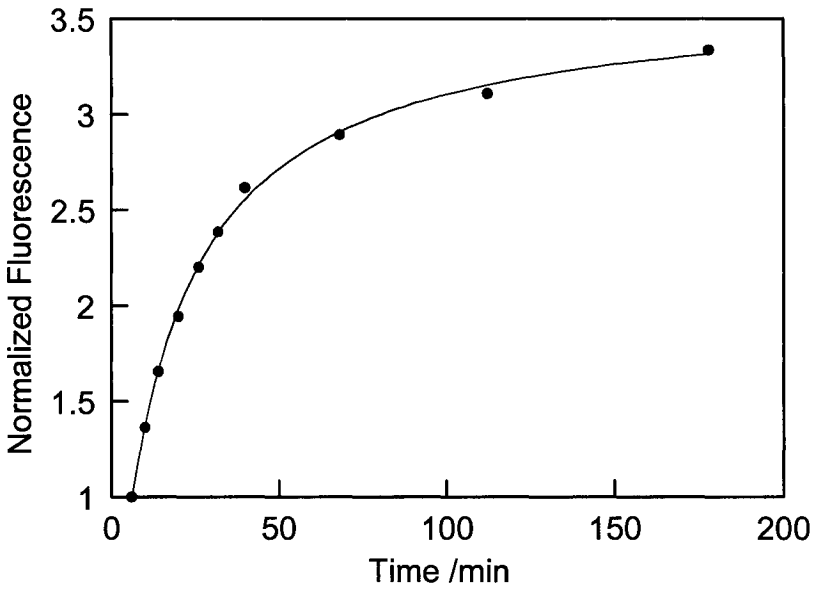

Figure 6.5 Fluorescence growth (normalized to 1.0 at t = 5 min) for a slurry containing 1.0 mg mL^{-1} DT@NaY in a deaerated benzene solution of 3-phenyl-3-coumaranone (0.01 M) at room temperature.

6.2.4 Conclusions to this Section

We have described the first example of a base-catalyzed ship-in-a-bottle synthesis for the immobilization of a pre-fluorescent probe in the cavities of faujasite zeolite NaY to give a new material, DT@NaY, capable of monitoring radicals within the supramolecular assembly. This material was successfully employed in the solid state to study the intercavity diffusion of carbon-centered radicals generated by thermolysis of co-encapsulated AIBN. DT@NaY was also used in a slurry to study the penetration and percolation of carbon-centered radicals produced by thermolysis in the solution phase, external to the zeolite particle. The results obtained indicate that at elevated temperatures the penetration of small organic molecules occurs within minutes. The radical sensing ability of the prepared material should prove useful in mechanistic investigations of intrazeolite

chemistry. Considering that the most common uses of zeolites are as catalysts in a variety of industrially important reactions, encapsulated probes such as this one may help to determine mechanistic details of zeolite-catalyzed reactions thereby aiding in the intelligent design of more efficient catalytic materials.

DT@NaY was also shown to be reactive towards hydrogen-atom abstraction from synthetic antioxidant, 3-phenyl-2-coumaranone. This is, to our knowledge, the first report of an intrazeolitic hydrogen-abstraction reaction between a nitroxide and a non-phenolic antioxidant. However, despite the non-phenolic structure, recent investigations into the mechanism of H-transfer in PCH and related molecules, have suggested that the antioxidant properties of these lactones may be due to the enolic, rather than the lactonic, form.[33] Participation of the enol was determined by the solvent polarity dependence of the H-abstraction rate constant. Within the zeolite cavity, the polar environment may favour the enolic form, suggesting that intrazeolitic H-transfer occurs from the phenol, rather than from the lactone. Regardless of the mechanism, the process is subdivided into the fast initial reaction between the antioxidant and the easily accessible DT molecules and a slower, residual reaction with probe molecules rendered less accessible by the formation of bulky coupling products.

The supramolecular pre-fluorescent radical sensor described here has several advantages over traditional methodologies for the study of radicals in heterogeneous systems. The fluorescence-based probe methodology offers greatly improved sensitivity with respect to other spectroscopic methods for radical detection, such as differential diffuse reflectance spectroscopy. In addition, the matrix-immobilized probe methodology is complementary to the technique of electron paramagnetic resonance (EPR). EPR is an extremely sensitive technique for the detection of unpaired spins that can also be applied to optically opaque samples. However, the supramolecular probe technique surpasses EPR in terms of simplicity; the equipment required for fluorescence measurements is relatively inexpensive and commonly available in many research laboratories.

6.3 Fluorescently Labeled Zeolites for Imaging

6.3.1 Preparation and Characterization

In the context of our project relating to zeolite-hosted supramolecular sunscreens, a fluorescent-labeled zeolite probe was required in order to examine the interaction between zeolite particles and skin cells. This interaction is important due to the proposed cutaneous application of these new hybrid zeolite/sunscreen materials. The details of our work on supramolecular sunscreens will be described in detail in the following chapter. In this section, the preparation, characterization, and the use of the probe in microscopic imaging will be discussed.

The intended use of the probe in this work was to track the behaviour of zeolite particles as they interact with skin cells over a period of time. To examine this interaction, the modified zeolite probe was incubated with the skin cells suspended in a biological medium and the system analyzed by laser scanning confocal microscopy (LSCM) and differential interference contrast (DIC) microscopy. Given the intended conditions of use there are several important considerations in designing an appropriate fluorescent-modified probe:

1. The fluorophore must be permanently entrapped within the zeolite particle with no chance of escape into the bulk medium.
2. The absorption and emission characteristics of the probe must be convenient for confocal fluorescence microscopy and must have a suitable window for the cellular counter-stain.
3. The probe itself should be biologically inert.
4. The labeled zeolite complex should not behave as a photocatalyst under conditions of irradiation (like TP^+@NaY for example).
5. The complex should be stable under the conditions of the experiment and insensitive to the presence of oxygen.

Preparation of an irreversibly encapsulated guest molecule via ship-in-a-bottle synthesis easily addresses the first point. Successful ship-in-a-bottle

syntheses must be high yielding, uncomplicated reactions that proceed from precursors with molecular dimension of less than ~ 7 Å (along at least one axis). The precursors must react to form a product which will be accommodated within the 13 Å cavity of the zeolite, but cannot escape through the cavity windows. The photocatalytic activity of other complexes described in this thesis should preclude their use as probes in biological systems.

Instrumentation for fluorescence microscopy most often employs an argon-ion laser (λ_{em} = 488 nm) as the excitation source. To address the question of suitability for fluorescence microscopy, we considered several dyes commonly used in conjunction with this technique and, therefore, possessing the appropriate absorption and emission qualities. Fluorescein (see structure in Scheme 6.6) was chosen as the synthetic target based on its extensive use in biological imaging, low toxicity (as evidenced by its ophthamological use in fluorescein angiography of the retina), and simple, acid-catalyzed preparation.

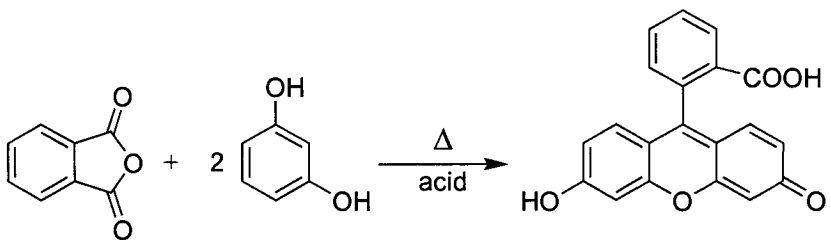

Scheme 6.6 Acid-catalyzed synthesis of fluorescein.

Fluorescein (2-(6-hydroxy-3-oxo-3*H*-xanthen-9-yl)-benzoic acid, F) was prepared within the pores of acidic zeolite HY via the acid catalyzed condensation of phthalic anhydride with two equivalents of resorcinol, as shown in Scheme 6.6, to give F@HY. Faujasite zeolite HY is effectively an H^+-exchanged zeolite where the charge-balancing countercations have been replaced by protons, resulting in a material with enhanced Brønstead acidity. HY was prepared according to literature procedures by high temperature calcination of a sample of NH_4Y.[34] The starting materials were included in the zeolite by mechanical mixing giving a white powder. Synthesis of F@HY was accomplished by heating the loaded material under

vacuum. Interestingly, when the starting materials were included from solution the reaction did not proceed efficiently. In the solid-state preparation, F@HY was obtained as an extremely bright yellow powder after one hour. Heating at higher temperatures or for prolonged periods of time resulted in a brownish powder, indicating product decomposition. The yellow powder was treated by solid-liquid extraction with DCM, to remove any un-reacted starting materials, and washed with water to remove any fluorescein molecules attached to the particle surface. Combustion elemental analysis of a rigorously dried sample indicated a final loading of <S> ~ 0.5, assuming fluorescein is the only carbon-containing material within the zeolite, this corresponds to an approximately quantitative reaction yield.

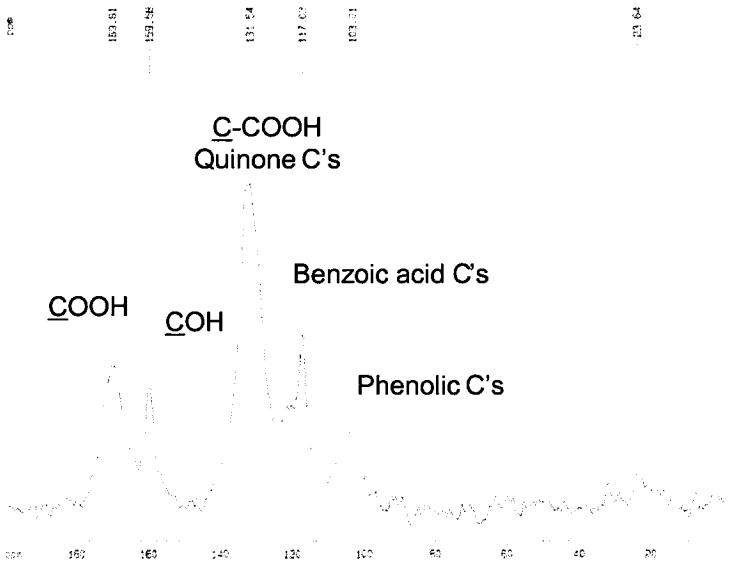

Figure 6.6 CP/MAS ^{13}C NMR spectrum of F@HY.

The CP/MAS ^{13}C NMR of F@HY (shown above in Figure 6.6) agrees with the spectrum of fluorescein recorded in solution. The DRS and the emission spectrum are shown below in Figure 6.7. The maximum in the diffuse reflectance spectrum is *ca.* 440 nm, in agreement with the reported absorption maximum for fluorescein in mildly acid solution (pH < 5), and this band has been attributed to the $S_0 \rightarrow S_n$ transition of the neutral form of fluorescein.[35] This result is also coincident with the

reported maximum in the excitation spectrum of a fluorescein-MCM-41 complex; note that fluorescein can easily enter, and exit, the large pores of MCM-41 directly.[36]

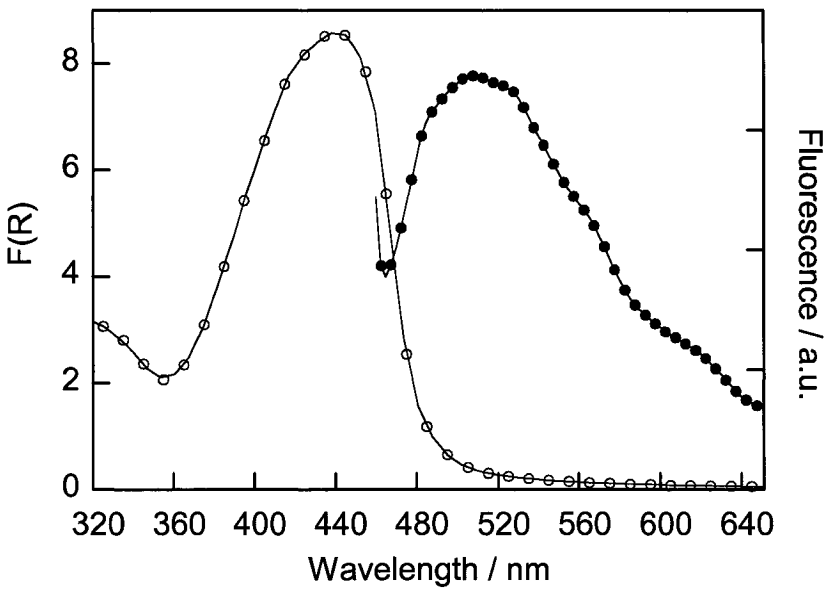

Figure 6.7 DRS (O) and emission spectrum (●) of F@HY recorded under air following excitation at 440 nm.

The interesting pH dependent photophysics of fluorescein and many of its derivatives have been well studied. [35, 37-39] In aqueous solutions above pH 9, both the phenol and the carboxylic acid group are almost completely ionized (Scheme 6.7). Acidification results in protonation of the phenolate to give the monoanion, followed by protonation of the carboxylate to yield the neutral molecule. Further acidification can generate a cation with pKa ~ 2. It has been reported that only the mono- and dianion are fluorescent with quantum yields of 0.37 and 0.93 respectively.[35, 37] Excitation of the neutral species leads to excited-state deprotonation resulting in emission from the anion with an overall quantum yield of 0.31.[37] In acidic or aprotic solutions, the neutral species is also suggested to be in equilibrium with a colourless, non-emissive lactone structure (see Scheme 6.7). This species is not believed to be a major contributor in the F@HY complex, based on the absence of a characteristic signal for the bridging carbon of the lactone in the ^{13}C

NMR (*ca.* 80-85 ppm relative to TMS). The absorption spectrum of fluorescein shows a shift to shorter wavelengths with increasing acidity, from *ca.* 480 nm at pH 12 to *ca.* 440 nm at pH 3.3. This is consistent with the maximum observed at 440 nm in the DRS of fluorescein encapsulated in acidic zeolite HY.[35]

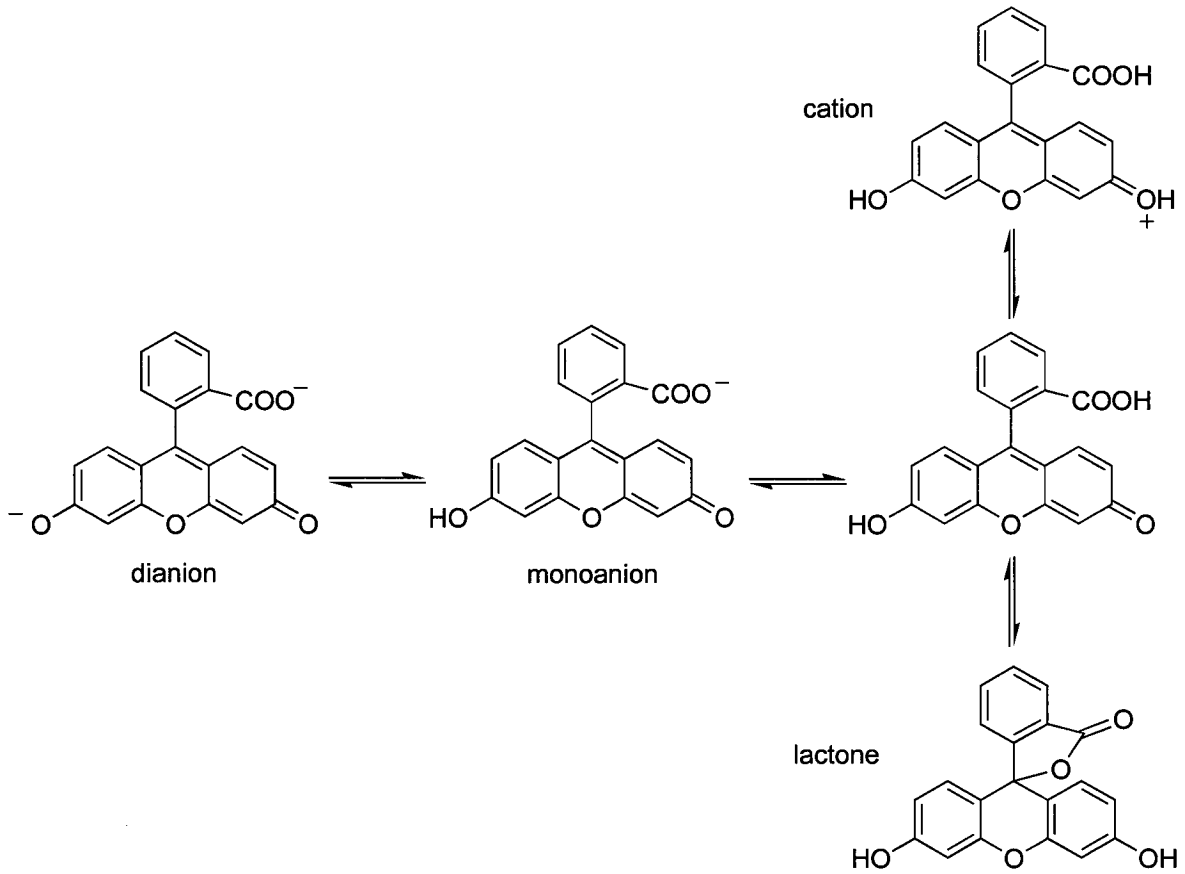

Scheme 6.7 The protolytic equilibria of fluorescein in the ground state.

It was initially assumed that, once encapsulated, fluorescein would be partially deprotonated, as has been observed for other carboxylic acids encapsulated in HY.[40] However, based on the DRS, it appears that neutral fluorescein is the predominant species within the cavities. The F@HY complex emission maximum is at *ca.* 510 nm with slight shoulders at *ca.* 550 and 600 nm, characteristic of the monoanionic species. The cation emission is bathochromically shifted to 475 nm and the dianion emission appears as a narrow band at 550 nm only; neither was observed for this sample. Based on the available spectroscopic

data, the highly emissive material, F@HY, contains largely neutral, but not lactonic, fluorescein. The presence of a small amount of the anionic form cannot be ruled out. Many species exhibit enhanced emission in zeolite cavities due to the suppression of non-radiative modes associated with molecular motions. Zeolite encapsulation may enhance the fluorescence from the neutral form of fluorescein in this manner. Alternatively, the electrostatic environment within the zeolite cavity may favour the excited-state deprotonation, increasing the formation of the fluorescent monoanion.[37]

To evaluate the effect of the zeolite acidity on the preparation and spectroscopic properties of fluorescein, F@NaY and F@CsY were also prepared. NaY is commonly considered a "neutral" zeolite but does in fact contain some acid sites and Cs^+-exchanged Y zeolite has a more basic character. Reduced fluorescence intensity was observed for both samples, most significantly for F@CsY. The more basic zeolite environment decreased the observed luminescence instead of increasing the emission intensity by favouring the formation of the highly emissive anionic forms. This may seem counterintuitive, however, the DRS shows a much lower yield of fluorescein in the less acidic zeolites, emphasizing the importance of acid sites for successful synthesis. The overall effect of increased intrazeolite basicity, was to disfavour the acid-catalyzed formation of fluorescein resulting in lower emission due to the formation of fewer fluorophores. The reduced efficiency of fluorescein formation in Cs^+-exchanged zeolite Y is likely due to reduced acidity and the reduced cavity volume of CsY (~780 $Å^3$) as compared to HY (~800 $Å^3$).

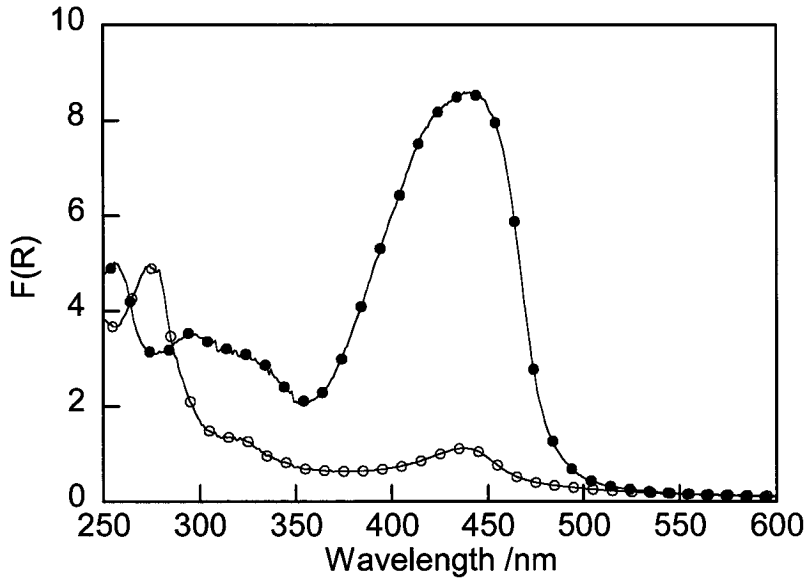

Figure 6.8 DRS recorded of F@HY (●) and F@CsY (○).

6.3.2 Photophysical Studies

The time-resolved emission profiles were recorded for both F@HY and F@CsY. The emission decay following 355 nm laser excitation is shown in Figure 6.9 for F@HY and Figure 6.10 for F@CsY. Although the zeolite environment heavily influenced other properties, the measured fluorescence lifetimes were similar for both samples. Unsurprisingly, the decays were multi-exponential in nature and the data were fitted with a tri-exponential expression, as a reasonable approximation, to obtain an estimate of the lifetimes. For F@HY the calculated lifetimes were τ_1 = 130 ps, τ_2 = 810 ps, and τ_3 = 3.8 ns. The lifetimes observed for F@CsY were very similar; τ_1 = 180 ps, τ_2 = 850 ps, and τ_3 = 3.1 ns. The major contributor to the overall decay is the fast component (~130-180 ps), which accounts for approximately 80%. In both cases there is a minor contribution (< 4%) from a long-lived component but the data quality at long times are compromised by a low signal-to-noise ratio. Examination of the data by lifetime distribution analysis also showed three lifetimes populations and supported the assignment of the short lifetime as the major contributor and the long-lived component as minor.

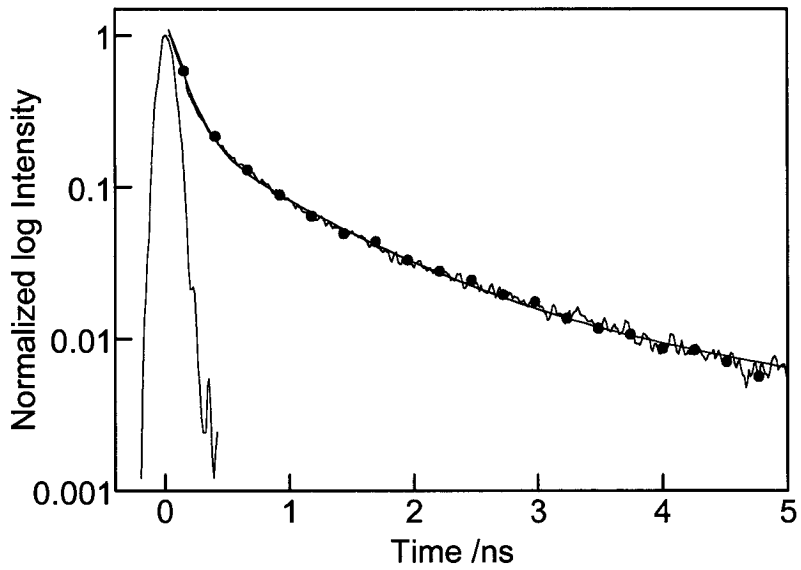

Figure 6.9 Fluorescence decay of F@HY following pulsed excitation at 355 nm under air. Instrument function is shown (—).

The fluorescence lifetime of fluorescein in aqueous solution varies between *ca.* 4.1-4.8 ns, depending on solvent polarity and viscosity, with a trend towards shorter lifetimes with increasing polarity and decreasing viscosity.[38, 39] The lifetimes were also shorter in more acidic solutions where the neutral form predominates, decreasing to *ca.* 3.5 ns at pH 5.8.[41] Moreover, Song *et al.* have noted that ester-ether analogues of fluorescein (i.e. where formation of the mono- and dianion are blocked) exhibit reduced fluorescence lifetimes of *ca.* 3.2-3.8 ns under the conditions studied.[42] The cavities of zeolite HY are certainly both polar and acidic and these factors may contribute to the truncated fluorescence lifetimes, but they cannot be invoked to account for the entire magnitude of the observed decrease.

The reduced lifetimes may be due to an effect of encapsulation beyond the polarity/acidity of the cavity environment. The photophysical behaviour of fluorescein and derivatives included in α-, β-, and γ-cyclodextrins and micelles has been reported. The lifetimes observed in the case of encapsulation in these "soft" cavities were the same or slightly longer than observed in aqueous solution and did not depend on the cyclodextrin size.[42, 43] The lifetime of fluorescein which had been

immobilized on non-ionic, polystyrene resins was found to depend heavily on the concentration of the initial solution used to load the resins. At higher concentrations (*ca.* 10^{-3} M) the observed lifetime was reduced to *ca.* 1.5 ns for one of the resins studied.[44]

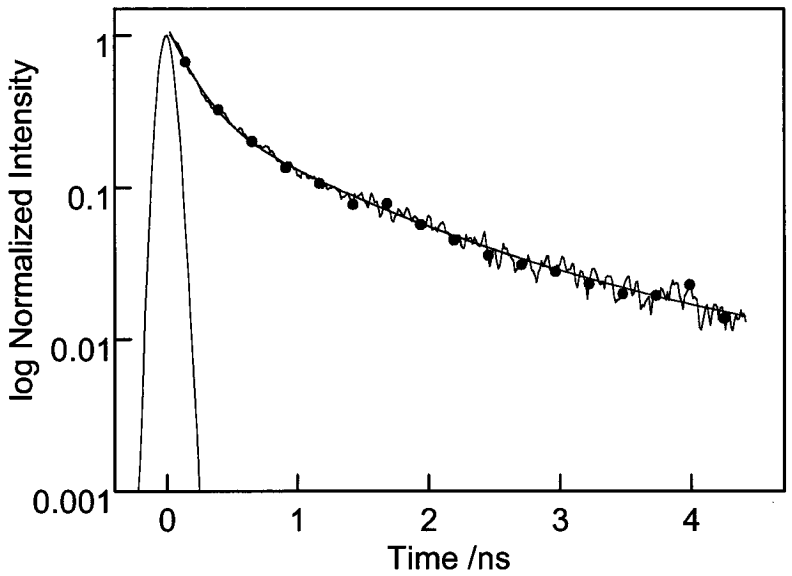

Figure 6.10 Fluorescence decay of F@CsY following 355 nm pulsed excitation under air. Instrument response is shown (—).

In agreement with data reported for highly loaded resins, the increased importance of a short lifetime component in the decay of encapsulated fluorescein was attributed to increased self-quenching interactions in the zeolite complex. The starting materials for the ship-in-a-bottle synthesis of F@Y were included in the solid state and, therefore, may be located primarily in the first several layers of cavities in the particle. If the starting materials are clustered in cages close to the particle surface, fluorescein formation will occur in the outermost cages as well. As a consequence, each encapsulated fluorescein molecule would have many near neighbours, drastically increasing the occurrence of self-quenching. By monitoring the time-dependent behaviour of the fluorescence in the presence of an externally located quencher it was possible to test this hypothesis.

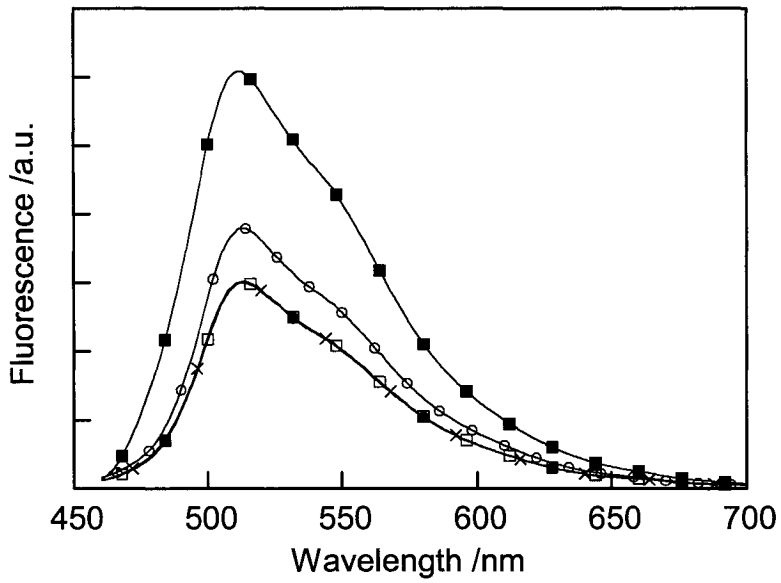

Figure 6.11 Emission spectra of F@HY in water before (■) and 0.5 min (□), 5 min (●), 15 min (×), and 45 min (○) after the addition of TEMPO.

A sample of F@HY was suspended in water and the fluorescence spectrum was recorded while stirring. A dilute, aqueous solution of TEMPO was added to the cuvette and the emission was re-measured. As discussed above, the paramagnetic nitroxide moiety of TEMPO is an efficient fluorescence quencher. As seen in Figure 6.11 above, the fluorescence is partially quenched almost immediately (□) and the emission remains at the same level for several minutes. Re-recording the fluorescence after 45 minutes (○) reveals that the emission has been partially restored. This behaviour may support the idea that fluorescein is primarily located in cavities near the surface and that very little is formed near the center of the particle. Due to the non-homogeneous distribution of the fluorophore, emission quenching is observed immediately as the quencher penetrates the particle, and interacts with the bulk of the fluorophores. As the quencher molecules penetrate the particle further and find no further fluorophores the residual emission is partially restored. This concept is shown graphically in Figure 6.12.

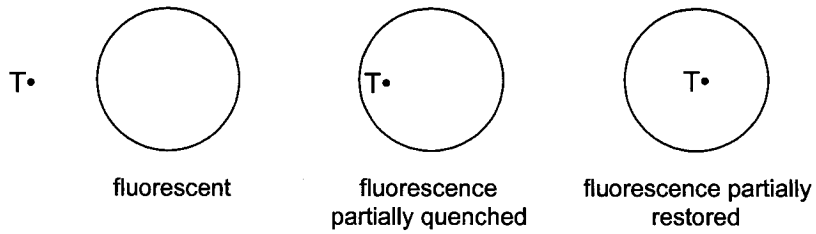

Figure 6.12 Graphical representation of time dependent fluorescence quenching. T•= TEMPO.

6.3.3 Microscopy Studies

One of the drawbacks to the use of fluorescein in microscopy applications is its rapid photobleaching. Depending on experimental details, fluorescein is generally seen to undergo significant bleaching after 30-90 seconds under the conditions of fluorescence microscopy (i.e illumination by the excitation light source). This photobleaching behaviour is the impetus behind the design of a multitude of fluorescein derivatives having the same favourable spectroscopic properties but greater photostability. Two popular examples are AlexaFluor and Oregon Green from Molecular Probes Inc. (structures in Scheme 6.8).

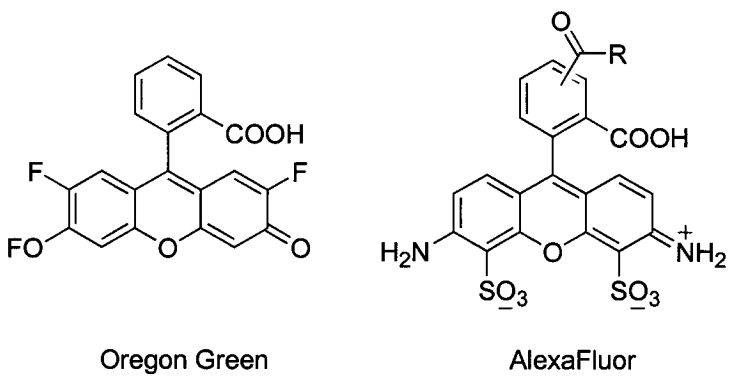

Scheme 6.8 Structures of fluorescein derivatives.

The mechanisms of photobleaching in fluorescein are complicated and depend heavily on lamp power, dye concentration, and temperature. At lower concentrations of the dye, the photobleaching kinetics are monoexponential and are thought to be dominated by the interaction of a long-lived triplet excited-state with

molecular oxygen.[45] At higher concentrations, the bleaching behaviour becomes more complex and the kinetics are no longer well described by a single exponential. Participation of the triplet excited-state is still implicated since the bleaching is reduced in the presence of triplet and radical quenchers.[46]

The photostability of fluorescein encapsulated in zeolite HY under the conditions of fluorescence microscopy was investigated. F@HY was suspended in water and the image shown in Figure 6.14a was recorded by monitoring emission > 400 nm. Figure 6.14a clearly shows the fluorescently labeled particles as bright green dots, the intensity was not visually observed to decrease over a period of 30 minutes under constant illumination by the 30 W xenon excitation lamp. The same sample was re-suspended in a slightly basic aqueous solution of fluorescein and the fluorescence image was recorded every ten seconds. It can be clearly seen in Figure 6.14b-d that the emission intensity from the solution phase faded rapidly with continuous illumination for only 30 seconds, whereas the zeolite particles retain their luminosity.

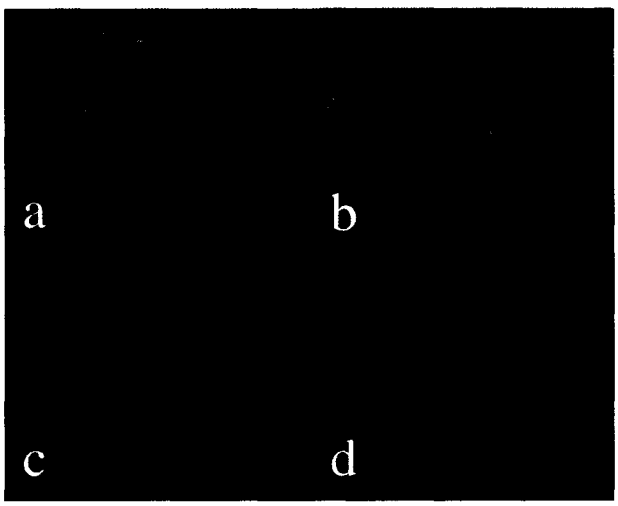

Figure 6.13 Fluorescence microscope image of F@HY suspended in water (a) and in an aqueous solution of fluorescein after 10 s (b), 20 s (c), and 30 s (d) of continuous illumination by the microscope excitation source. Filter set XF02-02, 330 nm WB excitation and > 400 nm emission.

Having successfully prepared stable, fluorescently labeled zeolite particles, we were interested in exploring the interaction between zeolites and cells, in the context of the proposed use of modified zeolites as components of topically applied creams. For the application of zeolites as protective encapsulators, it is vital that they do not penetrate into living cells. These preliminary confocal and DIC microscopy studies were carried out at Concordia University in collaboration with Prof. A. M. English.

LSCM is a technique that allows the non-invasive, 3D microscopic imaging of relatively "thick" samples. In LSCM, the excitation beam is focused onto a single plane within the specimen. The emitted light is focused, using a dichroic mirror and interference filters, onto an aligned confocal aperture or pinhole. Fluorescence from points outside of the focal plane will be largely obstructed by the confocal aperture and so only light from the in-focus plane is sensed by the PMT detector. One of the advantages of LSCM is the ability to image live cells by collection of three-dimensional data in the form of a Z-series. A Z-series is a sequence of optical sections collected at different planes within the sample. By labeling the zeolite particles and the cells with different fluorophores, this technique allows the detection of zeolite particles that have penetrated the cells. DIC is a complimentary technique that allows the visualization of surface features in the sample. In the DIC image, zeolite particles which have penetrated the cells will not appear.

The interaction between labeled zeolites and human skin fibroblasts was examined. It was previously determined that when stained with a 0.9% saline solution of fluorescein, dye uptake by human skin fibroblasts was efficient and the cells did not exhibit auto-fluorescence at the excitation wavelength used.[47] The question of penetration was addressed by incubating the cells with 30 $\mu g\ ml^{-1}$ of F@HY in the cell medium (Dubelco's modified Eagle medium, DMEM) for a specified period of time (maximum incubation was 27 hours). After this time the cells were washed and stained with a fluorescent rhodamine dye (5-(and6-)-(((4-chloromethyl)benzoyl)amino)tetramethylrhodamine, CMTMR). CMTMR was

chosen as the cellular counterstain because its emission did not overlap with that of F@HY. After staining, the cells were imaged by LSCM and DIC microscopy.

Microscopic imaging revealed an interesting interaction between the labeled zeolite particles and the skin cells. The zeolites were not observed to penetrate the cells but as can be seen below for the human skin fibroblasts, the particles show a tendency to aggregate and collect on the cell surface after long incubation times (Figure 6.14b). The fluorescent zeolite particles in a and b are still observable in the DIC images in Figure 6.14c and d indicating that they are not located inside of the cell. The external location of the particles is further supported by the Z-series images shown in Figure 6.15 for the system incubated for one hour and Figure 6.16 for the system after 27 hours. The aggregation of zeolite particles on the cell surface is especially apparent in Figure 6.16 where virtually all of the particles in the sample have accumulated on top of the cells.

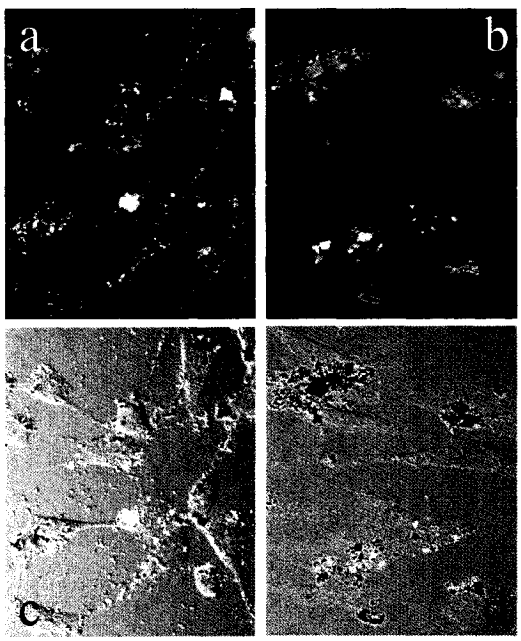

Figure 6.14 Confocal fluorescence microscopy images of CMTMR stained human skin fibroblasts after 1 h (a) and 27 h (b) and incubation with F@HY. λex = 543 nm for CMTMR and 488 nm for F@HY, emission monitored between 560-580 nm and 510-530 nm respectively. DIC images (c) and (d) recorded of the same samples as shown in (a) and (b). Different regions of the sample were imaged at 1 and 27 h.

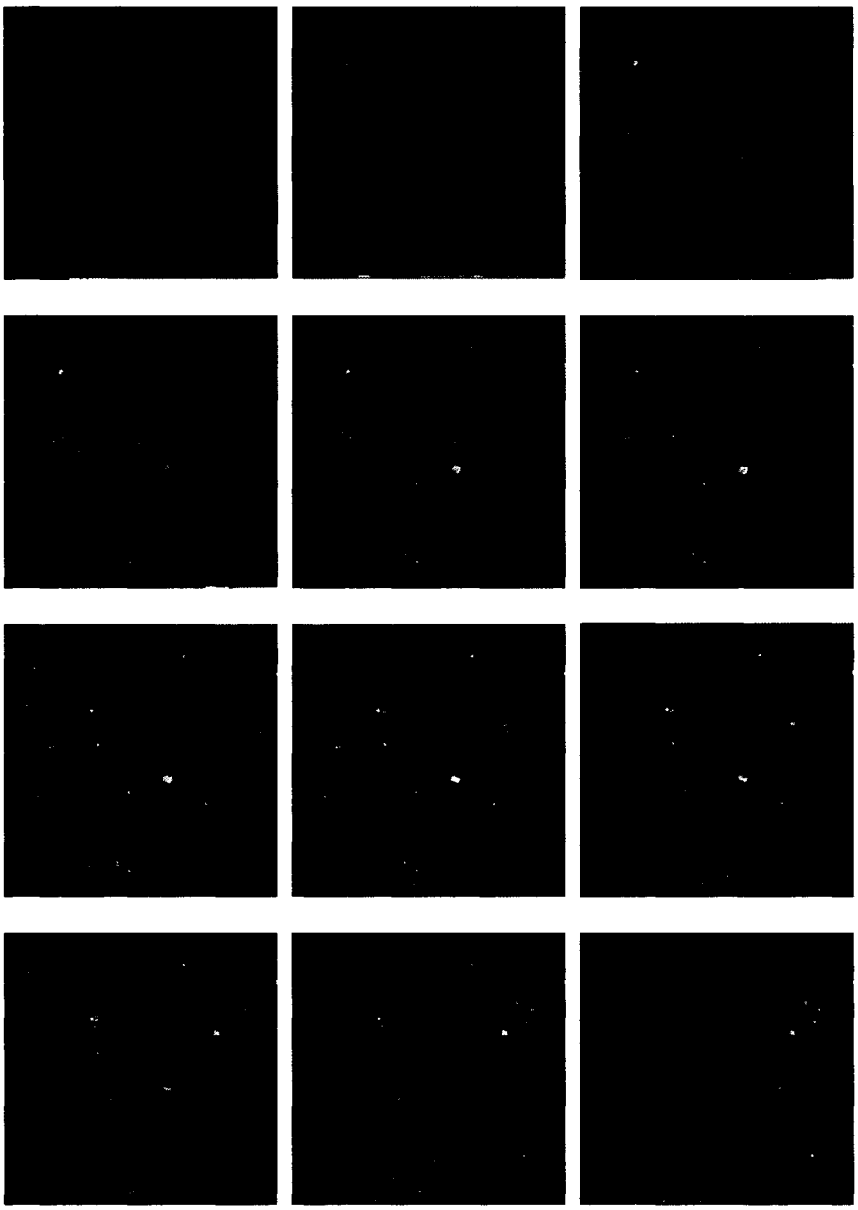

Figure 6.15 Z-series compliled from confocal fluorescence microscopy images of CMTMR stained human skin fibroblasts after 1 h incubation with F@HY in 0.9% saline. Excitation at 543 nm for CMTMR and at 488 nm for F@HY, emission monitored at 560-580 nm and 510-530 respectively. Image slices were recorded beginning at the "bottom" of the sample (top left).

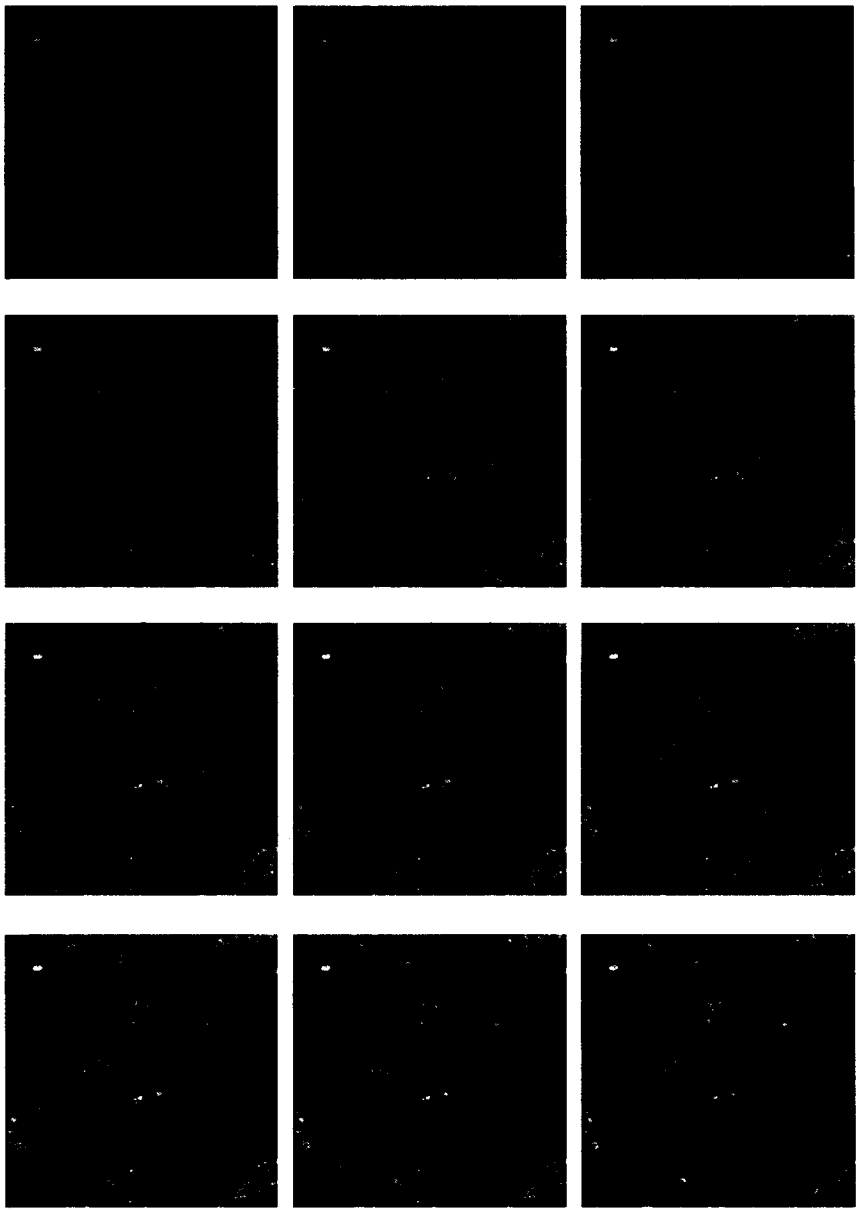

Figure 6.16 Z-series compiled from confocal fluorescence microscopy images of CMTMR stained human skin fibroblasts after 27 h incubation with F@HY in 0.9% saline. Excitation at 543 nm for CMTMR and at 488 nm for F@HY, emission monitored at 560-580 nm and 510-530 respectively. Image slices were recorded beginning at the "bottom" of the sample (top left).

6.3.4 Conclusions to this Section

Fluorescently-labeled zeolite particles were successfully prepared by the acid-catalyzed ship-in-a-bottle synthesis of fluorescein in zeolite HY. The complex was characterized spectroscopically and determined to contain primarily the neutral or monoanionic form of fluorescein based on comparison with the absorption and emission spectra of fluorescein in solutions of various pH. The use of less acidic zeolites in the synthesis resulted in lower yields of the fluorophore and consequently a less emissive material. The fluorescence from encapsulated fluorescein was observed to decay multi-exponentially and with little to no effect of the charge-balancing countercation. The major component of the decay (> 80%) had $k \sim 6\text{-}7 \times 10^9\ s^{-1}$ corresponding to a lifetime of *ca.* 150 ps. This is much shorter than the value of *ca* 4.5 ns obtained in solution, and an order of magnitude shorter than the lifetime observed for samples of resin-bound fluorescein. The reduced lifetime was attributed to the increased occurrence of self-quenching in the material, due to non-homogeneous dye distribution resulting from the solventless preparation. The truncated fluorescence lifetimes did not impact on the desirable optical properties of the material with respect to imaging.

Fluorescence microscopy studies showed that F@HY is significantly more stable than free fluorescein in solution. The usefulness of this material for imaging applications was tested in a preliminary study of the interaction between zeolite particles and skin cells. LSCM and DIC microscopy showed that zeolite particles did not penetrate the fibroblast cells used in the experiment but did show a tendency to collect at the cell surface. This behaviour may be due to an electrostatic interaction between the zeolite particle and the cell membrane. Importantly, incubation with the zeolite particles was also not observed to affect cell viability. For more detailed cell studies using F@HY and studies exploring the use of $Ru^{2+}(bpy)_3$@Y as a probe in biological systems the reader is referred to reference 46.

6.4 Experimental

6.4.1 Sample Preparation

All chemicals used for sample preparation were obtained from Aldrich in their highest available purity and used as received, unless otherwise indicated.

6.4.1.1 DT@NaY

A sample of zeolite NaY (*ca.* 1 g) was thermally dehydrated at 480°C overnight and added to 15 mL of hexane, the resulting slurry was purged with nitrogen. Pyridine (50 μL, 0.62 mmol) was added to the hexane slurry at room temperature and stirred overnight. 4-Amino TEMPO, 4-amino-2,2,6,6-tetramethylpiperidin-1-oxyl, (50 mg, 0.29 mmol) was then added and the entire mixture stirred for a further 24 h. TLC analysis (hexane/ethylacetate) after this time showed no 4-amino TEMPO present in the slurry solvent, indicating complete uptake by the zeolite. Dansyl chloride, 5-dimethylamino-1-naphthalenesulphonyl chloride, (80 mg, 0.29 mmol) was then added and the slurry stirred under nitrogen for 72 h. The solid was collected by filtration and washed with 5 x 5 mL of hexane. The material was subjected to solid-liquid extraction with DCM for a further 72 h. Small amounts of dansyl-TEMPO were recovered from the extraction solutions indicating that product formation also occurred outside of the zeolite particle. Combustion elemental analysis (M-H-W Laboratories, Phoenix AZ) of a rigorously dried sample gave an occupancy of <S> ~ 0.1, corresponding to a reaction yield of *ca.* 20%.

6.4.1.2 F@HY, F@NaY, and F@CsY

CsY was prepared from NaY via three consecutive ion-exchange cycles using cesium acetate in deionized water (Millipore, MilliQ) as described previously.[48] NH_4Y was also prepared by typical ion-exchange protocols using ammonium acetate in deionized water. HY was generated by steam calcination of NH_4@Y at 500°C as reported.[34] Encapsulated fluorescein was prepared by mechanical mixing

of *ca.* 1 g of the zeolite of choice (previously treated by heating at 480°C overnight) with phthalic anhydride (44 mg, 0.29 mmol) and resorcinol (65 mg, 0.59 mmol). The resulting white powder was heated under vacuum at 200°C for 1 h. The resulting bright yellow solid was subjected to solid-liquid extraction with DCM for 48 hours and was then washed with deionized water, until the filtrate was non-fluorescent, and collected by filtration. Combustion elemental analysis (M-H-W Laboratories, Phoenix, AZ) of a rigorously dried sample gave an occupancy of <S> ~ 0.5 corresponding to an approximately quantitative reaction yield.

6.4.2 Steady-state Spectroscopy

Absorption and DR spectra were recorded as described in Section 5.4.2. Samples were recorded under air unless otherwise indicated. CP/MAS ^{13}C NMR were recorded with the assistance of Dr. G. Facey on a Bruker ASX-200 solid-state NMR spectrometer operating at 50.3 MHz with a sample spin rate of 5.5 kHz (TMS standard). Time-dependent fluorescence growth curves were recorded using a v.1.2 X luminescence spectrometer from Photon Technology International. Emission spectra were recorded on either the PTI instrument or the LS-50 spectrofluorimeter from Perkin Elmer. Fluorescence from slurry samples were recorded while stirring and under nitrogen where indicated.

6.4.3 Time-Resolved Spectroscopy

Time-resolved emission spectra were recorded using the streak camera based system described in detail in Section 2.3 of this thesis. Samples were contained in 3 x 7 mm^2 fused quartz cells (Friedrich & Dimmoch) and recorded under air. The samples were excited with pulses from the third harmonic of a Continuum PY-61 Nd-YAG laser with an average pulse width of 35 ps and a typical power output at 355 nm of *ca.* 5 mJ $pulse^{-1}$. All time-resolved data were manipulated, and kinetic parameters extracted, using the Kaleidagraph program from Synergy software. Lifetime distribution analysis was carried out using the ESM program described in Section 2.2.4, from Photon Technology International.

6.4.4 Intrazeolite Reactivity of DT@NaY

6.4.4.1 Thermal Decomposition of AIBN

A sample of DT@NaY (0.5 g) was suspended in 10 mL of hexane and AIBN (49 mg, 0.30 mmol) was added. The slurry was stirred overnight at room temperature and then collected by filtration and washed with 5 x 5 mL of hexane. UV-vis analysis of the recovered washing solution indicated complete inclusion of AIBN (<S>= 0.5). The solid sample was then dried under nitrogen to completely remove the solvent and heated at 70°C in a sandbath to induce AIBN thermolysis. After heating the sample was cooled to room temperature by immersion in a water bath for ten minutes. The fluorescence intensity at 550 nm was recorded at intervals and plotted versus time. The excitation wavelength was λ_{ex}=305 nm.

6.4.4.2 Diffusion of 3-Phenyl-2-coumaranone Radicals

A sample of DT@NaY (2.0 mg) was added to a fluorescence cuvette containing 2 mL of 3,3'-diphenyl-3*H*,3'*H*-[3,3']bisbenzofuranyl-2,2'-dione (PC-PC, prepared by A. Ricci according to literature procedures)[32] in hexane (1.2 x10^{-3} M). The DT@Y slurry (1.0 mg mL^{-1}) was purged with nitrogen and stirred for 10 min at room temperature. The cuvette was then placed in the fluorimeter chamber and heated to 50°C while stirring. The fluorescence intensity at 550 nm was measured using an excitation wavelength of λ_{ex}=330 nm, and plotted versus time.

6.4.4.3 Hydrogen Abstraction from 3-Phenyl-2-coumaranone

DT@NaY (2.0 mg) was added to a fluorescence cuvette containing 2 mL of 3-phenyl-2-coumaranone (prepared from mandelic acid and phenol according to reported procedures)[49] in benzene (0.01 M). The DT@Y (slurry 0.5 mg mL^{-1}) was purged with nitrogen and stirred for 5 min at room temperature. After this time the fluorescence evolution at 550 nm was monitored at room temperature, while stirring, using an excitation wavelength of λ_{ex}=330 nm. The data were plotted versus time.

6.4.5 Fluorescence Microscopy

6.4.5.1 Instrumentation

Confocal and differential interference contrast (DIC) images were obtained using a Leica TCS SP2 laser scanning confocal microscope. The excitation source was an Ar-Kr laser and the excitation wavelengths were 488 nm for F@Y and 543 nm for CMTMR. The emission was monitored at 510-530 nm and 560-580 nm for F@HY and CMTMR respectively. The single plane fluorescence signals were collected by a computer and a Z-series was compiled. Conventional fluorescence images were obtained with a Leica DMLS fluorescence microscope using filter set XF02-02 from Omega Optical (330 nm wideband excitation filter and > 400 nm band pass emission filter). LSCM and DIC images were obtained with the assistance of Mr. B. Shen.

6.4.5.2 Preparation of Samples for Microscopy

Human skin fibroblasts were obtained from Victoria Royal Hospital (Montréal, QC). Culture cells were maintained at 37°C under an atmosphere of 5% CO_2 in 100 mm cell culture dishes containing Dulbecco's modified Eagle's medium (DMEM, Sigma) supplemented with 10% fetal calf serum (FCS, Sigma). After ~20 h incubation, subconfluent cells were harvested by trypsin-EDTA (ethylenediaminetetraacetic acid, Sigma) solution treatment and re-suspended in 15 mL DMEM. In preparation for the experiment, 1 mL of the cell suspension was placed in each chamber on a chamber slide and incubated under the same conditions as above. The cells were then incubated with a 30 μg suspension of F@Y in DMEM for 1, 4, and 27 h at 37°C in a 5% CO_2 atmosphere. Following this exposure the cells were washed twice with a 0.9% saline solution and then stained using 1 mL of a 0.9% saline solution containing 4.5 μM of 5-(and-6-)-(((4-chloromethyl)benzoyl)amino) tetramethylrhodamine (CMTMR, Molecular Probes Inc.). The staining solution was prepared from a 9.0 mM stock solution of CMTMR

in DMSO. Cell manipulations were undertaken with the assistance of Mr. B. Shen and Dr. F. Mohamed.

6.5 References

1. N. V. Blough and D. J. Simpson, Chemically mediated fluorescence yield switching in nitroxide-fluorophore adducts: Optical sensors of radical/redox reactions, *J. Am. Chem. Soc.*, **1988**, *110*, 1915-1917.

2. S. A. Green, D. J. Simpson, G. Zhou, P. S. Ho and N. V. Blough, Intramolecular quenching of excited singlet states by stable nitroxyl radicals, *J. Am. Chem. Soc.*, **1990**, *112*, 7337-7346.

3. S. A. Green and M. A. Fox, Intramolecular photoinduced electron transfer from nitroxyl radicals, *J. Phys. Chem.*, **1995**, *99*, 14752-14757.

4. S. E. Herbelin and N. V. Blough, Intramolecular quenching of excited singlet states in a series of flourescamine-derivatized nitroxides, *J. Phys. Chem. B*, **1998**, *102*, 8170-8176.

5. V. W. Bowry and K. U. Ingold, Kinetics of nitroxide radical trapping. 2. Structural effects *J. Am. Chem. Soc.*, **1992**, *114*, 4992-4996.

6. J. Chateauneuf, J. Lusztyk and K. U. Ingold, Absolute rate constants for the reaction of some carbon centered radicals with 2,2,6,6-tetramethyl-1-piperidinoxyl, *J. Org. Chem.*, **1998**, *53*, 1629-1632.

7. A. L. Beckwith, A. L. Bowry and K. U. Ingold, Kinetics of nitroxide radical trapping. 1. Solvent effects, *J. Am. Chem. Soc.*, **1992**, *114*, 4983-4992.

8. W. G. Skene, J. C. Scaiano, N. A. Listigovers, P. M. Kazmaier and M. K. Georges, Rate constants for the trapping of various carbon-centered radicals by nitroxides: Unimolecular initiators for living free radical polymerization, *Macromolecules*, **2000**, *33*, 5065-5072.

9. J. L. Gerlok, P. J. Zacmanidis, D. R. Bauer, D. J. Simpson, N. V. Blough and I. T. Salmeen, Fluorescence detection by free radical nitroxide scavenging, *Free Radical Res. Commun.*, **1990**, *10*, 119-121.

10. D. J. Kieber and N. V. Blough, Fluorescence detection of carbon-centered radicals in aqueous solution, *Free Radical Res. Commun.*, **1990**, *10*, 109-117.

11. D. J. Kieber and N. V. Blough, Determination of carbon-centered radicals in aqueous-solution by liquid-chromatography with fluorescence detection, *Anal. Chem.*, **1990**, *62*, 2275-2283.

12. B. Li, J. P. L. Gutierrez and N. V. Blough, Trace determination of hydroxyl radical in biological systems, *Anal. Chem.*, **1997**, *69*, 4295-4302.

13. K. Hiramoto, N. Ojima and K. Kikugawa, Conversion of nitroxide radicals by phenolic and thiol antioxidants, *Free Radical Res.*, **1997**, *27*, 45-53.

14. C. Aliaga, E. A. Lissi, O. Augusto and E. Linares, Kinetics and mechanism of the reaction of a nitroxide radical (Tempol) with a phenolic antioxidant, *Free Radical Res.*, **2002**, *34*, 659-665.

15. C. Aliaga, A. Aspee and J. C. Scaiano, A new method to study antioxidant capability: Hydrogen transfer from phenols to a prefluorescent nitroxide, *Org. Lett.*, **2003**, *5*, 4145-4148.

16. E. Lozinsky, V. V. Martin, T. A. Berezina, A. I. Shames, A. L. Weis and G. I. Likhtenshtein, Dual fluorophore-nitroxide probes for analysis of vitamin C in biological liquids, *J. Biochem. Biophys. Methods*, **1999**, *38*, 29-42.

17. N. J. Turro, From boiling stones to smart crystals: Supramolecular and magnetic isotope control of radical-radical reactions, *Acc. Chem. Res.*, **2000**, *33*, 634-646.

18. A. Aspee, O. Garcia, L. Maretti, R. Sastre and J. C. Scaiano, Free radical reactions in poly(methylmethacrylate) films monitored using a pre-fluorescent quinoline-TEMPO sensor, *Macromolecules*, **2002**, *36*, 3550-3556.

19. C. Coenjarts, O. G. Ballesteros, L. Llauger, J. Palfreyman, A. L. Vinette and J. C. Scaiano, Mapping photogenerated radicals in thin polymer films: Fluorescence imaging using a pre-fluorescent radical probe, *J. Am. Chem. Soc.*, **2003**, *125*, 620-621.

20. O. G. Ballesteros, L. Maretti, R. Sastre and J. C. Scaiano, Kinetics of cap separation in nitroxide-regulated "living" free radical polymerization: Application of a novel methodology involving a prefluorescent probe nitroxide switch, *Macromolecules*, **2001**, *34*, 6184-6187.

21. G. Weber, Polarization of the fluorescence of macromolecules. II. Fluorescent conjugates of ovalbumin and bovine serum albumin, *Biochem. J.*, **1952**, *51*, 155-167.

22. R. P. Haughland, Fluorophores and their amine-reactive derivatives In *Handbook of Flruoescent Probes and Research Products 9th Edition*; Molecular Probes Inc.: Eugene, 2002.

23. J. C. Scaiano, M. Kaila and S. Corrent, Intrazeolite photochemistry. 19. Effect of the "spectator" pyridine on the behaviour of carbonyl triplet states in the zeolite NaY, *J. Phys. Chem. B*, **1997**, *101*, 8564-8568.

24. S. Corrent, L. J. Martínez, J. C. Scaiano, H. García and V. Fornés, Intrazeolite photochemistry. Photochemistry of 1-azaxanthone in zeolites in the presence of hydrogen donors, electron donors, and energy donors, *J. Phys. Chem. B*, **1999**, *103*, 8097-8103.

25. J. C. Scaiano and H. García, Intrazeolite photochemistry: Toward supramolecular control of molecular photochemistry, *Acc. Chem. Res.*, **1999**, *32*, 783-793.

26. A. Corma and H. García, Supramolecular host-guest systems in zeolites prepared by ship-in-a-bottle synthesis, *Eur. J. Inorg. Chem.*, **2004**, 1143-1164.

27. J. Fossey, D. Lefort and J. Sorba *Free Radicals in Organic Chemistry;* Wiley: New York, 1995.

28. P. Karafiloglou, L. P. Catteau, A. Lablanche-Combier and H. Ofenberg, Electron spin resonance study of a stable benzo[*b*]furanyl radical, *J. Chem. Soc. Perkin Trans. II*, **1977**, 1545-1548.

29. B. B. Lohray, C. V. Kumar, P. K. Das and M. V. George, Photochemical and thermal transformations of 2(3*H*)-furanones and bis(benzofuranones). A laser flash photolysis study, *J. Am. Chem. Soc.*, **1984**, *106*, 7352-7359.

30. J. P. Catteau, P. Karafiloglou and A. Lablanche-Combier, Unsymmetrical coupling of radicals derived from benzo[*b*]furan, *J. Chem. Res.*, **1980**, 3901-3910.

31. E. V. Bejan, E. Font-Sanchis and J. C. Scaiano, Lactone-derived carbon-centered radicals: Formation and reactivity with oxygen, *Org. Lett.*, **2001**, *3*, 4059-4062.

32. M. Frenette, C. Aliaga, E. Font-Sanchis and J. C. Scaiano, Bond dissociation energies for radical dimers derived from highly stabilized carbon-centered radicals, *Org. Lett.*, **2004**, *6*, 2579-2582.

33. C. Aliaga, D. R. Stuart, A. Aspee and J. C. Scaiano, Solvent effects on hydrogen abstraction reactions from lactones with antioxidant properties, *Org. Lett.*, **2005**, submitted.

34. M. J. Climent, A. Corma, H. García and J. Primo, Zeolites as catalysts in organic reactions: Condensation of aldehydes with benzene derivatives, *J. Catal.*, **1991**, *130*, 138-146.

35. M. M. Martin and L. Lindqvist, The pH dependence of fluorescein fluorescence, *J. Luminescence*, **1975**, *10*, 381-390.

36. Y. Yao, M. Zhang, J. Shi, M. Gong, H. Zhang and Y. Yang, Encapsulation of fluorescein into MCM-41 mesoporous molecular sieve by a sol-gel method, *Mater. Lett.*, **2001**, *48*, 44-48.

37. R. Sjöback, J. Nygren and M. Kubista, Absorption and fluorescence properties of fluorescein, *Spectrochim. Acta A*, **1995**, *51*, L7-L21.

38. D. Magde, G. E. Rojas and P. G. Seybold, Solvent dependence of the fluorescence lifetimes of xanthene dyes, *Photochem. Photobiol.*, **1999**, *70*, 737-744.

39. D. Magde, R. Wong and P. G. Seybold, Fluorescence quantum yields and their relation to lifetimes of rhodamine 6G and fluorescein in nine solvents: Improved absolute standards for quantum yields, *Photochem. Photobiol.*, **2002**, *75*, 327-334.

40. F. L. Cozens, M. L. Cano, H. García and N. P. Schepp, Alkali metal cation control of oxidation reactions of radicals in zeolites, *J. Am. Chem. Soc.*, **1998**, *120*, 5667-5673.

41. A. G. Ryder, S. Power, T. J. Glynn and J. J. Morrison, Time-domain measurement of fluorescence lifetime variation with pH, *Proc. SPIE*, **2001**, *4259*, 102-109.

42. A. Song, J. Zhang, M. Zhang, T. Shen and J. Tang, Spectral properties and structure of fluorescein and its alkyl derivatives in micelles, *Colloids Surf., A*, **2000**, *167*, 253-262.

43. L. Flamigni, Inclusion of fluorescein and halogenated derivatives in α–, β–, and γ-cyclodextrins. A steady-state and picosecond time-resolved study, *J. Phys. Chem.*, **1993**, *97*, 9566-9572.

44. W. A. Wyatt, G. E. Poirier, F. V. Bright and G. M. Hieftje, Fluorescence spectra and lifetimes of several fluorophores immobilized on nonionic resins for use in fibre-optic sensors, *Anal. Chem.*, **1987**, *59*, 572-576.

45. L. Song, E. J. Hennink, I. T. Young and H. J. Tanke, Photobleaching kinetics of fluorescein in quantitative fluorescence microscopy, *Biophys. J.*, **1995**, *68*, 2588-2600.

46. L. Song, C. A. Varma, J. W. Verhoeven and H. J. Tanke, Influence of the triplet excited state on the photobleaching kinetics of fluorescein in microscopy, *Biophys. J.*, **1996**, *70*, 2959-2968.

47. B. Shen *Cell penetration of supramolecular sunscreen components and the effects of these components on UVA-irradiation of cells;* M.Sc. thesis, Concordia University: Montreal, 2003.

48. A. Corma, V. Fornés, R. M. Martin-Aranda, H. García and J. Primo, Zeolites as base catalysts: Condensation of aldehydes with derivatives of malonic acid esters, *Appl. Catal.*, **1990**, *59*, 237-48.

49. A. Pawda, D. Dehm, T. Oine and G. A. Lee, Photochemical transformations of small ring heterocyclic compounds. LXII. Competitive keto-enolate photochemistry in the 3-phenylcoumaran-2-one system, *J. Am. Chem. Soc.*, **1975**, *97*, 1837-1842.

7. Supramolecular Sunscreens

7. Supramolecular Sunscreens 245

7.1 Background 246
7.2 Modified Sunscreens 254
7.2.1 Oxybenzone 256
7.2.2 Octyl Salicylate 257
7.2.3 Octyl Methoxycinnamate 258
7.2.4 Octocrylene 260
7.2.5 *p*-Aminobenzoic Acid 261
7.3 Photophysical Studies 263
7.3.1 Oxybenzone 263
7.3.2 Octyl Salicylate 268
7.3.3 Octyl Methoxycinnamate 271
7.3.4 Octocrylene 274
7.3.5 *p*-Aminobenzoic Acid 275
7.4 Photostability Studies 278
7.4.1 Photostability of Sunscreens in Solution 278
7.4.2 Photostability of Supramolecular Sunscreens 286
7.5 Photobiological Studies 293
7.5.1 PABA: A Case Study 293
7.5.2 Biological Impact of Supramolecular Sunscreens 297
7.6 Concluding Remarks 311
7.7 Experimental 314
7.7.1 Zeolite Sample Preparation 314
7.7.2 Spectroscopy 314
7.7.3 Photostability of Sunscreens in Solution 315
7.7.4 Photostability of Supramolecular Sunscreens 317
7.7.5 Biological Impact Studies 317
7.8 References 322

7.1 Background

Electromagnetic radiation emitted by the sun can be subdivided into ultraviolet (100-400 nm), visible (400-700 nm) and infrared (700-5000 nm). This solar radiation is attenuated as a result of absorption by atmospheric components and the modulated spectrum reaching the earth's surface is shown in Figure 7.1. The UV region of the spectrum is further subdivided into UVC (100-280 nm), UVB (280-315 nm), and UVA (315-400 nm). As can be seen in Figure 7.1, wavelengths of light below 280 nm are significantly absorbed by atmospheric ozone and, therefore, UVC radiation does not reach the earth's surface. From a human health perspective UVC from sunlight is of little practical concern, however, both UVA and UVB radiation penetrate the atmosphere to a significant degree.

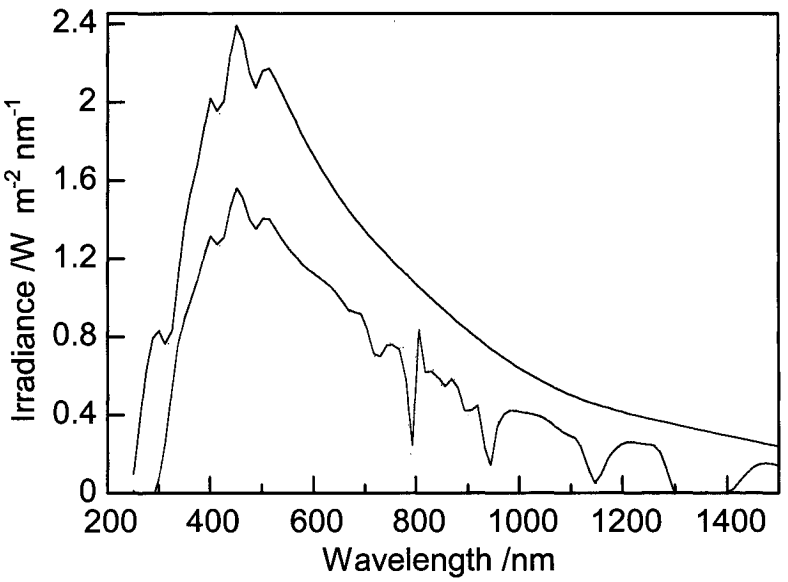

Figure 7.1 Spectral distribution of solar radiation before (red) and after (blue) attenuation by the atmosphere.[1]

Despite the fact that living organisms have developed pigmentation and other strategies to protect themselves from solar radiation, the damaging effects of ultraviolet radiation (UVR) on human and animal skin are well documented.[2-4] Radiation is absorbed by various components of tissue, and the penetration of

different wavelengths through the skin is a function of their frequency; lower frequencies (i.e. lower energies) have a higher transmittance through tissue. In the case of UVB radiation, these frequencies are largely absorbed in the first layers of the skin or stratum corneum. Wavelengths in the UVA region are able penetrate more significantly, reaching components of the circulatory system (Figure 7.2).

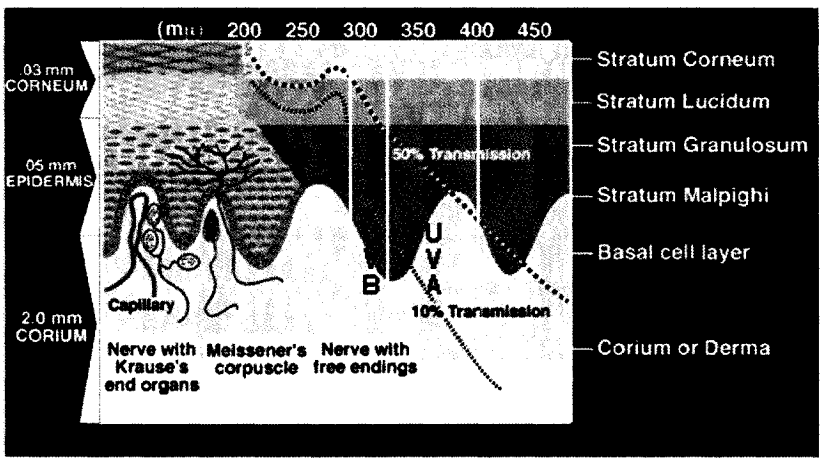

Figure 7.2 Penetration of human skin by ultraviolet radiation.[5]

Exposure to UVR has both acute and chronic or delayed effects on the skin. Acute effects include responses such as inflammation (i.e. sunburn or erythema), pigmentation, hyperplasia (thickening of the epidermis), and immunosuppression.[2, 6-8] The chronic effects of exposure to sunlight are primarily photocarcinogenesis and photoaging. There is a good deal of evidence linking UVR exposure to the development of non-melanoma skin cancers (NMSC). For example, NMSC are most common on areas of the body that receive the largest UVR dose, people who sunburn easily are more susceptible to NMSC, and exposure to UVR produces dose, time, and wavelength dependent skin cancers in animals. [3, 9-11] The role of sunlight in malignant melanoma is more complex because other factors, such as heredity, are also important determinants for its development. There is, however, both epidemiological and direct experimental evidence supporting the role of sunlight as a risk factor for melanoma.[3, 12] Severe sunburn in childhood and the inability to tan have both been implicated as indicators of susceptibility to melanoma.[12, 13]

Malignant melanoma is one of the most rapidly increasing cancers, with an incidence that has more than doubled in the last 25 years.[12] Skin cancer is the most commonly occurring cancer in Canada, accounting for one third of all newly diagnosed cancers.[14] In all, over one million people in Canada and the USA are diagnosed with melanoma, basal cell, and squamous cell cancers each year.[14, 15]

Sunscreens were not originally developed to reduce the risk of skin cancer but to minimize erythema; they were designed to let through the "tanning" UVA radiation while blocking the "burning" UVB radiation. These initial products provided very little protection. Eventually, concern over the consequences of long-term UVR exposure and the increasingly apparent correlation with the development of cancer later on in life, triggered a public education campaign promoting sunscreen use. The impact of this campaign was later strengthened by growing appreciation of the effects of atmospheric ozone depletion on the amount of UVB radiation reaching the earth's surface. As the effects of UVB radiation, beyond sunburn, were more clearly elucidated and awareness of the contribution of UVA exposure to photoaging and skin cancer increased, the use of sunscreens amongst the general population exploded. Sunscreens have become ubiquitous, appearing in a surprising number of products ranging from shampoo to lipstick.

In light of the huge increase in usage, it is perhaps not unexpected that there has been an accompanying increase in the reported occurrences of photoallergy and phototoxicity; it is currently estimated that *ca.* 20% of the population are photosensitive to one or more sunscreen active ingredients. Increased usage has also spurred an increased interest in sunscreen photostability and photobiology. Intensive investigations of the stability of commercial UV filters have been undertaken in recent years (see Section 7.2 for specific examples) and several products were eventually voluntarily removed from commercial formulations due to their photoreactivity and the high incidence of reported photoallergy. A key example is the once-popular UVB sunscreen, *p*-aminobenzoic acid (PABA) and its

derivatives. Interestingly, PABA remains on the Food and Drug Administration (FDA) Federal Register of approved sunscreen components.[16]

There are two categories of sunscreen materials; organic and inorganic. Organic sunscreens, also called soluble or chemical sunscreens, have historically been the most widely used in commercial sunscreen formulations. These molecules are designed to absorb radiation in the UVB or UVA and dissipate this energy by re-emission at a less energetic wavelength or by undergoing some cyclic photochemical process such as *cis-trans* isomerization or keto-enol tautomerization. In 1999 there were 23 organic sunscreen ingredients approved by the US FDA for use in over-the-counter sunscreen products.[16] As of 2000, five of these organic sunscreens were found in the majority of the commercial products used in the world (Table 7.1). The organic sunscreens are almost always used in combination due to the regulatory concentration limits set by the FDA.[16] A "cocktail" of sunscreen ingredients can provide higher sun protection factors (SPF) and can help to overcome the relatively narrow absorption spectrum of the individual ingredients in order to provide more broadband protection. Considering that virtually every sunscreen product marketed today contains a cocktail of active ingredients, it is somewhat surprising that component-component interactions are not a required element of screening prior to commercialization.

UV Filter	Maximum Concentration	Comment
Octyl methoxycinnamate (OMC)	7.5%	Found in over 90% of sunscreen formulations worldwide
Oxybenzone	6%	Most popular UVA sunscreen, used in combination with OMC
Octyl salicylate	5%	Used with OMC/oxybenzone for its solubilizing properties
Octocrylene	10%	Found in many recreational sunscreen products
2-Phenyl-benzimidazole-5-sulfonic acid (PBSA)	4%	Used with OMC in many daily UV protectant products
p-Aminobenzoic acid (PABA)	15%	Rarely used

Table 7.1 Five most commonly used organic sunscreens in order of popularity as well as PABA. For structures see Table 7.2. (Compiled from reference 16).

The second class of active ingredients are the physical or insoluble sunscreens. These components are intended to protect the skin by scattering incident radiation in a particle-size dependent manner (i.e. visible wavelengths are not scattered so that the product appears invisible). Inorganic sunscreens have rapidly increased in popularity over the last decade due, in part, to their effectiveness at blocking UVA radiation and to their purported safety, in light of concerns over adverse effects related to the use of organic filters. The most popular inorganic sunscreens are titanium dioxide (TiO_2) and zinc oxide (ZnO); they are used as coated or uncoated microfine powders with particle diameters of less than 200 nm (usually 20-50 nm).[17] These inorganic sunscreens are increasingly used in combination with organic filters in high SPF, UVB/UVA sunscreen products.

Although TiO_2 and ZnO are marketed as inert light scatterers in the context of sunscreens, food whiteners, and cosmetics; both materials are well-known semiconductors and, especially in the case of TiO_2, have well-described photocatalytic properties.[18] As described in Chapter 3, the *ca.* 3.2 eV band gap in TiO_2 is easily

accessed by wavelengths shorter than 380 nm, allowing UVA light to effectively promote an electron into the conduction band generating an electron-hole pair. In an aqueous, aerobic environment the electron and hole can react to generate reactive oxygen species (ROS) as described in Scheme 3.7. By generating these reactive species, TiO_2 acts as a photocatalyst in the degradation of organic molecules, eventually leading to their complete mineralization; the photocatalytic activity of TiO_2 has long been employed in the environmental purification of wastewater.[19] More recently, it has been revealed that under UVA irradiation, TiO_2 catalyzes the degradation of biomolecules such as DNA, RNA, and amino acids,[20-23] destroys peroxidase enzymatic activity,[24] and induces non-specific cytotoxicity.[25] Importantly, TiO_2 extracted from commercial sunscreen formulations is equally effective in causing DNA damage[22] and enzyme de-activation.[26]

In light of the facts presented above it is somewhat surprising that TiO_2 is still considered a safe and effective sunscreen ingredient. In fact, it seems reasonable to assume that when incorporated in a sunscreen formulation and exposed to light, TiO_2 will generate ROS that may degrade other organic sunscreen components and possibly cause cellular damage.

With increasing reports of photoallergy and phototoxicity, and commercial formulations containing complex mixtures of components whose interaction remains largely uninvestigated we wondered whether there might be one simple solution to the problems associated with current commercial sunscreens. Might it be possible to enjoy the protective benefits intrinsic to UV-filtering chemicals yet eliminate the risks associated with direct skin contact? The answer may lie in a concept commonly employed by the pharmaceutical industry for the controlled release of drugs. Encapsulation of the sunscreen active ingredient in a suitable host may effectively prevent interaction with biological substrates, while at the same time preserving the desirable scattering/absorbing properties of the filter. We suggest that sunscreens could be encapsulated within the cavities of zeolite materials, giving a *supramolecular sunscreen* that would retain the beneficial

characteristics of the parent sunscreen but prevent interaction between the skin and the sunscreen itself.

There are numerous intrinsic advantages to this strategy. The aluminosilicate framework is transparent in the UVA and UVB, enabling the encapsulated sunscreen to absorb the incident radiation as usual. From a regulatory perspective, the encapsulation of an FDA approved chemical to improve its safety and efficacy represents an economic advantage with respect to the cost required to design and approve a completely new product. Due to the particulate nature of zeolites, the supramolecular sunscreens themselves can act as effective light scatterers, thereby eliminating the need for semi-conductor oxides in a topically applied product.

Encapsulation will eliminate the contact between sunscreens and skin components, but it may also eliminate the interaction between the various active ingredients in a sunscreen cocktail. This is extremely important because the interaction between ingredients and the result of their combined interactions with biological tissues and sunlight, are largely unexplored. In fact, although the literature is replete with studies of the *in vitro* photostability of individual sunscreen components there is very little general agreement. The results depend heavily on the media in which the experiment was conducted and the radiation source. In addition, there are relatively few examples where the photostability of the sunscreen formulation as a whole was investigated. In one study of 16 commercial sunscreen products, the overall absorbance of each product was observed to decrease significantly following exposure to solar simulated radiation (SSR), despite the fact that each of the individual active ingredients were considered to be photostable.[27] The authors note that, due to component-component interactions, the behaviour of a complete product upon exposure to UVR cannot be predicted based on the behaviour of the individual active ingredients.[27]

In this work we have evaluated the viability of supramolecular sunscreens as potential replacements for the organic and inorganic filters currently employed in

commercial formulations. We have prepared a first generation of supramolecular sunscreens combining common organic filters and the well-characterized faujasite zeolite NaY. The photophysical properties of these materials were investigated and compared with the free sunscreens in solution. We also probed photostabilty, sunscreen-sunscreen interactions, and undertook preliminary studies aimed at determining the toxicity and phototoxicity of these new materials. This project was initiated as a collaboration between the University of Ottawa and Health Canada (Radiation Protection Bureau). Photobiological studies were carried out at Health Canada with the technical assistance of M. Cybulski. E. Heafey, a talented undergraduate student, contributed to the DNA and cell studies as part of her summer research project; her hard work is gratefully acknowledged.

7.2 Modified Sunscreens

In order to explore the concept of supramolecular sunscreens, five FDA approved commercial sunscreen active ingredients were studied. We chose to investigate zeolite/sunscreen combinations (sunscreen@Y) comprising the four most commonly used commercial sunscreens; oxybenzone (OXB), octyl salicylate (OSA), octyl methoxycinnamate (OMC), and octocrylene (OCT). Together, these compounds (structures given in Table 7.2) are found in *ca.* 90% of commercial sunscreen formulations worldwide. We also chose to prepare and study a supramolecular sunscreen containing *p*-aminobenzoic acid (PABA@Y). PABA has long been considered an "undesirable" sunscreen ingredient, despite its desirable optical properties, due to the many incidences of reported photoallergy. The claim "PABA-free" is now a common selling point for many sunscreen products. We reasoned that if zeolite encapsulation could render even PABA non-offensive, this would be convincing support for the supramolecular sunscreen concept.

Structure	Name	ε_{hexane} M^{-1} cm^{-1}	$\varepsilon_{ethanol/H2O}$ M^{-1} cm^{-1}
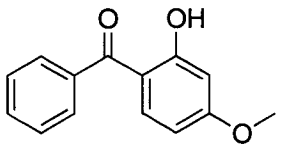 **OXB**	**Oxybenzone** 4-Methoxy-2-hydroxybenzophenone	8800 λ_{max}=328 nm	9300 λ_{max}=321 nm
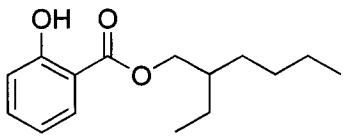 **OSA**	**Octyl salicylate** 2-Hydroxy-benzoic acid 2-ethyl-hexyl ester	5400 λ_{max}=334 nm	5600 λ_{max}=336 nm
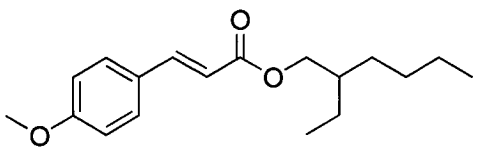 **OMC**	**Octyl methoxycinnamate** 3-(4-Methoxy-phenyl)-acrylic acid 2-ethyl-hexyl ester	22900[a] λ_{max}=289 nm	24200[a] λ_{max}=312 nm
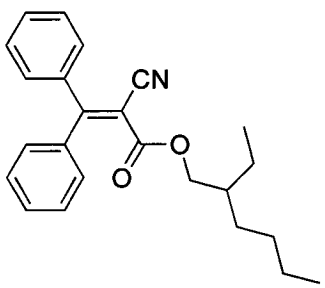 **OCT**	**Octocrylene** 2-Cyano-3,3-diphenyl-acrylic acid 2-ethyl-hexyl ester	13800 λ_{max}=297 nm	12300 λ_{max}=305 nm
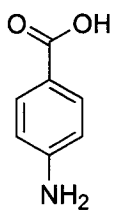 **PABA**	***p*-Amino benzoic acid**	not soluble	13600 λ_{max}=266 nm

Table 7.2 Structures, names, abbreviations, and spectral data for sunscreens studied.[28] [a]These values correspond to the *trans* isomer.

7.2.1 Oxybenzone

Oxybenzone was one of the first compounds incorporated in sunscreen formulations to offer enhanced UVA protection; its absorption spectrum (Figure 7.3, O) has a tail extending past 350 nm. Unfortunately, this material has certain disadvantages including its yellow colour and poor solubility. In addition, the molar absorption coefficient is relatively low and the absorption spectrum is solvent dependent; in non-polar environments (see spectrum in hexane in Figure 7.3) the spectrum is highly structured resulting in "holes" in the effective UVR protection range. Low absorption coefficients make it necessary to use the product in relatively high concentration, this often leads to crystallization within the formulation since OXB is a solid at room temperature.

In addition to these unfavourable physical properties oxybenzone has been increasingly implicated in cases of photoallergy.[29-32] A brief survey of the epidemiological dermatology literature, reveals that OXB is second only to PABA in the number of reported cases of photoallergy. This is rather surprising in view of the numerous *in vitro* studies of OXB photostability reporting it to be one of the most photostable sunscreen ingredients.[33-37] The case of oxybenzone is an excellent example of how *in vitro* laboratory testing cannot always predict the unanticipated, and unfavourable reactions which may occur in the presence of a complex matrix like biological tissue. Schallreuter *et al.* have observed that in the presence of OXB, UVA irradiation induces the deactivation of thioredoxin reductase, an important antioxidant enzyme in the skin. The studies were conducted by enzymatic assay of skin biopsies and *in vivo* Raman spectroscopy of the skin.[38, 39] The authors suggest that irradiation of OXB results in the generation of small amounts of the related semi-quinone species, which then conjugatively deactivates thioredoxin reductase via Michael addition to the thiolate active site of the enzyme.[38, 39] Although this mechanism has not been confirmed, the incidences of photoallergy and enzyme deactivation clearly indicate that encapsulation may offer significant improvements with respect to the use of the naked material as a sunscreen.

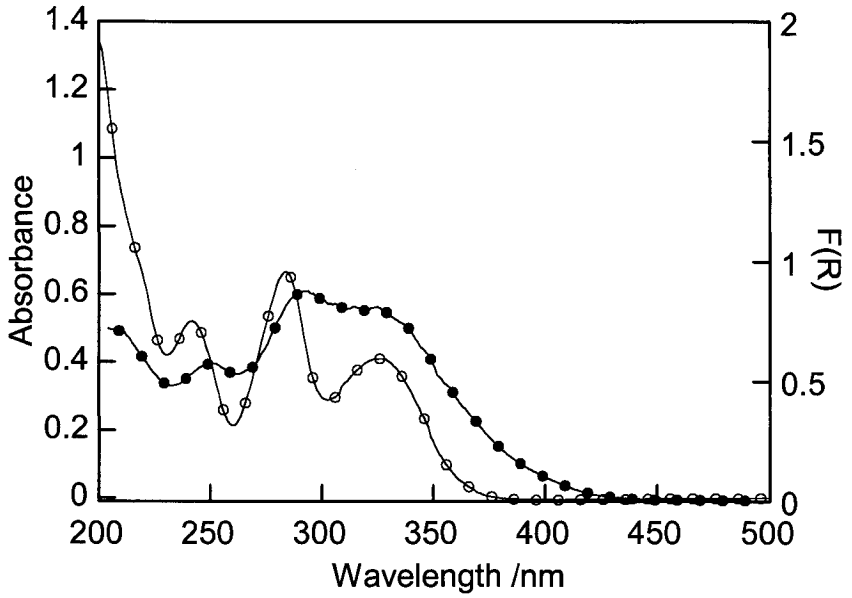

Figure 7.3 Absorption spectrum of OXB in hexane (○, 4.4 x 10^{-5} M) and DRS of OXB@Y (●, <S> ~ 0.1).

Encapsulation of OXB in zeolite NaY was performed as usual by contacting a solution of OXB in a non-polar solvent with a sample of activated NaY. The loadings were determined by spectroscopic analysis of the filtrate. The DRS of a sample of OXB@Y with <S> ~ 0.1 is compared with the spectrum of OXB in hexane in Figure 7.3. It is immediately obvious from these spectra that encapsulation produces two desirable effects. In the case of OXB@Y, the structured absorption observed for OXB in hexane is lost, effectively removing any holes in the spectral region of interest. The absorption spectrum also shows considerable broadening, implying that this material would offer significantly more protection in the UVA. This broadening and loss of structure is typical for benzophenone chromophores in polar solvents; the broadening observed for OXB@Y is even larger than observed for OXB in water.

7.2.2 Octyl Salicylate

Octyl salicylate, sometimes called octisalate, is primarily used as a UVB sunscreen. Salicylates are relatively weak UVB absorbers and are normally used in

combination with other UV filters. Salicylates are generally considered to have a good safety record although they are far less ubiquitous than OXB, reducing the amount of epidemiological photoallergy data available. *In vitro* studies have indicated that OSA is largely photostable, however, the results vary depending on the solvent and the light source.[34, 36, 37] In one example OSA was reported to undergo 10% photodegradation in alcohol but none in mineral oil.[37]

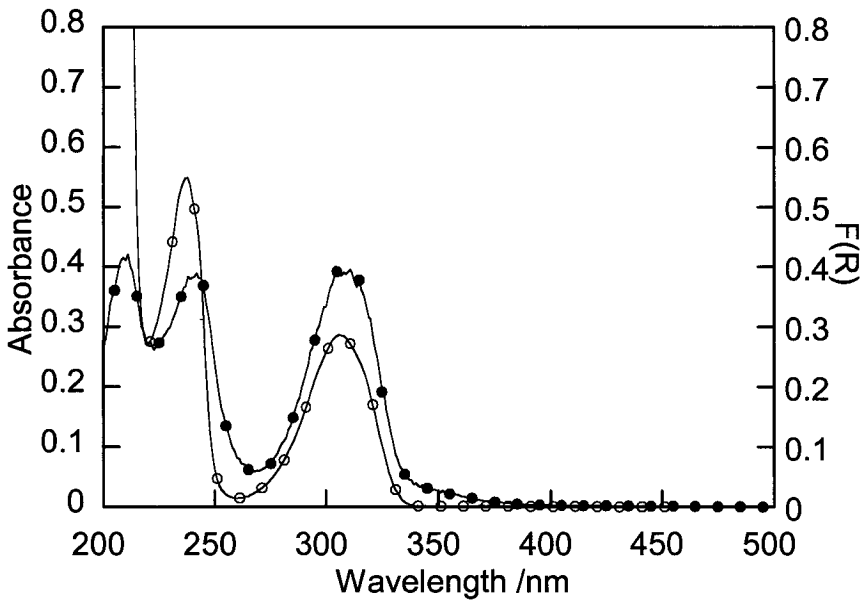

Figure 7.4 Absorption spectrum of OSA in hexane (O, 6.0 x 10^{-6} M) and DRS of OS@Y (●, <S> ~ 0.1).

OSA@Y was prepared as described above by diffusion from a solution of OSA in a non-polar solvent. The DRS of the prepared solid matches extremely well with the absorption spectrum of OSA recorded in hexane (Figure 7.4). This is consistent with previous results indicating that the absorption maximum of OSA does not undergo a solvent dependent shift (Table 7.2).[28]

7.2.3 Octyl Methoxycinnamate

OMC is the most widely used UVB sunscreen, found in over 90% of commercial formulations. As with the previous two examples, OMC is generally considered by sunscreen manufacturers to be photostable despite conflicting

reports in the literature. HPLC analysis of the photostability of OMC in polar solvents showed the *cis*-isomer as the sole product following irradiation.[34, 40] However at higher concentrations, as might be found in an actual sunscreen formulation, OMC has been observed to undergo an intermolecular 2+2 cycloaddition across the double bond to give truxillic acid type products.[41]

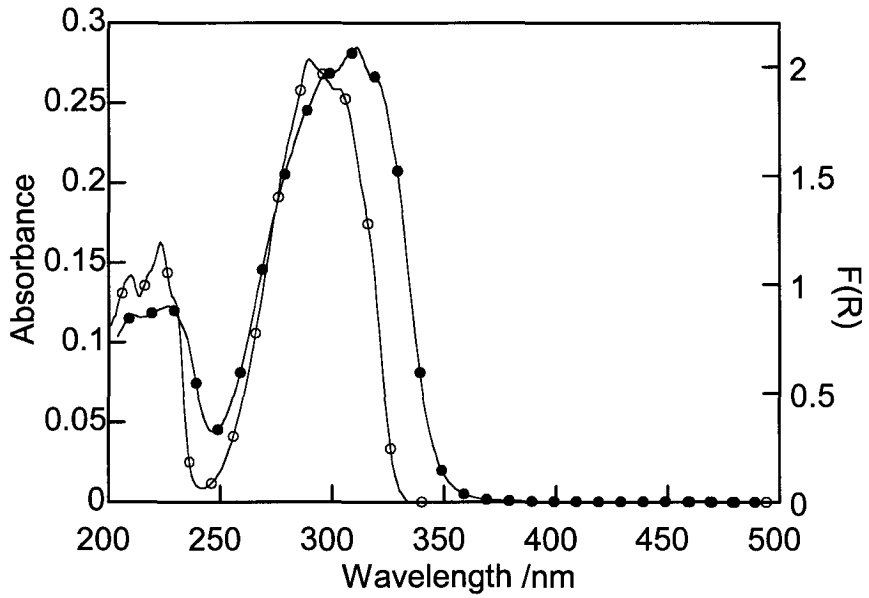

Figure 7.5 Absorption spectrum of OMC in hexane (○, 1.0 x 10^{-5} M) and DRS of OMC@Y (●, <S> ~ 0.1).

OMC has also been observed to photosensitize the formation of singlet oxygen. Under the specific conditions used in one study the rate of $^1O_2$ formation was found to be 3.8 x 10^{11} M s^{-1}; approximately 10% of the value determined for PABA under identical conditions.[36] Singlet molecular oxygen has been implicated in oxidative damage to biological systems and its formation is frequently the first step in the photosensitivity caused by some drugs and porphyrin dyes.[36] There have been reports of photosensitization and photoallergic reactions to OMC and if singlet oxygen is generated by illumination of OMC at the skin surface, it likely plays a role in these adverse reactions.[32, 42]

Encapsulation of OMC was achieved by diffusion into the zeolite from a solution of OMC in a non-polar solvent. In the case of OMC, a shift in the position of the absorption maximum of *ca.* 20 nm has been observed on going from hexane to aqueous alcohol solvents. Therefore, the observed shift in the maximum of the DR spectrum as compared to the maximum in hexane was expected (Figure 7.5). This bathochromic shift was also accompanied by significant broadening of the absorption band. As was the case with OXB, these features improve the characteristics of OMC as a sunscreen in terms of broadband protection.

7.2.4 Octocrylene

Octocrylene is primarily used as a UVB filter and is often included in commercial formulations specifically for its emollient properties. As is typical in literature relating to sunscreen photostability, there are conflicting reports regarding the properties of OCT in solution. OCT has been observed to undergo 3% degradation after receiving an equivalent of 5 minimum erythemal doses (MED) in mineral oil, and in water was observed to undergo photolysis with a half-life of *ca.* 96 hours to form an unidentified product.[34, 37] Under the conditions reported for OMC, OCT has also been shown to sensitize the formation of singlet molecular oxygen at a rate of 2.3×10^{11} M s^{-1}.[36]

The preparation of OCT@Y was achieved as described above by contacting a sample of NaY with a solution of OCT in a non-polar solvent. Not unlike OMC, the OCT absorption maximum is observed to shift bathochromically by *ca.* 10 nm on going from hexane to aqueous alcohol solvents. The measured DRS of OCT@Y is given in Figure 7.6 (O) and clearly shows both a blue-shift in the spectral maximum and broadening of the band, analogous to OMC. As mentioned above, a broadened spectra and longer wavelength absorption are both desirable properties with respect to sunscreens.

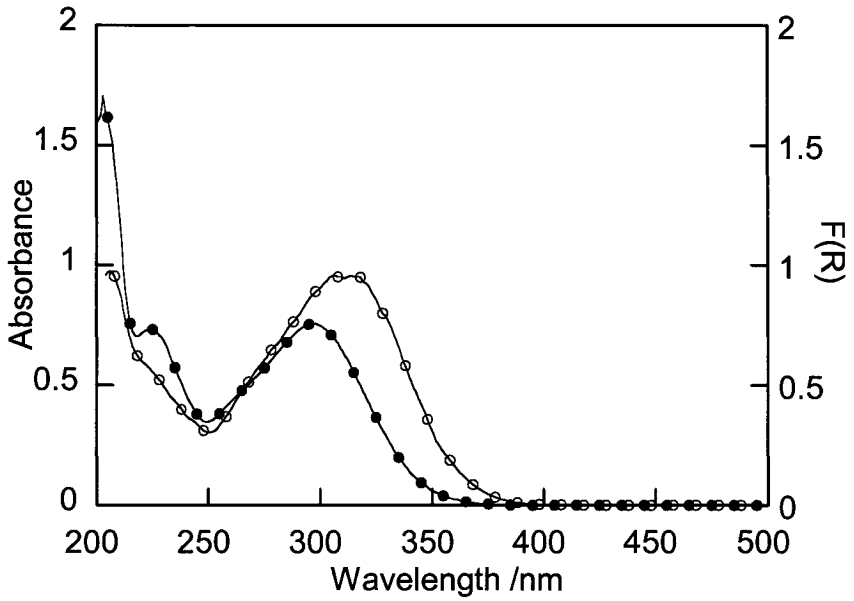

Figure 7.6 Absorption spectrum of OCT in hexane (●, 6.7 x 10^{-6} M) and DRS of OCT@Y (○, <S> ~ 0.1).

7.2.5 *p*-Aminobenzoic Acid

PABA was one of the first commercially used UVB sunscreens. Historically, PABA was one of the most widely used sunscreen ingredients but by the mid-1980's had almost completely disappeared from the market due to the extremely high incidence of adverse dermatological effects. The photochemistry of PABA has since been extensively studied and it is known to undergo efficient photolysis in aqueous and non-polar media to generate a variety of products including 4-amino-3-hydroxybenzoic acid, 4-aminophenol, and 4-[(4'-hydroxyphenyl)amino]benzoic acid.[35, 43, 44] There is also evidence for the formation of several reactive intermediates during PABA photolysis including free radicals, solvated electrons, and singlet oxygen.[36, 43, 45] The sensitized formation of singlet oxygen by PABA is quite efficient and it is believed that $^1O_2$ and $O_2^{-\bullet}$ (superoxide anion), formed by reaction of solvated electrons with oxygen, are responsible for the observed photosensitivity. For example, the oxidative alteration of proteins by $^1O_2$ may result in the formation of antigens thereby eliciting an allergic response.

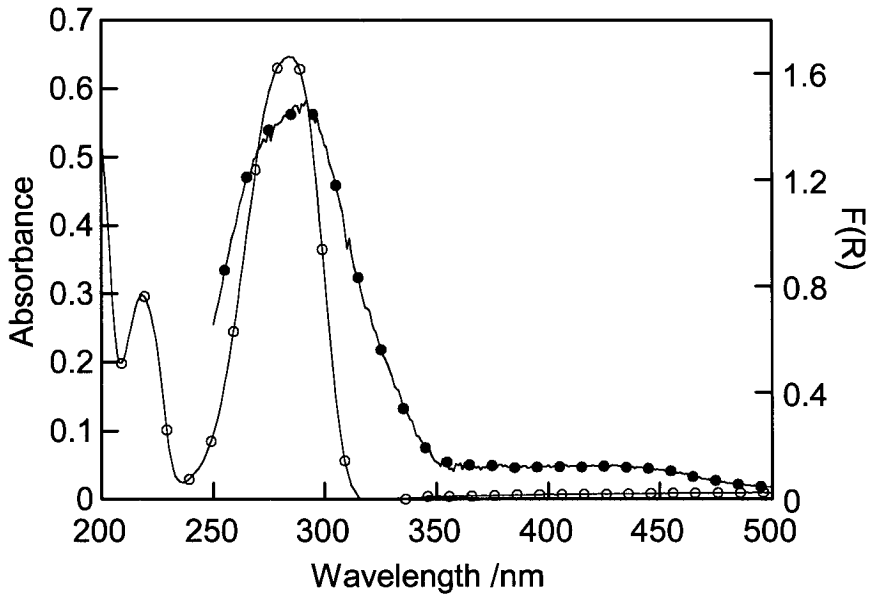

Figure 7.7 Absorption spectrum of PABA in ACN (○, 2.9 x 10^{-6} M) and DRS of PABA@Y (●, <S> ~ 0.8).

PABA@Y was also prepared as described above by contacting a sample of NaY with an ACN solution of PABA. The DRS shows a slight shift in the spectral maximum and a significant broadening of the band. The positive reflectance signal seen extending from 350 nm into the visible was attributed to decomposition products generated during the inclusion procedure.

7.3 Photophysical Studies

7.3.1 Oxybenzone

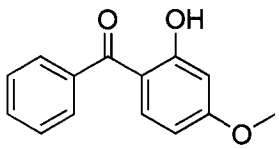

OXB is an example of a substituted *o*-hydroxybenzophenone, many of which have found applications as polymer photostabilizers. In solution at room temperature, *o*-hydroxybenzophenone does not undergo benzophenone-like photoreduction and does not phosphoresce.[46] Room temperature laser flash photolysis showed no significant transient absorptions but, at low temperatures and in hydroxylic media, it is possible to observe both the phosphorescence and the triplet-triplet absorption spectrum (λ_{max} ~ 500 nm).[47] The triplet lifetime at 175 K was reported to be 24 ns. The short lifetime and inefficient triplet formation in these systems has been attributed to an extremely fast and reversible excited-state intramolecular proton transfer (ESIPT). Many organic molecules have weakly acidic or basic functionalities, that experience enhanced acidity and basicity following electronic excitation. This simultaneous change in proton donating and accepting ability is often sufficiently significant to promote the transfer of a proton from the 'acidic' group to the 'basic' group via ESIPT.[48, 49] Most examples of ESIPT involve an -OH or -NH group as the acidic moiety and a heteroatomic group as the base, for example an aromatic heterocyclic nitrogen or a carbonyl oxygen atom, as is the case for OXB (Scheme 7.1). This type of proton transfer is typically rapid and reversible and this highly efficient, energy-wasting pathway is responsible for OXB's sunscreen properties; enabling it to absorb radiation and dissipate the energy in a cyclic process.

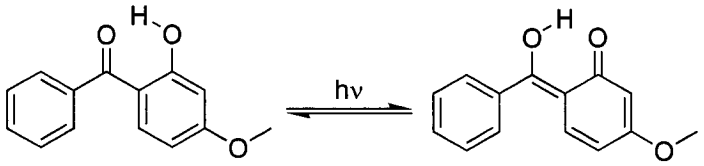

Scheme 7.1 Excited-state intramolecular proton transfer in oxybenzone.

The transient absorption spectrum, recorded following laser excitation of OXB in ACN, is shown in Figure 7.8. The observed spectrum shows an extremely weak band ($\Delta OD < .002$) at *ca.* 400 nm that did not decay significantly over a period of 20 μs. For comparison, under similar conditions the transient absorption spectrum of benzophenone has a signal at *ca.* 530 nm that is *ca.* 100 times more intense. As shown in the inset of Figure 7.8, the transient was completely unaffected by the presence of oxygen, suggesting that the signal is neither due to a triplet nor a reactive carbon-centered radical species. The lifetime of the 400 nm transient was also insensitive to 1,3-CHD (a good triplet energy acceptor), further confirming its non-triplet nature. Based on the lack of oxygen reactivity and the position of the absorption band, this transient was assigned to the phenoxyl radical derived from oxybenzone.

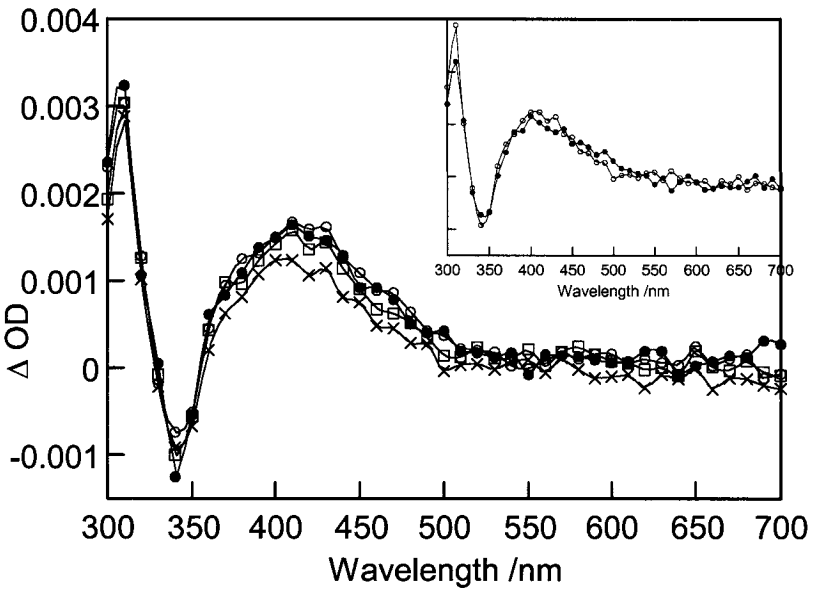

Figure 7.8 Transient absorption spectrum recorded 0.32 μs (●), 1.36 μs (○), 6.88 μs (□), and 14.2 μs (×) after 308 nm laser excitation of a deaerated solution of OXB in ACN (3.5×10^{-5} M). Inset: Comparison of spectra recorded for the same solution under nitrogen (○) and oxygen (●) after 14.2 μs.

Phenoxyl radicals are quite un-reactive and are, therefore, difficult to definitively assign based on their scavenging behaviour. Nevertheless, experiments using hydrogen-donor moieties were attempted. We attempted to observe the interaction between the phenoxyl radical and the hydroxylamine of TEMPO (prepared by reduction of the stable free radical). Unfortunately, and not unexpectedly, the hydroxylamine was unstable under the conditions of the experiment as evidenced by the rapid reappearance of the red-orange colour due to the free radical species. The polymer stabilizer HP-136, from CIBA, was also tested as a possible quencher of phenoxyl radicals. HP-136 is a chain breaking antioxidant that generates an extremely stable free radical upon undergoing hydrogen abstraction. Although the reaction with phenoxyl radicals is thermodynamically feasible it is too slow to be observed on the laser flash photolysis time scale.

To confirm that the small amounts of transient generated in the LFP of OXB were related to the benzophenone hydroxy-substituent, the transient absorption

spectrum of 4-methoxybenzophenone was recorded in deaerated ACN. As can be seen in Figure 7.9, the profile is very different from that obtained for OXB. This spectrum was assigned to the triplet-triplet absorption spectrum of 4-methoxybenzophenone and was efficiently quenched by oxygen across the entire wavelength range (see Figure 7.9 inset).[50]

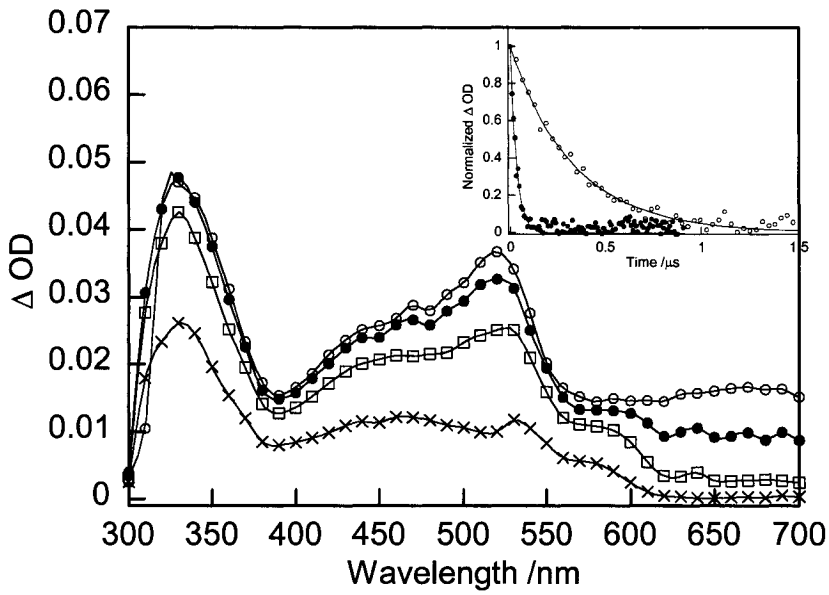

Figure 7.9 Transient absorption spectrum recorded 48 ns (●), 0.24 μs (○), 0.66 μs (□), and 2.58 μs (×) after 308 nm laser excitation of a deaerated solution of 4-methoxybenzophenone in ACN (3.5×10^{-5} M). Inset: Transient decay traces recorded at 500 nm for the same solution under nitrogen (○) and oxygen (●).

The photo-ejection of electrons is not an uncommon process for molecules undergoing ESIPT. The process typically proceeds with low quantum yields (< 10%) and is not known to give rise to photoproducts.[51] In light of this information we concluded that the small concentration of phenoxyl radicals generated under the conditions of LFP were likely a result of electron photo-ejection from OXB, followed by loss of a proton. Photo-ejection of an electron is often, but not always, a two-photon process. In this case, the amount of phenoxyl radical generated would depend quadratically on the photon density. If the process is monophotonic in nature, the phenoxyl radical signal would be seen to increase linearly with laser

power. In the case of OXB, the signal at 400 nm was observed to increase in a linear fashion with increasing laser power, suggesting a monophotonic process. However, based on the many reports of OXB photostability *in vitro*, this is likely a very minor reactive pathway.

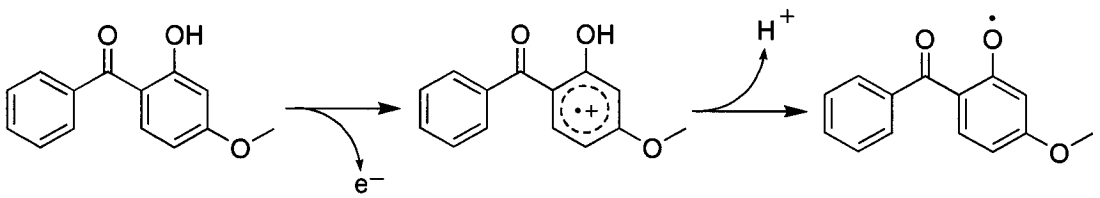

Scheme 7.2 Possible mechanism for generation of phenoxyl radicals in OXB.

In order to confirm that the same photophysical pathways are operative for OXB when encapsulated in zeolite Y, the transient DRS of OXB@Y was recorded. The spectrum (shown in Figure 7.10) resembles the transient absorption spectrum generated following pulsed excitation of OXB in ACN given in Figure 7.8. The transient DRS had a broad band at 400 nm that was assigned to the phenoxyl radical from oxybenzone. The broad absorption band from 550-700 nm was assigned to Na_4^{3+}. This species is formed when cationic sodium clusters, which are present within the cage as charge-balancing counterions, trap an electron.[52] The observation of Na_4^{3+} is further evidence for the formation of the phenoxyl radical via photo-ejection of an electron. The spectrum recorded under air is nearly identical, except for the reduced intensity at longer wavelengths. Since no other species were detected it was concluded that, upon excitation, OXB encapsulated in NaY undergoes the same deactivation pathways as the molecule in solution.

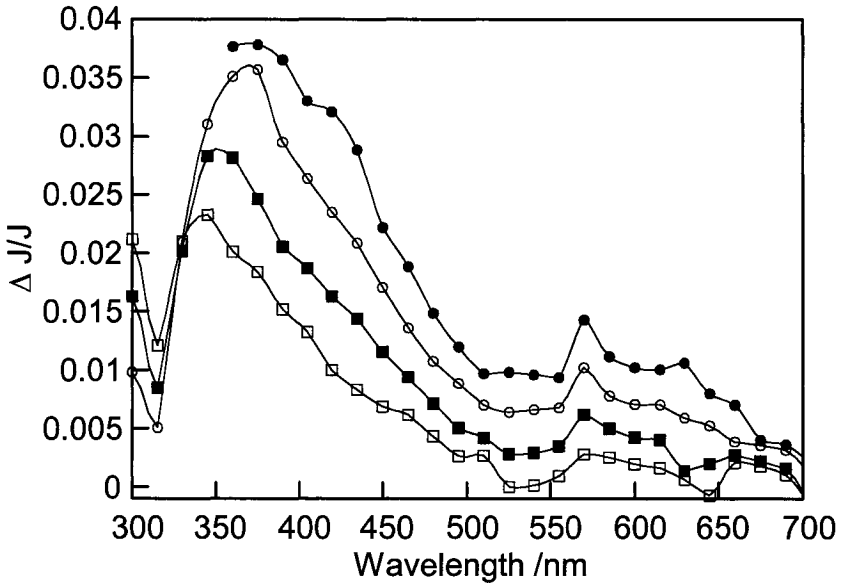

Figure 7.10 Transient DRS recorded 0.64 μs (●), 2.56 μs (○), 8.64 μs (■), and 26.7 μs (□) after 308 nm excitation of OXB@Y under vacuum (<S> ~ 0.1). Data below 350 nm in the first time window, corresponding to bleaching of the ground state, have been omitted for clarity.

7.3.2 Octyl Salicylate

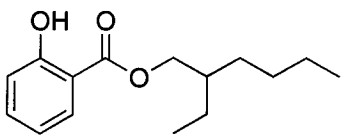

Salicylates are also well-known to undergo efficient and reversible ESIPT reactions as a major deactivation pathway, contributing to their popularity as UV-stabilizers.[49] Laser flash photolysis of OSA in deaerated ACN revealed a transient spectrum comprised of more than one component. The band at *ca.* 440 nm was efficiently quenched by oxygen and was assigned to the excited triplet state of OSA. Quenching the triplet revealed a weaker band with a maximum at *ca.* 400 nm that was insensitive to the presence of the oxygen. In analogy with OXB, this band was assigned to small amounts of the related phenoxyl radical, likely generated by a minor electron photo-ejection pathway.

The 2-ethylhexylbenzoate ester (an OSA analogue with no hydroxy substituent) was prepared by esterification and the transient absorption spectrum was recorded in deaerated ACN. The spectrum of the ester has one main feature at 260 nm. This band was completely quenched by oxygen and matches exactly with the short wavelength band in the transient spectrum of OSA (Figure 7.12).

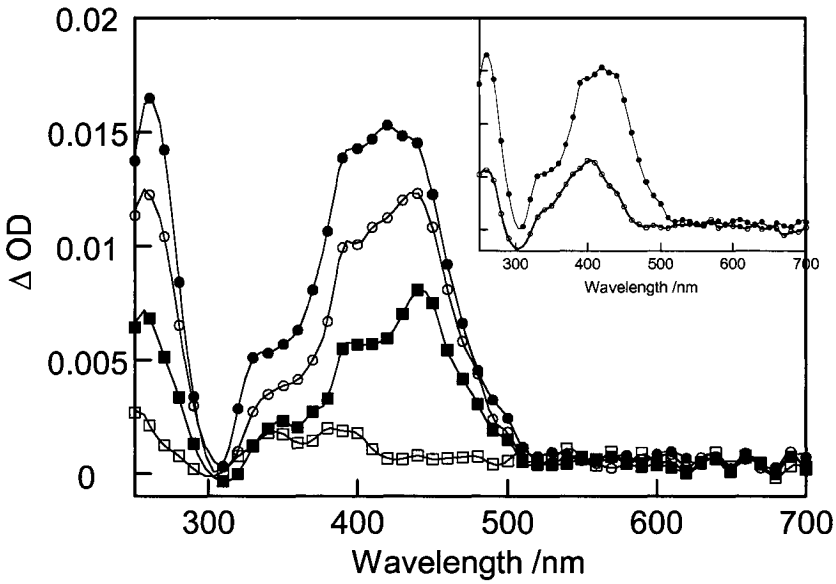

Figure 7.11 Transient absorption spectrum recorded 0.40 μs (●), 1.12 μs (○), 2.40 μs (■), and 13.2 μs (□) after 308 nm laser excitation of a deaerated solution of OSA in ACN (7.5×10^{-5} M). Inset: Comparison of spectra recorded for the same solution under nitrogen (●) and oxygen (○) after 0.40 μs.

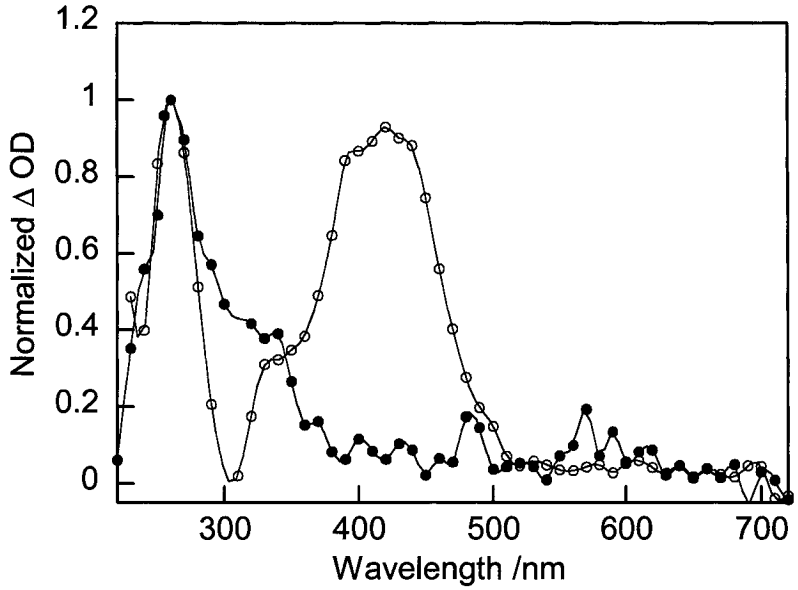

Figure 7.12 Transient absorption spectrum recorded 0.40 μs after 308 and 266 nm laser excitation of deaerated ACN solutions of OSA (○, 7.5 x 10^{-5} M) and 2-ethylhexylbenzoate (●, 4.4 x 10^{-5} M).

The transient DRS of OSA included in zeolite NaY was fairly noisy, but shows the same behaviour as observed in solution. Under vacuum the spectrum had a very broad band extending from *ca.* 350 nm to 550 nm. Under air the triplet excited state was largely quenched and the residual absorption had a maximum at *ca.* 400 nm, suggesting that it may be the phenoxyl radical. The signals at long wavelengths are again attributed to the Na_4^{3+} species. For the spectra of zeolite samples recorded under air, no special precautions were taken to prevent the sample from absorbing water; sunscreens are unlikely to be used under anhydrous conditions in any case. Zeolite NaY is a relatively hydrophilic material and the air-exposed samples most certainly contain co-adsorbed water. It has been noted that water present in the zeolite cavity either quenches or impedes the formation of Na_4^{3+}, thereby reducing the intensity in the long wavelength region of the spectrum. Overall, it was concluded that photophysical deactivation of OSA occurs similarly in solution and in zeolite supercages.

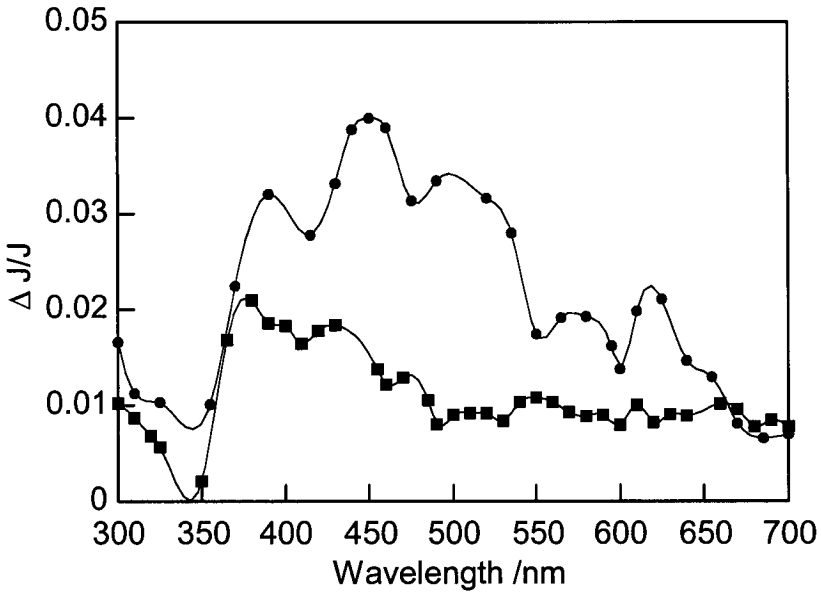

Figure 7.13 Transient DRS recorded 0.8 μs after 308 nm laser excitation of OSA@Y under vacuum (●) and under air (■).

7.3.3 Octyl Methoxycinnamate

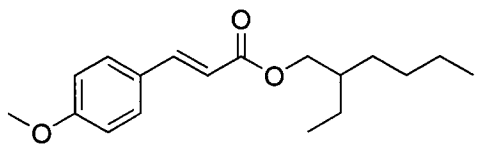

Cinnamates dissipate excitation energy by undergoing a *cis-trans* isomerization about the propenyl double bond. In cinnamic acids this process is highly dependent on solvent polarity since intermolecular hydrogen-bonding between carboxylic acid groups will disrupt the photoisomerization.[53] The photoinduced isomerization of cinnamic esters is fairly rapid and reversible with highly solvent and wavelength dependent quantum yields ranging from 0.5 to 1.[54] In relatively non-polar solvents, a photostationary equilibrium of *ca.* 50:50 *cis:trans* is attained within approximately two minutes. Unfortunately, from a sunscreen perspective, the molar absorption coefficient of the *cis* isomer is less than that for the *trans* and the absorbance of the photostationary mixture is only 60-70% of the initial *trans* isomer.[54] The laser flash photolysis of OMC in ethanol under 265 nm

excitation has been reported,[55] we recorded the transient absorption spectrum of OMC in ACN following excitation at 308 nm.

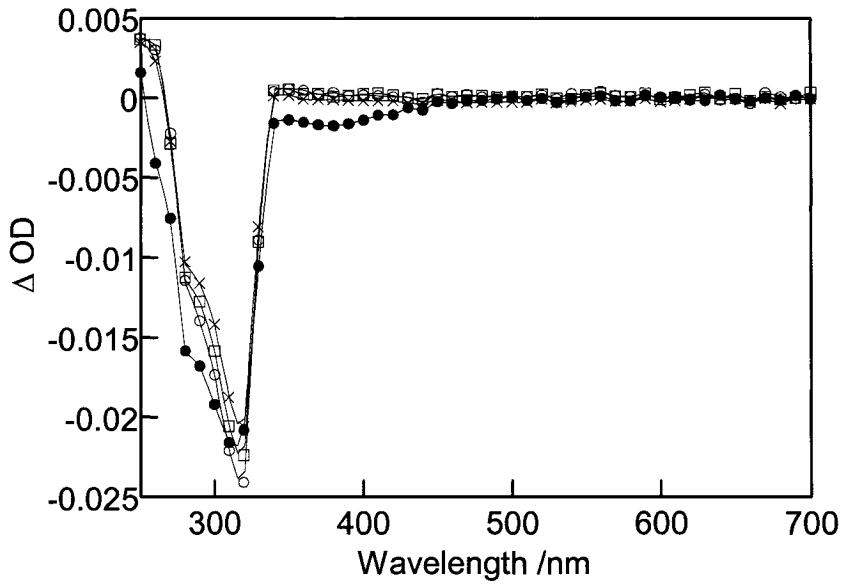

Figure 7.14 Transient absorption spectrum recorded 0.64 μs (●), 3.84 μs (○), 13.6 μs (□), and 28.6 μs (×) after 308 nm excitation of OMC in deaerated ACN (4.6×10^{-5} M).

The experimental spectrum, given in Figure 7.14, shows the un-recovered bleaching of the *trans*-OMC ground state at *ca.* 300 nm. The inverted peak is a result of the reduced absorbance of the *cis* isomer with respect to the starting *trans* isomer, and is a reasonable mirror image of the absorption spectrum of OMC in ACN.

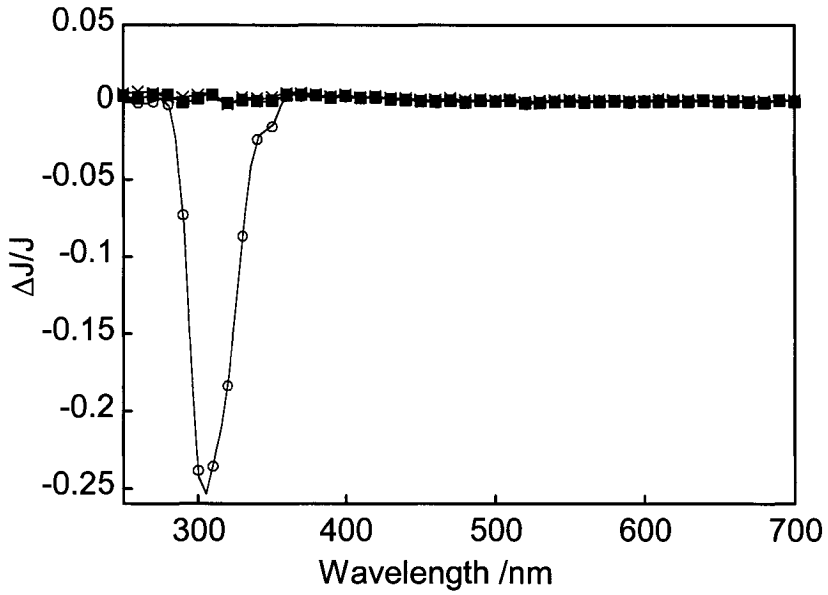

Figure 7.15 Transient DRS recorded 0.60 μs (○), 2.44 μs (■), and 6.40 μs (×) after 308 nm excitation of OMC@Y under air (<S> ~ 0.1).

The transient DRS recorded following laser excitation of OMC@Y shows the same negative reflectance signal at *ca.* 300 nm as seen in solution, with one major difference. In solution, the bleaching signal is un-recovered because the "product" of laser irradiation has the same absorption spectrum as the starting material, but a smaller molar absorption coefficient. In the zeolite, the negative signal returns to the pre-pulse level within *ca.* 2 μs. Reversible bleaching of the *trans*-OMC ground state has been interpreted as due to restricted conformational mobility within the zeolite supercage. Upon excitation, OMC undergoes the expected isomerization but, due to the spatial restrictions within the zeolite cavity, the resulting ground-state pseudo-*cis* isomer is highly strained. The lack of conformational mobility prevents the molecule from becoming fully relaxed and delocalized, resulting in a reduced absorbance and therefore a negative signal. The baseline signal is regenerated when the strained *cis* isomer undergoes thermal reversion to the *trans* isomer. This mechanism is analagous to the behaviour of *cis*-cycloalkenes where, due to strain, the smaller rings do not undergo photoisomerization, the *trans*

isomers of six- and seven-membered rings have been detected but are not isolable, and the eight- and nine-membered rings form *trans*-cycloalkenes as stable species. Regeneration of the *trans* isomer may be a desirable characteristic with respect to sunscreen applications since irradiation would not result in a product with decreased absorption.

7.3.4 Octocrylene

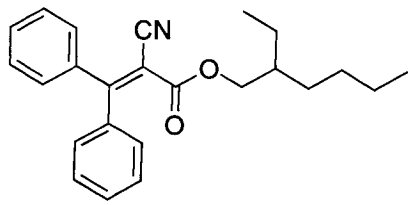

In analogy to the closely related OMC, octocrylene dissipates excitation energy via rotation about the propenyl double bond. In the case of the symmetrically substituted OCT molecule, rotation about the propenyl bond is an energy-wasting pathway only and does not result in the observation of a new OCT isomer. As expected, the laser flash photolysis of OCT in solution showed no absorbing transients. However the transient DRS shown below in Figure 7.16 clearly indicates that at short times the ground state of OCT is bleached, resulting in a negative signal that returns to the pre-excitation value in *ca.* 2 μs. In this case the negative signal may also be attributed to the formation of an incompletely delocalized ground state species, that thermally reverts to the fully delocalized starting species, as in OMC. However, since the final product of rotation about the propenyl bond regenerates the starting material, it would be impossible to determine the exact process without labeling one of the phenyl rings.

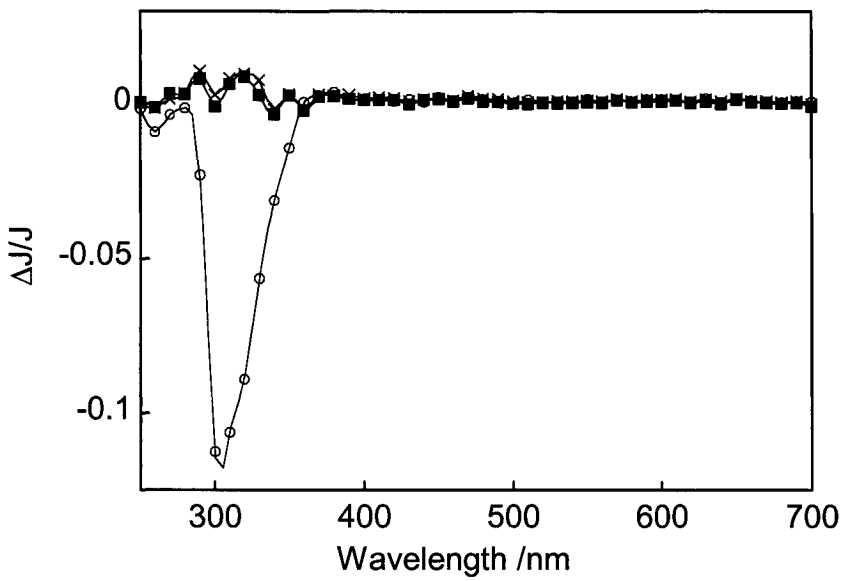

Figure 7.16 Transient DRS recorded 0.80 μs (○), 2.12 μs (■), and 5.92 μs (×) after 308 nm excitation of OCT@Y under air (<S> ~ 0.1).

7.3.5 *p*-Aminobenzoic Acid

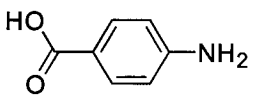

The products of PABA photolysis, both stable and transient, have been well characterized. The excited triplet state of PABA is able to sensitize the formation of singlet molecular oxygen (E_T = 75 kJ mol^{-1})[45] and this ROS has been implicated in the large number of photoallergic responses elicited by PABA. The transient absorption spectrum of PABA in solution (Figure 7.17) is characterized by an intense band at *ca.* 400 nm, due to the absorption of the PABA triplet excited-state. The triplet had a lifetime of 170 ns in deaerated ACN and was completely quenched in the presence of oxygen. The spectrum also has a weak, positive absorption in the 600-700 nm region that is absent in the presence of nitrous oxide (N_2O), a well-known scavenger of free electrons. Since ACN also scavenges solvated electrons, the long-wavelength absorption may be due to a rapidly formed, electron-derived species or some other intermediate.

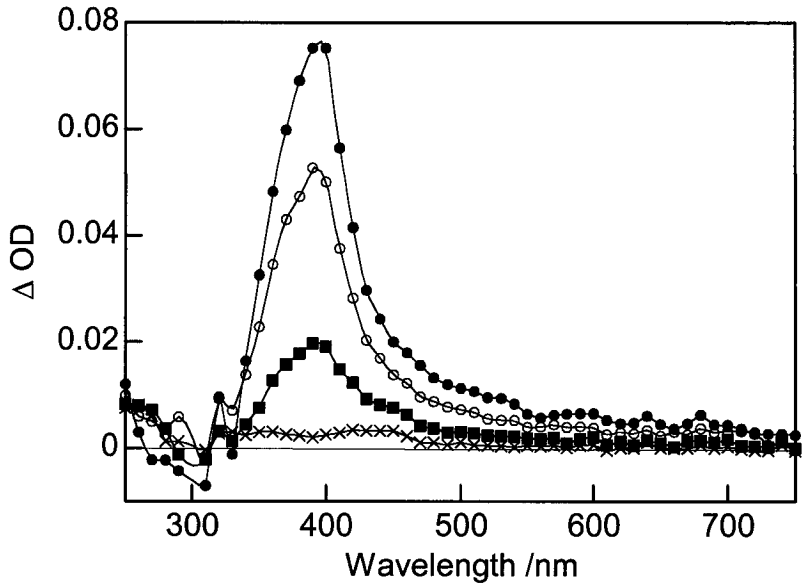

Figure 7.17 Transient absorption spectrum recorded 16 ns (●), 0.11 μs (○), 0.30 μs (■), and 1.22 μs (×) after 308 nm excitation of PABA in deaerated ACN (1.8×10^{-4} M).

Diffuse reflectance LFP reveals the same behaviour for PABA encapsulated in zeolite Y. The transient DRS of PABA@Y, shown in Figure 7.18, is characterized by a triplet-triplet absorption band at *ca.* 400 nm and a positive signal between 600 and 700 nm corresponding to cationic sodium clusters (Na_4^{3+}) generated as a result of electron-trapping. These observations suggest that, in the presence of oxygen, encapsulated PABA may still sensitize the formation of singlet oxygen.

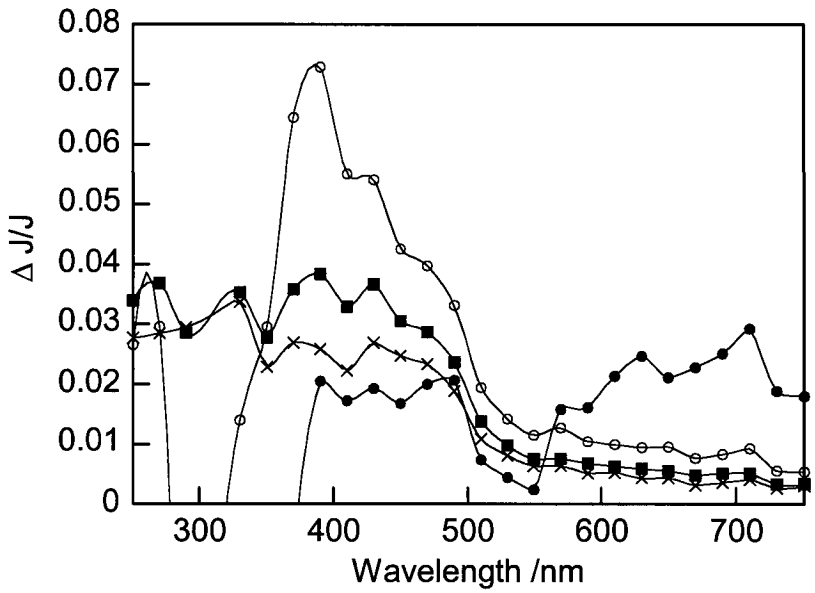

Figure 7.18 Transient DRS recorded 0.32 μs (●), 0.68 μs (○), 2.80 μs (■), and 6.72 μs (×) after 308 nm excitation of PABA@Y under air (<S> ~ 0.5). Data below 350 nm in the first time window, corresponding to bleaching of the ground state, have been omitted for clarity.

7.4 Photostability Studies

7.4.1 Photostability of Sunscreens in Solution

As mentioned in the Section 7.1, approved sunscreen ingredients are often used in combination in commercial formulations, in order to broaden the protective spectral range and improve the SPF. Filters must be used in combination in order to provide high SPF's while staying at or below FDA regulatory concentration limits; at the currently allowed concentrations no individual sunscreen component would be able to provide an SPF greater than 15. Surprisingly, the interactions between ingredients and the results of their combined interactions with biological tissues and sunlight are largely unstudied. This is especially important with respect to formulations combining both organic and inorganic components. TiO_2 is a commonly employed inorganic ingredient, despite its demonstrated ability to generate ROS capable of degrading organic materials. In addition to monitoring the photo-stability of organic sunscreens under controlled conditions, we also investigated the interaction between these organic filters and TiO_2 in aqueous media and in the presence of other non-active formulation ingredients.

Commercial sunscreen formulations typically have no less than 20 non-active ingredients including preservatives, emulsifiers, humectants, and polymers (as waterproofing agents).[56] It is of significant interest to determine the effect of these "inactive" ingredients on the photochemistry of the system. Investigation of the photochemistry occurring in a complex matrix, such as the full formulation, would be unlikely to reveal mechanistic details so we chose to study the effect of just one additional ingredient, namely a surfactant. TiO_2 is primarily included in sunscreen products as a UVA filter and so all studies were conducted under UVA irradiation.

Figure 7.19 shows the comparative absorption properties of the four sunscreens of interest and the combination of absorption and light scattering for TiO_2; note that the apparent absorption coefficient of TiO_2 is at least twice the value of each of the organic sunscreens at 365 nm. To investigate the effect of irradiated

TiO_2 on the photostability of organic sunscreens it was preferable to have the incident light largely absorbed (and partly scattered) by the inorganic filter. This was achieved by irradiating with a UVA lamp (LZC-UVA) having λ_{max} = 365 nm and using samples with the following general composition: [sunscreen] = 5.0 x 10^{-4} M and [TiO_2] = 1.0 mg mL^{-1} prepared in distilled, deionized water (ddH_2O). The titanium dioxide used in this study was the same polymorph as employed by manufacturers of sunscreens and cosmetics (anatase) with an average particle size of 32 nm. This particle size is within the recommended optimum range (20-50 nm) for sunscreen formulations.[17]

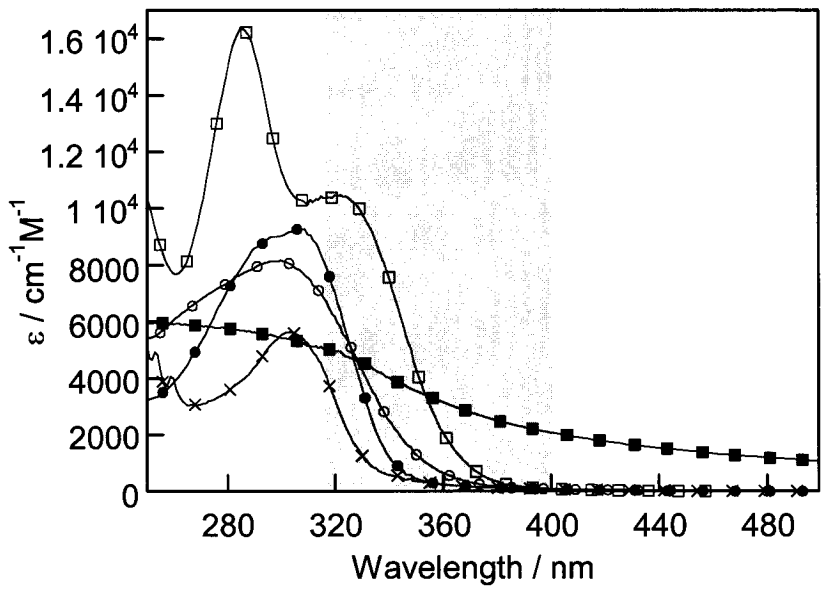

Figure 7.19 Absorption spectra of OCT (○), OXB (□), OSA (×), and OMC (●) in methanol and absorption/scattering by TiO_2 in water (■). The shaded area indicates the UVA portion of the spectrum.

All irradiations were conducted under air-equilibrated conditions, with continuous stirring, and at neutral pH. The pH is an important consideration due to its ability to attenuate the surface charge of metal oxides. For TiO_2, the pH at which the net surface charge is zero (zpc) is *ca.* 6, so at pH 7 the surface of the titanium dioxide particle would have a slight negative charge. Anionic surfactants are widely used in sunscreen preparations and so the simple anionic surfactant

sodium dodecyl sulphate (SDS) was used in these studies. Given the slight negative charge on the oxide particles, the surfactant was not expected to have a particularly strong interaction with the inorganic sunscreen. In order to calculate the micelle concentration in the system a critical micelle concentration (CMC) of 8.2 x 10^{-3} M and an aggregation number of 66 were used.

Mixtures containing the organic sunscreen (OXB, OSA, OMC, OCT) and various combinations of TiO_2 and SDS were irradiated for 20 hours (1.5 hours for OMC) in water or ACN as indicated in Table 7.3. The fraction of organic sunscreen recovered following irradiation was determined by GC-FID analysis with anthracene as an internal standard.

Conditions	% Sunscreen Recovery				
	OXB	**OSA**	**OCT**	**OMC**	***E*:*Z***
ACN	100	100	100	100	50:50
Water	100	100	100	100	65:35
SDS micelles	100	100	100	100	34:66
Water + TiO_2	40	75	55	84	72:12
SDS micelles + TiO_2	20	35	40	73	25:48

Table 7.3 Sunscreen recovery (%) as determined by GC after 20 h (OXB, OSA, OCT) and 1.5 h (OMC) UVA irradiation. Concentrations: [sunscreen] = 5.0 x 10^{-4} M, [TiO_2] = 1.0 mg mL^{-1}, [micelles] = 6.5 x 10^{-4} M. All samples prepared in ddH_2O.

As can be seen in Table 7.3, the four sunscreens studied exhibited excellent photostability under the conditions of irradiation in water, ACN, or aqueous micellar solution ([micelles] = 6.5 x 10^{-4} M). As expected, in the case of OMC a photostationary state of 50:50 *E*:*Z* was quickly established in ACN. Formation of *Z*-OMC was confirmed by GC-MS where both the starting material (*E*-OMC) and the new product had identical fragmentation patterns. Interestingly, the composition of the photostationary seems to be solvent dependent with *E*:*Z* being 65:35 in water

and 34:66 in micellar solution. In ACN, a solvent of intermediate polarity, an intermediate value of 50:50 was observed. In general, these results are in agreement with the reported *in vitro* stability of these compounds under similar conditions.

Remarkably, when the irradiation was carried out in the presence of suspended TiO_2, the organic sunscreens suffered significant degradation. Even more surprising was that the presence of SDS resulted in even more extensive photodegradation of the sunscreen. No photodegradation products were observed by GC or TLC analysis in any case (except for the *cis* isomer in the case of OMC). The isomerization of OMC was still observed in the presence of suspended TiO_2 indicating that not all of the incident radiation was absorbed or scattered by the oxide particles. Elemental analysis of TiO_2 recovered after irradiation of the aqueous sunscreen solutions showed the presence of carbon, suggesting that the sunscreens were completely mineralized. The different degradation rates observed in water as compared to SDS micelles may reflect different mineralization mechanisms in the two systems. The concentration of TiO_2 is much higher than the sunscreen concentration and, once the sunscreens are suspended in water, mineralization is likely to occur at the TiO_2 particle surface. This conclusion is supported by the presence of carbon on the recovered oxide, the absence of detectable photoproducts, and comparable results obtained in the photocatalytic degradation of organic dyes by TiO_2.[57]

The SDS-mediated enhancement of the sunscreen degradation was somewhat surprising and was further investigated by changing the surfactant concentrations while maintaining the concentrations of sunscreen and TiO_2 constant at 5.0×10^{-4} M and 1.0 mg mL^{-1} respectively. In a study of the TiO_2-photocatalyzed degradation of organic dyes, Kiriakidou *et al.* remarked that, at neutral and near-neutral pH, a moderate amount of the organic substrate had adsorbed onto the oxide surface.[57] We note that even if the maximum available surface area of the oxide particles used in this study were coated with SDS, the concentration

remaining in solution would still be well above the CMC (assuming mono-layer coverage). The results of this study are given in Table 7.4.

Micelle concentration /10^{-4} M	% Sunscreen Recovery				
	OXB	OSA	OCT	OMC	*E:Z*
6.5	72	78	79	73	25:48
3.9	58	69	62	65	23:42
1.9	45	41	43	55	19:36

Table 7.4 Sunscreen recovery (%) measured by GC after 7 h (OXB, OSA, OCT) and 1.5 h (OMC) irradiation. Concentrations: [sunscreen] = 5.0 x 10^{-4} M, [TiO_2] = 1.0 mg mL^{-1}. All samples were prepared in ddH_2O.

Inclusion of the organic sunscreens in micelles reduces direct contact between the TiO_2 particles and the organic species and may prevent deposition of the sunscreens on the oxide surface. As a result, the primary target of TiO_2 photocatalysis becomes the surfactant. The reactivity of TiO_2 towards sodium dodecyl sulphate has been previously studied and it was shown that titanium dioxide may be employed as a photocatalyst for the photodegradation of SDS.[58] Lea *et al.* have studied the TiO_2-induced mineralization of SDS, below the critical micelle concentration, as a function of different parameters such as pH, temperature, SDS concentration, and light intensity.[59] They have proposed a photooxidation mechanism where the photogenerated electrons and holes on TiO_2 act as targets for dodecyl sulphate anions and dissolved molecular oxygen. The result is generation of hydroxyl or peroxyl radicals that can attack surface organosulphate ions, liberating HSO_4^- and ultimately generating carbon-centered radicals. Any reactive radical species that are generated will be able to participate in hydrogen-abstraction from the alkyl chains of the surfactant, leading to further generation of carbon-centered radicals.

To learn more about the involvement of carbon-centered radicals in surfactant-enhanced sunscreen degradation, the irradiation of SDS in the presence of TiO_2 and a pre-fluorescent radical probe was investigated. The concept and methodology of radical detection by pre-fluorescent radical probes has been discussed in Section 6.1 and 6.2. In these experiments a pre-fluorescent probe was employed to determine the participation of carbon-centered radicals in irradiated systems containing both TiO_2 and surfactant. The probe structure is given in the inset of Figure 7.20; quinoline-TEMPO (4-(3-hydroxy2-methylquinolineoxy)-2,2,6,6-tetramethyl piperidine-1-oxyl, QT) has been previously employed by this research group for the detection of free radicals in a variety of systems, including radical polymerization and enzymatic catalysis.[60, 61] The fluorescence increase with time was measured at 405 nm (λ_{ex} = 350 nm) after short times and low conversions in order to prevent the TiO_2-induced mineralization of the probe itself.

As seen in Figure 7.20, irradiation of QT included in SDS micelles in the absence of TiO_2 afforded only a very weak fluorescence increase (Figure 7.20, ○). When 1.0 mg mL^{-1} of TiO_2 was suspended in the solution and the mixture was irradiated, a measurable increase in the fluorescence intensity over time was observed (Figure 7.20, ●). Interestingly, the radical production rate was also observed to be both TiO_2 and micelle concentration dependent. Lowering the TiO_2 concentration resulted in a slower fluorescence increase (Figure 7.20, □) while lowering the micelle concentration caused an acceleration in the rate of fluorescence increase (Figure 7.20, ■).

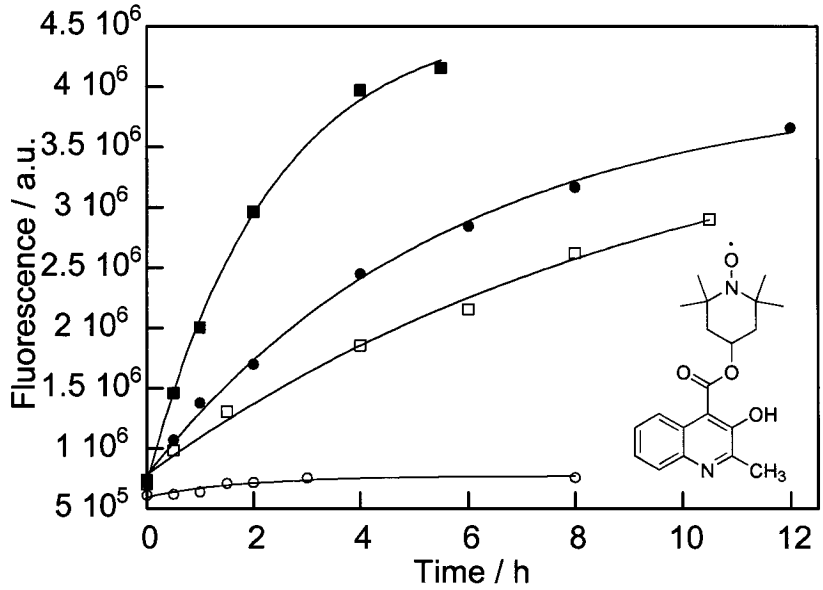

Figure 7.20 QT fluorescence increase monitored under the following conditions; [micelles] = 6.5 x 10^{-4} M, no TiO_2 (○), [micelles] = 6.5 x 10^{-4} M, [TiO_2] = 0.5 mg mL^{-1} (□), [micelles] = 6.5 x 10^{-4} M, [TiO_2] = 1.0 mg mL^{-1} (●), and [micelles] = 1.9 x 10^{-4} M, [TiO_2] = 1.0 mg mL^{-1} (■). Inset: QT structure.

A complex mixture of products was observed by TLC analysis following irradiation of QT in SDS micelles in the presence of TiO_2. Column chromatographic separation identified three products in isolable yields (< 10%). Although not unambiguously identified, two of these products were analyzed by ^1H and ^{13}C NMR and appeared to be species consisting of complex, unresolved alkyl chains attached by the nitroxide moiety to the QT core. Interestingly, the third product revealed that ACN, the co-solvent used for inclusion of QT and sunscreens in micelles, was also involved in the complex photochemistry of this system. The QT-ACN adduct, formed when QT traps an ACN-derived radical (Scheme 7.4), was isolated in *ca.* 10% yield and characterized by ^1H and ^{13}C NMR. It has been reported that electronically excited nitroxides can abstract hydrogen from acetonitrile.[62] The QT-ACN adduct may be formed as a result of hydrogen abstraction by QT* to generate the hydroxylamine QTH and $^{\bullet}CH_2CN$, which is subsequently trapped by a QT free radical (Scheme 7.3).

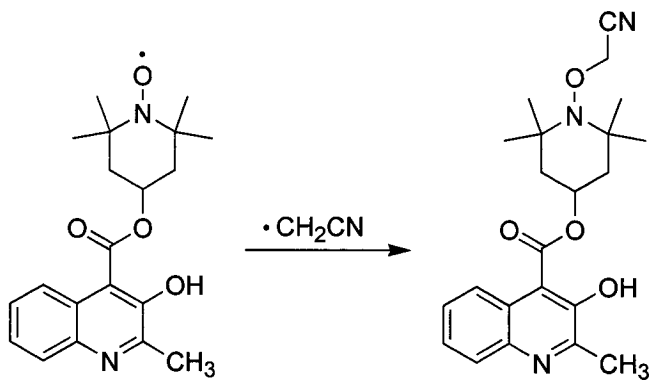

Scheme 7.3 Trapping of an acetonitrile-derived radical by QT.

The observation of a complex distribution of products in this reaction is indicative of the variety of carbon-centered radical intermediates possible during surfactant degradation. In such a reactive environment, we suggest that the synergistic action of hydroxyl, peroxyl, and carbon-centered radicals on the sunscreen associated with the micelle is likely to induce faster mineralization in surfactant solutions than in water alone. In light of this, the enhanced rate of sunscreen degradation with decreased micelle concentrations may be explained by simple statistics. Under the experimental conditions, all of the reaction participants (QT, sunscreen, and surfactant) have a pre-association due to the preferential location of the organic species within the hydrophobic micelle core. As a result, radical-induced damage occurs predominantly in the micelles in which the radicals are initially generated. When a large proportion of the micelles in the system are empty, the damage is concentrated on the surfactant itself with reduced sunscreen degradation. In contrast, when a greater number of micelles are occupied by sunscreen or QT, more of the radicals formed will participate in either sunscreen degradation or radical trapping by QT.

These results show that, while individual sunscreens may be largely photostable when irradiated in water or ACN, UVA irradiation in the presence of a popular inorganic filter results in mineralization of the organic components. These data confirm our suspicions regarding the validity of including TiO_2 in sunscreen

formulations and, along with other studies, highlight the utility of segregating sunscreen active ingredients by encapsulation, prior to inclusion in a commercial "cocktail" formulation. The surprising degradation enhancement caused by surfactants suggests that when examining sunscreen photostability, not only the filters must be considered since other "photochemically inactive" components may participate adversely to a significant extent.

7.4.2 Photostability of Supramolecular Sunscreens

We next examined both the photostability of sunscreen@Y complexes and the ability of encapsulation to prevent sunscreen-sunscreen interactions. Initially, qualitative experiments were conducted where the zeolite/sunscreen complexes were irradiated as powders or as water slurries for periods of 1.5-24 hours, with stirring. After irradiation, the zeolites were collected by filtration and the powders were subjected to solid-liquid (Soxhlet) extraction with DCM. The aqueous phase was also extracted with DCM and both solutions were analyzed by GC with FID or MS detection. No new products were observed by GC analysis in any case. For the slurry irradiation of OXB@Y, minor amounts of OXB were detected in the aqueous phase after 24 hours of irradiation. OSA@Y, OMC@Y, and OCT@Y showed no evidence of leaching into the aqueous phase even after 24 hours, in the case of OXB the leaching was < 1%.

To determine whether or not zeolite encapsulation would protect the organic sunscreen from TiO_2-induced degradation we irradiated the encapsulated sunscreens in the presence of suspended TiO_2. The zeolite samples were prepared with loadings such that the results could be compared to the data collected in solution. Although the sunscreen was encapsulated as opposed to free in solution, the total sunscreen:TiO_2 ratio was comparable to the solution study described above. The zeolite concentration was *ca.* 2.5 mg mL^{-1}, in order to avoid excessive light scattering by the zeolite as opposed to absorption/scattering by TiO_2. In order to quantitatively determine the amount of sunscreen recovered from the zeolite

before and after irradiation, a protocol that enabled reproducible collection of the zeolite sample from the slurry was required. Several filtering methodologies were attempted but, due to the small sample size, dissolution of the zeolite framework with concentrated acid, followed by liquid-liquid extraction ultimately proved to be the most reproducible method. We note that although this procedure was the best one identified there are many points in the protocol where error may be introduced. In addition, OSA was observed to undergo hydrolysis to a minor extent under the extraction conditions. The extent of this side-reaction was determined under the acidic conditions used for framework dissolution in the absence of zeolite and the reported sunscreen recoveries were corrected for this amount.

The general experimental protocol was as follows:

1. sunscreen@Y samples with the appropriate occupancy (<S> ~ 0.2-0.3) were prepared as described in Section 7.2
2. suspensions containing the sunscreen/zeolite composite with and without TiO_2 were prepared in ddH_2O
3. samples were irradiated (UVA) for 20 h (control samples were un-irradiated)
4. concentrated HCl was added to dissolve the zeolite framework and the solution was extracted with ether
5. the organic phase was collected and the solvent removed under vacuum
6. the amount of sunscreen recovered was analyzed by GC-FID to determine

The sample composition and experimental conditions are given in Table 7.5.

Label	Sample composition (in 10 mL ddH_2O)	Experimental Conditions
A	~25 mg sunscreen@Y	Dark
B	~25 mg sunscreen@Y + 10 mg TiO_2	Dark
C	~25 mg sunscreen@Y	UVA (20 h)
D	~25 mg sunscreen@Y + 10 mg TiO_2	UVA (20 h)

Table 7.5 Sample composition and experimental conditions. All samples were prepared in 10 mL of ddH_2O and irradiated in Pyrex tubes.

The results from UVA irradiation of OXB@Y in the presence and absence of suspended TiO_2 are shown graphically in Figure 7.21. The horizontal line in the left plot indicates the theoretical maximum amount of recovered sunscreen based on the occupancy and the amount of zeolite complex used. As indicated in Table 7.5, column A is the control sample where OXB@Y was incubated in the dark in the absence of TiO_2; theoretically, recovery of OXB from this sample should be 100%. As can be seen in Figure 7.21, OXB was recovered more or less completely in each case except D, the irradiated sample containing both OXB@Y and TiO_2. Calculating the percentage of OXB recovered as compared to the control sample (A) shows that in an illuminated suspension containing TiO_2, OXB undergoes *ca.* 20% photodegradation. This value is much less than the 60% degradation observed for unencapsulated OXB in water indicating that encapsulation was able to protect the organic sunscreen from TiO_2-induced mineralization. Notably, some degradation may also have occurred in the solution phase since OXB was previously observed to undergo minor leaching after 24 hours. No other products were recovered. Importantly, zeolite encapsulation was shown to preserve OXB photostability, as seen by the near 100% recovery from the irradiated sample (C).

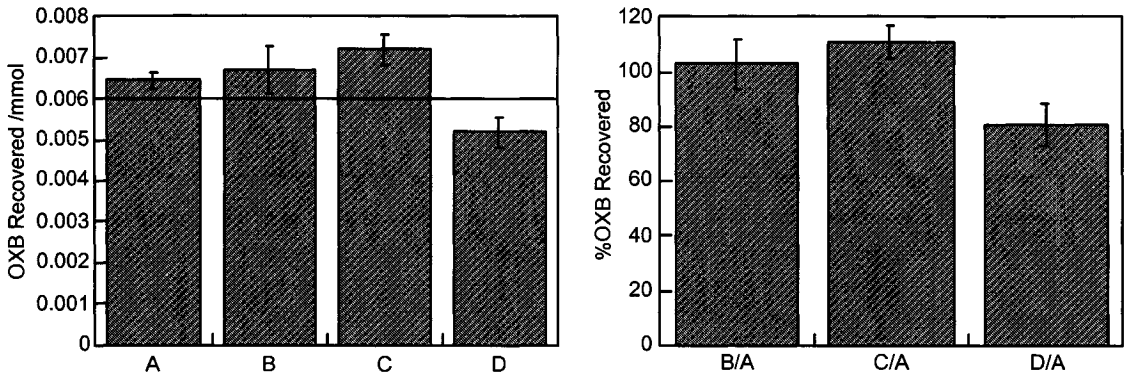

Figure 7.21 Amount of OXB recovered following framework dissolution (left), expressed as a percentage of the amount recovered from the control (right). Horizontal line (left) indicates the theoretical recovery value.

In the case of OSA, the salicylate was observed to undergo 10±2% (n = 4) hydrolysis in 15 minutes in 3 M HCl. The values reported below were corrected for this amount and the standard deviation was incorporated. Figure 7.22 shows that, within a reasonable amount of error, OSA was completely recovered from all samples. These results demonstrate that encapsulation does not affect the photostability of OSA and that inclusion in the zeolite complex protects OSA from interaction with TiO_2. Recall that in aqueous suspension, OSA underwent 25% photodegradation when illuminated in the presence of TiO_2.

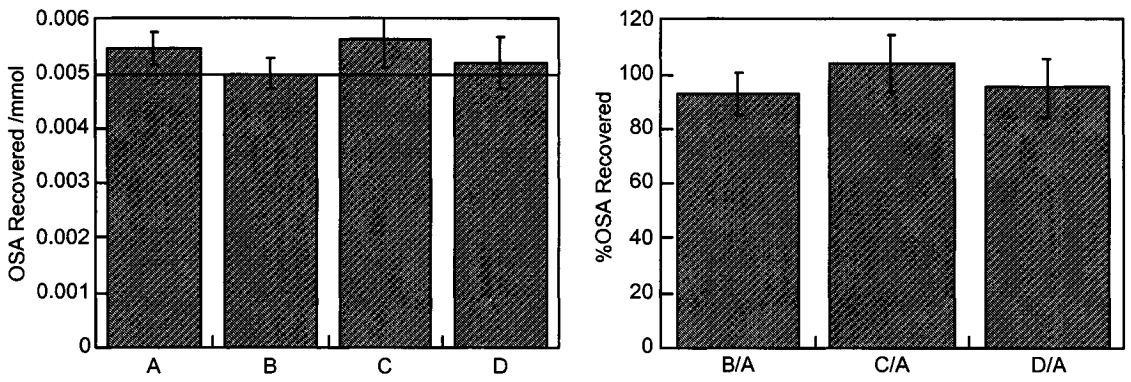

Figure 7.22 Amount of OSA recovered following framework dissolution (left), expressed as a percentage of the amount recovered from the control (right). Horizontal line (left) indicates the theoretical recovery value.

The case of OMC is slightly more complex due to the *cis-trans* isomerization. To calculate the amount of OMC recovered, the areas of the chromatographic peaks for the *cis* and *trans* isomers were added and this value was compared with the calibration curve to determine the recovery. This additional source of error could account for the apparent incomplete recovery of OMC in the case of sample A (control). However, as can be seen in Figure 7.23, there is a more pronounced loss of OMC in each of the other samples. In particular, irradiation of OMC@Y alone (C) results in the lowest percent recovery, with greater than 60% of OMC unrecovered. Curiously, the amount of OMC recovered was equally low for OMC@Y in the presence of TiO_2 regardless of whether or not the sample had been irradiated.

OMC was treated with 3 M HCl in order to confirm that it was stable in the acidic conditions required for zeolite framework dissolution. Analysis by GC-FID showed quantitative recovery of OMC following acidic treatment. The entire experiment was repeated (again with n = 3) and similar results were obtained. No photodegradation products were isolated in the case of illuminated samples (C and D). It is possible that the reduced ability of OMC to dissipate energy by isomerization to a stable *cis* form, results in the redirection of this energy through a

degradative pathway. The reason for the low recovery of OMC in un-irradiated samples containing TiO_2 (B) is difficult to definitively assign. However, the apparent reduced photostability of OMC when irradiated in zeolite Y probably precludes the use of this material as a potential sunscreen.

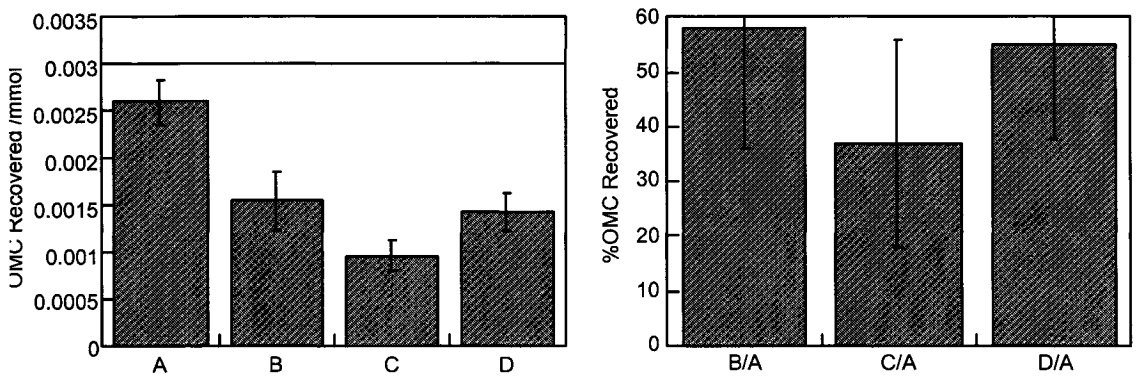

Figure 7.23 Amount of OMC recovered following framework dissolution (left), expressed as a percentage of the amount recovered from the control (right). Horizontal line (left) indicates the theoretical recovery value.

OCT was also suspected to undergo restricted rotation about the propenyl bond within the zeolite cavity; this was not shown definitively since the result of a bond rotation is spectroscopically identical to the starting structure as a result of the symmetrical substitution. However, when OCT@Y was irradiated in the presence and absence of TiO_2 the observed behaviour was similar to both OXB and OSA. Namely, OCT was almost completely recovered in each case, demonstrating both the photostability of OCT when included in zeolite Y and the ability of the zeolite to protect the organic sunscreen from mineralization in the presence of TiO_2. Recall that in aqueous suspension, OCT underwent 45% mineralization when irradiated in the presence of TiO_2.

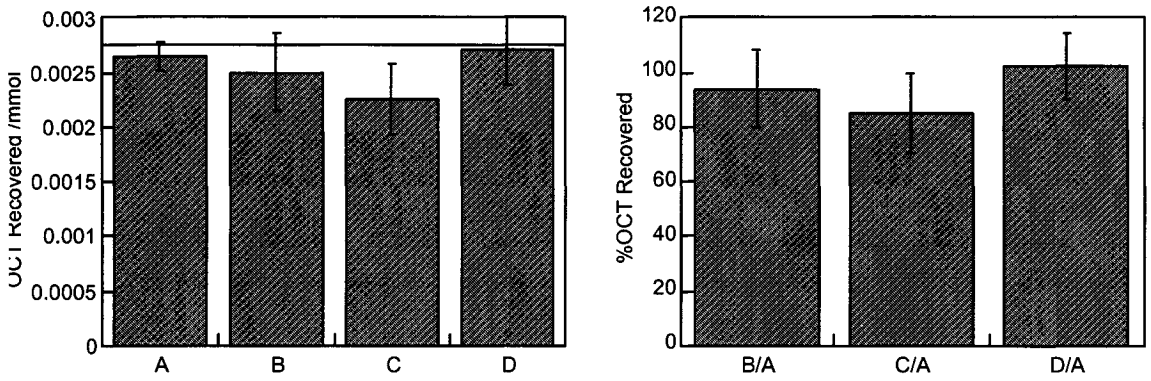

Figure 7.24 Amount of OCT recovered following framework dissolution (left), expressed as a percentage of the amount recovered from the control (right). Horizontal line (left) indicates the theoretical recovery value.

The results presented above indicate that, with the exception of OMC, each of the sunscreens under investigation were photostable when encapsulated in zeolite Y. It was also shown that, when irradiated in aqueous media in the presence of the inorganic sunscreen TiO_2, each of the organic filters underwent considerable degradation. This degradation was largely prevented when the organic filters were encapsulated, demonstrating that zeolite encapsulation is able to prevent the destructive interaction between sunscreen ingredients.

7.5 Photobiological Studies

7.5.1 PABA: A Case Study

As mentioned above, PABA is well-known to sensitize the formation of singlet oxygen and has also been implicated in the generation of other ROS such as superoxide anion.[44, 45] PABA has also been shown to cause DNA damage both *in vivo* and *in vitro*; types of damage include increased pyrimidine cyclobutane dimer formation as well as photoaddition to nucleosides.[63] A fundamental question in the evaluation of supramolecular sunscreens as a viable solution to problems related to conventional sunscreens, is whether or not they have the ability to protect biological systems from damage. Taking PABA as a worst-case scenario in terms of sunscreens, we chose to evaluate the effects of PABA@Y on a model biological system. If encapsulation of PABA in zeolite NaY modulates PABA-induced damage in a model biological system, this would provide an elegant proof of our concept. As discussed in Chapter 3, the oxidoreductase enzyme horseradish peroxidase (HRP) is susceptible to attack by ROS resulting in a loss of enzymatic activity. In Chapter 3 it was shown that HRP underwent photo-deactivation in the presence of TiO_2 and, to a much lesser extent, TiO_2@Y.

For this experiment, HRP was irradiated in aqueous suspensions containing either free PABA in solution or an equivalent amount of PABA encapsulated in zeolite NaY. After two hours of UVB irradiation with continuous stirring, the activity of the enzyme was assayed as described in Sections 3.2.4 and 3.5.4. Briefly, the ability of the enzyme to catalyze the oxidation of ABTS to its radical cation in the presence of hydrogen peroxide, was used to estimate enzymatic activity. The growth of the absorbance due to the highly coloured radical cation was monitored over time; the initial slope of this growth curve was extracted from these data and used as an indicator of enzymatic activity. Irradiation with UVB lamps (λ_{max} = 313 nm) was chosen because PABA is primarily intended as a UVB sunscreen. In all cases, samples were prepared in triplicate and assayed three times each.

As can be seen in Figure 7.25, after two hours of irradiation in the presence of PABA, HRP was almost completely deactivated. The enzyme itself suffers very little damage from exposure to UVB radiation alone, at this exposure time. Plotting the ratio of enzymatic activity in the exposed and unexposed samples (Figure 7.25 right) reveals that in the absence of PABA, HRP undergoes *ca.* 10% UVB-induced photodeactivation; when PABA is included in the solution this number increases to greater than 90%. By examining different irradiation times, it was determined that HRP enzymatic activity is reduced by *ca.* 50% after 30 minutes. These results support the many reports of PABA-induced damage to biological systems.

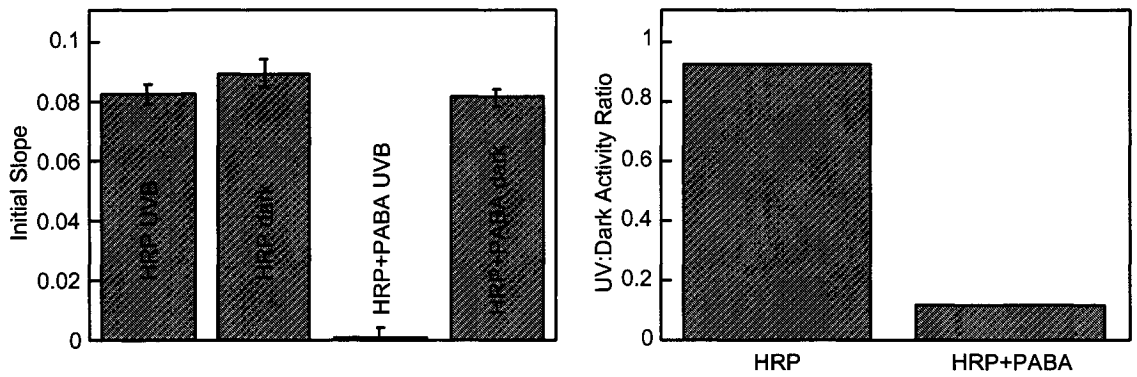

Figure 7.25 Calculated initial slopes for samples of HRP (0.1 mg mL^{-1}) in ddH_2O with or without PABA (7.3×10^{-4} M) after 2 h UVB irradiation or dark incubation (left) and relative enzymatic activities for the same samples (right).

When the experiment was repeated using an equivalent amount of PABA encapsulated in zeolite NaY, the difference was quite remarkable. After two hours of irradiation, the enzyme activity was again reduced by 10% in the absence of PABA. When the system was irradiated in the presence of PABA@Y (Figure 7.26), the enzymatic activity was reduced by only 30%, as compared to 90% in the case of un-encapsulated PABA. This significant improvement demonstrates that zeolite encapsulation is able to protect a model biological system from sunscreen-induced damage.

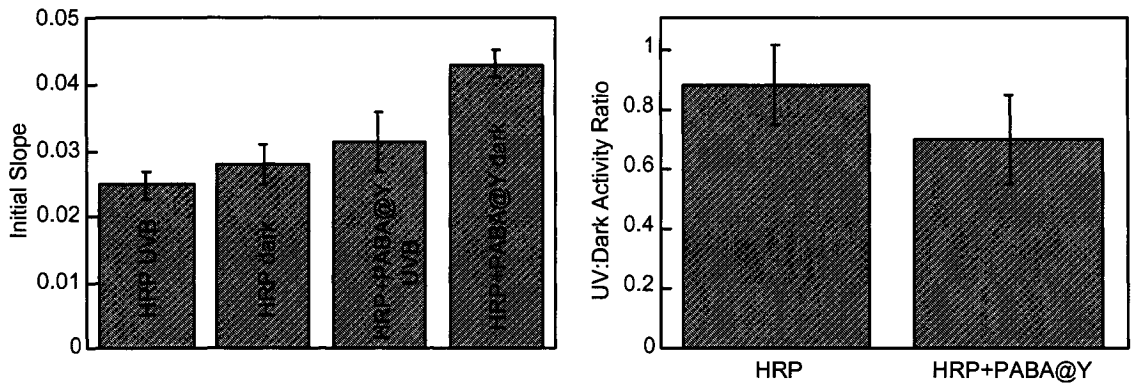

Figure 7.26 Calculated initial slopes for samples of HRP (0.1 mg mL^{-1}) in ddH_2O with or without PABA@Y (1.0 mg mL^{-1}, <S> ~ 0.99, equivalent to *ca.* 6.0×10^{-4} M) after 2 h UVB irradiation or dark incubation (left) and relative enzymatic activities for the same samples (right).

To ensure that the 30% deactivation observed was not due to NaY itself, a control experiment was conducted using a sample of NaY containing no PABA. The enzyme was irradiated or incubated (no light) in the presence and absence of NaY and the enzyme activity was determined by assay. The plot of relative enzyme activity (Figure 7.27 right) indicates that, within experimental error, the presence of NaY does not have an adverse effect on the enzyme activity.

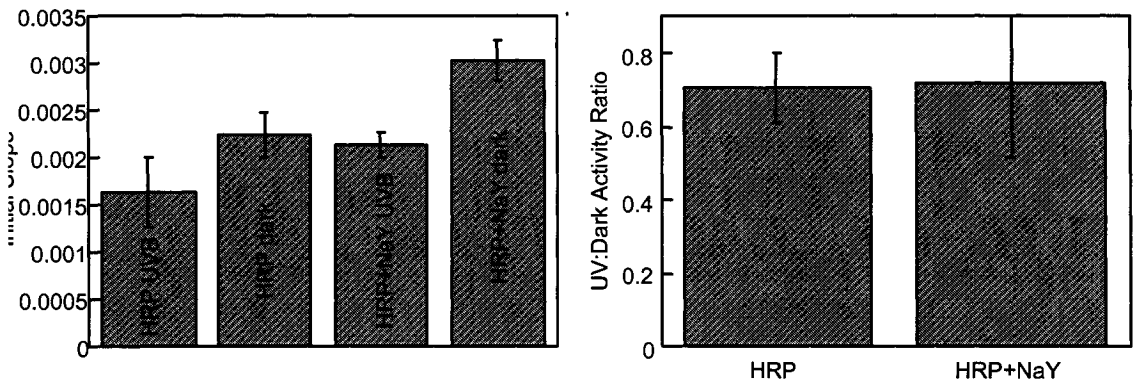

Figure 7.27 Calculated initial slopes for samples containing HRP (1.0 mg mL^{-1}) with or without NaY (1.0 mg mL^{-1}) after 2 h UVB irradiation or dark incubation (left), and relative enzymatic activity ratios for the same samples (right).

Interestingly, there was an unexpected trend observed in samples containing both HRP and zeolite materials, the effect is visible in both Figures 7.26 and 7.27. The enzymatic activity, as indicated by the value of the initial slope, was higher in each of the samples containing zeolite as compared to the corresponding sample with no zeolite. In fact, further investigation revealed that incubating HRP in the presence of PABA@Y, or simply NaY, resulted in a reproducible, 30% increase in enzymatic activity. This result was initially surprising, however, it was subsequently discovered that faujasite zeolites have been used in lieu of ion-exchange chromatography for protein purification. In particular, incubation of crude extracts of HRP with zeolite Y has been observed to result in a five-fold increase in activity depending on solution pH.[64, 65] Klint *et al.* observed that impurities interfering with HRP activity are adsorbed onto the zeolite particles. It seems reasonable to suggest that an inadvertent "purification" is the explanation for the increased HRP activity observed for zeolite-containing samples in this case.

7.5.2 Biological Impact of Supramolecular Sunscreens

7.5.2.1 Preliminary Notes

In order to evaluate the biological compatibility of these new materials in the context of their use as sunscreen ingredients, we examined the effects of supramolecular sunscreen materials on human epidermal keratinocytes. The keratinocyte cell is the building block of the outermost layer of our skin, the epidermis. The epidermis is composed of five different layers (Figure 7.2) and consists largely of keratinocyte cells embedded in a matrix of skin lipids. The outermost portion of the epidermis, the stratum corneum, is waterproof and when undamaged, prevents bacteria, viruses, and other foreign substances from entering the body. The epidermis also protects the internal organs, muscles, nerves, and blood vessels from trauma. Clearly, the effect of new sunscreen materials on this cell type is of utmost importance.

The cells used in this study were human epidermal keratinocytes (HEK). The HEK cells were cultured and maintained at 37°C in a humidified atmosphere containing 5% CO_2. In each of the experiments described below, cells were typically used *ca.* 96 hours after seeding, when the culture had reached 80% confluence (i.e. 80% coverage) in a 60 mm Petri dish.

After cells were subjected to the experimental conditions described in the following sections, the cell viability was determined by fluorescein diacetate/ethidium bromide fluorometric assay and the integrity of the DNA was assessed by alkaline comet assay. To assess cell viability, the cells were first detached from the Petri dish, re-suspended in media, and then stained with a solution of fluorescein diacetate (FD) and ethidium bromide (EBr) in Hank's Balanced Salt Solution (HBBS). FD is a non-polar, non-fluorescent compound that readily diffuses into cells when incorporated into the culture medium. Once inside, intracellular esterases hydrolyse the diacetate to generate fluorescein, a fluorescent, and highly polar molecule that will diffuse very slowly out of intact cells.[66] As a

result of this slow leakage, green-fluorescent FD will accumulate in healthy cells having intact membranes. Fluorescein labeling does not provide an indication of the number of non-viable cells and so the cells are also exposed to the red-fluorescent dye, EBr. EBr is taken up non-specifically by both living and dead cells and therefore, when a sample stained with both dyes is examined by fluorescence microscopy, viable cells will fluoresce green and dead cells will fluoresce red. Using a counting chamber or hemocytometer (a special microscope slide comprising a grid of known dimensions) the cell concentration as well as the percentage of live cells can be determined.

The comet assay, also known as single-cell gel electrophoresis, is a sensitive technique for DNA damage quantification. The name is derived from the comet-shaped DNA migration pattern observed after completion of the assay (Figure 7.28). This technique is generally recognized as a sensitive, reliable, and moderately rapid method for detection of DNA damage in the form of double-strand breaks (DSBs), single-strand breaks (SSBs), cross-linking, and alkali labile sites (ALS). In comparison with other sensitive damage detection methods, the advantages of the comet assay are its relatively inexpensive materials, the small number of cells required, and the fact that data are obtained on a single cell level within hours of sampling. The comet assay was originally introduced by Ostling *et al.* who improved upon existing techniques for whole cell DNA analysis, by incorporating an electrophoretic step that allows improved quantification of damaged DNA.[67] This early version of the technique was only capable of detecting DSBs. The alkaline comet assay, developed by Singh *et al.*,[68] is able to detect both DSBs and SSBs, as well as ALS; the alkaline treatment allows these other types of damage to be expressed. A modified version of the alkaline assay was used in this work and the method is described briefly below.[69]

In the first step of the assay, the cells are embedded in agarose gel and cast onto a solid support. The cells are then exposed to a high salt lysis buffer (2.5 M NaCl, pH 10) containing a surfactant. The detergents in the lysis buffer break down

the cellular membrane as well as the nuclear membrane leaving naked DNA embedded in the agarose gel. The gel-embedded DNA is then subjected to an alkaline unwinding buffer at a pH > 12.3, causing the DNA to unwind. The basic environment disrupts the hydrogen bonding between the nucleobases of DNA, forcing them apart and resulting in the formation of DNA single strands. ALS (structurally modified sites on the DNA) and DSBs are converted to SSBs under these unwinding conditions. After unwinding, each SSB results in the formation of truncated single strands of DNA; as a consequence, more heavily damaged samples will have a higher concentration of short strands. During electrophoresis, the shorter strands (representing damaged DNA) will migrate faster than the longer ones resulting in the formation of comet-shaped features. After electrophoresis the gels are dried and stained with a nucleic acid dye (propidium iodide) in order to visualize the DNA damage by fluorescence microscopy.

Quantification is achieved by analyzing selected cells according to four parameters designed to represent the amount of DNA damage. The comet length (distance from the head to the tip of the comet) and tail length (distance from the end of the head to the tip of the tail) were the first parameters used to quantify DNA damage in the comet assay, since more damage would result in more SSBs and longer comets. However, since comet length was found to be heavily dependent on the electrophoresis conditions,[70] the head-to-tail ratio (the ratio of fluorescence in the tail over total fluorescence of the comet) and tail moment (product of the head-to-tail ratio and the distance between the center of gravity in the head and the center of gravity in the tail) have become more commonly used parameters. A cell with damaged DNA would have a higher value for the head-to-tail ratio and tail moment than an undamaged cell. These values are determined with the aid of an image analysis computer program.

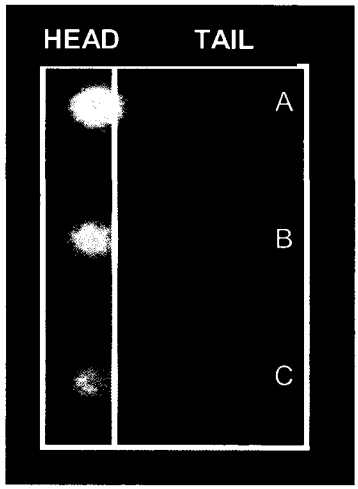

Figure 7.28 Typical comets observed by fluorescence microscopy from an undamaged (A), moderately damaged (B), and heavily damaged (C) cell after alkaline comet assay. (Figure from A. L. Vinette)

Prior to experimentation with supramolecular sunscreens, it was necessary to determine that the zeolite itself was sterile and would not infect the cells. This was accomplished by culturing the zeolites in a cell culture medium containing no antibiotics and monitoring for bacterial growth. No contamination was observed and the zeolites were deemed sterile. It was also important to evaluate the amount of zeolite that could be applied to the cell culture without affecting the cell viability. The viability was assessed by FD/EBr assay following incubation of the cells for 18 hours with 2.0-20.0 mg of NaY in a humidified, 5% CO_2 atmosphere. It was determined that up to 2.5 mg of NaY can be applied to subconfluent cells with no effect on cell viability, as compared to a control sample containing no zeolite. In all subsequent experiments NaY or sunscreen@Y were applied to the cells in amounts less than 2.5 mg.

7.5.2.2 Effect of Encapsulated Sunscreens on HEK Cells

To determine the effect of encapsulated and un-encapsulated sunscreens on HEK cells, the cells were incubated with culture media containing free sunscreen, zeolite-encapsulated sunscreen, or empty zeolite. An aliquot of each sunscreen

suspension was exposed to solar simulated radiation (SSR) for ten minutes corresponding to a dose of *ca.* 1 J/cm^2 (250-350 nm). The control samples were treated with irradiated and un-irradiated culture media. In summary, the following four suspensions were prepared:

1. 0.2-0.3 mg sunscreen in culture media
2. 1.5 mg of sunscreen@Y (<S> ~ 1.0) in culture media
3. 1.5 mg NaY in culture media
4. plain culture media (control)

When the keratinocytes were 80% confluent (*ca.* 96 hours after seeding), the existing culture medium was removed and replaced by one of the irradiated or un-irradiated suspensions described above (1-4). The cells were then incubated with the test suspension for 24 hours in a humidified, 5% CO_2 atmosphere. After the incubation period, the cell viability was evaluated by FD/EBr assay and the DNA integrity was determined by alkaline comet assay. In the data presented below the striped bars represent the media suspensions exposed to solar simulated radiation and the grey bars represent the un-irradiated suspensions. Irradiated samples are designated with a subscript "UV", for example OXB@Y_{UV} is the OXB@Y suspension that was exposed to SSR.

In the case of oxybenzone, the cell viability data show that when the cells were incubated with the modified media that had <u>not</u> been irradiated (grey bars) there was no effect on the health of the cell culture in any case (Figure 7.29 left). In the case of cells incubated with OXB_{UV} there was a minor decrease in the number of viable cells after 24 hours. This result is in agreement with the increased amount of DNA damage observed for the same sample following alkaline comet assay (recall that a larger tail moment corresponds to more damage). Interestingly, incubation with the supramolecular sunscreen, OXB@Y_{UV}, showed no increase in the tail moment (TM) as compared to the controls, demonstrating that encapsulation reduces OXB-induced DNA damage under these conditions.

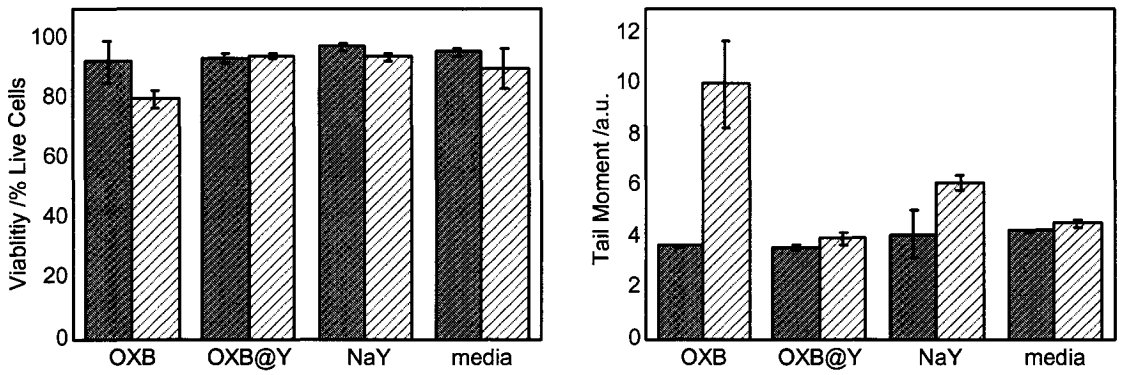

Figure 7.29 Cell viability (left) and DNA damage determined by alkaline comet assay (right) for HEK cells incubated for 24 h with irradiated (stripes) or un-irradiated (grey) media containing OXB, OXB@Y, or NaY. Data is given as the mean value ± standard error for three experiments, 100 comets were evaluated per experiment.

The results of trials involving octyl salicylate were very similar to the data obtained for the OXB example. When incubated with un-irradiated samples, the cell viability and DNA integrity were largely unaffected. When exposed to OSA_{UV} the number of viable cells remaining in the sample decreased to less than *ca.* 60% from a baseline value of *ca.* 90%, as seen in Figure 7.30 (left). This decrease in cell viability was accompanied by a corresponding increase in DNA damage as determined by alkaline comet assay. In summary, prior to irradiation neither OSA nor OXB have a discernable negative impact on cultured HEK cells *in vitro*. However, once these sunscreens were exposed to SSR (dose ~ 1 J cm^{-2}), incubation with HEK cells resulted in DNA damage in both cases, as well as a reduction in overall cell viability. Notably, the encapsulated sunscreen materials OSA@Y and OXB@Y had no observable impact on cell viability when compared to control samples and did not cause increased DNA damage.

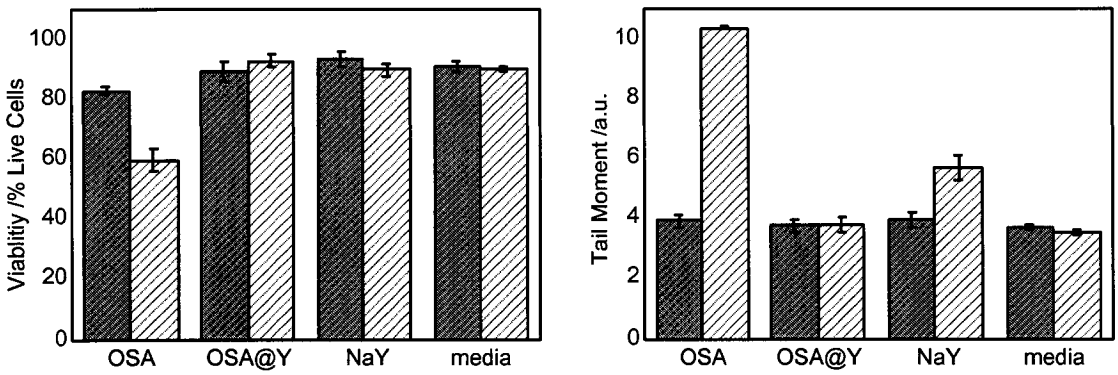

Figure 7.30 Cell viability (left) and DNA damage determined by alkaline comet assay (right) for HEK cells incubated for 24 h with irradiated (stripes) or un-irradiated (grey) media containing OSA, OSA@Y, or NaY. Data is given as the mean value ± standard error for three experiments, 100 comets were evaluated per experiment.

The impact of OMC and OCT on HEK cells is shown graphically in Figures 7.31 and 7.32. The most noticeable difference between the data obtained for this pair of sunscreens, as compared to the results discussed above for OXB and OSA, is that both OMC and OCT were observed to cause significant reductions in cell viability, even prior to irradiation. The loss of cell viability became more pronounced when the cells were incubated with OMC_{UV} and OCT_{UV}. The cell mortality observed in the case of irradiated sunscreens was accompanied by a large increase in TM indicating increased DNA damage. Notably, the increased mortality induced by un-irradiated sunscreens was not accompanied by an increase in DNA damage, implying a different mechanism for cellular death in the case of irradiated and un-irradiated sunscreens. Most remarkably, when the cells were incubated with these same sunscreens encapsulated in zeolite Y, there was no adverse effect on cell viability or DNA integrity, regardless of whether or not the samples had been irradiated.

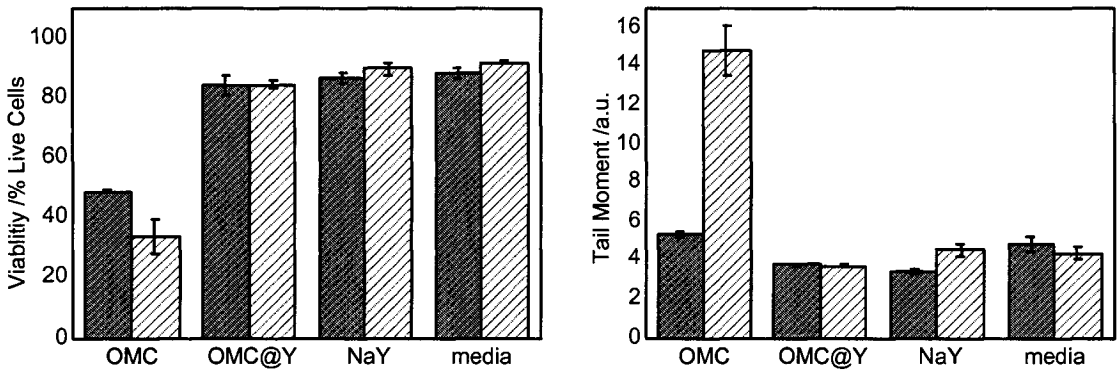

Figure 7.31 Cell viability (left) and DNA damage determined by alkaline comet assay (right) for HEK cells incubated for 24 h with irradiated (stripes) or un-irradiated (grey) media containing OMC, OMC@Y, or NaY. Data is given as the mean value ± standard error for three experiments, 100 comets were evaluated per experiment.

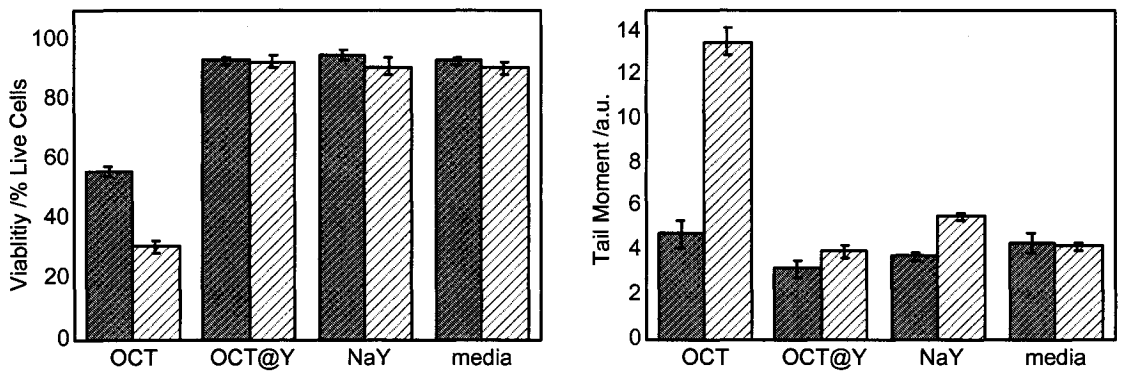

Figure 7.32 Cell viability (left) and DNA damage determined by alkaline comet assay (right) for HEK cells incubated for 24 h with irradiated (stripes) or un-irradiated (grey) media containing OCT, OCT@Y, or NaY. Data is given as the mean value ± standard error for three experiments, 100 comets were evaluated per experiment.

The data presented above demonstrate two important points. Firstly, zeolite-encapsulated sunscreens do not have a negative impact on the viability of cultured human epidermal keratinocyte cells *in vitro*, nor do they induce DNA

damage as determined by the alkaline comet assay. Secondly, encapsulation of all four sunscreens in zeolite NaY prevented both cell death and DNA damage induced by the un-encapsulated sunscreens.

In the experiments described above, the amount of free sunscreen used was roughly equivalent to the amount of sunscreen encapsulated within the zeolite complexes. It was determined that the effects on cell viability and DNA integrity were not dependent on the zeolite loading (data not shown).

7.5.2.3 Protective Capability of Encapsulated Sunscreens

Having determined that the supramolecular sunscreens under investigation were both photostable (with the exception of OMC@Y) and non-toxic to human keratinocyte cells, we proceeded to determine the protective capability of the prepared materials. By definition, sunscreen SPF is determined *in vivo* by the increased exposure time required to induce erythema (i.e. reddening or sunburn); SPF 4 indicates that the radiation dose must be increased by a factor of four, before induction of erythema. This methodology suffers from several disadvantages, including the subjectivity associated with determination of the erythemic end-point as well as the different erythemic responses elicited from different skin types. Although *in vivo* SPF determination is the industry standard, despite the drawbacks mentioned above, a number of *in vitro* techniques for SPF determination have emerged. The *in vitro* SPFs of both, free and supramolecular sunscreens were determined in order to compare their ability to provide sun protection.

In vitro SPFs were measured using a Lapsphere UV-1000S Ultraviolet Transmittance Analyzer (UTA), the sunscreens were suspended in ethylene glycol and sandwiched between two quartz plates. The SPF was determined by measuring the transmittance of the sample between 280 and 400 nm and weighting the transmittance by a standard solar spectral irradiance curve (i.e. the average amount of solar radiation at the earth's surface as a function of wavelength) and an erythemal action spectrum (the sunburn response of human skin to solar radiation

as a function of wavelength). The inverse of the area under the weighted transmittance curve is the factor by which the sample attenuates harmful radiation. The SPF was calculated using the Labsphere software according the following equation;[71]

Equation 7.1

$$SPF = \frac{\int_{280nm}^{400nm} E_\lambda \cdot S_\lambda \cdot d\lambda}{\int_{280nm}^{400nm} E_\lambda \cdot S_\lambda \cdot T_\lambda \cdot d\lambda}$$

Where E_λ is the CIE (Commission International de l'Eclairage) erythemal action spectrum, S_λ is the spectral distribution provided by Labsphere and T_λ is the recorded transmittance of the sample. The results of these measurements are given below in Figure 7.33.

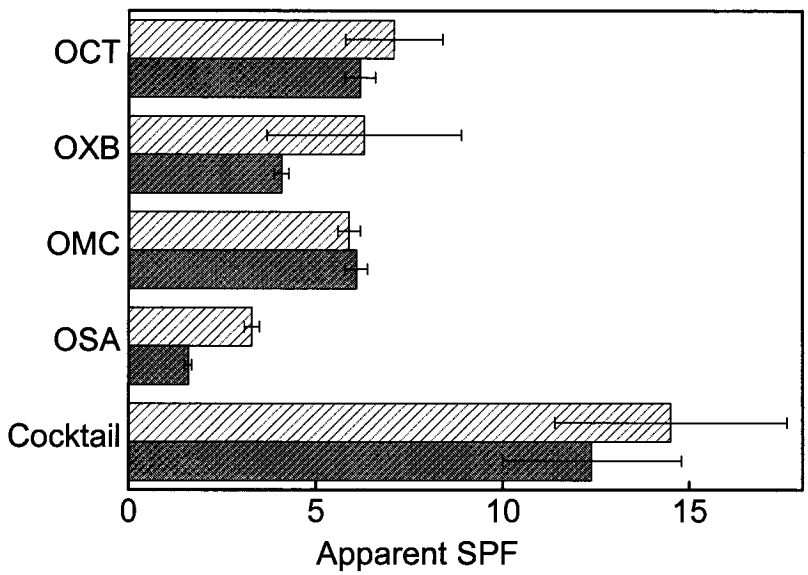

Figure 7.33 *In vitro* SPF values determined using the Labsphere UTA for free (0.12 mmol, stripes) and encapsulated (200 mg of <S> ~ 1.0, 0.12 mmol equiv., grey) sunscreens suspended in ethylene glycol. The cocktail contained equal amounts of all four free (0.12 mmol total) or encapsulated (200 mg total) sunscreens.

The above figure clearly shows that the encapsulated sunscreens are able to provide *in vitro* SPFs that are similar to the un-encapsulated sunscreens.

In the final set of experiments, we compared the ability of the supramolecular sunscreens to protect epidermal keratinocytes from radiation-induced damage. For these experiments the sunscreens were suspended in benzene and sandwiched between two quartz plates, according to the protocol of Reinhardt *et al.* for determination of the protective capabilities of commercial sunscreen products.[69] The quartz plates were placed directly on top of the Petri dishes containing the cells and the cells were irradiated through the plates with SSR for ten minutes (*ca.* 1 mJ cm^{-2}). Prior to irradiation, the culture media was removed and replaced with PBS, in order to avoid absorption by culture media components such as phenol red. Following irradiation, the cells were re-suspended in culture media and incubated in the dark for 24 hours. The cell viability was then determined using FD/EBr as described above and the DNA integrity was assessed by alkaline comet assay.

The experimental results for each of the four sunscreens are given in Figures 7.34-7.37. For each sunscreen the cell viability and DNA damage were assessed following irradiation of the cells through the quartz sandwich, with and without the sunscreen. The results were very similar for all of the samples investigated and, in general, after ten minutes of irradiation, cells protected by both the encapsulated and free sunscreens were indistinguishable from the un-irradiated controls (labeled as "total protection"). In the case of OXB, for example, the fraction of viable cells remaining after ten minutes of irradiation is less than 30% in the absence of protection (Figure 7.34). This number increases to 40% when the cells were irradiated through a thin film of benzene and to *ca.* 100% when the sunscreen was also present in the thin film. In all of the data given below, "total protection" refers to the cell viability and DNA damage observed for un-irradiated control samples.

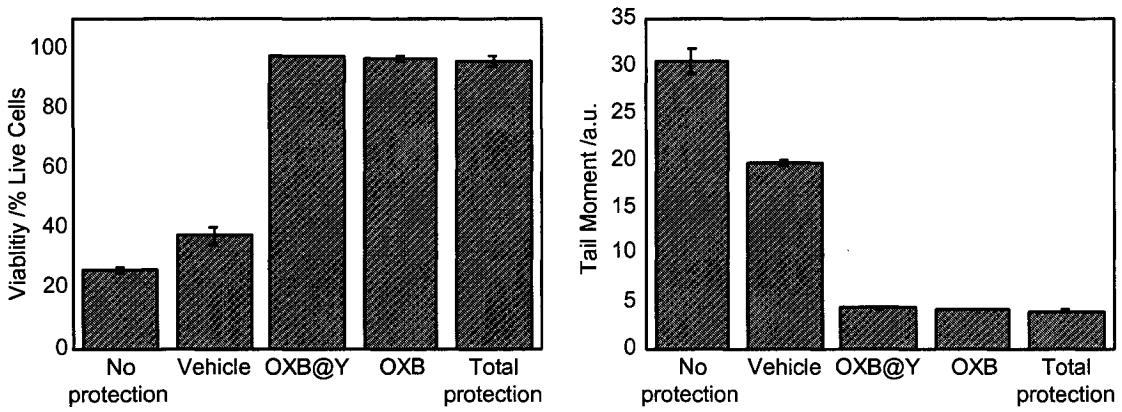

Figure 7.34 Cell viability (left) and DNA damage determined by alkaline comet assay (right) for samples exposed to SSR without or with protection (vehicle, OXB, or OXB@Y). Data is given as the mean value ± standard error for three experiments, 100 comets were evaluated per experiment.

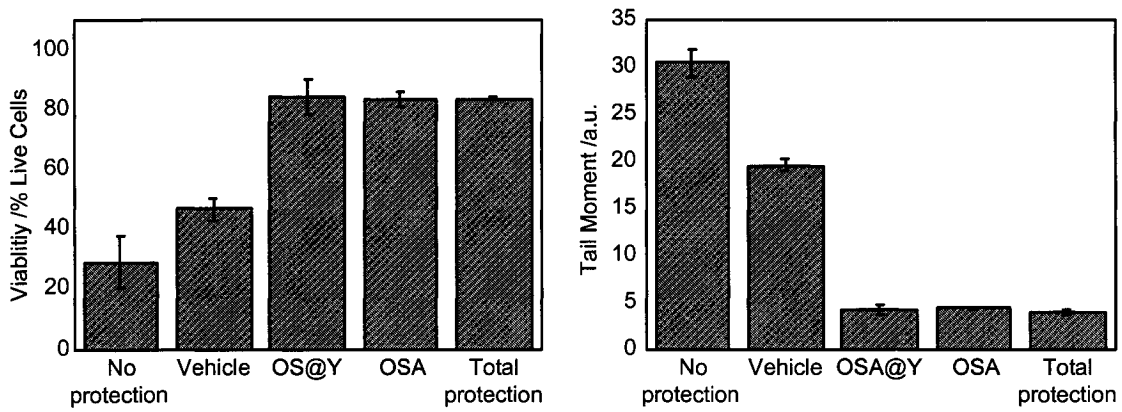

Figure 7.35 Cell viability (left) and DNA damage determined by alkaline comet assay (right) for samples exposed to SSR without or with protection (vehicle, OSA, or OSA@Y). Data is given as the mean value ± standard error for three experiments, 100 comets were evaluated per experiment.

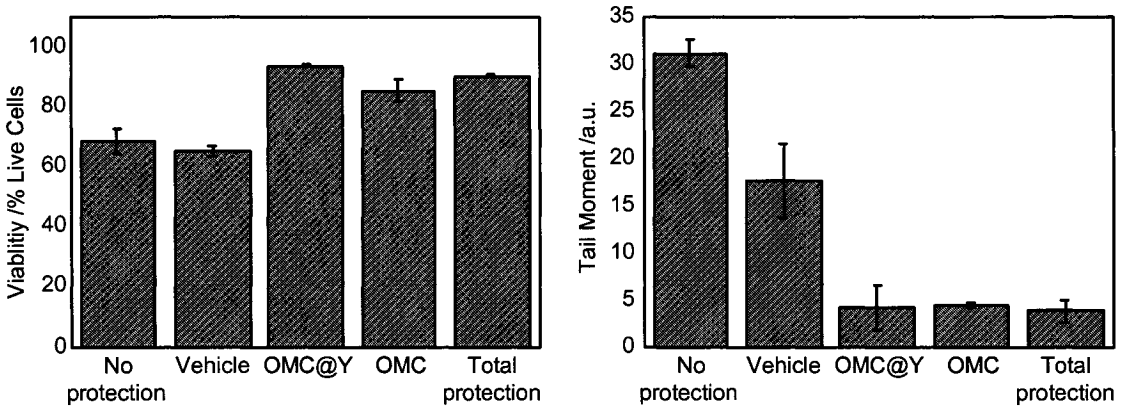

Figure 7.36 Cell viability (left) and DNA damage determined by alkaline comet assay (right) for samples exposed to SSR without or with protection (vehicle, OMC, or OMC@Y). Data is given as the mean value ± standard error for three experiments, 100 comets were evaluated per experiment.

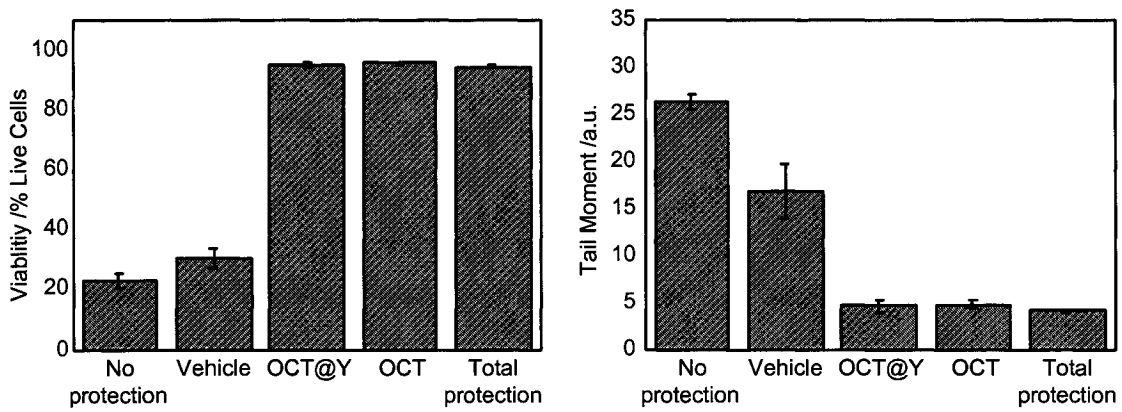

Figure 7.37 Cell viability (left) and DNA damage determined by alkaline comet assay (right) for samples exposed to SSR without or with protection (vehicle, OCT, or OCT@Y). Data is given as the mean value ± standard error for three experiments, 100 comets were evaluated per experiment.

In order to more clearly compare the protective capability of the encapsulated and un-encapsulated sunscreens, the experiments described above

were repeated with increasing irradiation times. Cell viability was not affected in either sample after ten minutes of irradiation, therefore the radiation dose had to be increased in order to determine whether the protection provided by the encapsulated sunscreens is truly comparable to the un-encapsulated filters. Figure 7.38 shows that when the cell cultures were irradiated without protection for 10, 15, and 20 minutes, the cell viability decreased with increasing irradiation time. The cell viability was observed to decrease similarly, with increased radiation dose, for both free and encapsulated sunscreens, indicating that zeolite-encapsulated sunscreens are able to provide protection from radiation commensurate with un-encapsulated sunscreens in solution.

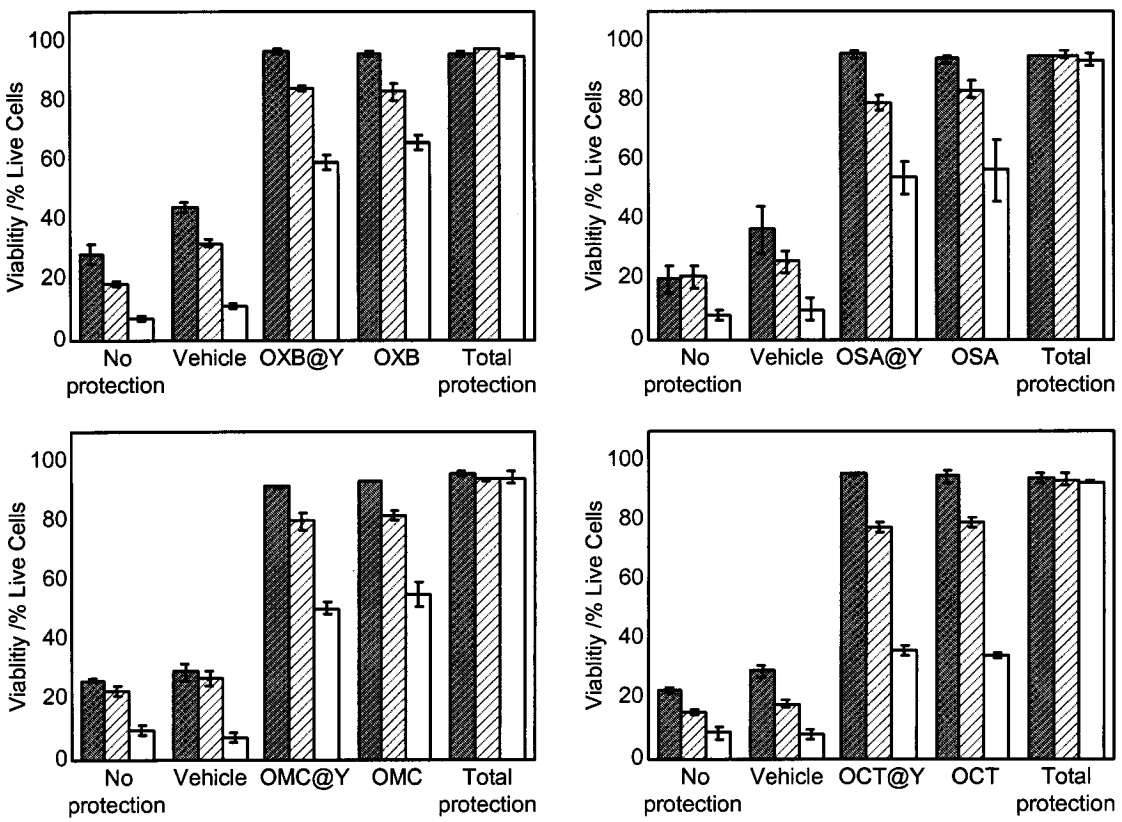

Figure 7.38 Cell viability for samples exposed to SSR for 10 min (grey), 15 min (striped), and 20 min (white) with or without protection as indicated. Data is given as the mean value ± standard error for three experiments.

7.6 Concluding Remarks

A new class of *supramolecular sunscreen* ingredients (OXB@Y, OSA@Y, OMC@Y, OCT@Y, and PABA@Y), based on currently approved sunscreen components, were prepared and fully characterized. These new sunscreen materials were observed to have similar or improved spectroscopic properties as compared to the parent compounds, with respect to their use as sunscreens. In each case, spectral broadening was observed for the encapsulated sunscreens, resulting in enhanced absorbance of supramolecular sunscreens in the UVA region of the spectrum. A growing appreciation of the deleterious effects of UVA exposure has made the development of UVA sunscreens a major industrial focus. The simple modification of existing sunscreen materials to provide improved performance in the UVA represents a significant advancement in itself. Laser flash photolysis studies in solution and the solid state revealed that the excited-state behaviour of zeolite-encapsulated sunscreens was consistent with their behaviour in solution. Similar transient behaviour suggests that the non-destructive deactivation pathways operative in solution will continue to be available when the molecule is encapsulated within the zeolite cavity.

The ultimate aims of this study were, to prepare encapsulated sunscreens in order to protect biological substrates from sunscreen-induced damage, and to prevent potentially detrimental sunscreen-sunscreen interactions. In initial studies of sunscreen photostability in aqueous or ACN solutions (Section 7.4) it was determined that the products under investigation were stable to UVA radiation when irradiated in dilute solution. We also found that, when irradiated in the presence of TiO_2, an increasingly popular inorganic sunscreen additive, all of the organic sunscreens underwent significant degradation (20-60%). This suggests that a commercial sunscreen product containing TiO_2 would rapidly lose its protective ability upon exposure to sunlight!

Commercial sunscreen products contain more than radiation filtering chemicals, rather, they are complex mixtures of preservatives, emulsifiers, humectants, etc. When the photostability of organic sunscreens was investigated in the presence of TiO_2 with the addition of a surfactant (a common non-active ingredient) the degradation was observed to increase dramatically. This surprising result implies that, not only is it important to control sunscreen-sunscreen interactions, but the participation of other photochemically "inactive" ingredients must also be considered. These observations highlight the advantage of segregating light absorbing molecules by encapsulation, prior to inclusion in a complex mixture, such as a commercial sunscreen formulation.

In the latter part of Section 7.4 it was shown that, when organic sunscreens were encapsulated in zeolite NaY and irradiated in the presence of TiO_2, the induced degradation was either significantly decreased or prevented altogether. The encapsulated sunscreens were also observed to retain their photostability demonstrating that zeolite inclusion does not negatively impact sunscreen stability and that encapsulation is capable of preventing the destructive interaction between sunscreen ingredients. The one exception was OMC, which was not completely recovered from the zeolite under any of the experimental conditions. No degradation products were recovered and it remains unclear whether the low recovery was due to zeolite-related degradation or associated with the recovery protocol. It is possible that molecular crowding within the zeolite favours the 2+2 cyclodimerization reaction that is observed for cinnamic acids in the solid state, however, no cyclobutane products were recovered.[41]

One of the major goals of this research was to prevent sunscreen-induced damage or deleterious effects in biological systems. The current dermatological literature is replete with reports of photoallergic responses to common sunscreen ingredients such as OXB and PABA. In an initial proof-of-concept experiment we examined the effects of free and encapsulated PABA on a model biological system, peroxidase enzyme HRP. PABA, once a popular UVB sunscreen, was voluntarily

removed from the market by manufacturers due the to high number of adverse reactions reported. PABA is now known to be an efficient sensitizer of singlet oxygen and other ROS.[45] HRP, the model biological substrate, has a known susceptibility to oxidative damage that is expressed as a loss of enzymatic activity.[24, 26] When HRP was irradiated in an aqueous solution of PABA, the enzymatic activity was largely destroyed. However, when irradiated in an aqueous suspension of PABA@Y, the enzymatic activity was reduced by only 20% as compared to the control. These results clearly indicate the potential of supramolecular sunscreens in preventing adverse biological responses.

We also investigated the impact of these new materials on human epidermal keratinocytes, a major cellular component of the human stratum corneum. The cellular viability and sunscreen-induced DNA damage were assessed for cell cultures exposed to irradiated and un-irradiated sunscreens, supramolecular sunscreens and empty zeolites. Two important pieces of information were derived from these experiments. First, each of the four organic sunscreens studied induced both cell death and DNA damage, despite the fact that they were observed to be photostable in solution. Secondly, in all cases, incubation of the cells with the supramolecular sunscreens did not cause increased cell mortality nor did it induce DNA damage. Undeniably, with respect to cellular toxicity, supramolecular sunscreens offer a significant improvement over the products currently employed.

In the final part of this research, it was demonstrated that encapsulated sunscreens are able to provide both a similar *in vitro* SPF and similar protection from irradiation as compared to the unencapsulated compounds currently in use.

7.7 Experimental

7.7.1 Zeolite Sample Preparation

All chemicals used for sample preparation were obtained from Aldrich in their highest available purity and used as received, unless otherwise indicated.

Supramolecular sunscreens, OXB@Y, OSA@Y, OMC@Y, OCT@Y, and PABA@Y, were each prepared according to the same general procedure. A sample of NaY (*ca.* 1 g) was thermally dehydrated by heating at 480°C overnight and then added to 15 mL of cyclohexane containing the sunscreen. All sunscreens were obtained from Aldrich with the exception of OMC, which was obtained from Spectrum Chemicals. OXB was recrystallized from ethanol prior to use. The zeolite/sunscreen slurry was stirred at room temperature for 5 h. The solid was then collected by filtration and washed with 3 x 5 mL of DCM. The zeolite powder was dried under air and the occupancy was determined by spectroscopic analysis of the filtrate. Zeolite samples with occupancies of <S> ~ 0.1 (0.06 mmol of sunscreen per 1 g of NaY) and <S> ~ 1.0 (0.6 mmol of sunscreen per 1 g of NaY) were prepared.

7.7.2 Spectroscopy

Steady-state absorption and DR spectra data were recorded on a Cary 1E spectrophotometer from Varian as described in Section 5.4.2. Samples were recorded under air unless otherwise indicated. Fluorescence measurements were recorded using a v.1.2 X spectrofluorimeter from Photon Technology International.

Time-resolved spectroscopic data were acquired using the LFP system for transient absorbance and diffuse-reflectance as described in detail in Section 2.2. All transient absorption spectra were recorded in deaerated or oxygenated, spectroscopic grade ACN (OmniSolv) as indicated. The spectra were recorded using a 7 x 7 mm^2 flow cell to avoid possible interference from photoproducts or long-lived transients. The zeolite samples were irradiated in 3 x 7 mm^2 quartz cells

(Friedrich & Dimmoch) under vacuum or air. Both solution and powder samples were excited with 308 nm pulses from a Lumonics EX-530 laser and the average power was *ca.* 90 mJ per pulse.

7.7.3 Photostability of Sunscreens in Solution

7.7.3.1 Sunscreen Irradiation

Photostability studies were carried out in 20 mL Pyrex tubes under magnetic stirring in a multi-lamp photoreactor equipped with LZC-UVA lamps delivering an average of 0.25 mJ cm^{-2}. Solutions were prepared by addition of 500 μL of a 1.0 x 10^{-2} M ACN solution of the sunscreen to 10 mL of ACN (OmniSolv), water (Millipore, MilliQ) or aqueous sodium dodecyl sulfate solution (Fluka) to give a final sunscreen concentration of *ca.* 5.0 x 10^{-4} M. The initial micelle concentration was 6.5 x 10^{-4} M based on a CMC of 8.2 x 10^{-3} M and an aggregation number of 66. 10 mg of TiO_2 (Alfa Aesar, 99.9% anatase, particle size ~ 32 nm) was then added to selected samples and the suspensions were stirred for 30 min prior to irradiation. After irradiation (20 h) the aqueous phase was extracted with 6 x 10 mL of diethyl ether. The resulting organic phase was dried with $MgSO_4$ and the solvent removed by evaporation. The residue was re-dissolved in a 5 mL ACN solution of the GC standard and analyzed by GC-FID (Fisons 8000 series equipped with a J&W DBS 30 m x 0.32 mm fused silica column) and GC-MS (Fisons 8000/8060 series equipped with the same column as above). The effect of micelle concentration on sunscreen degradation was determined by repeating the experimental protocol given above using micellar solutions with concentrations of 6.5 x 10^{-4} M, 3.9 x 10^{-4} M, and 1.9 x 10^{-4} M (micelle concentration determined as above).

7.7.3.2 Elemental Analysis of TiO_2

An aqueous solution of each sunscreen was prepared by addition of 2 mL of an ACN solution of the sunscreen (1.0 x 10^{-2} M) to 200 mL of ddH_2O in a Pyrex tube. 200 mg of TiO_2 were then added and the suspension was irradiated with stirring, in

a photoreactor equipped with LZC-UVA lamps. Irradiation was continued until GC-FID analysis indicated 80% conversion of the sunscreen. After irradiation, TiO_2 was collected by centrifugation, thoroughly dried, and evaluated by combustion elemental analysis (M-H-W Laboratories, Pheonix AZ). Elemental analysis revealed the presence of carbon on the oxide surface (50-80% of the mineralized amount), no carbon was detected on a reference sample of TiO_2 that was simply treated by stirring in ACN.

7.7.3.3 Pre-fluorescent Probe Studies

The solutions of SDS were prepared in ddH_2O having micelle concentrations of 6.5×10^{-4} M, 3.9×10^{-4} M, and 1.9×10^{-4} M. To 10 mL of each surfactant solution was added 500 μL of an ACN solution of 4-(3-hydroxy2-methylquinolineoxy)-2,2,6,6-tetramethyl piperidine-1-oxyl (QT) to give a final concentration of 5.0×10^{-4} M. QT was prepared by L. Maretti according to reported procedures.[60] TiO_2 was added to the solutions to give suspensions containing either 0.5 or 1.0 mg mL^{-1} and the resulting mixtures were stirred for 30 min and then irradiated (UVA) with stirring for various lengths of time. After irradiation, TiO_2 was removed by filtration and the filtrate was diluted 1:20 with the surfactant solution for measurement of the fluorescence evolution (λ_{ex} = 350 nm, λ_{em} = 405 nm).

7.7.3.4 Characterization of the QT-ACN Adduct

QT-ACN (3-hydroxy-2-methyl-quinoline-4-carboxylic acid 1-cyanomethoxy-2,2,6,6-tetramethyl-piperidin-4-yl ester) was characterized following isolation from a large-scale irradiation. A 6.5×10^{-4} M micellar solution was prepared and 2 mL of a solution of QT in ACN (1.0×10^{-2} M) was added to 200 mL of the surfactant solution in a Pyrex tube. TiO_2 (200 mg) was added and the suspension was irradiated (UVA) with stirring for 24 h. Following irradiation the aqueous suspension was extracted with 6 x 200 mL of ethyl acetate, dried, and separated by column chromatography (silica gel) using chloroform: methanol, 10:2 , as the eluant. 5 mg of the QT-ACN adduct was isolated and analyzed by ^1H and ^{13}C NMR: ^1H

NMR (500 MHz, $CDCl_3$) δ 12.0 (b, 1H, phenol), 8.50 (m, 1H), 8.0 (m, 1H), 7.51 (m, 2H), 5.40 (q, 1H), 4.5 (s, 2H), 2.69 (s, 3H), 2.1 (m, 2H), 1.81 (m, 2H), 1.35 (s, 6H), 1.28 (s, 6H); ^{13}C NMR (500 MHz, $CDCl_3$) δ 171 (CO), 155 (q, C-3), 153 (q, C-2), 142 (q, C-9), 128 (CH-8), 126(CH-5), 124.4(CH-6, CH-7), 124 (q, C-10), 116 (q, CN), 69 (CH-4'), 63 (CH_2CN), 60 (q, C-2', C-6'), 44 (CH_2-3', CH_2-5'), 33 (CH_3), 20 (CH_3).

7.7.4 Photostability of Supramolecular Sunscreens

To determine the photostability of supramolecular sunscreens in the presence and absence of TiO_2, zeolite samples were prepared such that 25 mg of the zeolite complex contained the same amount of sunscreen as used in the solution studies described in Section 7.3.3.1. Typically, this corresponded to a loading of *ca.* 0.2 to 0.3. Samples were irradiated in 20 mL Pyrex tubes with magnetic stirring, in a multi-lamp photoreactor equipped with LZC-UVA lamps delivering an average of 0.25 mJ cm^{-2}. Each sample contained 2.5 mg mL^{-1} of the sunscreen@Y complex and selected samples contained 1.0 mg mL^{-1} TiO_2 in ddH_2O. Samples were prepared in triplicate and the suspensions were irradiated with stirring for 20 h. Control samples were covered with foil and placed in the photoreactor for 20 h. After irradiation, 3.4 mL of concentrated H_2SO_4 (18 M) was added to each sample giving a final molarity of ~ 4.5 M; the acidic mixture was stirred vigorously for 15 min. After this time the mixture had become translucent and the solution was extracted with 6 x 10 mL diethyl ether. The ether was removed by rotary evaporation and the residue dried under vacuum (*ca.* 50 mTorr). The residue was then re-dissolved in ACN containing anthracene as the internal standard; this solution was analyzed by GC-FID as described above to determine the amount of sunscreen recovered.

7.7.5 Biological Impact Studies

7.7.5.1 PABA Case Study

Solutions were prepared in ddH_2O containing 0.1 mg mL^{-1} horseradish peroxidase (Type V1-A, Sigma) and either 7.3 x 10^{-5} M PABA or 0.1 mg mL^{-1}

PABA@Y (<S> ~ 1.0). Solutions were prepared in triplicate and irradiated with stirring in a multi-lamp photoreactor equipped with LZC-UVB lamps, the temperature was maintained at 28°C. Control samples were covered with foil and placed in the photoreactor for 2 h. After 2 h, an aliquot of each sample was diluted in acetate buffer (pH 4.4). For the assay, an aliquot of the diluted enzyme solution was added to a freshly prepared, buffered solution containing 250 μM hydrogen peroxide and 25 μM ABTS co-factor (Sigma). The final enzyme concentration was *ca.* 10 ng mL^{-1}. The increase in absorbance for the ABTS radical cation was monitored at 412 nm using a Cary 1E spectrophotometer operating in Kinetics mode. Data were manipulated using Kaleidagraph software and the initial slope was extracted as described in Section 3.2.4.

7.7.5.2 Cell Culture and Cell Viability

Human epidermal keratinocytes (HEK), from Cascade Biologics, were cultured in EpiLife medium with calcium (Cascade Biologics) supplemented with a human keratinocyte growth supplement kit (Cascade Biologics) and were maintained at 37°C in a humidified, 5% CO_2 atmosphere. Typically, 60 mm Petri dishes were seeded with keratinocytes at a density of *ca.* 1.5 x 10^5 cells/Petri and covered with culture media. The media was replaced 24 and 72 h after seeding. After 5 days, cells had typically reached 80% confluence (80% coverage of the Petri dish surface) and were then used for experiments. Cell culture and maintenance were accomplished with the technical help of M. Cybulski of Health Canada (Radiation Protection Bureau). All buffers and aqueous solutions used in these experiments were prepared with distilled, deionized water (Millipore, MilliQ) and treated with a chelating resin.

After the prescribed experimental protocol, cell viability was determined according to the following procedure. The existing culture media was removed and the cells were washed with 1 mL of a phosphate buffer solution (PBS). Cells were detached from the culture dishes by incubation with an aqueous solution of

trypisin/EDTA for 8 min (0.25% trypsin, 0.1% EDTA, Life Technologies). EDTA is ethylenediaminetetraacetic acid. The solution was neutralized by the addition of 1.5 mL of the culture media and a portion of the cells were stained by addition of a solution of ethidium bromide (200 μg mL^{-1}, Molecular Probes) and fluorescein diacetate (5 mg mL^{-1}, Sigma) in Hank's Balanced Salt Solution (HBBS, Sigma). A measured volume of the cell solution was placed on a hemocytometer and the cell number and viability were assessed by fluorescence microscopy (Olympus BX-60F fluorescence microscope with narrow band "B" excitation filter cube from Olympus). Under these fluorometric assay conditions, dead cells fluoresce red and live cells fluoresce green.[66]

7.7.5.3 Alkaline Comet Assay

DNA damage was assessed by alkaline comet assay. After determining cell viability and concentration, 1.5 x 10^5 cells were mixed with 2 mL of liquefied, low-melting-point agarose (Fisher Scientific) in PBS. The solution was quickly dispensed onto a 6.5 x 10 cm^2 rectangle of GelBond® (BMA Bioproducts); a flexible support consisting of an agarose-coated, polyester sheet. After 2 min the agarose had solidified and was transferred to a large Petri dish. The gel was covered with 20 mL of cold lysis buffer (2.5 M NaCl, 100 mM EDTA, 10 mM *tris*(hydroxymethyl)aminomethane, 1% sodium lauryl sarcosinate, 1% Triton-X, 10% dimethylsulfoxide; Sigma) and refrigerated at 4°C for 4 h. After this time the lysis buffer was replaced with the unwinding/electrophoresis buffer (300 mM NaOH, 1 mM EDTA, pH 13) and incubated in this buffer for 40 min at 4°C. The gels were then electrophoresed in 24 mL of fresh unwinding buffer for 20 min at 24 V.

After electrophoresis, the gel was neutralized for 15 min in a pH 7.5, Tris buffer (0.4 M *tris*(hydroxymethyl)aminomethane). The gels were washed twice with ddH_2O and immersed in 100% ethanol overnight. The next day the gels were dried in air for 1 h and stained with a nucleic acid stain, propidium iodide (25 μg mL^{-1}, Molecular Probes). Comets were assessed (100 per sample) using the

Alkomet v3.0 image analysis system from Richard Branker Research Ltd. coupled with an Olympus microscope (BX-60) using a G band filter cube from Olympus.

7.7.5.4 Effect of Supramolecular Sunscreens on HEK Cells

To assess the effect of sunscreens on HEK cells, the cultures were grown to 80% confluence and then incubated, under the usual conditions, for 24 h with culture media containing free sunscreen, encapsulated sunscreen, or empty zeolite. In each case the media suspension was added either directly after preparation or following a 10 min exposure to SSR (dose ~ 1 mJ cm^{-2}). The control samples were incubated with irradiated and un-irradiated culture media. Encapsulated sunscreens with an occupancy of <S> ~ 1.0 were used in this experiment and in each case 1.5 mg of the supramolecular sunscreen was suspended in 5 mL of culture media. The free sunscreens were also suspended in 5 mL of culture media in the following amounts; 0.20 mg (0.88 μmol) OXB, 0.22 mg (0.87 μmol) OSA, 0.26 mg (0.89 μmol) OMC, and 0.32 mg (0.88 μmol) OCT. Following incubation with the modified culture media, the cell viability was evaluated by fluorescein diacetate/ethidium bromide assay and the integrity of the DNA was determined by alkaline comet assay.

7.7.5.5 Protective Capability of Supramolecular Sunscreens

For this experiment HEK cells were grown to 80% confluence and, prior to irradiation, the culture media was removed and replaced by PBS. Each sunscreen was suspended in benzene (0.12 mmol sunscreen in 300 μL benzene) and sandwiched between two 10 cm^2, 1 mm-thick quartz plates. In the case of supramolecular sunscreens, 200 mg (<S> ~ 1.0) were suspended in 300 μL of benzene and a similar sandwich was prepared. The protection provided to the HEK cells by the various sunscreens was evaluated by irradiation of the cells through the quartz plate sandwich. Control samples were either not irradiated or irradiated though a quartz plate sandwich containing only benzene. Cells were exposed to SSR through the quartz plates for 10 min. After irradiation, PBS was

removed and replaced with fresh culture media. The cells were then incubated at 37ºC for 24 h, in a humidified, 5% CO_2 atmosphere. Cell viability was evaluated by fluorescein diacetate/ethidium bromide assay and the integrity of the DNA was determined by alkaline comet essay.

7.8 References

1. The sun, *www.learn.londonmet.ac.uk/packages/clear/visual/daylight/sun/htm*.

2. F. Gasparro *Sunscreen Photobiology: Molecular, Cellular, and Physiological Aspects;* Springer Verlag: Berlin, 1997.

3. F. P. Gasparro, M. Mitchnick and J. F. Nash, A review of sunscreen safety and efficacy, *Photochem. Photobiol.*, **1998**, *68*, 243-256.

4. K. C. Smith *The Science of Photobiology;* Plenum Press: New York, 1989.

5. J. L. Bezzant, Penetration of human skin by ultraviolet light, *www.medlib.med.utah.edu/kw/derm/pages/meet_2.htm*.

6. H. Adhoute, J. de Rigal, J. P. Marchand, Y. Privat and J. L. Lévêque, Influence of age and sun exposure on the biophysical properties of the human skin: An *in vivo* study, *Photodermatol. Photoimmunol. Photomed.*, **1992**, *9*, 99-103.

7. L. L. Hruza and A. P. Pentland, Mechanisms of UV-induced inflammation, *J. Invest. Dermatol.*, **1993**, *100*, 35S-41S.

8. B. A. Gilchrist, H.-Y. Park, M. S. Eller and M. Yaar, Mechanisms of ultraviolet light-induced pigmentation, *Photochem. Photobiol.*, **1996**, *63*, 1-10.

9. R. P. Gallagher, G. B. Hill, C. D. Bajdik, A. J. Coldman, S. Fincham, D. I. McLean and W. J. Threlfall, Sunlight exposure, pigmentary factors, and risk of nonmelanocytic skin cancer. I. Basal cell carcinoma, *Arch. Dermatol.*, **1995**, *131*, 157-163.

10. R. P. Gallagher, G. B. Hill, C. D. Bajdik, A. J. Coldman, S. Fincham, D. I. McLean and W. J. Threlfall, Sunlight exposure, pigmentary factors, and risk of nonmelanocytic skin cancer. II. Squamous cell carcinoma, *Arch. Dermatol.*, **1995**, *131*, 164-169.

11. F. R. de Gruijl and P. D. Forbes, UV-induced skin cancer in a hairless mouse model, *Bioessays*, **1995**, *17*, 651-660.

12. E. C. De Fabo, F. P. Noonan, T. R. Fears and G. Merlino, Ultraviolet B but not ultraviolet A radiation initiates melanoma, *Cancer Res.*, **2005**, *64*, 6372-6376.

13. T. R. Fears, C. C. Bird, D. Guerrry, R. W. Sagebiel, M. H. Gail, D. E. Elder, A. Halpern, E. A. Holly, P. Hartge and M. A. Tucker, Average midrange ultraviolet radiation flux and time outdoors predict melanoma risk, *Cancer Res.*, **2002**, *62*, 3992-3996.

14. *Cancer Facts and Figures;* American Cancer Society: Atlanta, 2005.

15. *Canadian Cancer Statistics;* Canadian Cancer Society/National Cancer Institute of Canada: Toronto, 2005.

16. US Food and Drug Administration (Department of Health and Human Services), Sunscreen drug products for over-the-counter human use; final monograph, *Federal Register*, **1999**, *64*, 27666-27693.

17. Formulators fine tune TiO_2-based sunscreens, *Manuf. Chem.*, **1993**, *64*, 26-29.

18. A. Fujishima, T. N. Rao and A. Tryk, Titanium dioxide photocatalysis, *J. Photochem. Photobiol. C*, **2000**, *1*, 1-21.

19. D. E. Ollis and H. Al-Ekabi *Photocatalytic Purification and Treatment of Water and Air;* Elsevier: Amsterdam, 1993.

20. H. Hidaka, S. Horikoshi, N. Serpone and J. Knowland, *In vitro* photochemical damage to DNA, RNA, and their bases by an inorganic sunscreen agent on exposure to UVA and UVB radiation, *J. Photochem. Photobiol. A*, **1997**, *111*, 205-213.

21. M. R. Dhananjeyan, R. Annapoorani and P. Renganathan, A comparative study on the TiO_2 mediated photo-oxidation of uracil, thymine, and 6-methyluracil, *J. Photochem. Photobiol. A*, **1997**, *109*, 147-153.

22. R. Dunford, A. Salinaro, L. Cai, N. Serpone, S. Horikoshi, H. Hidaka and J. Knowland, Chemical oxidation and DNA damage catalysed by inorganic sunscreen ingredients, *FEBS Lett.*, **1997**, *418*, 87-90.

23. H. Hidaka, S. Horikoshi, K. Ajisaka, J. Zhao and N. Serpone, Fate of amino acids upon exposure to aqueous titania irradiated with UVA and UVB irradiation: Photocatalyzed formation of NH_3, NO_3^-, and CO_2, *J. Photochem. Photobiol. A*, **1997**, *108*, 197-205.

24. T. Hancock-Chen and J. C. Scaiano, Enzyme inactivation by TiO_2 photosensitization, *J. Photochem. Photobiol. B*, **2000**, *57*, 193-196.

25. R. R. Cai, Y. Kubota, T. T. Shuin, H. Sakai, K. Hashimoto and A. Fusjishima, Induction of cytotoxicity by photoexctited TiO_2 particles, *Cancer Res.*, **1992**, *52*, 2346-2348.

26. T. Hancock-Chen *Biologically relevant free radical reactions;* PhD thesis, University of Ottawa: Ottawa, 2001.

27. H. Maier, G. Schauberger, K. Brunnhofer and H. Hönigsmann, Change of ultraviolet absorbance of sunscreens by exposure to solar-simulated radiation, *J. Invest. Dermatol.*, **2001**, *117*, 256-262.

28. L. E. Agrapidis-Paloympis, R. A. Nash and N. A. Shaath, The effect of solvents on the ultraviolet absorbance of sunscreens, *J. Soc. Cosmet. Chem.*, **1987**, *38*, 209-221.

29. C. Szczurko, A. Dompmartin, M. Michel, A. Moreau and D. Leroy, Photocontact allergy to oxybenzone: Ten years of experience, *Photodermatol. Photoimmunol. Photomed.*, **1994**, *10*, 144-147.

30. M. Landers, S. Law and F. J. Storrs, Contact urticaria, allergic contact dermatitis, and photoallergic contact dermatitis from oxybenzone, *Am. J. Contact Derm.*, **2003**, *14*, 33-34.

31. P. Collins and J. Ferguson, Photoallergic contact dermatitis to oxybenzone, *Br. J. Dermatol.*, **1994**, *131*, 124-129.

32. S. Schauder and H. Ippen, Contact and photocontact sensitivity to sunscreens. Review of a 15 year experience and of the literature, *Contact Dermat.*, **1997**, *37*, 221-232.

33. N. Matheny Roscher, M. K. O. Lindemann, S. B. Kong, C. G. Cho and P. Jiang, Photodecomposition of several compounds commonly used as sunscreen agents, *J. Photochem. Photobiol. A*, **1994**, *80*, 417-421.

34. J. M. Allen, S. K. Allen and B. Lingg, Photostabilities of several chemical compounds used as active ingredients in sunscreens, *Special Publications, Royal Soc. Chem.*, **1998**, *225*, 171-181.

35. N. Serpone, A. Salinaro, A. V. Emeline, S. Horikoshi, H. Hidaka and J. Zhao, An *in vitro* systematic spectroscopic examination of the photostabilities of a random set of commercial sunscreen lotions and their *chemical* UVB/UVA active agents, *Photochem. Photobiol. Sci.*, **2002**, *1*, 970-981.

36. J. M. Allen and C. J. Gosset, Photochemical formation of singlet molecular oxygen in illuminated aqueous solutions of several commercially available sunscreen active ingredients, *Chem. Res. Toxicol.*, **1996**, *9*, 605-609.

37. N. A. Shaath, H. M. Fares and K. Klein, Photodegradation of sunscreen chemicals: Solvent considerations, *Cosm. Toil.*, **1990**, *105*, 41-44.

38. C. Sundaram, W. Köster and K. U. Schallreuter, The effect of UV radiation and sun blockers on free radical defense in human and guinea pig epidermis, *Arch. Dermatol. Res.*, **1990**, *282*, 526-531.

39. K. U. Schallreuter, J. M. Wood, D. W. Farwell, J. Moore and H. G. M. Edwards, Oxybenzone oxidation following solar irradiation of skin: Photoprotection versus antioxidant inactivation, *J. Invest. Dermatol.*, **1996**, *106*, 583-586.

40. S. Pattanaargson and P. Limphong, Stability of octyl methoxycinnamate and identification of its photo-degradation product, *Int. J. Cosmet. Sci.*, **2001**, *23*, 153-160.

41. V. Enkelmann, G. Wegner, K. Novak and K. B. Wagner, Single-crystal-to-single-crystal photodimerization of cinnamic acid, *J. Am. Chem. Soc.*, **1993**, *115*, 10390-10391.

42. K. Kimura and T. Katoh, Photoallergic contact dermatitis from the sunscreen ethylhexyl-*p*-methoxycinnamate (Parsol MCX), *Contact Dermat.*, **1995**, *32*, 304-305.

43. C. F. Chignell, B. Kalyanaraman, R. P. Mason and R. H. Sik, Spectroscopic studies of cutaneous photosensitizing agents. I. Spin trapping of photolysis products from sulfanilamide, 4-aminobenzoic acid, and related compounds, *Photochem. Photobiol.*, **1980**, *32*, 565-571.

44. A. A. Shaw, L. A. Wainschel and M. D. Shetlar, The photochemistry of *p*-aminobenzoic acid, *Photochem. Photobiol.*, **1992**, *55*, 647-656.

45. J. M. Allen, C. J. Gosset and S. K. Allen, Photochemical formation of singlet molecular oxygen ($^1O_2$) in illuminated aqueous solutions of *p*-aminobenzoic acid (PABA), *J. Photochem. Photobiol. B*, **1996**, *32*, 33-37.

46. A. Beckett and G. Porter, Primary photochemical processes in aromatic molecules. Part 10. Photochemistry of substituted benzophenones, *Trans. Faraday Soc.*, **1963**, *59*, 2051-2057.

47. J. C. Scaiano, Solution photochemistry of *o*-hydroxybenzophenone at low temperatures, *Chem. Phys. Lett.*, **1982**, *92*, 97-99.

48. S. M. Ormson and R. G. Brown, Excited-state intramolecular proton-transer. 1. ESIPT to nitrogen, *Prog. React. Kinet.*, **1994**, *19*, 45-91.

49. D. Legourrierec, S. M. Ormson and R. G. Brown, Excited-state intramolecular proton-transfer. 2. ESIPT to oxygen, *Prog. React. Kinet.*, **1994**, *19*, 211-275.

50. S. Baral-Tosh, S. K. Chattopadhyay and P. K. Das, A laser flash photolysis study of paraquat reduction by photogenerated aromatic ketyl radicals and carbonyl triplets, *J. Phys. Chem.*, **1984**, *88*, 1404-1408.

51. M. Lukeman and P. Wan, Photochemistry of hydroxyarenes In *CRC Handbook of Organic Photochemistry and Photobiology*; W. Horspool and F. Lenci, Eds.; CRC Press: Boca Raton, 2004.

52. K. K. Iu, X. Liu and J. K. Thomas, Spectroscopic studies of electron trapping by sodium cationic clusters in zeolites, *J. Phys. Chem.*, **1993**, *97*, 8165-8170.

53. T. J. Curley, K. P. Ghiggino, R. Sakurovs and G. J. Smith, The quenching of *m*-methoxycinnamic acid fluorescence, *J. Photochem. Photobiol. A*, **1988**, *45*, 289-294.

54. G. J. Smith and I. J. Miller, The effect of molecular environment on the photochemistry of *p*-methoxycinnamic acid and its esters, *J. Photochem. Photobiol. A*, **1998**, *118*, 93-97.

55. P. Morlière, O. Avice, T. Sa E Melo, L. Dubertret, M. Giraud and R. Santus, A study of the photochemical properties of some cinnamate sunscreens by steady state and laser flash photolysis, *Photochem. Photobiol.*, **1982**, *36*, 395-399.

56. K. Klein, A review of current sunscreen formulation techniques and technologies, *Cosmet. Toil.*, **2000**, *115*, 53-58.

57. F. Kiriakidou, D. I. Kondarides and X. E. Verykios, The effect of operational parameters and TiO_2-doping on the photocatalytic degradation of azo-dyes, *Catal. Today*, **1999**, *54*, 119-130.

58. S. C. Ameta, P. B. Punjabi, P. Rao and B. Singhal, Use of titanium dioxide as a photocatalyst for photodegradation of sodium lauryl sulfate, *J. Ind. Chem. Soc.*, **2000**, *77*, 157-160.

59. J. Lea and A. A. Adesina, The photo-oxidative degradation of sodium dodecyl sulphate in aerated aqueous TiO_2 suspension, *J. Photochem. Photobiol. A*, **1998**, *118*, 111-122.

60. O. G. Ballesteros, L. Maretti, R. Sastre and J. C. Scaiano, Kinetics of cap separation in nitroxide-regulated "living" free radical polymerization: Application of a novel methodology involving a prefluorescent nitroxide switch, *Macromolecules*, **2001**, *36*, 6184-6187.

61. M. G. Ivan and J. C. Scaiano, A new approach for the detection of carbon-centered radicals in enzymatic processes using prefluorescent probes, *Photochem. Photobiol.*, **2003**, *78*, 416-419.

62. L. J. Johnston, M. Tencer and J. C. Scaiano, Evidence for hydrogen transfer in the photochemistry of 2,2,6,6-tetramethylpiperidine-*N*-oxyl, *J. Org. Chem*, **1986**, *51*, 2806-2808.

63. A. A. Shaw, L. A. Wainschel and M. D. Shetlar, Photoaddition of *p*-aminobenzoic acid to thymine and thymidine, *Photochem. Photobiol.*, **1992**, *55*, 657-663.

64. D. Klint, P. Arvidsson, Z. Blum and H. Eriksson, Purification of proteins by the use of hydrophobic zeolite Y, *Protein Expres. Purif.*, **1994**, *5*, 569-576.

65. D. Klint and H. Eriksson, Conditions for the adsorption of proteins on ultrastable zeolite Y and its use in protein purification, *Protein Expres. Purif.*, **1997**, *10*, 247-255.

66. G. H. Strauss, Non-random cell killing in cryopreservation: Implications for performance of the battery of leukicyte tests (BLT), toxic, and immunotoxic effects, *Mutat. Res.*, **1991**, *252*, 1-15.

67. O. Ostling and K. J. Johanson, Microelectrophoretic study of radiation-induced DNA damages in individual mammalian cells, *Biochem. Biophys. Res. Commun.*, **1984**, *123*, 291-298.

68. N. P. Singh, M. T. McCoy, R. R. Tice and L. E. Schneider, A simple technique for quantitation of low levels of DNA damage in individual cells, *Exp. Cell. Res.*, **1988**, *175*, 184-191.

69. P. Reinhardt, M. Cybulski, J. P. McNamee, J. R. McLean, W. Gorman and Y. Deslauriers, Protection from solar simulated radiation-induced DNA damage in cultured human fibroblasts by three commercially available sunscreens, *Can. J. Physiol. Pharmacol.*, **2003**, *81*, 690-695.

70. P. L. Olive, J. P. Banáth and P. E. Durand, Detection of etoposide resistance by measuring DNA damage in individual Chinese hamseter cells, *J. Natl. Cancer. Inst.*, **1990**, *82*, 779-783.

71. *SPF Analysis of Sunscreens using the Labsphere UV-1000S Ultraviolet Transmittance Analyzer;* Labsphere Inc. (Technical Note): North Sutton, 1998.

8. Final Comments and Future Directions

8. Final Comments and Future Directions 327

8.1 Final Comments 328
8.2 Future Directions 331
8.3 Claims to Original Research 333
8.3.1 Work Presented in this Thesis 333
8.3.2 Work not Presented in this Thesis 335
8.4 Publications 337
8.4.1 Publications Resulting from Research Presented in this Thesis 337
8.4.2 Other Publications 338

8.1 Final Comments

The work presented in this thesis has explored the photochemical and photophysical properties of new materials, prepared by the encapsulation of organic or organometallic species within the cavities of aluminosilicate zeolites. Each chapter has examined a different facet of intrazeolite photochemistry with the aim of developing a more profound understanding of the influence of zeolite media on the behaviour of encapsulated guests.

The zeolite-based photocatalytic materials reported in this thesis were designed by taking advantage of the photocatalytic properties of a popular semiconducting oxide, TiO_2. Ultraviolet irradiation of TiO_2 results in the generation of reactive oxygen species, ultimately causing the photodegradation of various biological and organic materials. In order to prepare a catalyst that is able to further harness the sun's energy, the zeolite matrix was used to combine TiO_2 with highly-coloured dye molecules. The aim was to produce the same reactive species via a visible light-induced, electron transfer interaction. The electron transfer nature of the interaction in these multi-component systems was determined by steady-state and time-resolved spectroscopy. The catalytic behaviour was examined with respect to photodegradation of a model biological substrate and the material containing an electron-accepting dye was found to be more active than TiO_2 anatase, a popular commercial photocatalyst. The development of water-purification catalysts that can be used in combination with solar radiation is an important direction in the pursuit of an economically viable solution for wastewater remediation.

Zeolites have also been employed in a more traditional sense for the stabilization of reactive intermediates. In the case of HZSM-5, the tight fit of the dibenzotropylium cation within the cylindrical cavity caused this species to become indefinitely persistent. The spatial constriction, along with the extended lifetime, allowed the observation of excited state and electron transfer behaviour. In a

second example, the carbanion generated following intrazeolite decarboxylation of ketoprofenate, was also significantly stabilized within the zeolite cavity in comparison to its fleeting lifetime in solution. The persistence of the carbanion is likely related to the anhydrous environment provided by the zeolite interior, although contributions from stabilizing interactions with charge-balancing cations may also be significant. This represents the first example, to the best of our knowledge, of a carbanionic species stabilized by zeolite encapsulation. The observed lifetime enhancement opens the door to what is essentially Grignard-type chemistry, initiated photochemically.

Ship-in-a-bottle synthesis has been extensively employed in this work for the preparation of materials where the guest species is permanently entrapped within the zeolite framework. The preparation of DT@Y is especially significant since it represents the first example of a base-catalyzed, intrazeolite synthesis. The entrapped pre-fluorescent probe was shown to be a useful material for the detection of free radical species. It is hoped that this material may prove useful for elucidating the participation of radical species in intrazeolite and zeolite-catalyzed reactions.

Intrazeolite synthesis was also used to prepare F@Y. In combination with confocal and fluorescence microscopy, the interaction between fluorescent-labeled zeolite particles and human fibroblasts was examined. These results provided an early indication that zeolite particles would be non-toxic to human skin cells and encouraged the exploration of zeolites as host materials for a series of supramolecular sunscreens.

Finally, a new class of supramolecular sunscreen ingredients were developed and characterized. In the course of this work several important facets of sunscreen photochemistry were brought to light. For example, it was determined that the presence of TiO_2 in a sunscreen formulation is very likely to cause the degradation of other, organic, components. Interestingly, non-active formulation ingredients, such as surfactants, were also observed to play an active role in sunscreen

degradation. Also surprisingly, in light of their solution photostability, several popular sunscreens were observed to induce cell mortality and DNA damage in human epidermal keratinocytes. Encapsulation of these sunscreens in zeolite NaY prevented both the TiO_2-induced degradation as well as the deleterious effects with respect to human skin cells. Although the photobiological data is preliminary, the results thus far suggest that zeolite-encapsulation is a promising solution to the increasing problem of sunscreen photoallergy and phototoxicity.

8.2 Future Directions

1. In the context of zeolite-based photocatalysts, further exploration into the photocatalytic efficiency of these materials is warranted. Their performance under the conditions of actual solar irradiation and their fatigue resistance should be examined. Since the material incorporating TiO_2 and an electron-acceptor was by far the most active, it may be interesting to investigate the combination with other electron-acceptors having more favourable redox potentials, for example 2,4,6-triphenylthiapyrylium.
2. Ultrafast LFP studies of ketoprofen would be invaluable in unraveling the solvent dependence of the decarboxylation reaction. In addition, time-resolved studies on the femtosecond time scale would provide further evidence for the assignment of the process as singlet-mediated.
3. In the context of haloalkyl ketoprofen analogues mentioned in the introduction to Chapter 5, encapsulation of these species in zeolites and subsequent examination of their time-resolved behaviour would help to reveal the role of steric hindrance in intramolecular alkylation reactions.
4. Further optimization of the conditions for intrazeolite, intermolecular addition reactions employing the ketoprofen-derived carbanion should improve product yields resulting in a process with synthetic utility. The first step should be exploration of hydrophobic zeolite frameworks, such as USY, and manipulation of materials in a glove box. In light of the proposed interaction with charge-balancing cations, it may also be interesting to determine the stereochemistry of the intrazeolite reaction products and to investigate the behaviour of (R)- versus (S)-ketoprofen within the zeolite cavity.
5. Intrazeolite pre-fluorescent probe DT@Y was proven to be capable of detecting radical species generated both within, and external to, the

zeolite particle. An obvious application of this material is to investigate the participation of radical species in zeolite catalyzed reactions. Since the zeolite-bound probe is a discrete particle, it may also be used in combination with fluorescence microscopy to observe the migration time of radicals through polymers and other condensed media.

6. The facile preparation of zeolite-encapsulated fluorescein suggests that other xanthene-based dyes may also be easily prepared to give a series of biologically inert, labeled nano- or microparticles having absorption and emission wavelengths across the spectrum. Preliminary studies have shown that it is possible to prepare rhodamine@Y.
7. In the context of supramolecular sunscreens, further photobiological and toxicity studies are necessary to determine the suitability of these materials. Firstly, experiments using excised skin or skin-substitutes should be conducted and this should be followed up with animal studies. In terms of the materials themselves, host particles of a cosmetically acceptable size must be identified and tested. Long-term fatigue and leaching studies will also be required. Eventually the development of new organic filters, designed specifically for zeolite inclusion, may be pursued.

8.3 Claims to Original Research

8.3.1 Work Presented in this Thesis

1. Zeolite-based photocatalysts combining TiO_2 and a sensitizer were prepared and characterized. The interaction between the dye and the semiconductor was determined to be an electron transfer. These materials proved to be efficient photodegradation catalysts. The multi-component catalytic materials are brightly coloured, offering the advantage of photocatalysis under the conditions of solar irradiation.
2. Carbenium ion, dibenzotropylium, was rendered indefinitely stable by encapsulation in HZSM-5, allowing the clear observation of the cation triplet excited-state for the first time. Electron transfer between the cation excited-state and amines was also observed since the tight fit of the cation within the cavity precludes nucleophilic addition at the benzylic cation site.
3. The photophysical behaviour of 3-methylbenzophenone in various solvents was investigated at very short times using ultrafast LFP. The lifetime of the singlet excited-state was observed to decrease with increasing solvent polarity. Since the fluorescence increase in more polar solvents was very modest, the shorter singlet lifetime was attributed to a higher rate constant for intersystem crossing due to an "inverse gap effect". These results suggest that observation of the triplet excited-state of ketoprofen in ACN, but not in water, is unrelated to a difference in the rate constants for intersystem crossing in these solvents
4. The carboxylate anion of ketoprofen was included in zeolite NaY and observed to undergo a rapid photodecarboxylation reaction to generate an extremely long-lived carbanion. In the zeolite, the carbanion lifetime was more than fifty times longer than in aqueous solution. Although the carbanion is very sensitive to the presence of water, under appropriate

conditions, nucleophilic substitution reactions can be observed. Isolation of addition products furthers emphasizes the carbanionic nature of the intermediate arising from ketoprofen photodecarboxylation.

5. A pre-fluorescent probe, based on TEMPO and the dansylamide fluorophore, was prepared within the cavities of NaY by base-catalyzed, ship-in-a-bottle synthesis. The immobilized probe was successfully used to detect radicals generated both within, and external to, the zeolite particle. This is the first example of a base-catalyzed ship-in-a-bottle synthesis.
6. A popular biological fluorescent probe, fluorescein, was synthesized within the cavities of zeolite Y by ship-in-a-bottle synthesis. The fluorescent material was characterized and observed to have a much greater resistance to photobleaching than the species in solution and a shorter fluorescence lifetime. Using the fluorescent-labeled zeolite particles it was observed that, at this particle size, zeolites do not penetrate human fibroblast cells. Fluorescence microscopy also revealed an attractive interaction between the cells and the particles, resulting in accumulation of the zeolite at the cell membrane.
7. A new class of supramolecular sunscreen ingredients were prepared and characterized spectroscopically. The photochemistry and photophysics of the encapsulated sunscreens were found to be very similar to the sunscreens in solution. Encapsulation was shown to protect organic sunscreen components from radiation-induced degradation in sunscreen "cocktails". Supramolecular sunscreens were also demonstrated to have little or no impact on cell mortality and DNA integrity, in sharp contrast to the un-encapsulated sunscreen ingredients. The protective capability of supramolecular materials was comparable to the un-encapsulated sunscreens.

8.3.2 Work not Presented in this Thesis

1. A [2]-catanane molecular switch, consisting of a bipyridinium cyclophane and a dioxybenzene macrocyclic polyether, was prepared by ship-in-a-bottle-synthesis within the supercages of zeolite Y. This represents the first zeolite-encapsulated molecular switch. DR-LFP revealed that the lifetime of the charge-separated state is six orders of magnitude longer than the same complex in solution. A longer lifetime for the charge-separated species implies a reduction in energy-wasting BeT and greater efficiency for the molecular machine. (with B. Ferrer)
2. The photocyclization of anilides of α,β-unsaturated carboxylic acids was examined in solution and the mechanism for chiral induction was found to be an asymmetric protonation of the enolate intermediate. This mechanism is different from the sigmatropic H-migration proposed for the solid-state reaction. The zwitterionic precursor to the enolate intermediate was detected for the first time by LFP. Product studies revealed a modest **ee** (~40%) for photocyclization of the *p*-toluidides in the presence of chiral inductors. (with P. Formentin)
3. Complexes of ZSM-5-type zeolites and prototypical molecular wires were prepared and characterized spectroscopically. In the case of 1,4-*bis*(phenyethynyl)benzenes, zeolite-inclusion did not restrict rotation of the ring system and the spectroscopic properties were not affected. However, complexation of 1,4-*bis*(phenylethynyl)anthracene with ZSM-5, allowed the first spectroscopic observation of discrete rotamers, despite the low barrier for rotation about the ethynyl bonds. Assignment of the wavelength dependent behaviour as due to discrete conformers has been supported by DFT calculations (C. Carra). The triplet excited-states of these materials in zeolite and in solution were also characterized by LFP.
4. The selective quenching of pyrene excimer and monomer emission, by electron-rich and electron-poor compounds has been exploited in this

group in the context of fluorescence-based explosives-detection (K.-S. Focsaneanu). Samples of zeolite-encapsulated pyrene, where the monomer-excimer equilibrium is effectively frozen, were prepared and examined with respect to their ability to selectively detect explosives analogues. Using steady-state and time-resolved fluorescence spectroscopy, pyrene@Y was used to distinguish between electron-rich and -poor compounds with excellent selectivity. The results suggest that pyrene@Y may be developed as a cheap and disposable sensor material.

5. The photoinduced redox chemistry of 2-(hydroxymethyl)anthraquinone was exploited to prepare a material for the sensitive detection of oxygen. A highly-coloured, dihydroxy intermediate was generated by irradiation of the encapsulated anthraquinone in the absence of oxygen. When the bright yellow material is exposed to oxygen, the dihydroxy anthracene is rapidly oxidized to the quinone and the powder becomes white. In summary, a cheap, easy-to-prepare oxygen sensing material was developed. The intermediate species involved in this intrazeolite redox process were characterized by DR-LFP. (with K. McGilvray and M. Lukeman)

8.4 Publications

8.4.1 Publications Resulting from Research Presented in this Thesis

1. M. L. Cano, M. N. Chrétien, H. García, J. C. Scaiano, Photophysical properties of dibenzotropylium cation incorporated within acidic ZSM-5 zeolite, *Chem. Phys. Lett.*, **2001**, *345*, 409-414.
2. G. Cosa, M. N. Chrétien, M. S. Galletero, V. Fornés, H. García, J. C. Scaiano, Photocatalytic activity of a multi-component system assembled within zeolites: Case of 2,4,6-triphenylpyrylium or ruthenium tris(bipyridyl) photosensitizers and titanium dioxide relays within zeolite Y, *J. Phys. Chem. B*, **2002**, *106*, 2460-2467.
3. M. N. Chrétien, G. Cosa, H. García, J. C. Scaiano, Increasing the life expectancy of carbanions by zeolite inclusion, *Chem. Commun.*, **2002**, 2154-2155.
4. A. Ricci, L. Maretti, M. N. Chrétien, J.C. Scaiano, TiO_2-promoted mineralization of organic sunscreens in water suspension and sodium dodecyl sulphate (SDS) micelles, *Photochem. Photobiol. Sci.*, **2003**, *2*, 487-492.
5. R. M. Sayre, J. C. Dowdy, A. Ricci, M. N. Chrétien, J. C. Scaiano, Mineralization of organic sunscreens: interesting but relevant? Comment and response, *Photochem. Photobiol. Sci.*, **2003**, 1050-1051.
6. A. Ricci, M. N. Chrétien, J. C. Scaiano, Base-catalyzed ship-in-a-bottle synthesis of a pre-fluorescent, zeolite-incorporated sensor for monitoring radical processes in zeolites, *Chem. Mater.*, **2004**, *16*, 2669-2674.
7. M. Álvaro, M. N. Chrétien, V. Fornes, M. S. Galletero, H. García, J. C. Scaiano, Multi-component donor-acceptor-relay system assembled within the cavities of zeolite Y. Photoinduced electron transfer between $Ru(bpy)_3^{2+}$ and 2,4,6-triphenylpyrylium in the presence of interposed TiO_2, *J. Phys. Chem. B*, **2004**, *108*, 16621-16625.

8. M. N. Chrétien, B. Shen, H. García, A. M. English, J. C. Scaiano, Ship-in-a-bottle synthesis of fluorescence labeled nanoparticles: Applications in imaging, *Photochem. Photobiol.*, **2004**, *80*, 434-437.
9. J. C. Scaiano, C. Aliaga, M. N. Chrétien, M. Frenette, K.-S. Focsaneanu, Fluorescence sensor applications as detectors for DNA damage, free radical formation, and in microlithography, *Pure Appl. Chem.*, **2005**, in press.
10. M. N. Chrétien, J. C. Scaiano, Supramolecular sunscreens: Photophysics and photochemistry, in preparation.
11. M. N. Chrétien, E. Heafey, J. C. Scaiano, Supramolecular sunscreens: Photobiology and cellular toxicity, in preparation.

8.4.2 Other Publications

1. M. Álvaro, M. N. Chrétien, B. Ferrer, V. Fornés, H. García, J. C. Scaiano, First molecular switch encapsulated within the cavities of a zeolite. A dramatic lifetime increase of the charge-separated state, *Chem. Commun.*, **2001**, 2106-2107.
2. Sanjuan. G. Aguirre, M. Álvaro, H. García, J. C. Scaiano, M. N. Chrétien, K.-S. Focsaneanu, Product studies and laser flash photolysis of direct and 2,4,6-triphenylpyrylium-zeolite Y photocatalyzed degradation of fenvalerate, *Photochem. Photobiol. Sci.*, **2002**, *1*, 955-959.
3. P. Formentin, M. J. Sabater, M. N. Chrétien, H. García, J. C. Scaiano, Enantioselective photocyclization of *p*-toluidides of α,β-unsaturated carboxylic acids in solution. A mechanistic and preparative study, *Perkin Trans. 2*, **2002**, 164-167.
4. A. Ricci, M. N. Chrétien, A. Sayari, J. C. Scaiano, Photophysical properties of methyl triazole included in MCM-41, *Photochem. Photobiol*, **2005**, in press.